

# Carnegie Mellon University

CARNEGIE INSTITUTE OF TECHNOLOGY

## THESIS

SUBMITTED IN PARTIAL FULFILLMENT OF THE REQUIREMENTS

FOR THE DEGREE OF Doctor of Philosophy

TITLE Volatility and Chemical Aging of Atmospheric Organic Aerosol

PRESENTED BY Eleni Karnezi

ACCEPTED BY THE DEPARTMENT OF

Chemical Engineering

S. PANDIS

2/17/17

SPYROS PANDIS, ADVISOR

DATE

L. BIEGLER

2/17/17

LORENZ BIEGLER, DEPARTMENT HEAD

DATE

APPROVED BY THE COLLEGE COUNCIL

VIJAYAKUMAR BHAGAVATULA

2/17/17

DEAN

DATE

# **Volatility and chemical aging of atmospheric organic aerosol**

Submitted in partial fulfillment of the requirements for the degree of

Doctor of Philosophy

in

Chemical Engineering

Eleni Karnezi

B.S., Chemical Engineering, University of Patras

Carnegie Mellon University

Pittsburgh, PA

February 2017

*~To my parents, Charalampos and Christina  
and my brother Ioannis~*

## Acknowledgements

I am forever grateful to my advisor, Professor Spyros Pandis for all his excellent guidance and for giving me the opportunity to meet and collaborate with distinguished scientists of the field. I thank him for everything he has offered me, from the scientific advices to the emotional support, stories, insights and philosophical discussions. This dissertation would not have been possible without him.

I would like to acknowledge my advisory committee members, Professors Peter Adams, Neil Donahue, Allen Robinson and Erik Ydstie for taking the time to read my proposal and thesis and offering recommendations and valuable feedback to improve my research.

My deep thank you to Professor Ilona Riipinen for our collaboration in my first project. Her scientific advices made me think more independently and become inquisitive. I owe my gratitude to Dr. Benjamin Murphy for welcoming me in the research group the first years in Carnegie Mellon and for our excellent collaboration and scientific discussions.

I am grateful to Dr. Evangelos Louvaris for our creative and remarkable collaboration and problem sharing that we had all these years. His mentality and words were always helpful to me and made me overcome many difficult moments during my PhD and become more optimistic and confident.

In this journey, I was not alone. I want to thank my brotherly friend Dr. Antonios Tasoglou for being a fellow traveler with me all these years. I was very fortunate having him as a friend and colleague, despite our “fights” and conflicts about food choices, tidiness and sometimes almost everything. Even these were revival, in some cases.

I thank previous and current members of our research group, the Center for Atmospheric Particle Studies (CAPS). Specifically, thank you to all colleagues and friends Ningxin Wang, Dr. Laura Posner, Dr. Wayne Chuang, Dr. Andrea Paciga, Georges Saliba, Dr. Hassan Beydoun, Hugh Li, Pablo Garcia and Spiro Jorga for all their support, help, companionship and laughter. Life in CAPS has been incredible because of the amazing people I have met.

I would like to thank the prior and current members of our sibling research group in Greece, the Laboratory of Air Quality Studies (LAQS) in the university of Patras. Thank you to Dr. Michael

Pikridas, Dr. Evangelia Kostenidou, Dr. Christos Kaltsonoudis, Dr. Christos Fountoukis, Kalliopi Kiari, David Patoulas and Kalliopi Florou.

This journey that has reached to its end would have never been so fascinating without the people I met. Specifically, I am forever thankful to Dr. Javier Lanauze and Dr. Evangelos Papalexakis. Our memories together and their friendship is more than a treasure to me.

I would like to thank my Professor in undergraduate studies Dimitrios Spartinos for the emotional support through all of these years. Our discussions made me feel happy every time and were even relieving during tough times of doubt.

I would also like to thank my prior advisor Professor Costas Kravaris for the scientific insights and help during my undergraduate studies and my diploma thesis. He introduced me to the world of simulations and modeling and his help was fundamental.

My deepest thank you to Aikaterini Varvara Katsiki for her emotional support and friendship during my studies. Our discussions, of all kinds, laughter and companionship were crucial to me.

I would like to thank my best friend and part of my soul Marilena Dimotsantou for inspiring me and urging me to follow my dreams and initially begin this journey. Her love and support sustained me through the tough times. The debt I owe to you is immeasurable. Thank you.

I am eternally thankful to my “sister” Amalia Theofanopoulou. Her love and faith on me and my powers kept me motivated and her company and words during times of doubt were healing to me. She always makes me feel thirteen again.

I am grateful to all the graduate students, staff and faculty members of the Chemical Engineering department at Carnegie Mellon University for their help during my studies.

I would like to thank the US Environmental Protection Agency, the US Department of Energy and National Science Foundation for the funding of my research.

This thesis is dedicated to my family, my parents Charalampos and Christina and my brother Ioannis. Their support, encouragement and love are never ending and have made me the person that I am today. I love you.

## Abstract

Organic particulate matter represents a significant fraction of sub-micrometer atmospheric aerosol mass. However, organic aerosol (OA) consists of thousands of different organic compounds making the simulation of its concentration, chemical evolution, physical and chemical properties extremely challenging. The identity of the great majority of these compounds remains unknown. The volatility of atmospheric OA is one of its most important physical properties since it determines the partitioning of these organic compounds between the gas and particulate phases. The use of lumped compounds with averaged properties is a promising solution for the representation of OA in atmospheric chemical transport models. The two-dimensional volatility basis set (2D-VBS) is a proposed method used to describe OA distribution as a function of the volatility and oxygen content of the corresponding compounds.

In the first part of the work we evaluate our ability to measure the OA volatility distribution using a thermodenuder (TD). We use a new method combining forward modeling, introduction of ‘experimental’ error and inverse modeling with error minimization for the interpretation of TD measurements. The OA volatility distribution, its effective vaporization enthalpy, the mass accommodation coefficient and the corresponding uncertainty ranges are calculated. Our results indicate that existing TD-based approaches quite often cannot estimate reliably the OA volatility distribution, leading to large uncertainties, since there are many different combinations of the three properties that can lead to similar thermograms. We propose an improved experimental approach combining TD and isothermal dilution measurements. We evaluate this experimental approach using the same model and show that it is suitable for studies of OA volatility in the lab and the field.

Measurements combining a thermodenuder (TD) and a High Resolution Time-of-Flight Aerosol Mass Spectrometer (HR-ToF-AMS) took place during summer and winter in Paris, France as part of the collaborative project MEGAPOLI and during the winter of 2013 in the city of Athens. The above volatility estimation method with the uncertainty estimation algorithm is applied to these datasets in order to estimate the volatility distribution for the organic aerosol (OA) and its components during the two campaigns. The concentrations of the OA components as a function of temperature were measured combining data from the thermodenuder and the aerosol mass spectrometer (AMS) with Positive Matrix Factorization (PMF) analysis. Combining the bulk

average O:C ratios and volatility distributions of the various factors, our results are placed into the two-dimensional volatility basis set (2D-VBS) framework. The OA factors cover a broad spectrum of volatilities with no direct link between the average volatility and average O:C of the OA components. An intercomparison among the OA components of both campaigns and their physical properties is also presented.

The approach combining thermodenuder and isothermal dilution measurements is tested in smog chamber experiments using OA produced during meat charbroiling. The OA mass fraction remaining is measured as a function of temperature in the TD and as a function of time in the isothermal dilution chamber. These two sets of measurements are used together to estimate the volatility distribution of the OA and its effective vaporization enthalpy and accommodation coefficient. In the isothermal dilution experiments approximately 20% of the OA evaporate within 15 min. In the TD almost all the OA evaporated at approximately 200°C. The resulting volatility distributions suggest that around 60-75% of the cooking OA (COA) at concentrations around 500  $\mu\text{g m}^{-3}$  consists of low volatility organic compounds (LVOCs), 20-30% of semi-volatile organic compounds (SVOCs) and around 10% of intermediate volatility organic compounds (IVOCs). The estimated effective vaporization enthalpy of COA is  $100 \pm 20 \text{ kJ mol}^{-1}$  and the effective accommodation coefficient is around 0.05. The characteristics of the COA factor from the Athens campaign are compared to those of the OA produced from meat charbroiling in these experiments.

In the next step, different parameterizations of the organic aerosol (OA) formation and evolution in the two-dimensional Volatility Basis Set (2D-VBS) framework are evaluated using ground and airborne measurements collected in the 2012 Pan-European Gas AeroSOls-climate-interaction Study (PEGASOS) field campaign in the Po Valley, Italy. A number of chemical schemes are examined, taking into account various functionalization and fragmentation pathways for biogenic and anthropogenic OA components. Model predictions and measurements, both at the ground and aloft, indicate a relatively oxidized OA with little average diurnal variation. Total OA concentration and O:C ratios were reproduced within experimental error by a number of chemical aging schemes. Anthropogenic SOA is predicted to contribute 15-25% of the total OA, while SOA from intermediate volatility compounds oxidation another 20-35%. Biogenic SOA contributions varied from 15 to 45% depending on the modeling scheme. The average OA and O:C diurnal variation and their vertical profiles showed a surprisingly modest sensitivity to the assumed

vaporization enthalpy for all aging schemes. This can be explained by the intricate interplay between the changes in partitioning of the semivolatile compounds and their gas-phase chemical aging reactions.

The same set of different parameterizations of the organic aerosol (OA) formation and evolution in the two-dimensional Volatility Basis Set (2D-VBS) framework are evaluated using ground measurements collected in the 2013 PEGASOS field campaign in the boreal forest station of *Hyytiälä* in Southern Finland. The most successful is the simple functionalization scheme of Murphy et al. (2012) while all seven aging schemes have satisfactory results, consistent with the ground measurements. Despite their differences, these schemes predict similar contributions of the various OA sources and formation pathways. Anthropogenic SOA is predicted to contribute 11-18% of the total OA, while SOA from intermediate volatility compounds oxidation another 18-27%. The highest contribution comes from biogenic SOA, as expected contributing 40 to 63% depending on the modeling scheme. The primary OA contributes 4% while the SOA resulting from the oxidation of the evaporated POA varies between 4 to 6%. Finally, 5-6% is according to the model the results of long range transport from outside the modeling domain.

## Table of Contents

<b>Chapter 1. Introduction .....</b>	<b>1</b>
1.1 Atmospheric aerosols.....	2
1.2 Volatility of OA .....	4
1.3 Volatility-oxygen content distribution of OA (2D-VBS) .....	7
1.4 Thesis Overview .....	8
1.5 References .....	10
<b>Chapter 2. Measuring the atmospheric organic aerosol volatility distribution: A theoretical analysis.....</b>	<b>16</b>
2.1 Introduction.....	17
2.2 Thermodenuder Model.....	21
2.2.1 Pseudo-experimental data .....	24
2.2.2 Optimum OA volatility distribution.....	25
2.2.3 Estimation of uncertainty .....	28
2.3 Results.....	29
2.4 Improvements of Volatility Measurement Method.....	35
2.4.1 Use of two residence times .....	35
2.4.2 Isothermal dilution experiments .....	36
2.4.3 Combination of TD and isothermal dilution measurements .....	38
2.5 Conclusions.....	41
2.6 References.....	41
<b>Chapter 3. Estimation of the volatility distribution of ambient organic aerosol and its components using thermodenuder measurements.....</b>	<b>46</b>

3.1 Introduction.....	47
3.2 Methods.....	48
3.2.1 Paris campaigns .....	48
3.2.2 Athens campaign.....	49
3.3 Data Analysis .....	50
3.3.1 Paris campaigns .....	50
3.3.2 Athens campaign.....	53
3.4 Volatility Distribution Estimation.....	55
3.5 Effect of concentration on volatility distribution.....	56
3.6 Results and Discussion .....	57
3.6.1 Organic aerosol volatility during Paris campaigns .....	57
3.6.2 Organic aerosol volatility during the Athens campaign .....	59
3.6.3 Volatility of organic aerosol components during Paris campaigns .....	60
3.6.4 Volatility of OA components during Athens campaign .....	65
3.7 Synthesis of Results in the 2D-VBS .....	69
3.8 Estimation of vaporization enthalpy and accommodation coefficient.....	72
3.9 Effects of OA concentration on estimated volatility distribution .....	74
3.10 Conclusions.....	77
3.11 References.....	79
<b>Chapter 4. Estimation of the volatility distribution of cooking organic aerosol combining thermodenuder and isothermal dilution measurements .....</b>	<b>84</b>
4.1 Introduction.....	85
4.2 Experimental description .....	87

4.2.1 Loss corrections .....	89
4.2.2 Determination of the volatility distributions.....	90
4.3 Results and discussion .....	91
4.3.1 Volatility distribution of cooking organic aerosol (COA).....	91
4.3.2 Sensitivity analysis.....	96
4.3.2.1 Sensitivity to accommodation coefficient.....	96
4.3.2.2 Sensitivity to vaporization enthalpy.....	97
4.4 Benefits of combining TD and Isothermal dilution .....	97
4.5 Comparison of laboratory COA with the ambient COA factor .....	99
4.6 Conclusions.....	101
4.7 References.....	102
<b>Chapter 5. Simulation of atmospheric organic aerosol using its volatility-oxygen content distribution during the PEGASOS 2012 campaign in Po Valley, Italy .....</b>	<b>107</b>
5.1 Introduction.....	108
5.2 Lagrangian CTM Description .....	110
5.3 Simulated periods.....	111
5.4 Chemical Aging Schemes .....	112
5.4.1 Functionalization schemes .....	112
5.4.2 bSOA aging parameterizations .....	114
5.4.3 Fragmentation parameterizations.....	114
5.5 Combination of parameterizations .....	114
5.6 Evaluation of parameterizations .....	115
5.7 Results.....	116

5.7.1 Simple functionalization (1-bin case).....	116
5.7.2 Effect of functionalization scheme .....	121
5.7.3 Effect of bSOA production during aging.....	122
5.7.4 The role of fragmentation .....	123
5.7.5 Synthesis of results .....	123
5.7.6 The role of vaporization enthalpy .....	125
5.8 Conclusions.....	127
5.9 References.....	128
<b>Chapter 6. Simulation of atmospheric organic aerosol using its volatility-oxygen content distribution during the PEGASOS 2013 campaign in Finland .....</b>	<b>134</b>
6.1 Introduction.....	135
6.2 Application of 2D-VBS in Finland.....	136
6.2.1 Site description and measurement period .....	136
6.2.2 PMCAMx-Trj model .....	136
6.2.3 Simulated periods.....	137
6.2.4 Chemical Aging Schemes .....	138
6.2.5 Evaluation of parameterizations .....	139
6.3 Results.....	140
6.3.1 Simple functionalization scheme (1-bin case) .....	140
6.3.2 Effect of functionalization scheme .....	142
6.3.3 Effect of additional bSOA production during aging.....	143
6.3.4 The role of fragmentation .....	144
6.3.5 Synthesis of results .....	145

6.3.6 Predicted OA composition.....	145
6.4 Conclusions.....	146
6.5 References.....	147
<b>Chapter 7. Conclusions and future work.....</b>	<b>151</b>
7.1 Conclusions.....	152
7.2 Future work.....	156
7.2.1 Use of thermodenuder and Isothermal Dilution Measurements for the estimation of volatility of ambient OA.....	156
7.2.2 Simulation of volatility - oxygen content distribution of the OA during SOAS campaign.....	157
7.3 References.....	157
<b>Appendices.....</b>	<b>158</b>
<b>Appendix A.....</b>	<b>159</b>
<b>Appendix B.....</b>	<b>164</b>
<b>Appendix C.....</b>	<b>170</b>

## List of Figures

<b>Figure 1.1</b> Aerosol size and comparison with typical human hair (image courtesy of the US EPA).....	2
<b>Figure 1.2</b> Change of visibility for Patras, Greece for: (a) a day with $PM_{10}= 20 \mu\text{g m}^{-3}$ and (b) a day with $PM_{10}= 50 \mu\text{g m}^{-3}$ .....	3
<b>Figure 1.3</b> Schematic design of a thermodenuder (An et al., 2007) .....	4
<b>Figure 1.4</b> Effect of (a) vaporization enthalpy ( $\Delta H_{\text{vap}}$ ) and (b) accommodation coefficient $a_m$ on thermograms assuming $C^*=1 \mu\text{g m}^{-3}$ for: (a) $a_m=1$ and various $\Delta H_{\text{vap}}$ values and (b) $\Delta H_{\text{vap}}=80 \text{ kJ mol}^{-1}$ and various $a_m$ values. The mass fraction remaining versus the temperature were calculated using the mass transfer model of Riipinen et al. (2010) .....	5
<b>Figure 1.5</b> VBS presentation (Donahue et al. 2006) with total loadings (in $\mu\text{g m}^{-3}$ ) shown with full bars and the condensed-phase portion with filled (green) bars. Compounds are distributed according to their mass-equivalent effective saturation concentration ( $C^*$ , also in $\mu\text{g m}^{-3}$ ), which is presented as a logarithmically distributed basis set.....	6
<b>Figure 1.6</b> 2D-VBS representation (Donahue et al. (2012). The x axis represents volatility as effective saturation concentration $C^*$ and the y axis the OA oxygen content or else the O:C. Various aerosol factors and their location in the scheme are shown, as well as, paths with green due to chemistry .....	7
<b>Figure 2.1</b> Predicted thermograms (MFR versus $T_{\text{TD}}$ ) for OA with different properties. A single component aerosol ( $C^*=1 \mu\text{g m}^{-3}$ , $\Delta H_{\text{vap}}=80 \text{ kJ mol}^{-1}$ and $a_m=0.05$ ) gives practically the same thermogram as one with a much lower volatility ( $C^*=0.01 \mu\text{g m}^{-3}$ , $\Delta H_{\text{vap}}=100 \text{ kJ mol}^{-1}$ and $a_m=1$ ) .....	24
<b>Figure 2.2</b> Typical example of “construction” of TD pseudo-data. The red line is the thermogram corresponding to the true properties of the aerosol and the black dots correspond to the ‘measured’ MFR versus $T_{\text{TD}}$ for an aerosol consisting of two components: very low volatility material (60% $C^*=0.01 \mu\text{g m}^{-3}$ ) and relatively high volatility material (40% $C^*=10 \mu\text{g m}^{-3}$ ), vaporization enthalpy and mass accommodation coefficient equal to $100 \text{ kJ mol}^{-1}$ and	

1 correspondingly. Twelve ‘measurements’ were constructed for equally spaced temperatures between 24 and 140°C by corrupting the correct values with random experimental error..... 25

**Figure 2.3** Estimated (bars) and true (red lines) volatility distribution for OA consisting of 10%  $C^*=0.1 \mu\text{g m}^{-3}$ , 30%  $1 \mu\text{g m}^{-3}$ , 60%  $10 \mu\text{g m}^{-3}$ ,  $\Delta H_{\text{vap}}=50 \text{ kJ mol}^{-1}$  and  $a_m=1$ , based on TD pseudo-data. (a) Solution corresponding to a local minimum of the objective function. The estimated vaporization enthalpy and accommodation coefficient are  $\Delta H_{\text{vap}}=38 \text{ kJ mol}^{-1}$  and  $a_m=0.9$ . (b) Solution for the global minimum. The estimated  $\Delta H_{\text{vap}}$  and  $a_m$  are  $68 \text{ kJ mol}^{-1}$  and 0.84 respectively ..... 27

**Figure 2.4** Estimated (bars) and true (red lines) parameter values for an OA with 80%  $0.01 \mu\text{g m}^{-3}$ , 5%  $0.1 \mu\text{g m}^{-3}$ , 10%  $1 \mu\text{g m}^{-3}$ , 5%  $10 \mu\text{g m}^{-3}$ ,  $\Delta H_{\text{vap}}=80 \text{ kJ mol}^{-1}$  and  $a_m=1$  for: 6 measurements (a) volatility distribution, (b)  $\Delta H_{\text{vap}}$ , (c)  $a_m$ , and using 12 measurements for: (d) volatility distribution, (e)  $\Delta H_{\text{vap}}$  and (f)  $a_m$ . The error bars represent the uncertainty of the estimated value..... 30

**Figure 2.5** Estimated (bars) and true property values (red lines) using 12 TD measurements, for two types of OA. (a) volatility distribution, (b)  $\Delta H_{\text{vap}}$ , (c)  $a_m$  for OA with 60%  $0.01 \mu\text{g m}^{-3}$  and 40%  $10 \mu\text{g m}^{-3}$ ,  $\Delta H_{\text{vap}}=100 \text{ kJ mol}^{-1}$  and  $a_m=1$  and (d) volatility distribution, (e)  $\Delta H_{\text{vap}}$ , (f)  $a_m$  for OA with 50%  $0.01 \mu\text{g m}^{-3}$  and 50%  $1 \mu\text{g m}^{-3}$ ,  $\Delta H_{\text{vap}}=150 \text{ kJ mol}^{-1}$  and  $a_m=1$ . The error bars represent the uncertainty of the estimated value ..... 32

**Figure 2.6** Isothermal dilution measurements (MFR as function of time) for an aerosol with 60%  $0.01 \mu\text{g m}^{-3}$ , 40%  $10 \mu\text{g m}^{-3}$ ,  $\Delta H_{\text{vap}}=100 \text{ kJ mol}^{-1}$  and  $a_m=1$ . The red line corresponds to the true properties of the aerosol and the black dots are the ‘measured’ MFR values ..... 37

**Figure 2.7** Estimated (bars) volatility distribution and accommodation coefficient and true (red lines) values using isothermal dilution “measurements”, for an OA with 60%  $0.01 \mu\text{g m}^{-3}$  and 40%  $10 \mu\text{g m}^{-3}$ ,  $\Delta H_{\text{vap}}=100 \text{ kJ mol}^{-1}$  and  $a_m=1$ . (a) volatility distribution and (b)  $a_m$ ... 37

**Figure 2.8** Estimated (bars) and true (red lines) parameter values combining TD and isothermal dilution measurements, for an OA with 60%  $0.01 \mu\text{g m}^{-3}$  and 40%  $10 \mu\text{g m}^{-3}$ ,  $\Delta H_{\text{vap}}=100 \text{ kJ mol}^{-1}$  and  $a_m=1$  for: (a) volatility distribution, (b)  $\Delta H_{\text{vap}}$ , (c)  $a_m$ ..... 39

<b>Figure 2.9</b> Estimated (bars) and true (red lines) parameter values combining TD and isothermal dilution measurements, for an OA with 50% 0.01 $\mu\text{g m}^{-3}$ and 50% 1 $\mu\text{g m}^{-3}$ , $\Delta H_{\text{vap}}=150 \text{ kJ mol}^{-1}$ and $a_m=1$ for: (a) volatility distribution, (b) $\Delta H_{\text{vap}}$ , (c) $a_m$ .....	40
<b>Figure 3.1</b> Ambient (blue dots) and thermodenuder (red dots) organic mass concentration measurements for Paris during summer 2009.....	51
<b>Figure 3.2</b> Ambient (blue dots) and thermodenuder (red dots) OA mass time series for the winter Paris 2010 campaign.....	52
<b>Figure 3.3</b> Timeseries of OA mass concentration: ambient OA (blue line) and TD OA (red line) for Athens winter campaign .....	54
<b>Figure 3.4</b> OA composition versus the initial concentration of the OA. ELVOCs are shown with magenta, LVOCs with blue, SVOCs with cyan and IVOCs with yellow. The y axis represents the percentages of ELVOCs, LVOCs, SVOCs and IVOCs for each bin that represents the initial concentration of the OA .....	56
<b>Figure 3.5</b> Loss-corrected average OA thermograms for summer (red circles) and winter (blue squares) Paris campaigns. The error bars correspond to plus/minus 2 standard deviations of the mean. Points with no error bars correspond to a single measurement.....	57
<b>Figure 3.6</b> (a) Average loss-corrected OA thermograms for summer (up left panel) and (b) winter (up right panel) OA Paris campaigns. The error bars correspond to plus/minus 2 standard deviations of the mean. The black line represents the best fit estimated thermogram. (c) Estimated volatility distributions for summer (down left panel) and (d) winter total Paris OA (down right panel). The error bars correspond to the fitting uncertainties according to the algorithm of Karnezi et al. (2014).....	58
<b>Figure 3.7</b> (a) Average loss-corrected total OA thermogram for Athens campaign. Magenta circles represent the measurements with error bars representing the corresponding variability ( $\pm 1$ standard deviation of the mean). The black line represents the best fit estimated thermogram using the approach of Karnezi et al. (2014). (b) Estimated OA volatility distribution. Error bars represent the corresponding uncertainties according to the algorithm of Karnezi et al. (2014).....	59

<b>Figure 3.8</b> Estimated volatility distributions for summer PMF factors (left panel) and winter PMF factors (right panel) during Paris campaigns. The error bars correspond to the fitting uncertainties according to the algorithm of Karnezi et al. (2014) .....	61
<b>Figure 3.9</b> Estimated best-fit thermograms for all PMF factors during Paris campaigns. The solid lines represent the thermograms for the summer campaign and the dashed lines the thermograms for the winter campaign .....	62
<b>Figure 3.10</b> Seasonal mass spectra comparison for (a) HOA and (b) COA in Paris winter and summer campaigns. Red lines correspond to the summer measurements while blue symbols correspond to the winter data .....	63
<b>Figure 3.11</b> Average concentrations of OA components after the TD as a function of the TD temperature for Athens winter campaign.....	66
<b>Figure 3.12</b> Estimated volatility distributions of OA components during Athens winter campaign. Error bars represent the corresponding uncertainties according to the algorithm of Karnezi et al. (2014). Typical values of 100 kJ mol <sup>-1</sup> and 1.0 were assumed for the enthalpy of vaporization and accommodation coefficient.....	67
<b>Figure 3.13</b> Thermograms of the four PMF factors during Athens campaign. Circles correspond to the average loss corrected measurements along with their uncertainties ( $\pm 1$ standard deviation of the mean). Lines represent the best fit estimated thermograms by the model of Karnezi et al. (2014) .....	68
<b>Figure 3.14</b> Effective saturation concentration $C^*$ and O:C (oxidation state on the left y-axis) for classes of organic species as shown in Donahue et al. (2012) along with estimated factors from the summer and winter Paris campaigns. The red bars represent the HOA factors, the pink are the COA factors, the green the SVOOA and OOA, the blue represents the MOA factor, the brown the BBOA factor and the black the LVOOA factor. The darker shading of the colored bars denotes a larger mass fraction for a given $C^*$ bin. The diamonds represent the average $\log_{10}(C^*)$ value of each PMF factor .....	70
<b>Figure 3.15</b> Saturation concentration, mean O:C ratio (left y-axis) and mean carbon oxidation state ( $OS_c$ ) (right y-axis) for OA factors following Donahue et al. (2012) along with estimated	

factors from Athens winter campaign. The shaded areas indicate the locations of the various factors proposed by Donahue et al. (2012) while the colored horizontal bars the estimated locations of the factors. Blue bars represent OOA, red bars HOA, green bars BBOA, and cyan bars COA. Darker shading of the horizontal colored bars denotes larger mass fractional contribution for a given  $C^*$  bin. The stars represent the average  $\log_{10}(C^*)$  value for a given PMF factor ..... 71

**Figure 3.16** Comparison of estimated vaporization enthalpies in the Athens and Paris campaigns for (a) BBOA, (b) COA, (c) HOA and (d) OOA for winter campaigns and SVOOA for the Paris summer campaign..... 72

**Figure 3.17** Estimated accommodation coefficients for the Athens and Paris campaigns for: (a) BBOA, (b) COA, (c) HOA and (d) OOA for the winter campaigns and SV-OOA for Paris summer campaign ..... 73

**Figure 3.18** Estimated concentrations of the BBOA components in the particulate phase (green) and gas phase in Athens for (a) for BBOA equal to  $4.3 \mu\text{g m}^{-3}$  and (b) for BBOA= $0.6 \mu\text{g m}^{-3}$  ..... 74

**Figure 3.19** Fractional composition of the BBOA factor. For initial concentration  $4.3 \mu\text{g m}^{-3}$  (Athens winter campaign average concentration of BBOA) and for  $0.6 \mu\text{g m}^{-3}$  (corresponding to the average BBOA in Paris)..... 75

**Figure 3.20** Comparison of composition of the factors from the Athens and Paris winter campaigns at the Paris concentration levels. With magenta we represent the ELVOCs, with blue the LVOCs and with cyan the SVOCs..... 76

**Figure 4.1** Experimental setup used: The COA in the main chamber was characterized using a TD a HR-ToF-AMS, and an SMPS. A metal bellows MB 602 pump was used to transfer OA from the main to the dilution chamber. The COA in the dilution chamber was measured by the HR-ToF-AMS and the SMPS. A PTR-MS was used to measure the dilution ratio ..... 88

**Figure 4.2** Estimated volatility distributions for Experiment 1 (red bars) and for Experiment 2 (blue bars) using the approach of Karnezi et al. (2014). The error bars represent the uncertainty range..... 91

**Figure 4.3** (a) Estimated effective vaporizations enthalpies along with their uncertainties for both experiments using the approach of Karnezi et al. (2014). (b) Estimated effective accommodation coefficients along with their uncertainties for both experiments. (c) COA mass composition of both experiments. LVOCs are represented in magenta, SVOCs in red, and IVOCs in white ..... 92

**Figure 4.4** (a) Thermogram of the OA TD measurements of Experiment 1. The red circles represent the loss-corrected measurements and the black line represents the best fit estimated by the model of Karnezi et al. (2014). (b) Mass fraction during isothermal dilution as a function of time for Exp. 1. Red circles represent the loss-corrected measurements and the black line the estimated best model fit. (c) Predicted COA composition for different effective saturation concentrations as a function of TD temperature. Red color represents the contribution of the components with  $C^* = 10^{-3} \mu\text{g m}^{-3}$ , green the  $C^* = 10^{-2} \mu\text{g m}^{-3}$ , blue the  $C^* = 1 \mu\text{g m}^{-3}$ , magenta the  $C^* = 10 \mu\text{g m}^{-3}$ , orange the  $C^* = 10^2 \mu\text{g m}^{-3}$ , and finally violet for the  $C^* = 10^3 \mu\text{g m}^{-3}$ . (d) COA composition for different effective saturation concentrations as a function of time during isothermal dilution ..... 93

**Figure 4.5** (a) Normalized HR-ToF-AMS mass spectra of the COA at ambient temperature (red bars) compared to that in the TD at 200°C (blue crosses). (b) Normalized HR-ToF-AMS mass spectra at the onset of dilution experiment (red bars) compared to those measured after one hour (blue crosses), and those at the end of the experiment (magenta crosses)..... 94

**Figure 4.6** (a) Thermogram of the OA TD measurements of Experiment 2. The red circles represent the loss-corrected measurements and the black line represents the best fit estimated by the model of Karnezi et al. (2014). (b) Mass fraction during isothermal dilution as a function of time for Exp. 2. Red circles represent the loss-corrected measurements and the black line the estimated best model fit. (c) Predicted COA composition for different effective saturation concentrations as a function of TD temperature. Red color represents the contribution of the components with  $C^* = 10^{-3} \mu\text{g m}^{-3}$ , green the  $C^* = 10^{-2} \mu\text{g m}^{-3}$ , blue the  $C^* = 1 \mu\text{g m}^{-3}$ , magenta the  $C^* = 10 \mu\text{g m}^{-3}$ , orange the  $C^* = 10^2 \mu\text{g m}^{-3}$ , and finally violet for the  $C^* = 10^3 \mu\text{g m}^{-3}$ . (d) COA composition for different effective saturation concentrations as a function of time during isothermal dilution ..... 95

**Figure 4.7** (a) Estimated volatility distributions of the COA along with their uncertainties for Experiment 1 using the approach of Karnezi et al. (2014). Red bars represent the volatility distribution using the combination of thermodenuder and isothermal dilution measurements whereas blue bars represent the volatility distribution using only thermodenuder measurements (b) COA compositions for the two cases of (a). LVOCs are in magenta, SVOCs in red, and IVOCs in white. (c) Estimated volatility distributions of the COA for Experiment 2 using the approach of Karnezi et al. (2014). Red bars represent the volatility distribution using the combination of thermodenuder and isothermal dilution measurements whereas blue bars represent the volatility distribution using only thermodenuder measurements. (d) COA compositions for the two cases of (c). LVOCs are in magenta, SVOCs in red..... 98

**Figure 4.8** Partitioning of COA components, with total loadings (in  $\mu\text{g m}^{-3}$ ) shown with full bars and the condensed-phase portion with filled (green) bars. For experiment 1: (a) for initial concentration of OA, COA= $541 \mu\text{g m}^{-3}$  (laboratory level), (b) for COA= $1.2 \mu\text{g m}^{-3}$  (after repartitioning) and for experiment 2: (c) for initial concentration of OA, COA= $642 \mu\text{g m}^{-3}$  (laboratory level), (d) for COA= $1.2 \mu\text{g m}^{-3}$  (after repartitioning) ..... 100

**Figure 4.9** Comparison of the COA composition (a) between the Athens winter COA factor (Louvaris et al., 2017) and Experiment 1. and (b) between the Athens winter COA factor and Experiment 2. The comparison of estimated (c) vaporization enthalpy and (d) accommodation coefficient is also shown..... 101

**Figure 5.1** (a) The ensemble of 20 trajectories calculated by HYSPLIT for air parcels arriving at the San Pietro Capofiume site on 8 July 2012 at 3:00 LT and (b) the ensemble average trajectory calculated by the HYSPLIT clustering utility ..... 112

**Figure 5.2** Average O:C diurnal evolution at the ground level in San Pietro Capofiume for the 1-bin simulation. The black line shows the model predictions and the shaded area corresponds to one standard deviation. The red symbols represent the AMS measurements and the error bars correspond to one standard deviation ..... 119

**Figure 5.3** Average vertical predicted and measured (1-bin case) (a) O:C ratio and (b) organic aerosol mass concentration for the Zeppelin measurements over Po Valley. The black line shows the model predictions and the shaded areas the standard deviation. The red symbols

represent the AMS Zeppelin measurements and the error bars correspond to one standard deviation..... 120

**Figure 5.4** Average diurnal profile at the ground level OA in San Pietro Capofiume. With dark blue we represent the OA from long range transport, with blue the anthropogenic SOA produced during the oxidation of anthropogenic VOCs (aSOA-v), with cyan the biogenic SOA (bSOA), with yellow the SOA from oxidation of intermediate volatility compounds (SOA-iv), with red the SOA from the oxidation of semivolatile OA (SOA-sv) and finally with dark red the fresh primary organic aerosol (FPOA). The AMS measurements are shown with black symbols and the error bars correspond to one standard deviation ..... 121

**Figure 5.5** Predicted OA composition for the schemes with good performance for San Pietro Capofiume. The red line indicates the average measured OA equal to  $2.8 \mu\text{g m}^{-3}$ ..... 125

**Figure 5.6** Diurnally average (a) O:C ratios and (b) organic aerosol mass concentrations. Average vertical organic aerosol (c) O:C and (d) organic aerosol mass concentrations assuming in the model  $\Delta H_{\text{vap}} = 30 \text{ kJ mol}^{-1}$  (black line),  $\Delta H_{\text{vap}} = 75 \text{ kJ mol}^{-1}$  (blue line), and  $\Delta H_{\text{vap}} = 150 \text{ kJ mol}^{-1}$  (magenta line) for the Po Valley in Italy. The black symbols show the ground AMS measurements. The red symbols show the Zeppelin measurements. The error bars represent one standard deviation ..... 126

**Figure 6.1** (a) The ensemble of 20 trajectories calculated by HYSPLIT for air parcels arriving at the site of Hyytiälä on 7 May 2013 at 17:00 LT and (b) the ensemble average trajectory calculated by the HYSPLIT clustering utility..... 138

**Figure 6.2** Average diurnal OA mass concentration at the ground level in Hyytiälä for the 1-bin simulation. The red line shows the model predictions and the black symbols represent the ACSM measurements. The error bars correspond to one standard deviation..... 142

**Figure 6.3** Predicted contribution of (a) ASOA-v, (b) BSOA, (c) SOA from oxidation of intermediate volatility organic compounds, (d) FPOA, (e) SOA from oxidation of evaporated POA, and (f) OA from long range transport using various aging parameterizations ..... 143

**Figure 6.4** Predicted OA composition for the schemes with good performance for Hyytiälä. The red line indicates the average measured OA equal to  $2.1 \mu\text{g m}^{-3}$  ..... 145

**Figure A.1** Comparison of mass spectra of ambient OA PMF factors analysis (bars) and ambient plus thermodenuder PMF analysis (crosses) during Athens winter 2013 campaign ... 160

**Figure A.2** Corrected thermograms along with the error bars representing the standard deviation of the data, with best-fit volatility distributions (solid line) for PMF factors during Paris summer and winter campaign. A few points in the LV-OOA summer graph with very high uncertainties are not shown..... 161

**Figure A.3** Comparison of total OA volatility distributions during Athens winter 2013 campaign estimated by the model of Karnezi et al. (2014) (blue bars) with those calculated by the composition weighted average method (red bars) ..... 162

**Figure A.4** Estimated volatility distributions of various OA components during wintertime Athens and Paris summer and winter campaigns for 2 different approaches, using assumed (red bars) or variable (dark red bars)  $\Delta H_{\text{vap}}$  ..... 163

**Figure B.1** Wall loss rate constants as a function of particle size (red circles) for the isothermal dilution chamber during Exp. 1. The error bars represent the  $\pm 1$  standard deviation..... 165

**Figure B.2** (a) Number concentration during isothermal dilution of Exp. 1 as a function of time measured by the SMPS. (b) Mass fraction as function of time during isothermal dilution of Exp. 1 measured by the SMPS ..... 165

**Figure B.3** (a) Number concentration during isothermal dilution of Exp. 2 as a function of time measured by the SMPS. (b) Mass fraction as function of time during isothermal dilution of Exp. 2 measured by the SMPS ..... 166

**Figure B.4** (a) Measured mass fractions as function of time during isothermal dilution of Exp. 2. (b) Corrected mass fractions as a function of time during isothermal dilution of Exp. 2..... 166

**Figure B.5** (a) Estimated volatility distributions assuming different accommodation coefficients for Exp. 1 using the approach of Karnezi et al. (2014). The error bars represent the corresponding uncertainty ranges. Red, blue, green, and dark yellow bars represent the estimated volatility distributions for the base case,  $a_m=0.01$ ,  $a_m=0.1$ , and  $a_m=1.0$  respectively. (b) Corresponding COA composition of Exp. 1. LVOCs are represented in magenta, SVOCs

in red, and IVOCs in white. (c) Estimated volatility distributions for different accommodation coefficients for Exp. 2 using the approach of Karnezi et al. (2014). The error bars represent the corresponding uncertainty ranges. Red, blue, green, and dark yellow bars represent the estimated volatility distributions for the base case,  $a_m=0.01$ ,  $a_m=0.1$ , and  $a_m=1.0$  respectively. (d) Corresponding COA composition of Exp. 2. LVOCs are represented in magenta, SVOCs in red ..... 167

**Figure B.6** (a) Estimated volatility distributions assuming different vaporization enthalpies for Exp. 1 using the approach of Karnezi et al. (2014). The error bars represent the corresponding uncertainty ranges. Red, blue, and green bars represent the estimated volatility distributions for the base case,  $\Delta H_{vap}=80 \text{ kJ mol}^{-1}$ , and  $\Delta H_{vap}=150 \text{ kJ mol}^{-1}$  respectively. (b) Corresponding COA composition of Exp. 1. LVOCs are represented in magenta, SVOCs in red, and IVOCs in white. (c) Estimated volatility distributions assuming different vaporization enthalpies for Exp. 2 using the approach of Karnezi et al. (2014). The error bars represent the corresponding uncertainty ranges. Red, blue, and green bars represent the estimated volatility distributions for the base case,  $\Delta H_{vap}=80 \text{ kJ mol}^{-1}$ , and  $\Delta H_{vap}=150 \text{ kJ mol}^{-1}$  respectively. (d) Corresponding COA composition of Exp. 2. LVOCs are represented in magenta, SVOCs in red ..... 168

**Figure B.7** Bypass AMS spectra for Athens winter campaign and COA factor (Louvaris et al., 2017) for (a) Experiment 1 COA and (b) Experiment 2 COA from meat charbroiling ..... 169

**Figure C.1** The path that the Zeppelin followed during one representative day (July 4, 2012), over the Po Valley in Italy ..... 171

**Figure C.2** Average O:C-volatility distribution of OA mass concentration on San Pietro Capofiume using (a) the simple scheme (1-bin), (b) the two-bin shift simple scheme (2-bin) and (c) the detailed functionalization scheme (DET) ..... 171

**Figure C.3** Predicted contribution of (a) ASOA-v, (b) bSOA, (c) SOA from oxidation of intermediate volatility organic compounds (SOA-iv), (d) FPOA, (e) SOA from oxidation of evaporated POA, and (f) OA from long range transport for the various aging parameterizations ..... 172

**Figure C.4** Estimation of optimum branching ratio (fragmentation probability) for fragmentation for the: (a) simple functionalization (1-bin), (b) simple functionalization with bSOA aging (1-bin/bSOA), (c) 2-bin functionalization (2-bin), (d) 2-bin functionalization with bSOA aging (2-bin/bSOA), (e) detailed functionalization scheme (DET) and (f) detailed functionalization with bSOA aging (DET/bSOA). The red line shows the minimum absolute error. Note that for the first case of 1-bin parameterization the optimum is at  $b=0$  ..... 173

**Figure C.5** Averaged vertical profiles for (a) O:C ratio and (b) OA mass concentration using various parameterizations ..... 174

## List of Tables

<b>Table 2.1</b> Values of the true and estimated properties (volatility distribution, vaporization enthalpy, accommodation coefficient) for three OA examples .....	26
<b>Table 2.2</b> Sets of random volatility distributions used for the evaluation of different inversion approaches.....	33
<b>Table 2.3</b> Results for the sets of random volatility distributions using different inversion approaches.....	34
<b>Table 3.1</b> Average and threshold ambient concentrations for each PMF factor for Paris summer and winter campaigns.....	53
<b>Table 3.2</b> Average ambient concentrations and percentage of points above threshold for each PMF factor for the 2013 Athens winter campaign.....	55
<b>Table 4.1</b> Summary of the Experiments characteristics .....	89
<b>Table 5.1</b> Characteristics of the different parameterizations used in our simulations .....	115
<b>Table 5.2</b> Performance metrics of different parameterizations during the PEGASOS campaign for ground O:C measurements. The measured average O:C was 0.58.....	117
<b>Table 5.3</b> Performance metrics of different parameterizations during the PEGASOS campaign for ground OA mass measurements. The measured average organic aerosol concentration was $2.8 \mu\text{g m}^{-3}$ .....	118
<b>Table 6.1</b> Characteristics of different parameterizations used in our simulations .....	139
<b>Table 6.2</b> Performance metrics of different parameterizations during the PEGASOS 2013 campaign for ground OA concentration. The measured average organic aerosol mass concentration was $2.1 \mu\text{g m}^{-3}$ .....	141
<b>Table A.1</b> Estimated volatility distributions for the OA and the PMF factors from Paris summer and winter campaign .....	159

<b>Table A.2</b> Estimated volatility distributions for the OA and the PMF factors for Athens campaign.....	159
<b>Table A.3</b> Calculated average volatilities as $\log_{10}C^*$ values weighted by the mass fractions of each bin for Athens winter campaign .....	160
<b>Table B.1</b> Estimated volatility distributions for the COA along with estimated properties of the two experiments using both TD and isothermal dilution measurements and only TD measurements using the approach of Karnezi et al. (2014).....	164
<b>Table B.2</b> Estimated volatility distributions for the sensitivity to the parameter estimation using the approach of Karnezi et al. (2014).....	164
<b>Table C.1</b> Performance of simulations with various vaporization enthalpies for the 1-bin parameterization during PEGASOS campaign for O:C measurements at the ground.....	170

# **Chapter 1**

## **Introduction**

## 1.1 Atmospheric aerosols

The Atmospheric aerosol consists of airborne solid or liquid particles with sizes from a few nanometers to tens of micrometers. These particles are emitted directly (primary aerosol) or formed through gas/particle conversion processes in the atmosphere (secondary aerosol). Atmospheric particles are classified based on their size as fine particulate matter (PM) that is composed of particles with diameters smaller than  $2.5\ \mu\text{m}$ , coarse PM with diameters larger than  $2.5\ \mu\text{m}$ , and ultrafine particles with diameters smaller than  $0.1\ \mu\text{m}$  (Figure 1.1). They are usually removed from the atmosphere through deposition at the Earth's surface (dry deposition) and incorporation into cloud droplets during precipitation (wet deposition). These removal mechanisms, wet and dry deposition, lead to their relatively small average residence times in the atmosphere from a few days to a few weeks.

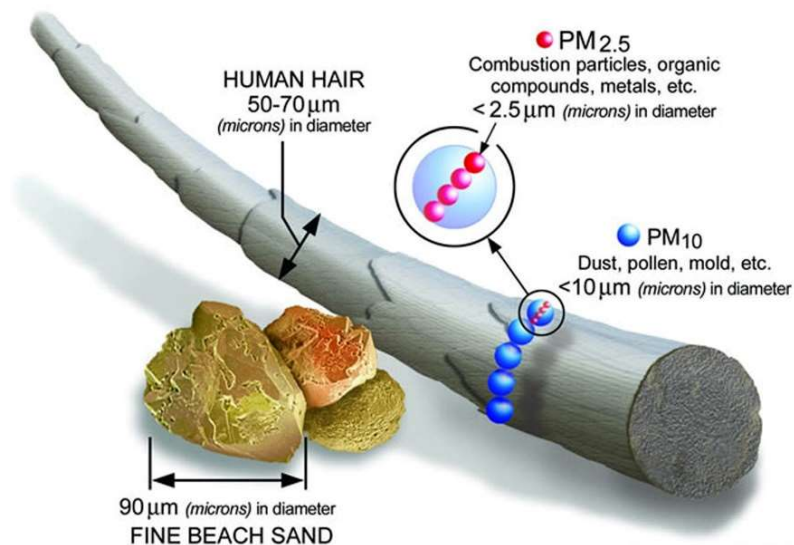


**Figure 1.1** Aerosol size and comparison with typical human hair (image courtesy of the US EPA).

Several epidemiological studies have shown that atmospheric PM can increase rates of respiratory and cardiovascular diseases and exposure to high concentrations can cause premature death (Nel et al., 2005; Pope and Dockery, 2006; Pope et al., 2009; Caiazzo et al., 2013). This has resulted to the need for legislation of ambient PM levels. The average annual PM<sub>2.5</sub> standard for the EU is 25

$\mu\text{g m}^{-3}$  compared to the  $12 \mu\text{g m}^{-3}$  annual US standard. For particles with diameters smaller than  $10 \mu\text{m}$  ( $\text{PM}_{10}$ ) the annual EU standard is  $40 \mu\text{g m}^{-3}$  and the daily standard  $50 \mu\text{g m}^{-3}$ .

Aerosols affect visibility creating “haze events” in high concentrations in polluted areas. (Figure 1.2). Aerosols have also direct and indirect effects on climate. They absorb and scatter solar radiation (direct effect). Particles containing black carbon or mineral dust are significant absorbers. All other particles scatter solar radiation back into space leading to an increase of the Earth’s albedo and thus have a cooling net effect (Seinfeld and Pandis, 2006). Atmospheric particles can also act as nuclei on which water can condense forming cloud droplets, influencing the properties and lifetime of clouds (indirect effect) (IPCC, 2014).

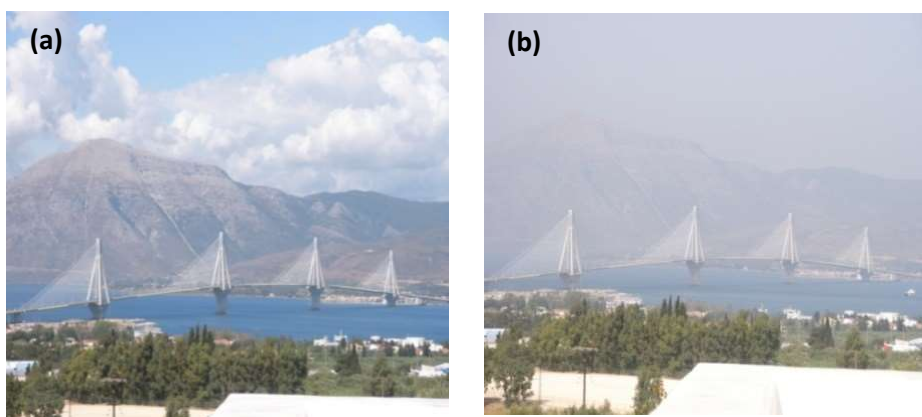


**Figure 1.2** Change of visibility for Patras, Greece for: (a) a day with  $\text{PM}_{10} = 20 \mu\text{g m}^{-3}$  and (b) a day with  $\text{PM}_{10} = 50 \mu\text{g m}^{-3}$ .

Aerosols contain a wide variety of inorganic and organic compounds, with organics often representing more than 50% of their submicron mass (Zhang et al., 2007; Jimenez et al., 2009). Organic aerosol (OA) originates from many different natural and anthropogenic sources and processes. It can be emitted directly, e.g. from fossil fuel and biomass combustion (so called primary organic aerosol, POA) or formed during the atmospheric oxidation of volatile, intermediate volatility and semivolatile organic compounds (secondary organic aerosol, SOA). Since the oxidation pathways for organic vapors are complex and the reactions lead to hundreds or thousands of oxygenated products, our understanding of organic aerosol formation mechanisms and the OA chemical and physical properties is still incomplete. Thus, there is limited knowledge of the sources, chemical evolution, and physical properties of OA due to the complexity of the mostly unknown thousands of organic compounds that OA particles contain. These uncertainties

often lead to erroneous predictions of OA concentrations by chemical transport models (Gaydos et al., 2007; Volkamer et al., 2007).

## 1.2 Volatility of OA

The volatility of atmospheric OA is one of its most important physical properties. It determines the partitioning of these organic compounds between the gas and particulate phases, the organic aerosol concentration and influences the rate of reactions and the atmospheric fate of the corresponding compounds. Measurement of the OA volatility distribution has been recognized as one of the major challenges in our efforts to quantify the rates of formation of secondary organic particulate matter (Donahue et al., 2012).

One of the most popular ways to measure volatility is using a thermodenuder (Burtcher et al., 2001; Wehner et al., 2002, 2004; Kalberer et al., 2004; An et al., 2007). Figure 1.3 shows the schematic design of a typical thermodenuder (TD). A TD consists of 2 basic parts: a heated tube where the more volatile particle components evaporate, leaving less volatile species behind and the denuder tube containing usually activated carbon where the evaporated material is adsorbed avoiding potential re-condensation when the sample is cooled to room temperature.

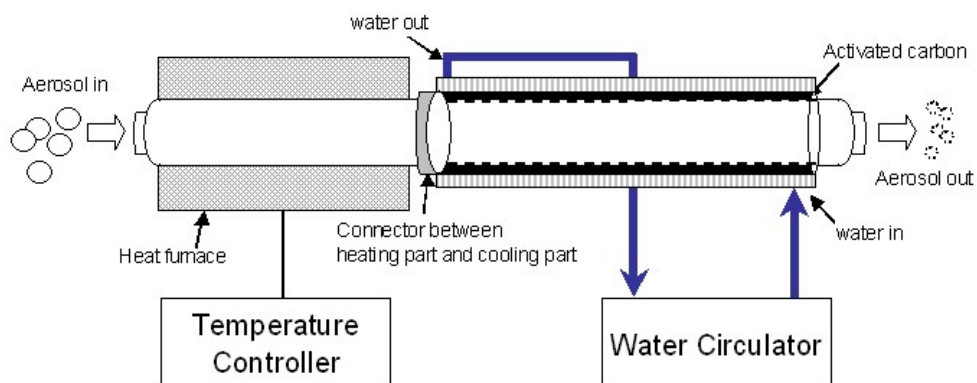


**Figure 1.3** Schematic design of a thermodenuder (An et al., 2007)

The measurement of the volatility of OA has received considerable attention recently and has been carried out both in the field (Engler et al., 2007; Huffman et al., 2009; Lee et al., 2010; Cappa and Jimenez, 2010) and in the laboratory (An et al., 2007; Jonsson et al., 2007; Saleh et al., 2008; Faulhaber et al., 2009). The aerosol mass fraction remaining (MFR) at a given temperature, after passing through the TD, is the most common way of reporting the TD measurements. The

quantitative estimation of volatility is not trivial though and dynamic aerosol evaporation models (Riipinen et al., 2010; Cappa, 2010; Fuentes and McFiggans, 2012) are needed in most cases for the interpretation of TD measurements and the estimation of OA volatility.

The MFR of OA in a TD depends not only on its volatility distribution but also on the vaporization enthalpy and potential mass transfer resistances as the particles evaporate. Thus, the inversion of the TD measurements to calculate the OA volatility distribution has proven to be challenging because of the many parameters affecting the resulting MFR. Figure 1.4 shows the sensitivity of thermograms to the assumed values for the vaporization enthalpy and mass accommodation coefficient (Riipinen et al., 2010). Previous studies have assumed a-priori values for the effective vaporization enthalpy and the mass accommodation coefficient (Lee et al., 2010; Cappa and Jimenez, 2010; Lee et al., 2011; Cappa and Wilson, 2011; Fuentes and McFiggans, 2012; Saleh et al., 2012; Saleh et al., 2013) in order to estimate the OA volatility. All existing techniques lead to big uncertainties for the estimated volatility distributions. The performance of different time scale experiments could allow the estimation of the volatility distribution together with the vaporization enthalpy and accommodation coefficient with lower uncertainty ranges.

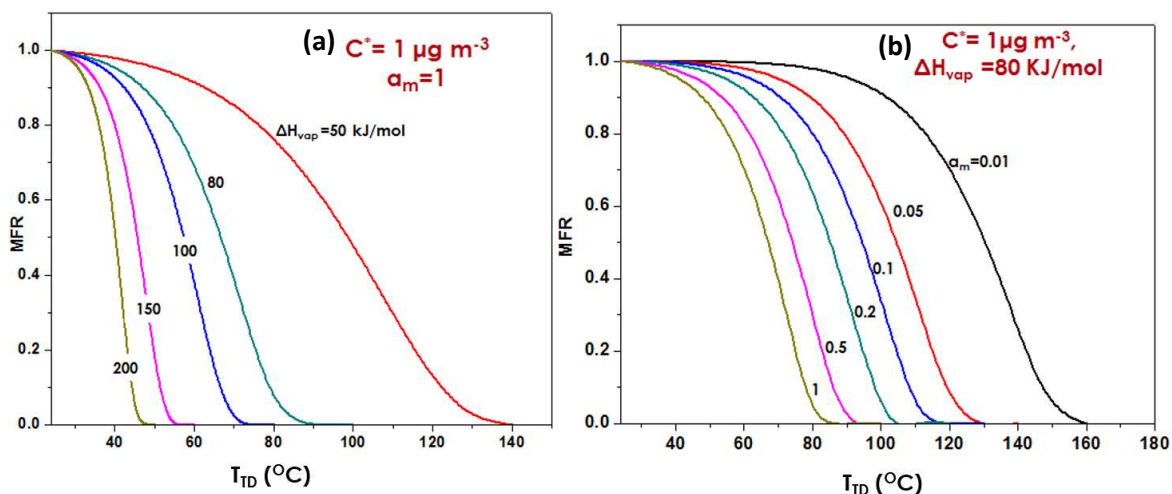


**Figure 1.4** Effect of (a) vaporization enthalpy ( $\Delta H_{vap}$ ) and (b) accommodation coefficient  $\alpha_m$  on thermograms assuming  $C^* = 1 \mu\text{g m}^{-3}$  for: (a)  $\alpha_m = 1$  and various  $\Delta H_{vap}$  values and (b)  $\Delta H_{vap} = 80 \text{ kJ mol}^{-1}$  and various  $\alpha_m$  values. The mass fraction remaining versus the temperature were calculated using the mass transfer model of Riipinen et al. (2010).

Positive matrix factorization (PMF) is a mathematical technique that separates the bulk OA mass spectra acquired by the AMS into individual factors, thus providing information about the processing and sources of the OA (Zhang et al., 2007; Lanz et al., 2007; Ulbrich et al., 2009). Common primary OA factors include hydrocarbon-like OA (HOA), biomass burning OA (BBOA), and cooking OA (COA) while for secondary OA one or more oxygenated OA factors are usually identified. A large number of studies have identified PMF factors in ambient datasets, however only a few of them have tried to directly determine their volatility (Huffman et al., 2009; Cappa and Jimenez., 2010).

OA consists of thousands of compounds, too few of which have been identified. The use of lumped species allows the computational efficient representation of OA in atmospheric chemical transport models (Pandis et al., 1992). The volatility basis set framework (Donahue et al., 2006) was developed to describe absorptive partitioning by lumping all these compounds into surrogates along an axis of volatility. This approach typically employs species with effective saturation concentrations at 298 K separated by one order of magnitude (bin), with values ranging from, say, 0.01 to  $10^6 \mu\text{g m}^{-3}$  (Figure 1.5).

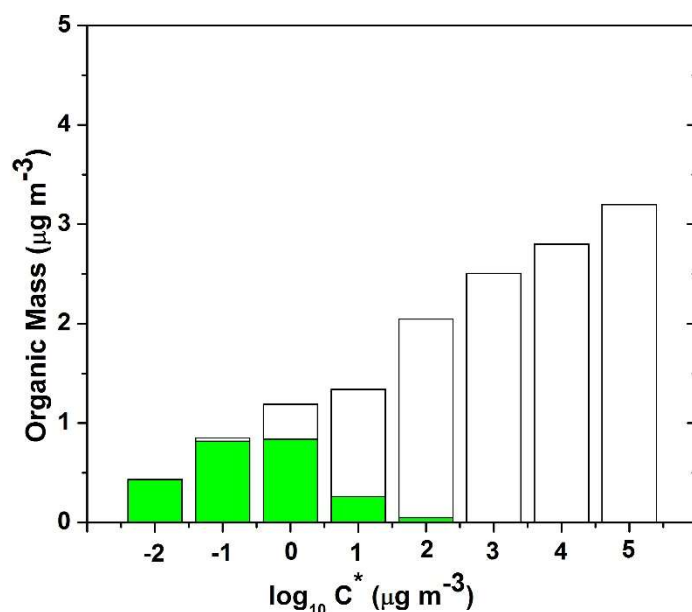


**Figure 1.5** VBS presentation (Donahue et al. 2006) with total loadings (in  $\mu\text{g m}^{-3}$ ) shown with full bars and the condensed-phase portion with filled (green) bars. Compounds are distributed according to their mass-equivalent effective saturation concentration ( $C^*$ , also in  $\mu\text{g m}^{-3}$ ), which is presented as a logarithmically distributed basis set.

The OA components are described as intermediate volatility organic compounds (IVOCs with  $C^* \geq 1000 \mu\text{g m}^{-3}$ ), semi-volatile (SVOCs with  $C^*$  of 1, 10, and  $100 \mu\text{g m}^{-3}$ ), low volatility (LVOCs with  $C^*$  of  $10^{-3}$ ,  $10^{-2}$ , and  $0.1 \mu\text{g m}^{-3}$ ), and extremely low volatility (ELVOCs with  $C^* \leq 10^{-4} \mu\text{g m}^{-3}$ ) in the rest of the thesis (Murphy et al., 2014). By quantifying the volatility distributions of primary and secondary OA, a physically reasonable, yet suitable for large-scale chemical transport models, description of semi-volatile organics can be obtained (Pathak et al., 2007; Stanier et al., 2008).

### 1.3 Volatility-oxygen content distribution of OA (2D-VBS)

The VBS framework was extended by Donahue et al. (2011; 2012) adding another dimension, the oxygen content (expressed as the O:C ratio), for the description of the OA chemical aging reactions (Figure 1.6). In the first application of this framework in a CTM, Murphy et al. (2011) used 12 logarithmically spaced volatility bins (effective saturation concentration  $C^*$  varying from  $10^{-5}$  to  $10^6 \mu\text{g m}^{-3}$  at 298 K) and 13 bins of O:C (from 0 to 1.2 with a step of 0.1). In this way 156 surrogate species were included in the model for each OA type. Five organic aerosol types were simulated separately: anthropogenic secondary organic aerosol (aSOA-v) produced during the oxidation of anthropogenic VOCs, biogenic secondary organic aerosol (bSOA), fresh primary organic aerosol (POA), secondary organic aerosol from the oxidation of semivolatile OA (SOA-sv) and SOA from the oxidation of intermediate volatility compounds (SOA-iv).

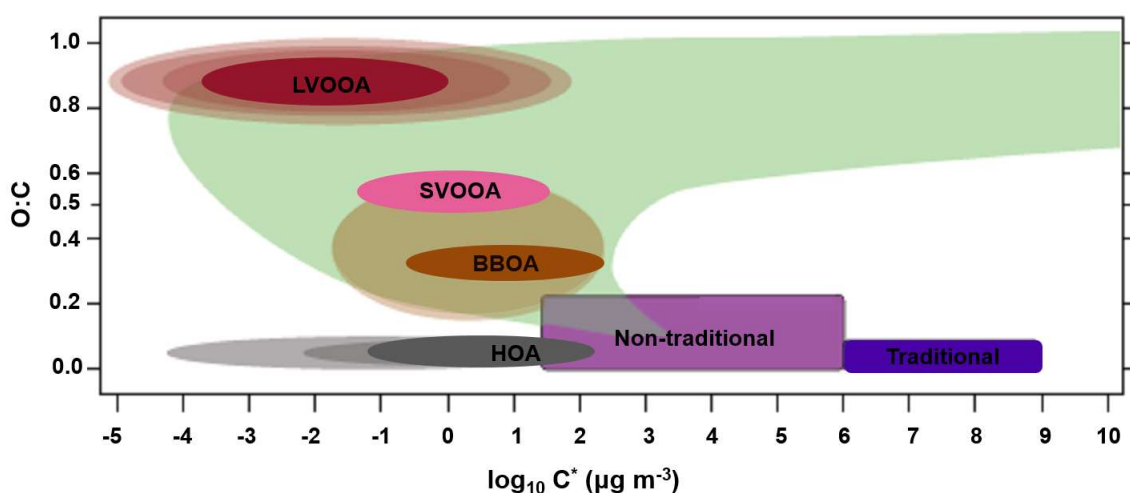


**Figure 1.6** 2D-VBS representation (Donahue et al. (2012)). The x axis represents volatility as effective saturation concentration  $C^*$  and the y axis the OA oxygen content or else the O:C. Various aerosol factors and their location in the scheme are shown, as well as, paths with green due to chemistry.

Three alternative parameterizations of the OA formation and chemical aging were evaluated using measurements of O:C and OA in three European sites by Murphy et al. (2011; 2012). The simplest approach parameterizing the chemical aging of anthropogenic compounds assuming a net reduction of volatility by one bin during every aging reaction step accompanied by an increase of one or two oxygen atoms with an equal probability was the most successful. A more complex formulation of the chemical aging assuming that functionalization is the only process taking place overpredicted the OA concentration and underpredicted the O:C ratio in most cases.

Murphy and Pandis (2009; 2010) and Murphy et al. (2012) suggested that formation of significant bSOA during the additional aging reactions led to overestimation of OA concentration at both urban and rural sites. However, the first generation products of the oxidation of biogenic VOCs do continue to react in the atmosphere (Ng et al., 2006; Szidat et al., 2006; Tritscher et al., 2011; Gilardoni et al., 2011; Yttri et al., 2011; Zhao et al., 2015). The net change in bSOA levels due to these chemical aging reactions remains uncertain.

Adding fragmentation reactions (Murphy et al. 2012) together with the functionalization gave promising results but it was clear that the various parameters of the scheme were not well constrained leading to large uncertainties in the simulation results especially during summertime. Lane et al. (2008), Murphy and Pandis (2009) and Hermansson et al. (2014) concluded that treating only the functionalization of bSOA while neglecting fragmentation might lead to overpredictions of OA concentrations. Murphy et al. (2012) concluded that the 2D-VBS scheme that was used needs additional testing before it is ready for application in three-dimensional CTMs.

## **1.4 Thesis Overview**

In Chapter 2, we explore methods for estimating the OA volatility distribution together with the effective vaporization enthalpy and mass accommodation coefficient. We develop a method combining forward modeling with known values for the three properties that we will try to estimate, introduction of random ‘experimental’ error and finally inverse modeling with least squares error minimization for the estimation of the OA volatility distribution, its effective vaporization enthalpy and the mass accommodation coefficient. We show that the best fit does not correspond to the most accurate estimate due to the multiple local minima occurring in this problem. We propose an approach of estimating an ensemble of solutions and use them to derive

a best guess and corresponding uncertainties for each of the three properties. Experimental approaches to improve these estimates and to reduce the corresponding uncertainties are explored. We examine the utility of using two residence times, using isothermal dilution instead of thermodenuder measurements (Grieshop et al., 2009), and finally combining TD and isothermal dilution measurements.

In Chapter 3, we use the mass transfer model of Riipinen et al. (2010), together with the uncertainty estimation algorithm introduced in Chapter 2 and apply it to data from two major cities, Paris and Athens. First, we estimate the volatility distributions of PMF factors derived from two month-long summer and winter campaigns in a suburban background site in Paris. We then focus on another large European urban center, Athens, during wintertime. We determine again the volatility distribution of the four OA PMF factors reported during a month-long winter campaign characterized by intense residential wood burning. We synthesize the corresponding OA findings using the 2D-VBS framework. Finally, we estimate the OA vaporization enthalpy and the accommodation coefficient.

In Chapter 4, we describe a new experimental technique to constrain the volatility distribution of organic aerosol using TD combined with isothermal dilution measurements following the suggestions of Chapter 2. The experiments were performed by Dr. Evangelos Louvaris in the University of Patras, Greece. The OA mass fraction remaining was measured as a function of temperature in the thermodenuder and as a function of time in a dilution chamber in parallel. TD measurements are corrected for size- and temperature- dependent losses and the dilution system measurements for size-dependent losses. Using these two sets of measurements together with the approach suggested in Chapter 2 we estimate the volatility distribution of the OA and its effective enthalpy of vaporization ( $\Delta H_{\text{vap}}$ ) and effective accommodation coefficient ( $a_m$ ). Meat from charbroiling (cooking OA) is used as an example for the application of the method. Finally, scaling the volatility distributions from the charbroiling measurements to ambient levels, the laboratory results are compared with those of the ambient measurements in Athens.

In Chapters 5 and 6, we simulate the atmospheric OA using its volatility-oxygen content distribution (2D-VBS) during PEGASOS campaigns during the years of 2012 in Po Valley in Italy and 2013 in Hyytiälä, Finland respectively. Extensive measurements were performed both at the ground and aloft with a Zeppelin. Po Valley has major air quality problems due to both industrial and agricultural sources and Hyytiälä has high biogenic SOA levels. A number of alternative

chemical aging mechanisms are evaluated comparing the 2D-VBS predictions against the PEGASOS measurements. The role of bSOA chemical aging is explored. Finally, the sensitivity of the model to the assumed effective vaporization enthalpy is quantified in an effort to constrain this uncertain variable using the measurements aloft.

## 1.5 References

- An, W. J., Pathak, R. K., Lee, B. H., and Pandis, S. N.: Aerosol volatility measurement using an improved thermodenuder: Application to secondary organic aerosol, *J. Aerosol. Sci.*, 38, 305–314, 2007.
- Burtscher, H., Baltensperger, U., Bukowiecki, N., Cohn, P., Hüglin, C., Mohr, M., Matter, U., Nyeki, S., Schmatloch, V., Streit, N., and Weingartner, E.: Separation of volatile and non-volatile aerosol fractions by thermodesorption: instrumental development and applications, *J. Aerosol Sci.*, 32, 427–442, 2001.
- Caiazzo, F., Ashok, A., Waitz, I. A., Yim, S. H. L. and Barrett, S. R. H.: Air pollution and early deaths in the United States. Part I: Quantifying the impact of major sectors in 2005, *Atmos. Environ.*, 79, 198–208, 2013.
- Cappa, C. D.: A model of aerosol evaporation kinetics in a thermodenuder, *Atmos. Meas. Tech.*, 3, 579–592, 2010.
- Cappa, C. D. and Jimenez, J.L.: Quantitative estimates of the volatility of ambient organic aerosol, *Atmos. Chem. Phys.*, 10, 5409–5424, 2010.
- Cappa, C. D. and Wilson, K. R.: Evolution of organic aerosol mass spectra upon heating: implications for OA phase and partitioning behavior, *Atmos. Chem. Phys.*, 11, 1895–1911, 2011.
- Donahue, N. M., Robinson, A.L., Stanier, C.O., and Pandis, S.N.: Coupled partitioning, dilution, and chemical aging of semivolatile organics, *Environ. Sci. Technol.*, 40, 2635–2643, 2006.
- Donahue, N. M., Kroll, J. H., Pandis, S. N., and Robinson, A. L.: A two-dimensional volatility basis set: 1. organic-aerosol mixing thermodynamics, *Atmos. Chem. Phys.*, 11, 3303–3318, 2011.

- Donahue, N. M., Kroll, J. H., Pandis, S. N., and Robinson, A. L.: A two-dimensional volatility basis set – Part 2: Diagnostics of organic-aerosol evolution, *Atmos. Chem. Phys.*, 12, 615–634, 2012.
- Engler, C., Rose, D., Wehner, B., Wiedensohler, A., Brüggemann, E., Gnauk, T., Spindler, G. Tuch, T., and Birmili, W.: Size distributions of non-volatile particle residuals ( $D_p < 800$  nm) at a rural site in Germany and relation to air mass origin, *Atmos. Chem. Phys.*, 7, 5785–5802, 2007.
- Faulhaber, A. E., Thomas, B. M., Jimenez, J. L., Jayne, J. T., Worsnop, D. R., and Ziemann, P. J.: Characterization of a thermodenuder-particle beam mass spectrometer system for the study of organic aerosol volatility and composition, *Atmos. Meas. Tech.*, 2, 15–31, 2009.
- Fuentes, E. and McFiggans, G.: A modeling approach to evaluate the uncertainty in estimating the evaporation behaviour and volatility of organic aerosols, *Atmos. Meas. Tech.*, 5, 735–757, 2012.
- Gaydos, T. M., Pinder, R., Koo, B., Fahey, K. M., Yarwood, G. and Pandis, S. N.: Development and application of a three-dimensional aerosol chemical transport model, PMCAMx, *Atmos. Environ.*, 41, 2594–2611, 2007.
- Gilardoni, S., Vignati, E., Cavalli, F., Putaud, J. P., Larsen, B. R., Karl, M., Stenstrom, K., Genberg, J., Henne, S., and Dentener, F.: Better constraints on sources of carbonaceous aerosols using a combined  $^{14}\text{C}$  - macro tracer analysis in a European rural background site, *Atmos. Chem. Phys.*, 11, 5685–5700, 2011.
- Grieshop, A. P., Miracolo, M.A., Donahue, N. M. and Robinson, A. L.: Constraining the volatility distribution and gas-particle partitioning of combustion aerosols using isothermal dilution and thermodenuder measurements, *Environ. Sci. Technol.*, 43, 4750–4756, 2009.
- Hermansson, E., Roldin, P., Rusanen, A., Mogensen, D., Kivekäs, N., Väänänen, R., Boy, M., and Swietlicki, E.: Biogenic SOA formation through gas-phase oxidation and gas-to-particle partitioning – a comparison between process models of varying complexity, *Atmos. Chem. Phys.*, 14, 11853–11869, 2014.
- Huffman, J. A., Docherty, K. S., Mohr, C., Cubison, M. J., Ulbrich, I. M., Ziemann, P. J., Onasch, T. B., and Jimenez, J. L.: Chemically-resolved volatility measurements of organic aerosol from different source, *Environ. Sci. Technol.*, 43, 5351–5357, 2009.

IPCC (Intergovernmental Panel on Climate Change): Climate Change 2014: Mitigation of Climate Change. Contribution of Working Group III to the Fifth Assessment Report of the Intergovernmental Panel on Climate Change, Cambridge University Press, Cambridge, UK and New York, 2014.

Jimenez, J. L., Canagaratna, M. R., Donahue, N. M., Prévôt, A. S. H., Zhang, Q., Kroll, J. H., DeCarlo, P. F., Allan, J. D., Coe, H., Ng, N. L., Aiken, A. C., Docherty, K., Ulbrich, I., Grieshop, A.P., Robinson, A. L., Duplissy, J., Smith, J. D., Wilson, K. R., Lanz, V. A., Hueglin, C., Sun, Y. L., Tian, J., Laaksonen, A., Raatikainen, T., Rautiainen, J., Vaattovaara, P., Ehn, M., Kulmala, M., Tomlinson, J. M., Collins, D. R., Cubison, M. J., Dunlea, E., Huffman, J. A., Onasch, T. B., Alfarra, M. R., Williams, P., Bower, K., Kondo, Y., Schneider, J., Drewnick, F., Borrmann, S., Weimer, S., Demerjian, K., Salcedo, D., Cottrell, L., Griffin, R. J., Takami, A., Miyoshi, T., Hatakeyama, S., Shimono, A., Sun, J. Y., Zhang, Y. M., Dzepina, K., Kimmel, J. R., Sueper, D., Jayne, J. T., Herndon, S. C., Trimborn, A., Williams, L. R., Wood, E. C., Middlebrook, A. M., Kolb, C. E., Baltensperger, U., and Worsnop, D. R.: Evolution of organic aerosols in the atmosphere, *Science*, 326, 1525–1529, 2009.

Jonsson, A. M., Hallquist, M., and Saathoff, H.: Volatility of secondary organic aerosols from the ozone initiated oxidation of  $\alpha$ -pinene and limonene, *J. Aerosol Sci.*, 38, 843–852, 2007.

Kalberer, M., Paulsen, D., Sax, M., Steinbacher, M., Dommen, J., Prevot, A. S. H., Fisseha, R., Weingartner, E., Frankevich, V., Zenobi, R., and Baltensperger, U.: Identification of polymers as major components of atmospheric organic aerosols, *Science*, 303, 1659–1662, 2004.

Lane, T. E., Donahue, N. M., and Pandis, S. N.: Simulating secondary organic aerosol formation using the volatility basis-set approach in a chemical transport model, *Atmos. Environ.*, 42, 7439–7451, 2008.

Lanz, V. A., Alfarra, M. R., Baltensperger, U., Buchmann, B., Hueglin, C. and Prévôt, A. S. H.: Source apportionment of submicron organic aerosols at an urban site by factor analytical modelling of aerosol mass spectra, *Atmos. Chem. Phys.*, 7, 1503–1522, 2007.

Lee, B.H., Kostenidou, E., Hildebrandt, L., Riipinen, I., Engelhart, G.J., Mohr, C., DeCarlo, P.F., Mihalopoulos, N., Prevot, A.S.H., Baltensperger, U. and Pandis, S.N.: Measurement of the

- ambient organic aerosol volatility distribution: application during the Finokalia Aerosol Measurement Experiment (FAME-2008), *Atmos. Chem. Phys.*, 10, 12149-12160, 2010.
- Lee, B.H., Pierce, J.R., Engelhart, G.J. and Pandis, S.N.: Volatility of secondary organic aerosol from the ozonolysis of monoterpenes, *Atmos. Environ.*, 45, 2443-2452, 2011.
- Murphy, B. N. and Pandis, S. N.: Simulating the formation of semivolatile primary and secondary organic aerosol in a regional chemical transport model, *Environ. Sci. Technol.*, 43, 4722–4728, 2009.
- Murphy, B. N. and Pandis, S. N.: Exploring summertime organic aerosol formation in the eastern United States using a regional-scale budget approach and ambient measurements, *J. Geophys. Res.*, 115, D24216, 10.1029/2010jd014418, 2010.
- Murphy, B. N., Donahue, N. M., Fountoukis, C., and Pandis, S. N.: Simulating the oxygen content of ambient organic aerosol with the 2D volatility basis set, *Atmos. Chem. Phys.*, 11, 7859-7873, 2011.
- Murphy, B. N., Donahue, N. M., Fountoukis, C., Dall'Osto, M., Dowd, C.O., Kiendler-Scharr, A., and Pandis, S. N.: Functionalization and fragmentation during ambient organic aerosol aging: application of the 2-D volatility basis set to field studies, *Atmos. Chem. Phys.*, 12, 10797-10816, 2012.
- Murphy, B. N., Donahue, N. M., Robinson, A. L., and Pandis, S. N.: A naming convention for atmospheric organic aerosol, *Atmos. Chem. Phys.*, 14, 5825-5839, 2014.
- Nel, A.: Air pollution-related illness: Effects of particles, *Science*, 308, 804–806, 2005.
- Ng, N. L., Kroll, J. H., Keywood, M. D., Bahreini, R., Varutbangkul, V., Flagan, R. C., and Seinfeld, J. H.: Contribution of first- versus second-generation products to secondary organic aerosols formed in the oxidation of biogenic hydrocarbons, *Environ. Sci. Technol.*, 40, 2283–2297, 2006.
- Pandis S. N., Harley R. A., Cass G. R. and Seinfeld J. H.: Secondary organic aerosol formation and transport, *Atmos. Environ.*, 26, 2266-2282, 1992.
- Pathak, R. K., Presto, A. A., Lane, T. E., Stanier, C. O., Donahue, N. M., and Pandis, S. N.: Ozonolysis of  $\alpha$ -pinene: Parameterization of secondary organic aerosol mass fraction, *Atmos. Chem. Phys.*, 7, 3811–3821, 2007.
- Pope, C. A., III, Ezzati, M. and Dockery, D. W.: Fine-particulate air pollution and life expectancy in the United States, *New England Journal of Medicine*, 360, 376–386, 2009.

- Riipinen I., Pierce, J. R., Donahue N. M., and Pandis S. N.: Equilibration time scales of organic aerosol inside thermodenuders: Kinetics versus equilibrium thermodynamics, *Atmos. Environ.*, 44, 597–607, 2010.
- Saleh, R., Walker, J., and Khlystov, A.: Determination of saturation pressure and enthalpy of vaporization of semi-volatile aerosols: The integrated volume method, *J. Aerosol. Sci.*, 39, 876–887, 2008.
- Saleh, R., Khlystov, A. and Shihadeh, A.: Determination of evaporation coefficients of ambient and laboratory-generated semivolatile organic aerosols from phase equilibration kinetics in a thermodenuder, *Aerosol Sci. Technol.*, 46, 22–30, 2012.
- Saleh, R., Donahue, N. M. and Robinson, A. L.: Time scales for gas-particle partitioning equilibration of secondary organic aerosol formed from alpha-pinene ozonolysis, *Environ. Sci. Technol.*, 47, 5588–5594, 2013.
- Seinfeld, J.H. and Pandis, S.N.: *Atmospheric Chemistry and Physics*, second ed., John Wiley and Sons, Hoboken, New Jersey, USA, 2006.
- Stanier, C. O., Donahue, N., Pandis, S. N.: Parameterization of secondary organic aerosol mass fractions from smog chamber data, *Atmos. Environ.*, 42, 2276–2299, 2008.
- Szidat, S., Jenk, T. M., Synal, H.-A., Kalberer, M., Wacker, L., Hajdas, I., Kasper-Giebl, A., and Baltensperger, U.: Contributions of fossil fuel, biomass-burning, and biogenic emissions to carbonaceous aerosols in Zurich as traced by  $^{14}\text{C}$ , *J. Geophys. Res.*, 111, D07206, 10.1029/2005JD006590, 2006.
- Tritscher, T., Dommen, J., DeCarlo, P. F., Barmet, P. B., Pra-plan, A. P., Weingartner, E., Gysel, M., Prévôt, A. S. H., Riipinen, I., Donahue, N. M., and Baltensperger, U.: Volatility and hygroscopicity of aging secondary organic aerosol in a smog chamber, *Atmos. Chem. Phys.*, 11, 11477-11496, 2011.
- Ulbrich, I. M., Canagaratna, M. R., Zhang, Q., Worsnop, D. R. and Jimenez, J. L.: Interpretation of organic components from Positive Matrix Factorization of aerosol mass spectrometric data, *Atmos. Chem. Phys.*, 9, 2891–2918, 2009.
- Volkamer, R., San Martini, F., Molina, L. T., Salcedo, D., Jimenez, J. L. and Molina, M. J.: A missing sink for gas-phase glyoxal in Mexico City: Formation of secondary organic aerosol, *Geophys. Res. Lett.*, 34, 1–5, 2007.

- Wehner, B., Philippin, S., and Wiedensohler, A.: Design and calibration of a thermodenuder with an improved heating unit to measure the size-dependent volatile fraction of aerosol particles, *J. Aerosol Sci.*, 33, 1087–1093, 2002.
- Wehner, B., Philippin, S., Wiedensohler, A., Scheer, V., and Vogt, R.: Variability of non-volatile fractions of atmospheric aerosol particles with traffic influence, *Atmos. Environ.*, 38, 6081–6090, 2004.
- Yttri, K. E., Simpson, D., Nøjgaard, J. K., Kristensen, K., Genberg, J., Stenström, K., Swietlicki, E., Hillamo, R., Aurela, M., Bauer, H., Offenberg, J. H., Jaoui, M., Dye, C., Eckhardt, S., Burkhardt, J. F., Stohl, A., and Glasius, M.: Source apportionment of the summer time carbonaceous aerosol at Nordic rural background sites, *Atmos. Chem. Phys.*, 11, 13339–13357, 2011.
- Zhang, Q., Jimenez, J. L., Canagaratna, M. R., Allan, J. D., Coe, H., Ulbrich, I., Alfarra, M. R., Takami, A., Middlebrook, A. M., Sun, Y. L., Dzepina, K., Dunlea, E., Docherty, K., DeCarlo, P. F., Salcedo, D., Onasch, T., Jayne, J. T., Miyoshi, T., Shimojo, A., Hatakeyama, S., Takegawa, N., Kondo, Y., Schneider, J., Drewnick, F., Borrmann, S., Weimer, S., Demerjian, K., Williams, P., Bower, K., Bahreini, R., Cottrell, L., Griffin, R. J., Rautiainen, J., Sun, J. Y., Zhang, Y. M., and Worsnop, D. R.: Ubiquity and dominance of oxygenated species in organic aerosols in anthropogenically-influenced Northern Hemisphere midlatitudes, *Geophys. Res. Lett.*, 34, L13801, 10.1029/2007GL029979, 2007.
- Zhao, B., Wang, S., Donahue, N. M., Chuang, W., Hildebrandt-Ruiz, L., Ng, N. L., Wang, Y., and Hao, J.: Evaluation of one-dimensional and two-dimensional volatility basis sets in simulating the aging of secondary organic aerosol with smog-chamber experiments, *Environ. Sci. Technol.*, 49, 2245–2254, 2015.

# **Chapter 2**

## **Measuring the atmospheric organic aerosol volatility distribution: A theoretical analysis<sup>1</sup>**

<sup>1</sup> Published as Karnezi, E., Riipinen, I. and Pandis, S. N.: Measuring the atmospheric organic aerosol volatility distribution: A theoretical analysis, *Atmos. Meas. Tech.*, 7, 2953–2965, 2014.

## 2.1 Introduction

Atmospheric aerosol particles play an important role in the Earth's energy balance by absorbing and scattering solar radiation (direct effect) and influencing the properties and lifetime of clouds (indirect effects) (IPCC, 2007). They have significant negative effects on human health, including premature death, increases in respiratory illnesses and cardiopulmonary mortality (Nel et al., 2005; Pope and Dockery, 2006).

Aerosols contain a wide variety of inorganic and organic compounds, with organics representing about 50% of the fine ( $< 1 \mu\text{m}$ ) aerosol mass (Zhang et al., 2007). Organic aerosol (OA) originates from many different natural and anthropogenic sources and processes. It can be emitted directly, e.g. from fossil fuels and biomass combustion (so called primary organic aerosol) or formed by atmospheric oxidation of volatile organic compounds (VOCs) (secondary organic aerosol, SOA). Since the oxidation pathways for VOCs are complex and the reactions lead to hundreds or thousands of oxygenated products, our understanding of organic aerosol formation mechanisms and the OA chemical and physical properties is still incomplete.

The volatility of atmospheric OA is one of its most important physical properties. It determines the partitioning of these organic compounds between the gas and particulate phases, the organic aerosol concentration and influences the rate of reactions and the atmospheric fate of the corresponding compounds. Measurement of the OA volatility distribution has been recognized as one of the major challenges in our efforts to quantify the rates of formation of secondary organic particulate matter (Donahue et al., 2012).

OA consists of thousands of compounds, too few of which have been identified. The volatility basis set framework (Donahue et al., 2006) was developed to describe absorptive partitioning by lumping all these compounds into surrogates along an axis of volatility. This approach typically employs species with effective saturation concentrations at 298 K separated by one order of magnitude (bin), with values ranging from, say, 0.01 to  $10^6 \mu\text{g m}^{-3}$ . By quantifying the volatility distributions of primary and secondary OA, a physically reasonable, yet suitable for large-scale chemical transport models, description of semi-volatile organics can be obtained (Pathak et al., 2007; Stanier et al., 2008).

Thermodenuders (TD) have been developed to measure the volatility of ambient aerosol (Burtsher et al., 2001; Wehner et al., 2002, 2004; Kalberer et al., 2004; An et al., 2007). A TD consists of 2 basic parts: a heated tube where the more volatile particle components evaporate,

leaving less volatile species behind and the denuder tube containing usually activated carbon where the evaporated material is adsorbed avoiding potential re-condensation when the sample is cooled to room temperature. The aerosol mass fraction remaining (MFR) at a given temperature, after passing through the TD, is the most common way of reporting the TD measurements.

The measurement of the volatility of OA has received considerable attention recently and has been carried out both in the field (Engler et al., 2007; Huffman et al., 2009; Lee et al., 2010; Cappa and Jimenez, 2010) and in the laboratory (An et al., 2007; Jonsson et al., 2007; Saleh et al., 2008; Faulhaber et al., 2009). One of the main issues related to the use of thermodenuders is whether equilibrium is reached in the heating section of the instrument. Saleh et al. (2008) used high organic aerosol concentrations allowing the model organic aerosol in their experiments to reach equilibrium in their TD. Then using their integrated volume method, they were able to determine the saturation concentration of the corresponding organic particles. Riipinen et al. (2010) showed that equilibration times in TDs depend on many factors, such as the organic aerosol loading and the accommodation coefficient. These authors argued that OA practically never reaches equilibrium in a TD in ambient concentration levels. For laboratory measurements, equilibrium can be reached with the use of high organic aerosol loadings (larger than  $200 \mu\text{g m}^{-3}$ ) and when the residence time in the heated section of the TD exceeds 30 s (Riipinen et al., 2010; Saleh et al., 2011). An et al. (2007) introduced an improved TD allowing larger residence times. Lee et al. (2010; 2011) performed thermodenuder experiments at two residence times and argued that multiple residence times are needed in order to decouple mass transfer effects from thermodynamics. Similar conclusions were reached by Riipinen et al. (2010) and Cappa (2010). Saleh et al. (2012) used a particle concentrator before passing the ambient aerosol through the thermodenuder to increase the aerosol concentration levels and to reduce the equilibration time scale. Volatility measurements at longer timescales, where equilibrium of the system can be reached, have been performed by Grieshop et al. (2009).

Dynamic aerosol evaporation models (Riipinen et al., 2010; Cappa, 2010; Fuentes and McFiggans, 2012) are needed in most cases for the interpretation of TD measurements and the estimation of OA volatility. However, the MFR of OA in a TD depends not only on its volatility distribution but also on the vaporization enthalpy and potential mass transfer resistances as the particles evaporate. The inversion of the TD measurements to calculate the OA volatility

distribution has proven to be challenging because of the many parameters affecting the resulting MFR.

Previous studies have assumed a-priori values for the effective vaporization enthalpy and the mass accommodation coefficient in order to estimate the OA volatility. Lee et al. (2010) trying to measure the volatility of ambient OA assumed values for the vaporization enthalpy and the accommodation coefficient equal to  $80 \text{ kJ mol}^{-1}$  and 0.05 respectively. They used the time dependent evaporation model by Riipinen et al. (2010), with least squares minimization, to reproduce ambient measurements collected in the Eastern Mediterranean. For most measurements it was difficult to estimate the volatility distribution especially for the less volatile components. Moreover, a change of the accommodation coefficient from 0.05 to 1 resulted in shifting of the estimated volatility distribution by one order of magnitude. Lee et al. (2011) used the same mass transfer model in order to reproduce experimental measurements from different precursors assuming values for the vaporization enthalpy and the accommodation coefficient. Cappa (2010) developed a new model of evaporation in a TD accounting for the cooling section and the velocity profile across the TD tube. They demonstrated the importance of the vaporization enthalpy especially for values less than  $100 \text{ kJ mol}^{-1}$ . They also underlined the importance of constraining the value of accommodation coefficient in order to quantify the volatility distribution of OA. Cappa and Jimenez (2010) used the model of Cappa (2010) to quantify the volatility distribution of ambient OA in Mexico City using measurements from the MILAGRO campaign. Assuming several values for the vaporization enthalpy, either using the relationship from Epstein et al. (2010) or assuming that the vaporization enthalpy depended linearly on temperature or that it had constant values from 50 to  $150 \text{ kJ mol}^{-1}$  they estimated different volatility distributions. Changing the value of the accommodation coefficient from 1 to 0.1 the estimated volatility distribution was shifted to higher values by approximately one order of magnitude. Fuentes and McFiggans (2012) used a dynamic aerosol evaporation model and the Epstein et al. (2010) relationship for the vaporization enthalpy, to calculate the volatility distribution for  $\alpha$ -pinene SOA together with small value of the accommodation coefficient. The estimation of the accommodation coefficient during the evaporation of atmospheric OA has been the focus of a number of studies. Saleh et al. (2012) developed a method combining a particle concentrator (in order to achieve high mass loadings) and a thermodenuder. Using the thermodenuder model by Saleh et al. (2011), they measured the effective evaporation coefficient of ambient aerosol. Their results suggested accommodation

coefficients with values around 0.3 for the ambient particles that they examined. Cappa and Wilson (2011) focused on the evolution of organic aerosol mass spectra from lubricating oil and secondary aerosol from  $\alpha$ -pinene oxidation upon heating, using the Cappa (2010) model. They adopted volatility distributions from previous studies (Pathak et al., 2007; Grieshop et al., 2009) and a vaporization enthalpy based on the Epstein et al. (2010) relationship. One of their major conclusions was that there were high mass transfer resistances (estimated accommodation coefficients of the order of  $10^{-4}$ ) during the evaporation of the  $\alpha$ -pinene SOA.

The sensitivity of TD results to several additional parameters has also been investigated in past studies. Lee et al. (2010) concluded that a monodisperse approximation using one effective value for the diameter of the particles instead of the full distribution resulted in changes of the thermograms of less than 2%. Lee et al. (2011) explored the effect of the cooling section and the role of surface free energy and Cappa (2010) the role of the assumed value for the diffusion coefficient or the average effective diameter of the particles. Once again the conclusion was that these parameters were not as important as the vaporization enthalpy and the accommodation coefficient for the estimation of the volatility distribution. Recondensation in the cooling section has been investigated in a number of studies (Cappa, 2010; Saleh et al., 2011; Fuentes and McFiggans, 2012). Fuentes and McFiggans (2012) through a parametric analysis concluded that recondensation depends on a combination of factors, as the mass loading, the particle size and the kinetic coefficient for re-condensation. Cappa (2010) showed that recondensation becomes significant for large aerosol loadings (larger than  $200 \mu\text{g m}^{-3}$ ) thus it is a problem mostly for laboratory experiments. Saleh et al. (2011) showed that a configuration with a small diameter for the cooling section can lead to negligible recondensation even for higher aerosol loadings.

In this Chapter we explore methods for estimating the OA volatility distribution together with the effective vaporization enthalpy and mass accommodation coefficient. We develop a method combining forward modeling with known values for the three properties that we will try to estimate, introduction of random ‘experimental’ error and finally inverse modeling with least squares error minimization for the estimation of the OA volatility distribution, its effective vaporization enthalpy and the mass accommodation coefficient. We show that the best fit does not correspond to the most accurate estimate due to the multiple local minima occurring in this problem. We propose an approach of estimating an ensemble of solutions and use them to derive a best guess and corresponding uncertainties for each of the three properties. Experimental

approaches to improve these estimates and to reduce the corresponding uncertainties are explored. We examine the utility of using two residence times, using isothermal dilution instead of thermodenuder measurements (Grieshop et al., 2009), and finally combining TD and isothermal dilution measurements.

## 2.2 Thermodenuder Model

We use the mass transfer model of Riipinen et al. (2010) modeling the time-dependent evaporation of multicomponent aerosol particles by solving the mass transfer equations for a monodisperse population of particles suspended in air. We assume a monodisperse population of particles. Lee et al. (2010) showed with the use of the same mass transfer model that this simplification resulted in errors of only a few percent (2%) and it reduced the computational time considerably. The mass flux of compound  $i$  from the gas phase to the particles,  $I_i$ , is calculated by (Seinfeld and Pandis, 2006):

$$I_i = \frac{2\pi d_p M_i \beta_{mi} D_i}{RT_{TD}} (p_i - p_i^0), \quad (1)$$

where  $d_p$  is the particle diameter,  $R$  the ideal gas constant,  $M_i$  and  $D_i$  the molecular weight and diffusion coefficient of compound  $i$  in the gas phase at temperature  $T_{TD}$  (the temperature in the heated part of the TD), and  $p_i^0$  and  $p_i$  are the partial vapor pressures of  $i$  at the particle surface and far away from the particle, respectively. In our simulations, we assume a particle diameter of 200 nm, a molecular weight of 0.2 kg mol<sup>-1</sup> and a diffusion coefficient of 10<sup>-5</sup> m<sup>2</sup>s<sup>-1</sup>.

The mass flux is corrected for kinetic and transition regime effects with the factor  $\beta_{mi}$  (Fuchs and Sutugin, 1970):

$$\beta_{mi} = \frac{1 + Kn_i}{1 + \left( \frac{4}{3a_{mi}} + 0.377 \right) Kn_i + \frac{4}{3a_{mi}} Kn_i^2}. \quad (2)$$

where  $Kn_i$  is the Knudsen number, that is the ratio of the mean free path of vapor  $i$  and the particle radius, and  $a_{mi}$  the mass accommodation coefficient of  $i$  on the particles.

The mean free path is estimated by:

$$\lambda_i = \frac{3 \cdot D_i}{\bar{c}} \quad (3)$$

where  $\bar{c}$  is the mean velocity of the gas molecules, given by:

$$\bar{c} = \sqrt{\frac{8 \cdot R \cdot T_{TD}}{\pi \cdot M_i}} \quad (4)$$

The partial vapor pressure of  $i$  at the particle surface,  $p_i^0$  is given by:

$$p_i^0 = x_i \gamma_i p_{sat,i} \exp\left(\frac{4M_i \sigma}{RT_p \rho d_p}\right) = x_{mi} \frac{C_i^* RT_{TD}}{M_i} \exp\left(\frac{4M_i \sigma}{RT_p \rho d_p}\right) \quad (5)$$

where  $x_i$  is the mole fraction and  $\gamma_i$  the activity coefficient of  $i$  in the particle phase,  $p_{sat,i}$  the pure component vapor pressure of  $i$  over a flat surface,  $T_p$  the particle temperature,  $C_i^*$  represents the effective saturation concentration of  $i$  in the volatility basis set (Donahue et al., 2006) and  $x_{mi}$  is the mass fraction of  $i$  in the particle. In this study, we will be using a fixed basis set with four volatility bins with effective saturation concentrations 0.01, 0.1, 1 and 10  $\mu\text{g m}^{-3}$  for each volatility bin. We assume a surface tension of 0.05  $\text{N m}^{-1}$ , as a median of the range used in Riipinen et al. (2010). We repeated our simulations with values of 0.05-0.2  $\text{N m}^{-1}$  for the surface energy but this choice had practically no effect on the results since the particles examined are too big and the Kelvin effect is not important. We also use a density of the surrogate compounds of 1500  $\text{kg m}^{-3}$ .

The saturation concentrations of the evaporating species at  $T_{TD}$  are estimated using the integrated form of the Clausius - Clapeyron equation:

$$C_i^*(T_{TD}) = C_i^*(298\text{K}) \exp\left[\frac{\Delta H_{vap,i}}{R} \left(\frac{1}{298} - \frac{1}{T_{TD}}\right)\right] \left(\frac{298}{T_{TD}}\right) \quad (6)$$

where  $\Delta H_{vap,i}$  is the vaporization enthalpy of species  $i$ .

The temperature dependence of the diffusion coefficients of the evaporating species is taken into account by using:

$$D_i(T_{TD}) = D_i(298) \left(\frac{T_{TD}}{298}\right)^\mu \quad (7)$$

where  $\mu$  is a constant usually ranging from 1.5 to 2.0 (Chen and Othmer, 1962). We used the value of 1.75 for all the studied compounds.

The time-dependent evaporation of the organic aerosol is simulated by solving the differential equations for total particle mass  $m_p$  and gas phase concentrations  $C_i$  of the evaporating species:

$$\frac{dm_p}{dt} = -\sum_{i=1}^n I_i \quad \frac{dC_i}{dt} = I_i \cdot N_{tot} \quad (8)$$

where  $N_{tot}$  is the total number concentration of the particles (assuming a monodisperse particle population). The MFR is then calculated from the ratio of the particle mass at  $t = t_{res}$  (where  $t_{res}$  is the residence time through the heating tube) to the initial mass of the particles. In this work, we study the evaporation of particles in a TD independently of the TD design and geometry: the only variables representing the instrument are the particle residence time and the temperature of the thermodenuder. We neglect the velocity and potential temperature gradients in the radial direction and thus focus on the particles moving along the centerline of the TD and at the corresponding centerline temperature. Saleh et al. (2011) showed that a similar model neglecting the radial dependence of the system reproduced well the behavior of model particles consisting of dicarboxylic acids.

We use, as inputs, values for the geometry of the TD (the length and the residence time in the heated tube), the temperature inside the TD ( $T_{TD}$ ), the initial mass concentration of the organic aerosol ( $C_{aer}$ ) and the properties of the organic compounds (such as the volatility distribution, vaporization enthalpy, accommodation coefficient, etc.). For the description of the geometry of the TD we used the values for the Carnegie Mellon TD of Lee et al. (2010). Specifically, for the heated tube we used a length of 55 cm and a centerline residence time of 17 s. Using the mass transfer model of Riipinen et al. (2010), modeling the time-dependent evaporation of multicomponent aerosol particles, we constructed theoretical thermograms (MFR versus  $T_{TD}$ ). Previous studies have often assumed that thermograms can be directly connected to the volatility of OA. Figure 2.1 indicates that we can have very similar thermograms for organic aerosols with very different volatilities (orders of magnitude different).

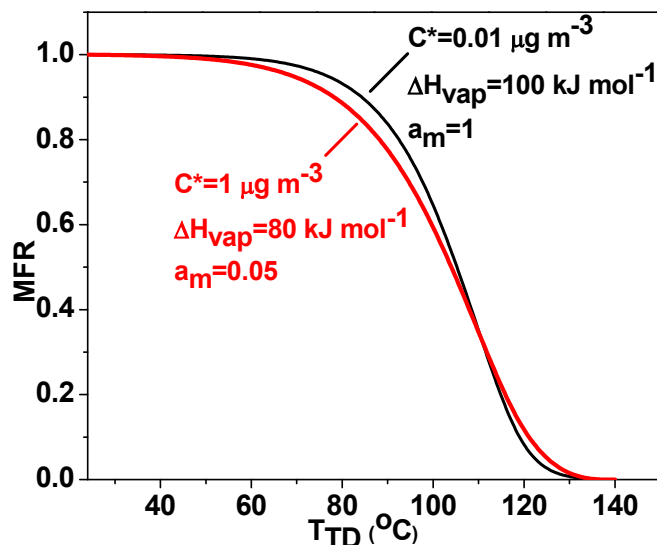


**Figure 2.1** Predicted thermograms (MFR versus  $T_{TD}$ ) for OA with different properties. A single component aerosol ( $C^*=1 \mu\text{g m}^{-3}$ ,  $\Delta H_{\text{vap}}=80 \text{ kJ mol}^{-1}$  and  $a_m=0.05$ ) gives practically the same thermogram as one with a much lower volatility ( $C^*=0.01 \mu\text{g m}^{-3}$ ,  $\Delta H_{\text{vap}}=100 \text{ kJ mol}^{-1}$  and  $a_m=1$ ).

In this example, the reduction of saturation concentration is balanced by changes in the accommodation coefficient and the vaporization enthalpy. The similarity of these suggests that the inversion of the thermograms in order to calculate the OA volatility will be very challenging.

### 2.2.1 Pseudo-experimental data

In order to evaluate how well we can estimate the volatility distribution we used ‘pseudo-experiments’ corrupting the output of the TD model, for systems with known volatility distributions and properties, with randomly generated ‘experimental’ error. In this way we could take into account the measurement uncertainty due to the variability of measurement conditions and produce relatively realistic ‘experimental results’ for systems with known volatility distributions and properties. We ‘corrupted’ the TD model predictions with random error assuming a normal distribution, based on the variability of laboratory measurements with the same TD conducted by Paciga et al. (2013), with a standard deviation given by:

$$\sigma = 0.51 \cdot MFR_{\text{true}} - 0.5 \cdot MFR_{\text{true}}^2 \quad (9)$$

where  $MFR_{\text{true}}$  are the correct MFR values. A typical example is shown in Figure 2.2.

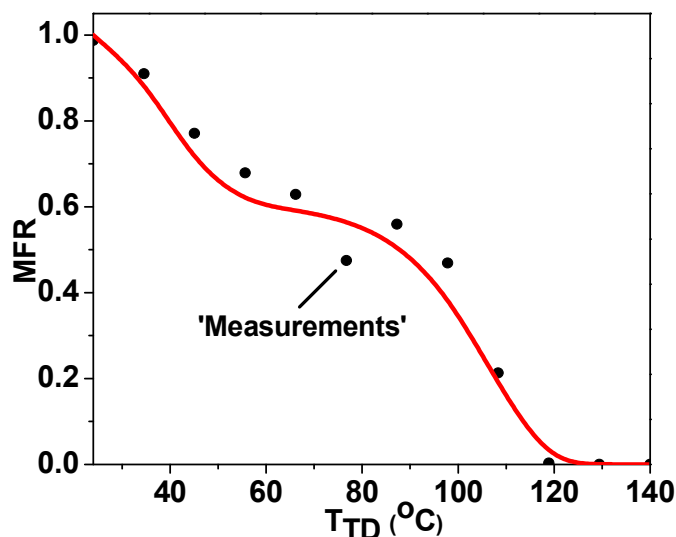


**Figure 2.2** Typical example of “construction” of TD pseudo-data. The red line is the thermogram corresponding to the true properties of the aerosol and the black dots correspond to the ‘measured’ MFR versus  $T_{TD}$  for an aerosol consisting of two components: very low volatility material (60%  $C^*=0.01 \mu\text{g m}^{-3}$ ) and relatively high volatility material (40%  $C^*=10 \mu\text{g m}^{-3}$ ), vaporization enthalpy and mass accommodation coefficient equal to  $100 \text{ kJ mol}^{-1}$  and 1 correspondingly. Twelve ‘measurements’ were constructed for equally spaced temperatures between 24 and 140 °C by corrupting the correct values with random experimental error.

In the rest of the inversion approaches, pseudo-experimental data were used. In this way, the experimental uncertainty was always taken into account and an overestimation / underestimation of the corresponding algorithm is avoided.

### 2.2.2 Optimum OA volatility distribution

The MATLAB least-squares fitting algorithm *lsqcurvefit* was used in order to obtain the best possible fit between the ‘measured’ and modeled MFRs. Four lognormally equally spaced volatility bins were used with volatilities from  $10^{-2}$  to  $10 \mu\text{g m}^{-3}$ . The corresponding volatility distribution, vaporization enthalpy and mass accommodation coefficient were estimated by the algorithm minimizing the sum of the squared differences between the MFR model predictions and the pseudo-measurements. In the least squares optimization a total of 12 pseudo-measurements were used in all cases.

A wide variety of compositions were tested during the simulations, including one component, two component or multicomponent aerosols with various volatility distributions and with different values for the vaporization enthalpy and the accommodation coefficient. The results for three of these tests that are used as illustrative examples are shown in Table 2.1.

**Table 2.1** Values of the true and estimated properties (volatility distribution, vaporization enthalpy, accommodation coefficient) for three OA examples.

	<b>Test 1 OA with very low and high volatility material</b>	<b>Test 2 Multiple component OA</b>	<b>Test 3 One component OA</b>
True values	$C_i^*=[0.01 \ 0.1 \ 1 \ 10]$ $X_i=[0.6 \ 0 \ 0 \ 0.4]$ , $\Delta H_{\text{vap}}=100 \text{ kJ mol}^{-1}$ $a_m=0.5$	$C_i^*=[0.01 \ 0.1 \ 1 \ 10]$ $X_i=[0 \ 0.1 \ 0.3 \ 0.6]$ , $\Delta H_{\text{vap}}=50 \text{ kJ mol}^{-1}$ $a_m=1$	$C_i^*=[0.01 \ 0.1 \ 1 \ 10]$ $X_i=[0 \ 0 \ 1 \ 0]$ , $\Delta H_{\text{vap}}=80 \text{ kJ mol}^{-1}$ $a_m=1$
Optimization results	$C_i^*=[0.01 \ 0.1 \ 1 \ 10]$ $X_i=[0.63 \ 0 \ 0 \ 0.37]$ $\Delta H_{\text{vap}}=92 \text{ kJ mol}^{-1}$ $a_m=0.97$ $E_i=1.09^a$	$C_i^*=[0.01 \ 0.1 \ 1 \ 10]$ $X_i=[0.07 \ 0.13 \ 0.49 \ 0.31]$ $\Delta H_{\text{vap}}=70 \text{ kJ mol}^{-1}$ $a_m=0.72$ $E_i=0.3$	$C_i^*=[0.01 \ 0.1 \ 1 \ 10]$ $X_i=[0 \ 0.88 \ 0 \ 0.12]$ $\Delta H_{\text{vap}}=181 \text{ kJ mol}^{-1}$ $a_m=0.04$ $E_i=0.81$

<sup>a</sup> The error, given by Equation (10), describes the quality of the fit.

For Test 1 corresponding to OA consisting of very low and high volatility material (60%  $0.01 \mu\text{g m}^{-3}$  and 40%  $10 \mu\text{g m}^{-3}$ ) the optimization resulted in absolute volatility error of less than 10% for all bins. The vaporization enthalpy was well-estimated (relative error equal to 8%) and the mass accommodation coefficient was estimated within a factor of two (0.97 instead of 0.5). For Test 2 corresponding to multicomponent OA (10%  $0.1 \mu\text{g m}^{-3}$ , 30%  $1 \mu\text{g m}^{-3}$  and 60%  $10 \mu\text{g m}^{-3}$ ), the estimated volatility distribution had a different shape than the true one, with more material

predicted for the bin of  $1 \mu\text{g m}^{-3}$  (predicted mass fraction equal to 0.49 instead of 0.3) and less for the  $10 \mu\text{g m}^{-3}$  bin (predicted mass fraction equal to 0.31 instead of 0.6). Also, some very low volatility material was estimated (predicted mass fraction equal to 0.07 while none was present). The vaporization enthalpy was estimated with a relative error equal to 40% and the accommodation coefficient was well estimated (0.72 instead of unity). For Test 3 with the case of one component OA with a volatility of  $1 \mu\text{g m}^{-3}$ , the estimates of all properties were far from the truth. Most of the material (88%) was estimated to be in the  $0.1 \mu\text{g m}^{-3}$  bin instead of  $1 \mu\text{g m}^{-3}$  and some material (12%) was predicted in the highest volatility bin of  $10 \mu\text{g m}^{-3}$ . The estimated vaporization enthalpy was more than a factor of two higher than the true value and the estimated accommodation coefficient was a factor of 25 lower than it should be.

The results, using different initial guesses, for the case of multiple-component OA (Test 2) are shown in Figure 2.3. For an initial guess of [0 0 0.3 0.7] for the mass fractions of the volatility bins ( $C^* = [0.01 \ 0.1 \ 1 \ 10] \mu\text{g m}^{-3}$ ),  $50 \text{ kJ mol}^{-1}$  for the vaporization enthalpy and 0.5 for the accommodation coefficient, the shape of the volatility distribution was estimated correctly but with significant errors of 0.1-0.2 in the 0.1, 1 and  $10 \mu\text{g m}^{-3}$  bins.

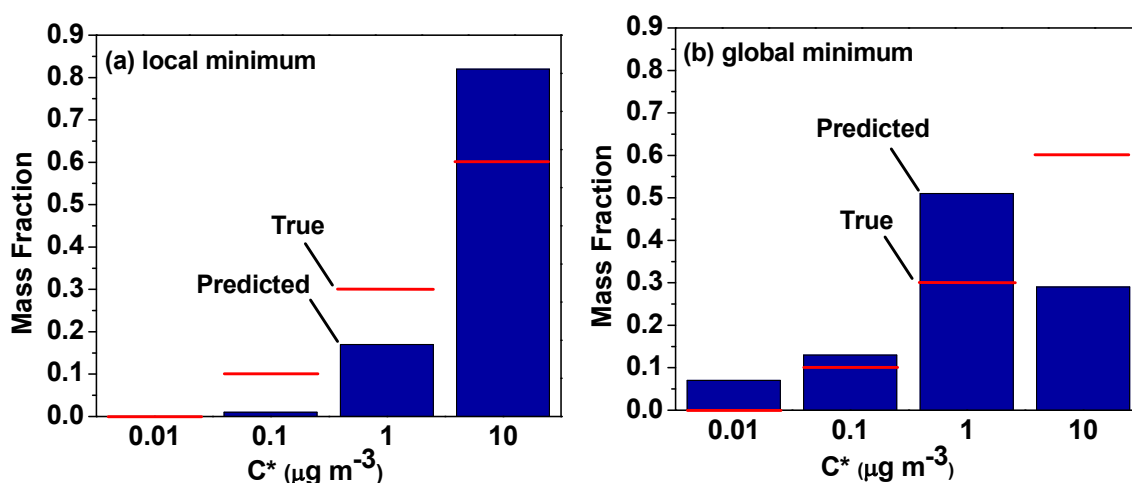


**Figure 2.3** Estimated (bars) and true (red lines) volatility distribution for OA consisting of 10%  $C^*=0.1 \mu\text{g m}^{-3}$ , 30%  $1 \mu\text{g m}^{-3}$ , 60%  $10 \mu\text{g m}^{-3}$ ,  $\Delta H_{\text{vap}}=50 \text{ kJ mol}^{-1}$  and  $a_m=1$ , based on TD pseudo-data. (a) Solution corresponding to a local minimum of the objective function. The estimated vaporization enthalpy and accommodation coefficient are  $\Delta H_{\text{vap}}=38 \text{ kJ mol}^{-1}$  and  $a_m=0.9$ . (b) Solution for the global minimum. The estimated  $\Delta H_{\text{vap}}$  and  $a_m$  are  $68 \text{ kJ mol}^{-1}$  and 0.84 respectively.

The vaporization enthalpy estimation error was 24% and the estimated accommodation coefficient was 0.9 close to the true value of unity. This is however a local minimum of the objective function.

The global minimum (minimum error) was found when we used an initial guess of [0.1 0.1 0.3 0.5] for the mass fractions, 80 kJ mol<sup>-1</sup> for  $\Delta H_{\text{vap}}$  and 0.2 for  $a_m$ . The estimated OA volatility distribution, in this case, is shown in Figure 2.3b. In this case, the shape of the volatility distribution is not correct and there are errors in the mass fractions of the volatility bins as large as 0.3. The estimated vaporization enthalpy and accommodation coefficient were similar to those of the previous guess with a relative error of 35% for  $\Delta H_{\text{vap}}$ . Due to the experimental error, the global minimum can correspond to volatility distributions that are far from the true values. We conclude that the optimization method may not be appropriate for the estimation of the volatility distribution, the vaporization enthalpy and the mass accommodation coefficient. It is also clear that we need an approach for estimating the corresponding uncertainties.

### 2.2.3 Estimation of uncertainty

In an effort to explore in more detail the solution space for the problem we discretized the parameter space and simulated all combinations of volatilities,  $\Delta H_{\text{vap}}$  and  $a_m$ . We used once more four bins for volatilities from 10<sup>-2</sup> to 10  $\mu\text{g m}^{-3}$  and varied the mass fraction of each bin from 0 to 1 with a step of 0.1. The values used for  $\Delta H_{\text{vap}}$  were from 20 to 200 with discrete values of 20, 50, 80, 100, 150 and 200 kJ mol<sup>-1</sup> and for  $a_m$  the values were from 0.01 (large mass resistance) to 1 (no mass resistance) with discrete values of 0.01, 0.05, 0.1, 0.2, 0.5 and 1. We tried in our simulations also other discretizations for the values of the vaporization enthalpy and the mass accommodation coefficient and they did not affect the results. In the rest of the paper, the discretizations for the  $\Delta H_{\text{vap}}$  and the  $a_m$  described above will be used for all of the simulations. For each simulation the percent error was estimated from:

$$E_i = \frac{100}{n} \sqrt{\sum_i^n (MFR_{i,\text{guess}} - MFR_i)^2} \quad (10)$$

where  $MFR_{i,\text{guess}}$  is the MFR for a certain combination of parameters for data point  $i$  (corresponding to a specific temperature),  $MFR_i$  is the ‘measured’ MFR and  $n$  is the number of the different temperatures  $T_{\text{TD}}$  used in our ‘measurements’.

After performing simulations for all combinations of all properties we identified the combinations which led to small errors (less than 2%). From these values we then calculated a ‘best estimate’ using the inverse error as a weighting factor:

$$\bar{x} = \frac{\sum_i^N \left[ x_i \cdot \left( \frac{1}{E_i} \right) \right]}{\sum_i^N \left[ \frac{1}{E_i} \right]} \quad (11)$$

where  $x_i$  is the value of property  $i$  (the mass fractions of volatility bin  $i$  or the vaporization enthalpy  $\Delta H_{\text{vap}}$  or accommodation coefficient  $\log(a_m)$ ).

We also calculated the uncertainty range for all three properties calculating the standard deviation ( $\sigma$ ) of the corresponding values:

$$\sigma = \sqrt{\frac{\sum_i^N \left[ \left( x_i - \bar{x} \right)^2 \cdot \left( \frac{1}{E_i} \right) \right]}{\sum_i^N \left[ \frac{1}{E_i} \right]}} \quad (12)$$

The logarithms of the accommodation coefficient values were used in order to avoid negative accommodation coefficient values inside the uncertainty range. We report one standard deviation as the uncertainty range in the rest of the paper.

## 2.3 Results

The first parameter of the thermodenuder experiments explored was the number of measurements at different temperatures in the thermogram under consideration. In previous studies, thermodenuder measurements vary between 6 (An et al., 2007) and 12 measurements (Faulhaber et al., 2009).

A wide variety of cases of OA were tested during the simulations once more. The results for a multicomponent OA with mostly nonvolatile material (80%  $0.01 \mu\text{g m}^{-3}$ , 5%  $0.1 \mu\text{g m}^{-3}$ , 10%  $1 \mu\text{g m}^{-3}$  and 5%  $10 \mu\text{g m}^{-3}$ ), for the case of 6 and 12 measurements, are given in Figure 2.4 as a representative example.

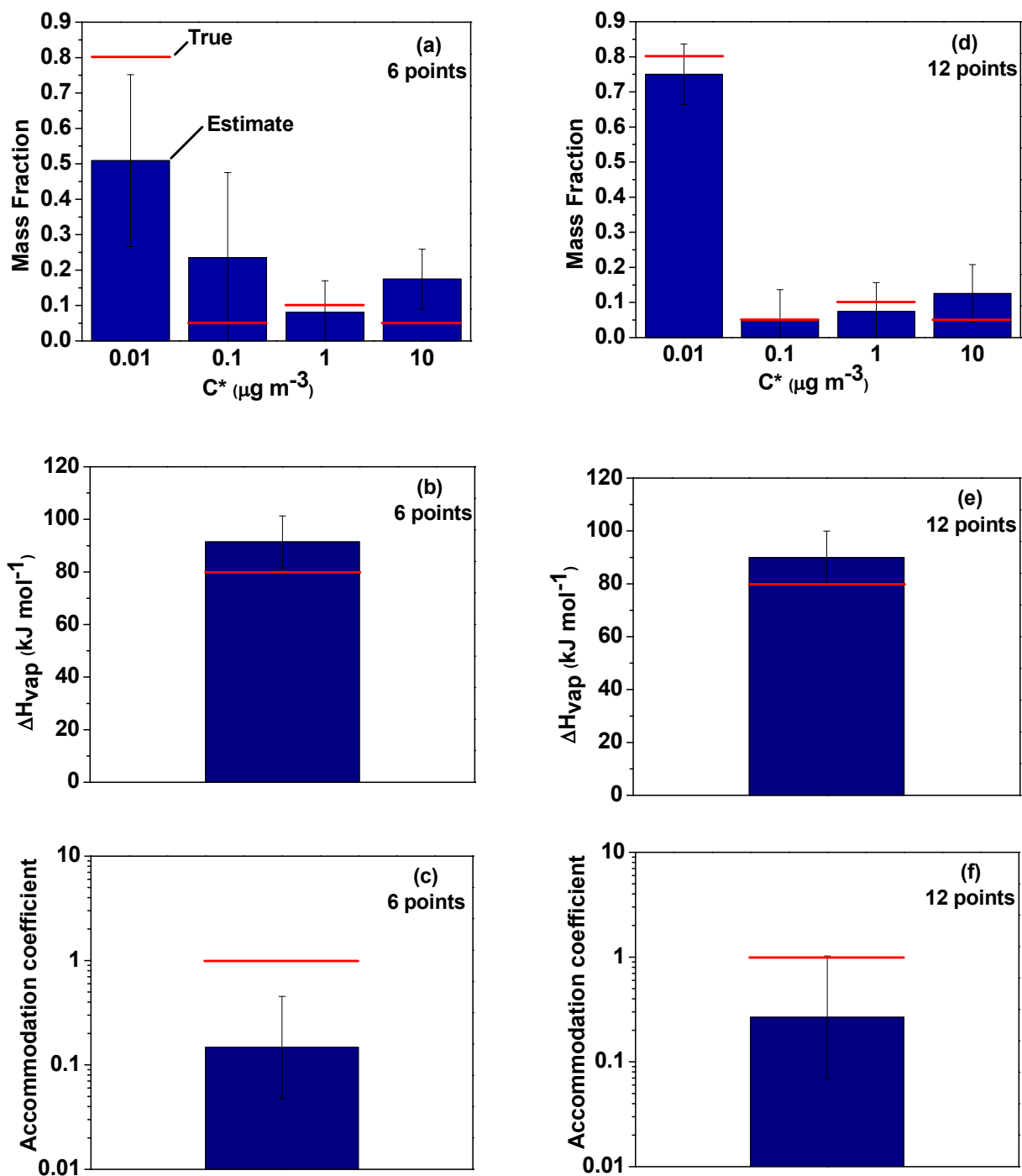


**Figure 2.4** Estimated (bars) and true (red lines) parameter values for an OA with 80%  $0.01 \mu\text{g m}^{-3}$ , 5%  $0.1 \mu\text{g m}^{-3}$ , 10%  $1 \mu\text{g m}^{-3}$ , 5%  $10 \mu\text{g m}^{-3}$ ,  $\Delta H_{\text{vap}}=80 \text{ kJ mol}^{-1}$  and  $a_m=1$  for: 6 measurements (a) volatility distribution, (b)  $\Delta H_{\text{vap}}$ , (c)  $a_m$ , and using 12 measurements for: (d) volatility distribution, (e)  $\Delta H_{\text{vap}}$  and (f)  $a_m$ . The error bars represent the uncertainty of the estimated value.

For the first experiment, with a small number of measurements (6 points), there is large uncertainty in the two least volatile bins (with a standard deviation up to 0.25). The uncertainty range, in the least and most volatile bins ( $0.01$  and  $10 \mu\text{g m}^{-3}$ ) does not include the correct values for the distribution. In the second experiment, twice as many measurements were used (12 points), the estimated uncertainty range is smaller (the standard deviation of all the predicted mass fractions is less than 0.08) and it contains the correct volatility distribution. The relative error of the estimated  $\Delta H_{\text{vap}}$  is 13%, in both experiments. Finally, the  $a_m$  is underestimated for both experiments but with the second experiment (using 12 measurements) the uncertainty range includes the correct value.

For cases of OA with more uniform volatility distributions (e.g., cases where the mass fraction varies less than 0.2 between the bins), the use of 12 measurements instead of 6 gave similar estimates for the three properties (volatility distribution, vaporization enthalpy and mass accommodation coefficient) and the same uncertainty ranges. In cases of extreme volatility distributions, where most material is in one or two volatility bins, as in the case of the example in Figure 2.4, using more measurements resulted in better estimates and smaller uncertainty ranges than using only a small number of measurements.

In Figure 2.5, we examine two more cases of OA with extreme volatility distributions using 12 pseudo-measurements. In the first test, which is the same OA as in Test 1 discussed in Section 2.2, the OA consists of two components: very low volatility material (60%  $0.01 \mu\text{g m}^{-3}$ ) and high volatility material (40%  $10 \mu\text{g m}^{-3}$ ). The estimated uncertainty range is large especially for the two least volatile bins (with an uncertainty equal to 0.2) but it includes the actual volatility distribution. Also, the estimated volatility distribution has the correct shape. The estimated vaporization enthalpy has an error of 5% while the accommodation coefficient error is around 20%.

In the second test, we assume that the OA consists of very low volatility material (50%  $0.01 \mu\text{g m}^{-3}$ ) and relatively high volatility material (50%  $1 \mu\text{g m}^{-3}$ ). The shape of the volatility distribution of the OA is not captured by the inversion results, the estimated uncertainty range is large (the uncertainty of all the predicted mass fractions is around 0.2) and the uncertainty range does not contain the actual volatility distribution. The error of the estimated  $\Delta H_{\text{vap}}$  is 8%. The accommodation coefficient is under-predicted by one order of magnitude (value equal to 0.15 instead of unity). The TD measurements are not sufficient in this case for the accurate estimation of the OA volatility distribution.

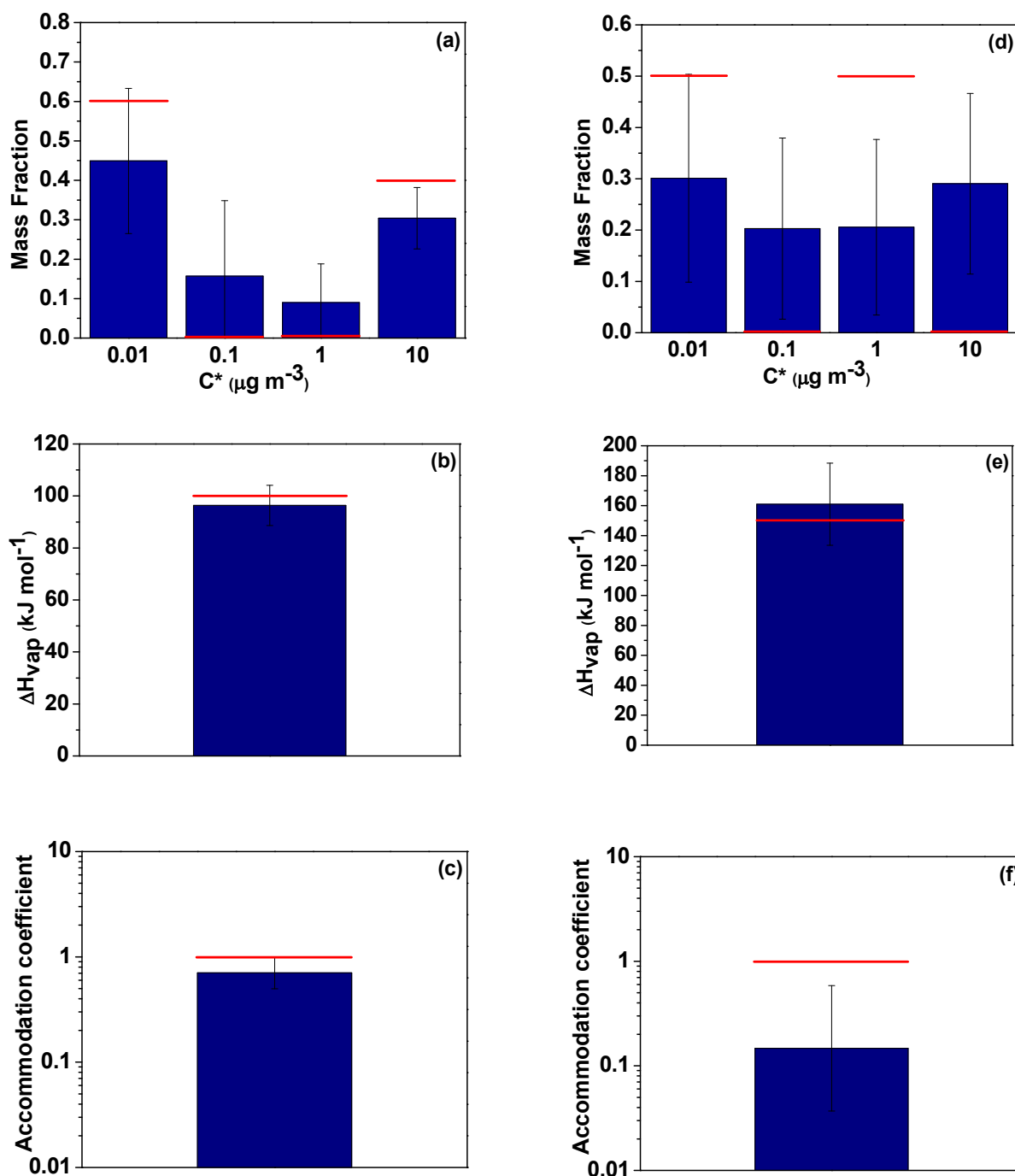


**Figure 2.5** Estimated (bars) and true property values (red lines) using 12 TD measurements, for two types of OA. (a) volatility distribution, (b)  $\Delta H_{\text{vap}}$ , (c)  $a_m$  for OA with 60% 0.01  $\mu\text{g m}^{-3}$  and 40% 10  $\mu\text{g m}^{-3}$ ,  $\Delta H_{\text{vap}}=100 \text{ kJ mol}^{-1}$  and  $a_m=1$  and (d) volatility distribution, (e)  $\Delta H_{\text{vap}}$ , (f)  $a_m$  for OA with 50% 0.01  $\mu\text{g m}^{-3}$  and 50% 1  $\mu\text{g m}^{-3}$ ,  $\Delta H_{\text{vap}}=150 \text{ kJ mol}^{-1}$  and  $a_m=1$ . The error bars represent the uncertainty of the estimated value.

In order to evaluate how general are the above results of the proposed volatility estimation method we performed additional tests using ten randomly generated volatility distributions. The sets of parameters used are shown in Table 2.2. The ten first parameter sets have random OA volatility distributions, a vaporization enthalpy equal to 90 kJ mol<sup>-1</sup> (chosen as a reasonable intermediate value between 20 and 200 kJ mol<sup>-1</sup>) and an accommodation coefficient of 0.1 (chosen as a medium mass resistance). Additional cases with either low (sets 11-13) or high mass transfer resistance (sets 14-16) and cases with low (sets 11 and 13) or higher vaporization enthalpies (sets 12, 15 and 16) were also examined.

**Table 2.2** Sets of random volatility distributions used for the evaluation of different inversion approaches.

OA Parameter Set	Mass Fraction				$\Delta H_{\text{vap}}$ (kJ mol <sup>-1</sup> )	$a_m$
	0.01 $\mu\text{g m}^{-3}$	0.1 $\mu\text{g m}^{-3}$	1 $\mu\text{g m}^{-3}$	10 $\mu\text{g m}^{-3}$		
1	0.135	0.06	0.14	0.665	90	0.1
2	0.45	0.04	0.315	0.195	90	0.1
3	0.255	0.115	0.47	0.16	90	0.1
4	0.235	0.045	0.025	0.695	90	0.1
5	0.565	0.23	0.175	0.03	90	0.1
6	0.105	0.21	0.59	0.095	90	0.1
7	0.375	0.405	0.15	0.07	90	0.1
8	0.375	0.095	0.07	0.46	90	0.1
9	0.145	0.435	0.25	0.17	90	0.1
10	0.245	0.085	0.08	0.59	90	0.1
11	0.565	0.23	0.175	0.03	70	1
12	0.565	0.23	0.175	0.03	140	1
13	0.245	0.085	0.08	0.59	60	1
14	0.245	0.085	0.08	0.59	120	0.01
15	0.135	0.06	0.14	0.665	120	0.01
16	0.105	0.21	0.59	0.095	140	0.01

The inversion results are shown in Table 2.3. They include the average absolute errors for the VBS bins, the relative error (%) for the vaporization enthalpy and the errors for  $a_m$  (in orders of magnitude).

**Table 2.3** Results for the sets of random volatility distributions using different inversion approaches.

OA Parameter Set	TD measurements			Dilution measurements		TD and Dilution measurements		
	Average absolute error for VBS bins	Relative error (%) for $\Delta H_{\text{vap}}$	Error for $a_m$ (orders of magnitude)	Average absolute error for VBS bins	Error for $a_m$ (orders of magnitude)	Average absolute error for VBS bins	Relative error (%) for $\Delta H_{\text{vap}}$	Error for $a_m$ (orders of magnitude)
<b>1</b>	0.05	6	0.43	0.13	0.39	0.02	11	0
<b>2</b>	0.13	3	0.06	0.11	0.17	0.02	2	0.16
<b>3</b>	0.1	8	0.1	0.51	0.19	0.07	2	0.02
<b>4</b>	0.08	10	0.45	0.19	0.36	0.02	4	0.1
<b>5</b>	0.14	4	0.28	0.12	0.44	0.14	0.7	0.46
<b>6</b>	0.1	10	0.02	0.15	0.02	0.07	10	0.04
<b>7</b>	0.14	7	0.13	0.06	0.19	0.07	2	0.05
<b>8</b>	0.07	4	0.17	0.18	0.34	0.04	0.9	0.06
<b>9</b>	0.09	3	0.04	0.07	0.21	0.09	0.1	0.34
<b>10</b>	0.06	11	0.45	0.16	0.46	0.06	11	0.37
<b>11</b>	0.14	14	1.17	0.12	1.06	0.1	14	0.77
<b>12</b>	0.11	14	0.95	0.12	1.06	0.06	23	0.96
<b>13</b>	0.06	2	0.3	0.07	0.17	0.08	0.04	0.24
<b>14</b>	0.18	25	1.22	0.2	0.75	0.33	17	1
<b>15</b>	0.22	14	1.12	0.21	0.83	0.3	8	1.22
<b>16</b>	0.11	11	0.63	0.18	0.50	0.17	4	0.32

These results indicate that an accurate estimation of the OA volatility distribution is challenging in most cases. The volatility distribution was estimated with average absolute errors less than 0.1 for six out of the sixteen cases tested (sets 1, 4, 8, 9, 10 and 13) and for the rest of the cases the errors were up to 0.22. The average relative error of the estimated  $\Delta H_{\text{vap}}$  was roughly 10%. The error for the estimated accommodation coefficient varied from half to almost one and half order of magnitude. Concerning the uncertainties (not shown), the uncertainty range of the volatility distribution in most of the cases was large (around 0.2). Exceptions are the cases with most material in the lowest and highest volatility bins where the uncertainty range is 0.05-0.15. The uncertainty of the estimated  $\Delta H_{\text{vap}}$  for most of cases was around 20%. The uncertainty of the estimated accommodation coefficient varied from less than one order of magnitude to two orders of magnitude.

Based on the above results, it is evident that it is very difficult to estimate the three properties accurately and with a small uncertainty range since there are many combinations of properties that can lead to a thermogram quite similar to the one from the pseudo-experiment. So, even if the uncertainty estimation method proposed here is a step forward, the TD inversion results are either too uncertain or sometimes erroneous. The TD measurements using one residence time (17 s) are not sufficient to constrain the three properties since equilibrium is not reached in most cases. It is clear that improvements in the volatility measurement approach itself are needed. A number of ideas are explored in the next section. These include, using more than one TD residence times, or, using measurements at much longer timescales (e.g., isothermal dilution measurements).

## **2.4 Improvements of Volatility Measurement Method**

### **2.4.1 Use of two residence times**

In order to improve the method for the estimation of the OA volatility distribution,  $\Delta H_{\text{vap}}$  and  $a_m$ , we simulated ‘measurements’ using two residence times (Lee et al., 2010) but with half the data points for each measurement (6 points for each residence time). We used two residence times of 17 and 34 s. The estimation of the volatility distributions was improved, but the improvement in most cases was small to modest. For example, for the case of OA consisting of very low volatility material (50%  $0.01 \mu\text{g m}^{-3}$ ) and relatively high volatility material (50%  $1 \mu\text{g m}^{-3}$ ), the correct volatility distribution was still not retrieved, the uncertainty range once again was large (equal to

0.2) and it did not contain the actual volatility distribution. The relative error of the estimated  $\Delta H_{\text{vap}}$  was 6%. The accommodation coefficient was under-predicted by one order of magnitude (value equal to 0.12 instead of unity).

We performed a number of tests with different OA systems. The use of two residence times resulted in improved estimates in some cases (e.g., single component systems) but in the majority of the cases the improvement was marginal. The results were often quite similar to those of the one residence time discussed above (with twice the data points). This was due to the fact that in most cases the system is still far from equilibrium. We concluded that just doubling the residence time was not sufficient and the residence time should increase to tens of minutes in most of cases. This is very difficult though for continuous flow systems so the next step was the exploration of the utility of evaporation measurements at much longer timescales than those that can be reached with a TD.

#### 2.4.2 Isothermal dilution experiments

We tested the effectiveness of performing only isothermal dilution measurements instead of TD measurements. The isothermal evaporation of OA can take place in a smog chamber and allows residence times of a few hours (Grieshop et al., 2009). The isothermal evaporation results at room temperature do not depend on  $\Delta H_{\text{vap}}$ , but only on  $C^*$  and  $a_m$ . We assume that we dilute our OA samples during the injection in the chamber with a 10-fold volume of clean air so in this way the initial gas and particle concentrations are lowered by a factor of 10 and the system is out of equilibrium. We allow the aerosol to evaporate in the chamber for 2 hours, and assume that its concentration is measured every ten minutes. The error distribution used for the isothermal dilution is also based on the variability of the corresponding laboratory data. We ‘corrupted’ the time dependent mass transfer model predictions with random error assuming a uniform distribution with a standard deviation given by:

$$\sigma = 0.05 \cdot MFR_{\text{true}} + 0.03 \quad (11)$$

where  $MFR_{\text{true}}$  are the correct MFR values.

A typical set of isothermal dilution ‘measurements’ is shown in Figure 2.6. The organic particles reach equilibrium with the gas phase after approximately thirty minutes in this pseudo-experiment.

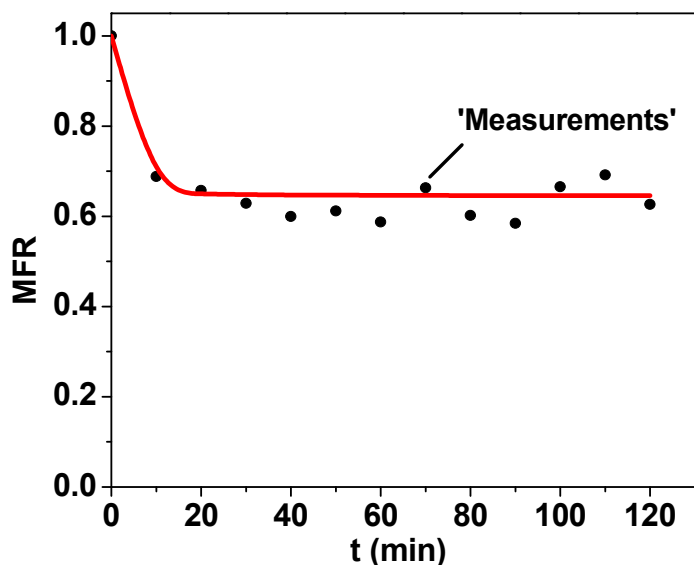


**Figure 2.6** Isothermal dilution measurements (MFR as function of time) for an aerosol with 60%  $0.01 \mu\text{g m}^{-3}$ , 40%  $10 \mu\text{g m}^{-3}$ ,  $\Delta H_{\text{vap}}=100 \text{ kJ mol}^{-1}$  and  $a_m=1$ . The red line corresponds to the true properties of the aerosol and the black dots are the ‘measured’ MFR values.

The inversion results for the case of OA consisting of very low volatility material (60%  $0.01 \mu\text{g m}^{-3}$ ) and high volatility material (40%  $10 \mu\text{g m}^{-3}$ ) and the OA with very low volatility material (50%  $0.01 \mu\text{g m}^{-3}$ ) and relatively high volatility material (50%  $1 \mu\text{g m}^{-3}$ ) are shown in Figure 2.7. The estimated volatility distribution had significant error and the uncertainty was large (equal to 0.2). The accommodation coefficient was estimated within 20%.

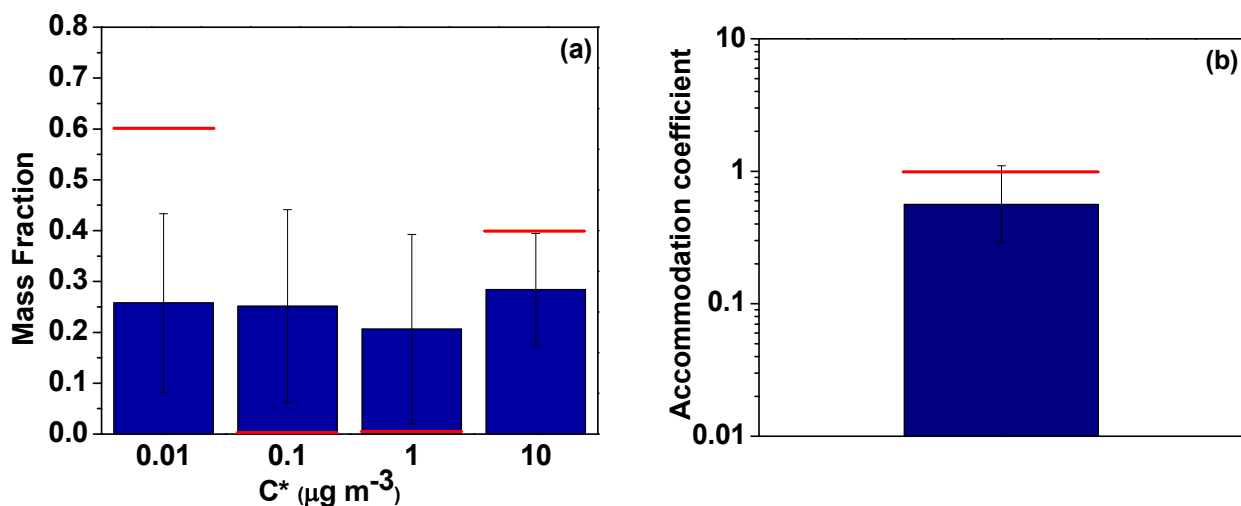


**Figure 2.7** Estimated (bars) volatility distribution and accommodation coefficient and true (red lines) values using isothermal dilution “measurements”, for an OA with 60%  $0.01 \mu\text{g m}^{-3}$  and 40%  $10 \mu\text{g m}^{-3}$ ,  $\Delta H_{\text{vap}}=100 \text{ kJ mol}^{-1}$  and  $a_m=1$ . (a) volatility distribution and (b)  $a_m$ .

The dilution method was also used for the random sets of volatility distributions shown in Table 2.2 and the results are shown in Table 2.3. The average absolute errors for the VBS bins were around 0.2 and the errors for the accommodation coefficient in all cases were up to one order of magnitude. Isothermal dilution did not consistently improve the estimated volatility distributions and the accommodation coefficient compared to the use of TD measurements. The uncertainty remains large, since there are still many combinations of the two properties that can lead to similar dilution curves.

### 2.4.3 Combination of TD and isothermal dilution measurements

We continued with the test of effectiveness of combining TD and isothermal dilution “measurements” using the same method as in Section 2.2.3. We used the same discretization for the values of the volatility distribution, the vaporization enthalpy and the accommodation coefficient and constructed, using the evaporation model, the theoretical thermograms. Using random numbers based on a normal distribution (for the case of thermodenuder pseudo-measurements) and uniform distribution (for the case of isothermal dilution measurements), we produced pseudo-measurements for the different experiments. Then for the resulting 24 measurements (12 for each TD and dilution pseudo-experiment) we performed the error minimization with the percent error given by equation 10, treating equally the TD and isothermal dilution measurements. In the case of Test 1 (Table 2.1) shown in Figure 2.8 the estimated volatility distribution has the correct shape and the corresponding uncertainty range is small (uncertainty less or equal than 0.1). The  $\Delta H_{\text{vap}}$  and the  $a_m$  were estimated within a few percent. In another challenging test (Figure 2.9) the shape of the volatility distribution is again correctly predicted. The estimated value of the vaporization enthalpy has an error of only 7% and the estimated accommodation coefficient is 0.4 instead of unity.

We also repeated all the tests of Table 2.2. The results are shown in Table 2.3. In 70% of the cases, the volatility distribution was reproduced with absolute errors less than 0.1. The average relative error of the estimated  $\Delta H_{\text{vap}}$  was roughly 7%. The error for the estimated accommodation coefficient, for the cases of OA varied from less than half order of magnitude up to one order of magnitude. The uncertainties (not shown) for the volatility distribution in 70% of the cases were not higher than 0.05-0.1. The uncertainties for the vaporization enthalpy were around 10%. The

accommodation coefficient, for the cases of OA with a value equal to 0.1, had an uncertainty of half an order of magnitude. For cases where the accommodation coefficient was equal to unity, it was underpredicted with an uncertainty varying from half an order of magnitude (set 13), to one order of magnitude (set 11) to two orders of magnitude (set 12). For the cases of OA (sets 14 to 16), where the accommodation coefficient is equal to 0.01, it was overestimated by up to one order of magnitude.

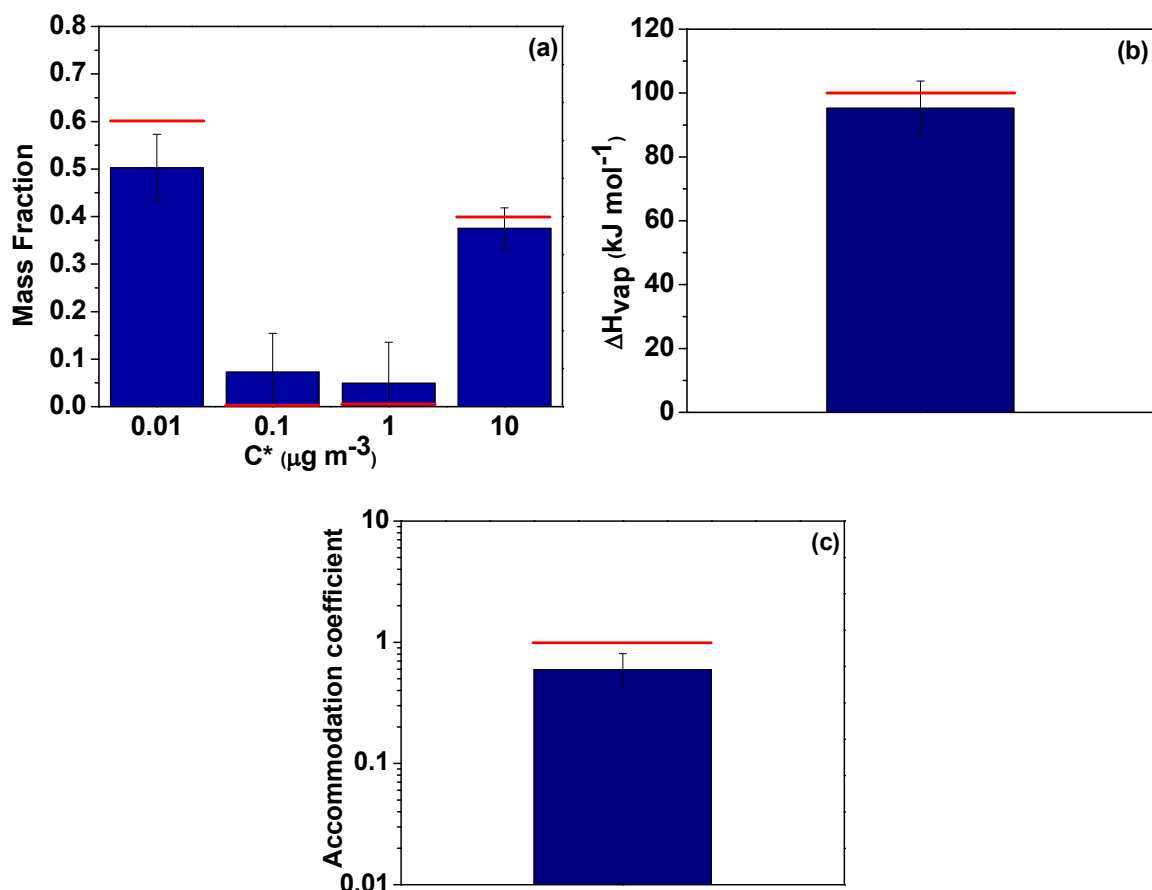


**Figure 2.8** Estimated (bars) and true (red lines) parameter values combining TD and isothermal dilution measurements, for an OA with 60%  $0.01 \mu\text{g m}^{-3}$  and 40%  $10 \mu\text{g m}^{-3}$ ,  $\Delta H_{\text{vap}}=100 \text{ kJ mol}^{-1}$  and  $a_m=1$  for: (a) volatility distribution, (b)  $\Delta H_{\text{vap}}$ , (c)  $a_m$ .

Problems appeared in three cases (set 5, 9, and 13) in which less than 20% of the OA evaporated and in the three cases where equilibrium was not reached (sets 14, 15, and 16). Using higher initial dilution (100 times dilution) the actual volatility distribution was captured in sets 9 and 13, with uncertainties equal to 0.2 and 0.1 correspondingly. Results for set 5 improved marginally because further evaporation could not be achieved due to the large amount of

nonvolatile material in the OA. The longer residence times improved the accuracy of the estimated volatility distributions (errors less than 0.1). The errors in  $\Delta H_{\text{vap}}$  and the accommodation coefficient were also reduced in all cases.

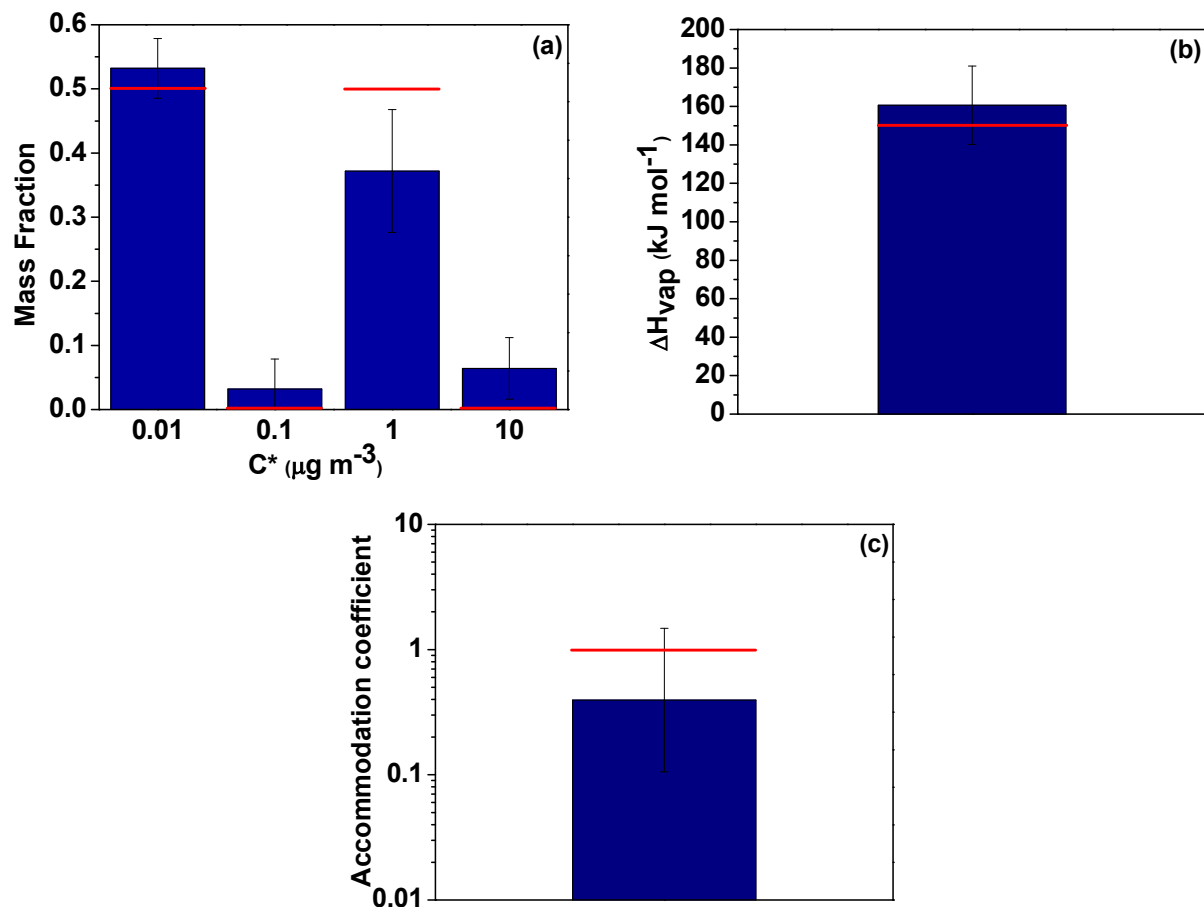


**Figure 2.9** Estimated (bars) and true (red lines) parameter values combining TD and isothermal dilution measurements, for an OA with 50% 0.01  $\mu\text{g m}^{-3}$  and 50% 1  $\mu\text{g m}^{-3}$ ,  $\Delta H_{\text{vap}}=150 \text{ kJ mol}^{-1}$  and  $a_m=1$  for: (a) volatility distribution, (b)  $\Delta H_{\text{vap}}$ , (c)  $a_m$ .

Summarizing, using both TD and dilution experiments reproduced volatility distributions with average uncertainties between 0.05-0.1 for most cases provided that more than 20% or so of the aerosol evaporated during dilution and that the system had enough time to come close to equilibrium. The vaporization enthalpy was estimated with average errors less than 10% in most cases. Estimation of the accommodation coefficient was more challenging than the other parameters. Problems occur mostly when evaporation in dilution experiments is less than 20% or when equilibrium is not reached.

## 2.5 Conclusions

Multiple combinations of parameters ( $C^*$ ,  $\Delta H_{\text{vap}}$ ,  $a_m$ ) can lead to practical indistinguishable thermograms during TD measurements. The estimated volatility distribution, based on the minimum error, can be wrong by several orders of magnitude due to the multiple solutions that exist leading to multiple local minima of the objective function. We introduce a new method combining forward modeling, introduction of experimental error and inverse modeling with error minimization for the interpretation of existing TD measurements. With this method, using an ensemble of ‘best solutions’ we were able to calculate a best estimate and an uncertainty range for the estimated volatility distribution, the vaporization enthalpy and the accommodation coefficient. We show that this uncertainty range is often large and sometimes does not even include the true value of the properties, with the exception in the estimation of the vaporization enthalpy where the errors are around 5-20% in most cases tested.

Experimental approaches that would improve the method were explored. The performance of TD measurements under multiple residence times results in a small to modest improvement of the results since equilibrium is still not reached. The idea of using experiments in a totally longer timescale in order to achieve equilibrium was then examined with the use of dilution measurements. Use of isothermal dilution on its own instead of TD measurements usually leads to worse estimates of the volatility distribution compared to the TD. However, combining both TD and isothermal dilution measurements leads to promising results in the majority of the cases. Cases for which problems remain include those in which the OA does not come close to equilibrium after dilution or when the corresponding evaporated fraction is less than 20%. Increased dilution and longer residence times can help in these cases. The approach combining TD and isothermal dilution measurements is recommended for future studies of OA volatility in both the lab and the field.

## 2.6 References

An, W. J., Pathak, R. K., Lee, B. H., and Pandis, S. N.: Aerosol volatility measurement using an improved thermodenuder: Application to secondary organic aerosol, *J. Aerosol. Sci.*, 38, 305– 314, 2007.

- Burtscher, H., Baltensperger, U., Bukowiecki, N., Cohn, P., Hüglin, C., Mohr, M., Matter, U., Nyeki, S., Schmatloch, V., Streit, N., and Weingartner, E.: Separation of volatile and non-volatile aerosol fractions by thermodesorption: instrumental development and applications, *J. Aerosol Sci.*, 32, 427–442, 2001.
- Cappa, C. D.: A model of aerosol evaporation kinetics in a thermodenuder, *Atmos. Meas. Tech.*, 3, 579–592, 10.5194/amt-3-579-2010, 2010.
- Cappa, C. D. and Jimenez, J.L.: Quantitative estimates of the volatility of ambient organic aerosol, *Atmos. Chem. Phys.*, 10, 5409-5424, 10.5194/acp-10-5409-2010, 2010.
- Cappa, C. D. and Wilson, K. R.: Evolution of organic aerosol mass spectra upon heating: implications for OA phase and partitioning behavior, *Atmos. Chem. Phys.*, 11, 1895-1911, 10.5194/acp-11-1895-2011, 2011.
- Chen, N.H. and Othmer, D.F.: New generalized equation for gas diffusion coefficient, *J. Chem. Eng. Data* 7, 37-41, 1962.
- Donahue, N. M., Robinson, A.L., Stanier, C.O., and Pandis, S.N.: Coupled partitioning, dilution, and chemical aging of semivolatile organics, *Environ. Sci. Technol.*, 40, 2635-2643, 2006.
- Donahue, N. M., Kroll, J. H., Pandis, S. N., and Robinson, A. L.: A two-dimensional volatility basis set – Part 2: Diagnostics of organic-aerosol evolution, *Atmos. Chem. Phys.*, 12, 615–634, 10.5194/acp-12-615-2012, 2012.
- Engler, C., Rose, D., Wehner, B., Wiedensohler, A., Brüggemann, E., Gnauk, T., Spindler, G. Tuch, T., and Birmili, W.: Size distributions of non-volatile particle residuals ( $D_p < 800$  nm) at a rural site in Germany and relation to air mass origin, *Atmos. Chem. Phys.*, 7, 5785–5802, 10.5194/acp-7-5785-2007, 2007.
- Epstein, S.A., Riipinen, I. and Donahue, N.M.: A semiempirical correlation between enthalpy of vaporization and saturation concentration for organic aerosol, *Environ. Sci. Technol.*, 44, 743-748, 2010.
- Faulhaber, A. E., Thomas, B. M., Jimenez, J. L., Jayne, J. T., Worsnop, D. R., and Ziemann, P. J.: Characterization of a thermodenuder-particle beam mass spectrometer system for the study of organic aerosol volatility and composition, *Atmos. Meas. Tech.*, 2, 15–31, 10.5194/amt-2-15-2009, 2009.

- Fuentes, E. and McFiggans, G.: A modeling approach to evaluate the uncertainty in estimating the evaporation behaviour and volatility of organic aerosols, *Atmos. Meas. Tech.*, 5, 735–757, 10.5194/amt-5-735-2012, 2012.
- Grieshop, A. P., Miracolo, M.A., Donahue, N. M. and Robinson, A. L.: Constraining the volatility distribution and gas-particle partitioning of combustion aerosols using isothermal dilution and thermodenuder measurements, *Environ. Sci. Technol.*, 43, 4750-4756, 10.1021/es8032378, 2009.
- Huffman, J. A., Docherty, K. S., Mohr, C., Cubison, M. J., Ulbrich, I. M., Ziemann, P. J., Onasch, T. B., and Jimenez, J. L.: Chemically-resolved volatility measurements of organic aerosol from different source, *Environ. Sci. Technol.*, 43, 5351–5357, 2009.
- IPCC: Climate Change: The Physical Science Basis – Contribution of Working Group I to the Fourth Assessment Report of the Intergovernmental Panel on Climate Change, edited by: Solomon, S., Qin, D., and Manning, M., Cambridge University Press, Cambridge, 996 pp., 2007.
- Jonsson, A. M., Hallquist, M., and Saathoff, H.: Volatility of secondary organic aerosols from the ozone initiated oxidation of  $\alpha$ -pinene and limonene, *J. Aerosol Sci.*, 38, 843–852, 2007.
- Kalberer, M., Paulsen, D., Sax, M., Steinbacher, M., Dommen, J., Prevot, A. S. H., Fisseha, R., Weingartner, E., Frankevich, V., Zenobi, R., and Baltensperger, U.: Identification of polymers as major components of atmospheric organic aerosols, *Science*, 303, 1659–1662, 2004.
- Lee, B.H., Kostenidou, E., Hildebrandt, L., Riipinen, I., Engelhart, G.J., Mohr, C., DeCarlo, P.F., Mihalopoulos, N., Prevot, A.S.H., Baltensperger, U. and Pandis, S.N.: Measurement of the ambient organic aerosol volatility distribution: application during the Finokalia Aerosol Measurement Experiment (FAME-2008), *Atmos. Chem. Phys.*, 10, 12149-12160, 2010.
- Lee, B.H., Pierce, J.R., Engelhart, G.J. and Pandis, S.N.: Volatility of secondary organic aerosol from the ozonolysis of monoterpenes, *Atmos. Environ.*, 45, 2443-2452, 2011.
- Nel, A.: Air pollution-related illness: Effects of particles, *Science*, 308, 804–806, 10.1126/science.1108752, 2005.
- Paciga, A., Riipinen I. and Pandis, S.N.: Effect of ammonia on the volatility of organic diacids, *Environ. Sci. Technol.*, 48 (23), 13769–13775, 2014.

- Pathak, R. K., Presto, A. A., Lane, T. E., Stanier, C. O., Donahue, N. M., and Pandis, S. N.: Ozonolysis of  $\alpha$ -pinene: Parameterization of secondary organic aerosol mass fraction, *Atmos. Chem. Phys.*, 7, 3811–3821, 10.5194/acp-7-3811-2007, 2007.
- Pope, C. A. and Dockery, D. W.: Health effects of fine particulate air pollution: Lines that connect, *J. Air Waste Manage. Assoc.*, 56, 709-742, 2006.
- Riipinen I., Pierce, J. R., Donahue N. M., and Pandis S. N.: Equilibration time scales of organic aerosol inside thermodenuders: Kinetics versus equilibrium thermodynamics, *Atmos. Environ.*, 44, 597–607, 2010.
- Saleh, R., Walker, J., and Khlystov, A.: Determination of saturation pressure and enthalpy of vaporization of semi-volatile aerosols: The integrated volume method, *J. Aerosol. Sci.*, 39, 876–887, 10.1016/j.jaerosci.2008.06.004, 2008.
- Saleh, R., Shihadeh, A. and Khlystov, A.: On transport phenomena and equilibration timescales in thermodenuders, *Atmos. Meas. Tech.*, 4, 571–581, 10.5194/amt-4-571-2011, 2011.
- Saleh, R., Khlystov, A. and Shihadeh, A.: Determination of evaporation coefficients of ambient and laboratory-generated semivolatile organic aerosols from phase equilibration kinetics in a thermodenuder, *Aerosol Sci. Technol.*, 46, 22–30, 2012.
- Seinfeld, J.H. and Pandis, S.N.: *Atmospheric Chemistry and Physics*, second ed., John Wiley and Sons, Hoboken, New Jersey, USA, 2006.
- Stanier, C. O., Donahue, N., Pandis, S. N.: Parameterization of secondary organic aerosol mass fractions from smog chamber data, *Atmos. Environ.*, 42, 2276–2299, 2008.
- Vesala, T., Kulmala, M., Rudolf, R., Vrtala, A. and Wagner, P.E.: Models for condensational growth and evaporation of binary aerosol particles. *J. Aerosol. Sci.* 28, 565-598, 1997.
- Wehner, B., Philippin, S., and Wiedensohler, A.: Design and calibration of a thermodenuder with an improved heating unit to measure the size-dependent volatile fraction of aerosol particles, *J. Aerosol Sci.*, 33, 1087–1093, 2002.
- Wehner, B., Philippin, S., Wiedensohler, A., Scheer, V., and Vogt, R.: Variability of non-volatile fractions of atmospheric aerosol particles with traffic influence, *Atmos. Environ.*, 38, 6081–6090, 2004.
- Zhang, Q., Jimenez, J. L., Canagaratna, M. R., Allan, J. D., Coe, H., Ulbrich, I., Alfarra, M. R., Takami, A., Middlebrook, A. M., Sun, Y. L., Dzepina, K., Dunlea, E., Docherty, K., DeCarlo, P. F., Salcedo, D., Onasch, T., Jayne, J. T., Miyoshi, T., Shimojo, A., Hatakeyama,

S., Takegawa, N., Kondo, Y., Schneider, J., Drewnick, F., Borrmann, S., Weimer, S., Demerjian, K., Williams, P., Bower, K., Bahreini, R., Cottrell, L., Griffin, R. J., Rautiainen, J., Sun, J. Y., Zhang, Y. M., and Worsnop, D. R.: Ubiquity and dominance of oxygenated species in organic aerosols in anthropogenically-influenced Northern Hemisphere midlatitudes, *Geophys. Res. Lett.*, 34, L13801, 10.1029/2007GL029979, 2007.

# Chapter 3

## Estimation of the volatility distribution of ambient organic aerosol and its components using thermodenuder measurements<sup>1</sup>

<sup>1</sup> Parts of the chapter have been published as:

Paciga, A., Karnezi, E., Kostenidou, E., Hildebrandt, L., Psychoudaki, M., Engelhart, G.J., Lee, B.H., Crippa, M., Prévôt, A.S.H., Baltensperger, U., Pandis, S.N.: Volatility of organic aerosol and its components in the megacity of Paris, *Atmos. Chem. Phys.* 16, 2013–2023, 2016.

Louvaris, E. E., Florou, K., Karnezi, E., Papanastasiou, D. K., Gkatzelis, G. I. and Pandis, S. N.: Volatility of source apportioned wintertime organic aerosol in the city of Athens, *Atmos. Env.* (under review), 2017.

### 3.1 Introduction

Atmospheric aerosols have adverse effects on human health (Caiazzo et al., 2013; Pope et al., 2009) and contribute to climate change (IPCC, 2014). Over 50% of the submicron particulate mass is often comprised of organic compounds (Zhang et al., 2007). OA (organic aerosol) originates from many different natural and anthropogenic sources and processes. It can be emitted directly, e.g., from fossil fuels and biomass combustion (so-called primary organic aerosol, POA) or can be formed by atmospheric oxidation of volatile, intermediate volatility and semi-volatile organic compounds (secondary organic aerosol, SOA). Since the oxidation pathways of organic vapors are complex and the corresponding reactions lead to hundreds or even thousands of oxygenated products for each precursor, our understanding of OA formation mechanisms and the OA chemical and physical properties remains incomplete.

The volatility of atmospheric OA is one of its most important physical properties. It determines the partitioning of these organic compounds between the gas and particulate phases, the OA concentration, and the atmospheric fate of the corresponding compounds. Measurement of the OA volatility distribution has been recognized as one of the major challenges in our efforts to quantify the rates of formation of secondary organic particulate matter (Donahue et al., 2012). Thermodenuders (TD) have been developed to measure the volatility of ambient aerosol (Burtscher et al., 2001; Wehner et al., 2002, 2004; Kalberer et al., 2004; An et al., 2007). The aerosol mass fraction remaining (MFR) at a given temperature, after passing through the TD, is the most common way of reporting the TD measurements. The MFR, though an indirect metric of volatility for a specific TD operation, also depends on the aerosol concentration, size, enthalpy of vaporization, potential resistances to mass transfer, etc (Riipinen et al., 2010).

The two-dimensional volatility basis set (2D-VBS) framework from Donahue et al. (2012) has been used in order to describe atmospheric OA formation and evolution by lumping all organic compounds (with the exception of VOCs) into surrogates along two axes of volatility and the oxygen content (expressed as the O:C ratio or carbon oxidation state). Using the 2D VBS requires the ability to measure the OA distribution as a function of volatility and O:C ratio (or carbon oxidation state).

Positive Matrix Factorization (PMF), aims to separate the bulk OA mass spectra obtained by the aerosol mass spectrometer (AMS) into combinations of individual “factors” that give information about the sources or processing of organic aerosol (Lanz et al., 2007; Ulbrich et al.,

2009; Huffman et al., 2009; Zhang et al., 2011). Typical factors correspond to either primary sources including HOA (hydrocarbon-like OA), BBOA (biomass burning OA) and COA (cooking OA) or secondary OA like SV-OOA (semi-volatile oxygenated OA) and LV-OOA (low volatility oxygenated OA). Although there have been numerous studies that have identified PMF factors in ambient datasets, there have been few studies that have attempted to estimate the corresponding factor volatility (Huffman et al., 2009; Cappa and Jimenez, 2010). Huffman et al. (2009) characterized the volatility of PMF factors derived for the MILAGRO campaign in Mexico City and for the SOAR-1 campaign in Riverside, CA. They concluded that BBOA was the most volatile and OOA was the least volatile component. HOA was more volatile than OOA in almost all cases. Cappa and Jimenez (2010), using a kinetic evaporation model, estimated the volatility distributions for the various PMF OA factors for the MILAGRO campaign.

Here we extend this work focusing on two major cities, Paris and Athens. Firstly, we estimate the volatility distributions of PMF factors derived from two month-long summer and winter campaigns in a suburban background site in Paris. The data analysis approach is first outlined and the corresponding challenges are discussed. We use the mass transfer model of Riipinen et al. (2010), together with the with the uncertainty estimation algorithm presented in Chapter 2 to estimate the volatility distributions for all PMF factors. Then we focus on another large European urban center, Athens, during wintertime. We determine again the volatility distribution of the four OA PMF factors reported during a month-long winter campaign. In these studies there were only TD measurements available. No isothermal dilution measurements were made during these studies.

## **3.2 Methods**

### **3.2.1 Paris campaigns**

Two comprehensive field campaigns were performed during July of 2009 and January/February of 2010 at an urban background sampling site, SIRTA (Site Instrumental de Recherche par Teledetection Atmospherique) (Haefelin et al., 2005) located about 20 km southwest of Paris' city center. The datasets were collected as part of the collaborative project MEGAPOLI (Megacities: Emissions, urban, regional, and Global Atmospheric POLution and climate effects, and Integrated tools for assessment and mitigation) (Baklanov et al., 2008; Beekmann et al., 2015).

A suite of instruments was used including a high-resolution time-of-flight aerosol mass spectrometer (HR-ToF-AMS) from Aerodyne (DeCarlo et al., 2006) for particle mass and composition, a scanning mobility particle sizer (SMPS) from TSI for particle size and number distributions and the Carnegie Mellon University thermodenuder (TD) for volatility measurements (An et al., 2007).

The TD, consisted of a heated tube followed by a denuding section, which uses activated charcoal to prevent recondensation of organic vapors. The TD was operated at temperatures ranging from about 20°C to 200°C during both campaigns, yielding thermograms of the organic aerosol mass remaining as a function of TD temperature. The TD scanned this temperature range using different temperatures each day. A centerline residence time of 25 s at 298 K was used for all measurements. This corresponds to mean residence time of approximately 50 s at 298 K.

Changes in composition, mass, and size as a result of aerosol evaporation were quantified by both the SMPS and the HR-ToF-AMS by alternate sampling between the TD and the ambient sample line, every 5 minutes. The SMPS was operated with a sheath flow of 5 L min<sup>-1</sup> and a sample flow rate of 0.5 L min<sup>-1</sup>. The HR-ToF-AMS, which measures the aerosol size-composition distribution of the submicron non-refractory material, was operated in both the higher sensitivity mode (V-mode) and the higher resolution mode (W-mode) (DeCarlo et al., 2006). The V-mode data are used in this study. The AMS collection efficiency was estimated at 0.38 during the summer (Crippa et al., 2013a) and 0.5 during the winter (Crippa et al., 2013b).

### **3.2.2 Athens campaign**

During the period from January 10, 2013 until February 10, 2013 intensive measurements were performed at an urban background site located in the center of the city of Athens. The National Observatory site (37° 58' 21.37" N, 23° 42' 59.94" E) is 200 m from the nearest road and can be described as urban background.

The TD used in this study, was placed upstream of a High-Resolution Time-of-Flight Aerosol Mass Spectrometer (HR-ToF-AMS Aerodyne Research Inc.) (Decarlo et al., 2006; Canagaratna et al., 2007) measuring the size-composition distribution of the submicron non-refractory material, and a Scanning Mobility Particle Sizer (SMPS 3936 TSI Inc.) measuring the particle size distributions. The TD design was similar to that developed by An et al. (2007).

Temperature was controlled by a PID controller (CNI3244-C24, I/32, Omega) through a heating tape (STH102-100, Omega) wrapped around the outer cylinder (100 cm ID) of the heating section based on the measurements of a thermocouple (TJ-36, Omega) placed in the center of the inner cylinder (inner diameter ID=36.4 mm) with actual heating length of 50 cm. Sand filled the space between the two cylinders to minimize temperature fluctuations. The heating section was insulated using a ceramic fiber blanket wrapped around the heating tape and an outer rectangular stainless steel case. The denuder section consisted of an inner tubular mesh (ID=36.4 mm) and an outer stainless steel cylinder (ID=100 mm). Activated carbon was placed between the two tubes as an adsorbent.

During the campaign the TD operated at a temperature range between 25°C and 400°C using several temperature steps. One cycle from 25 to 400°C and back to 25°C lasted approximately 10 h, resulting in a little more than two cycles per day. The starting time of the temperature cycle was different each day allowing the collection of measurements at each TD temperature during different periods of the day. Sampling was alternated between the ambient line and the TD line every 6 minutes with computer-controlled valves. Changes in particle mass concentration, composition, and size due to evaporation in the TD were detected by the HR-ToF-AMS and the SMPS resulting in thermograms of OA MFR as a function of TD temperature. The OA MFR was calculated as the ratio of organic mass concentration of a sample passing through the TD at time  $t_i$  over the average mass concentration of the ambient samples that passed through the bypass line at times  $t_{i-1}$  and  $t_{i+1}$ .

The SMPS was operated at a sampling flow rate of 1 L min<sup>-1</sup> and sheath flow rate of 5 L min<sup>-1</sup> sampling every 3 minutes. The HR-ToF-AMS was sampling with 0.1 L min<sup>-1</sup> and operated in both the higher sensitivity mode (V-mode) and the higher resolution mode (W-mode) (DeCarlo et al., 2006). V-mode data are used for this analysis. The sample residence time in the centerline of the TD was 14 s at 298 K corresponding to an average residence time in the TD of 28 s.

### **3.3 Data Analysis**

#### **3.3.1 Paris campaigns**

The processing of the TD measurements for Paris has been described by Paciga et al. (2016). Only a brief summary is presented here. TD raw measurements were corrected using the size and

temperature dependent corrections of Lee et al. (2010). The OA mass fraction remaining (MFR) was calculated dividing the loss-corrected OA concentration after the TD at time period  $i$  with that of the by-pass line at time period  $i+1$ .

The OA mass concentration data for the summer campaign is shown in Figure 3.1. Overall, the particulate matter mass concentration was surprisingly low during this period in Paris, with a campaign average  $PM_{10}$  OA for SIRTAs of only  $0.83 \mu\text{g m}^{-3}$ .

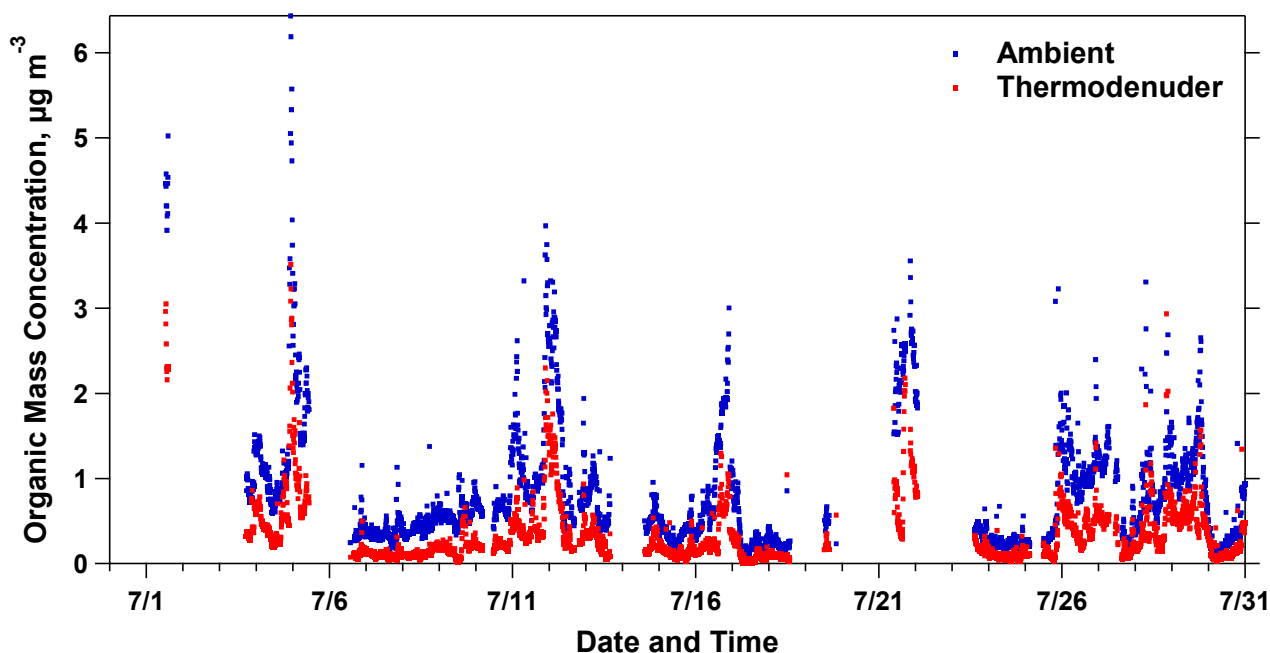


**Figure 3.1** Ambient (blue dots) and thermodenuder (red dots) organic mass concentration measurements for Paris during summer 2009.

Paris during winter, unlike the summer, was characterized by higher fine PM concentrations with an average  $PM_{10}$  OA concentration of  $3.1 \mu\text{g m}^{-3}$  (Figure 3.2).

Along with the bulk organic measurements, additional information can be derived from the HR-ToF-AMS V-mode mass spectra using the PMF analysis technique. A complete discussion of the PMF analysis of the ambient measurements and the resulting factors can be found in Crippa et al. (2013a; b). The PMF analysis was repeated, combining both ambient and thermodenuded spectra with guidance from the original analysis of the ambient-only data (e.g., the same number of factors was used). This second analysis produced for all practical purposes the same results for the ambient data set as that of the ambient measurements only.

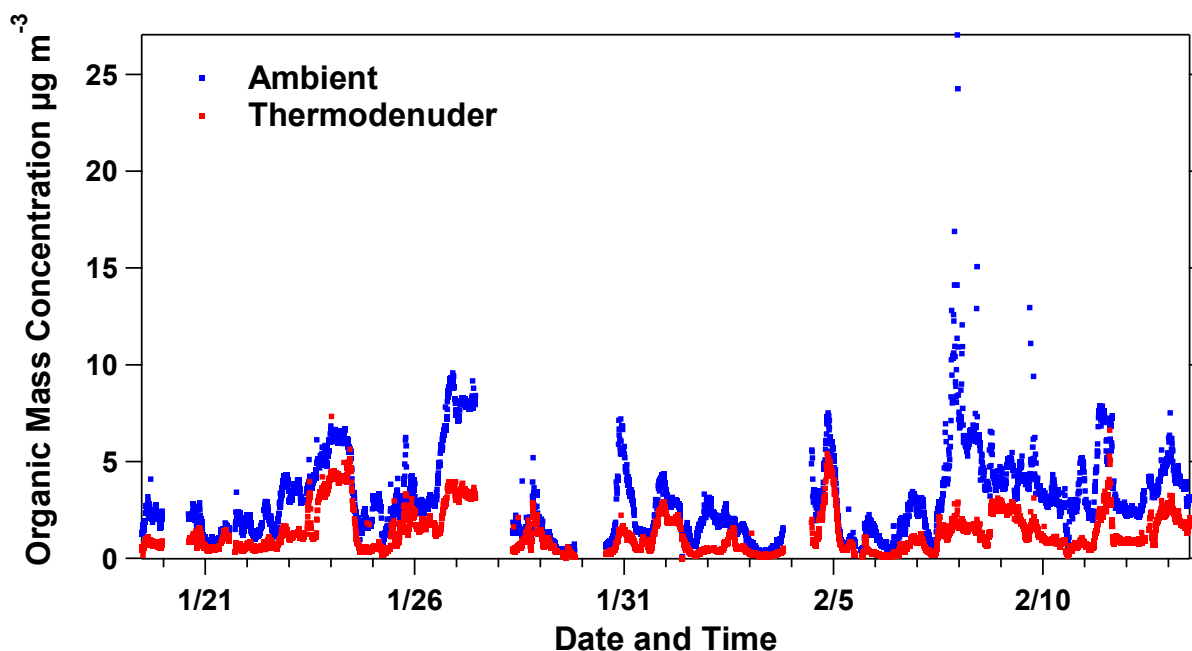


**Figure 3.2** Ambient (blue dots) and thermodenuder (red dots) OA mass time series for the winter Paris 2010 campaign.

The low OA concentrations especially during the summer resulted in very low concentrations of the corresponding factors and thus high MFR uncertainty. The MFRs of the various factors were, as expected, extremely variable when the factor concentrations were close to zero. Therefore, to minimize these problems, a minimum ambient mass concentration was determined for each PMF factor, based on the concentration range for which MFR measurements often exceeded 1.5. The average ambient concentration and threshold concentration with corresponding statistical information for each PMF factor is shown in Table 1. The corresponding factor concentration thresholds during the summer were in the  $0.05\text{-}0.1 \mu\text{g m}^{-3}$  range. MFR measurements of PMF factors with ambient levels less than  $0.1 \mu\text{g m}^{-3}$  are clearly quite uncertain. All the corresponding MFR values from these low factor concentration periods were excluded from the analysis. Few MFR measurements were excluded during the winter period, while 20-50% of the measurements for the various factors were excluded during the summer.

**Table 3.1** Average and threshold ambient concentrations for each PMF factor for Paris summer and winter campaigns.

<b>PMF Factor</b>	<b>Season</b>	<b>Average Mass Concentration</b> ( $\mu\text{g m}^{-3}$ )	<b>Threshold Concentration</b> ( $\mu\text{g m}^{-3}$ )	<b>Percentage of Measurements above Threshold</b>
HOA	Summer	0.16	0.08	53
COA		0.25	0.05	69
MOA		0.17	0.10	73
SV-OOA		0.65	0.10	82
LV-OOA		0.12	0.08	69
HOA	Winter	0.95	0.20	95
COA		0.48	0.08	92
BBOA		0.60	0.07	90
OOA		3.78	0.40	99

### 3.3.2 Athens campaign

The time series of the campaign organic aerosol mass concentration measured by the HR-ToF-AMS are shown in Figure 3.3. The average ambient OA mass concentration was  $8.5 \mu\text{g m}^{-3}$ . Several nighttime periods during the campaign were characterized by very high (more than  $60 \mu\text{g m}^{-3}$ ) OA concentration levels due to residential wood burning. The ambient data were corrected for the AMS particle collection efficiency ( $CE_{\text{amb}}$ ) which was calculated by the algorithm proposed by Kostenidou et al. (2007). The average value for the ambient measurements was  $0.85 \pm 0.23$ . The thermodenuded OA was also corrected for the AMS CE ( $CE_{\text{TD}} = 0.93 \pm 0.12$ ) using the same approach and additionally for particle losses in the TD. To account for these losses, sample flow rate and TD temperature-dependent loss corrections were applied following Lee et al. (2010). The corrected MFR values were then averaged using temperature bins of  $10^\circ\text{C}$ .

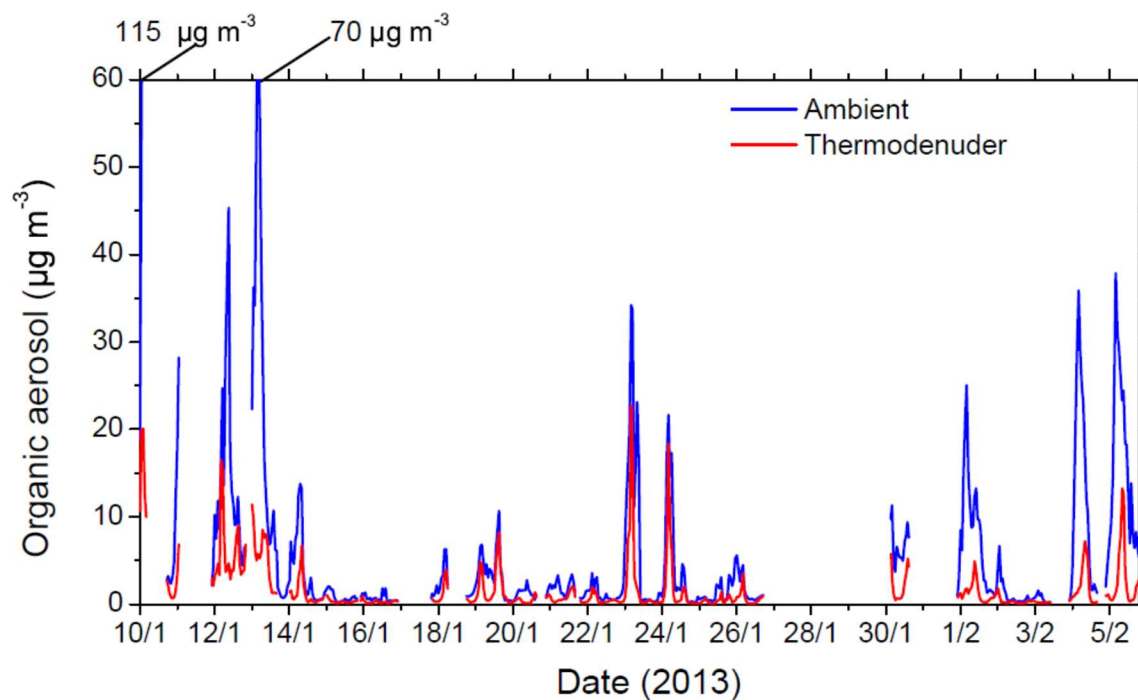


**Figure 3.3** Timeseries of OA mass concentration: ambient OA (blue line) and TD OA (red line) for Athens winter campaign.

Source apportionment of the OA was performed using the HR-AMS data. Details of the PMF analysis can be found in Florou et al. (2016). This analysis was performed both for the ambient and the thermodenuder AMS spectra resulted in the same factors for the complete dataset. Kostenidou et al. (2009) proposed the theta angle ( $\theta$ ) as an indicator of mass spectra similarity by treating the AMS spectra as vectors and calculating their corresponding angle  $\theta$ . Lower  $\theta$  implies more similar spectra. Comparing the results of the PMF on only the ambient data and on ambient plus TD spectra, the resulting angles were less than  $5^\circ$  for all four factors ( $3.1^\circ$  for COA,  $1.9^\circ$  for HOA,  $2.6^\circ$  for BBOA, and  $5^\circ$  for OOA) suggesting that the ambient plus TD PMF analysis gave practically the same factors as the ambient-only OA analysis. The ambient and TD mass spectra of the OOA, BBOA, HOA and COA are shown in Figure A.1 in the supplementary information.

In order to minimize the low concentration problems a minimum threshold value was selected for the factor ambient concentration following Paciga et al. (2016). A threshold value of  $0.05 \mu\text{g m}^{-3}$  was used for all factors. Table 3.2 summarizes the average ambient concentration of each factor and the corresponding fraction of measurements that were above the threshold.

**Table 3.2** Average ambient concentrations and percentage of points above threshold for each PMF factor for the 2013 Athens winter campaign.

<b>Factor</b>	<b>Average ambient mass concentration (<math>\mu\text{g m}^{-3}</math>)</b>	<b>Percentage of measurements above <math>0.05 \mu\text{g m}^{-3}</math> threshold</b>
BBOA	4.3	70
COA	1.2	83
HOA	1.9	78
OOA	1.3	98

### 3.4 Volatility Distribution Estimation

To estimate the volatility distributions from the corrected thermograms we employed the dynamic mass transfer model of Riipinen et al. (2010). The model simulates particle evaporation using experimental inputs including TD temperature and residence time, initial particle size, and ambient OA concentration. The volatility of these complex mixtures is defined using the corresponding effective saturation concentration,  $C^*$ , at 298 K. Along with saturation concentration, two parameters that can affect the evaporation rate and the corresponding volatility estimation are the enthalpy of vaporization and the mass accommodation coefficient. Unfortunately, these values are currently unknown for these complex multi-component systems. Typical values of  $100 \text{ kJ mol}^{-1}$  and 1.0 are assumed for the enthalpy of vaporization and accommodation coefficient, respectively. However, mass transfer limitations to evaporation have been observed in some experimental systems, leading to mass accommodation coefficient values of much less than one (Saleh et al., 2013).

The volatility distribution in the volatility basis set framework (VBS) is represented by surrogate species with a saturation concentration of  $C_i^*$  (Donahue et al., 2006). The  $C_i^*$  bins are logarithmically spaced, allowing for extremely low and high volatility species to be represented. The analysis here was limited to a 6-consecutive  $C^*$  bin solution with a variable mass fraction value for each bin. Different volatility ranges were tested and the best range was selected for each factor. The “goodness of fit” was quantified using the error analysis outlined in Karnezi et al. (2014). The standard error was calculated for all  $C^*$  bin-mass fraction combinations. For a given 6-bin solution, the top 2% of mass fraction combinations with the lowest error was used to find the average mass fraction in each bin and the corresponding standard deviation.

The OA components are described as intermediate volatility organic compounds (IVOCs with  $C^* \geq 1000 \mu\text{g m}^{-3}$ ), semi-volatile (SVOCs with  $C^*$  of 1, 10, and  $100 \mu\text{g m}^{-3}$ ), low volatility (LVOCs with  $C^*$  of  $10^{-3}$ ,  $10^{-2}$ , and  $0.1 \mu\text{g m}^{-3}$ ), and extremely low volatility compounds (ELVOCs with  $C^* \leq 10^{-4} \mu\text{g m}^{-3}$ ) in the rest of the chapter following Murphy et al. (2014).

### 3.5 Effect of concentration on volatility distribution

Donahue et al. (2006) have suggested that when the total mass concentration of the OA from a given source changes, volatility distribution will also change. At high concentration levels, specifically, the more volatile OA components partition into the particle phase and the OA becomes more volatile on the other hand dilution leads to repartitioning of the more volatile components into the gas phase effectively reducing the apparent volatility of the system. Figure 3.4 shows as an example how the composition of OA changes, as its total mass concentration varies.

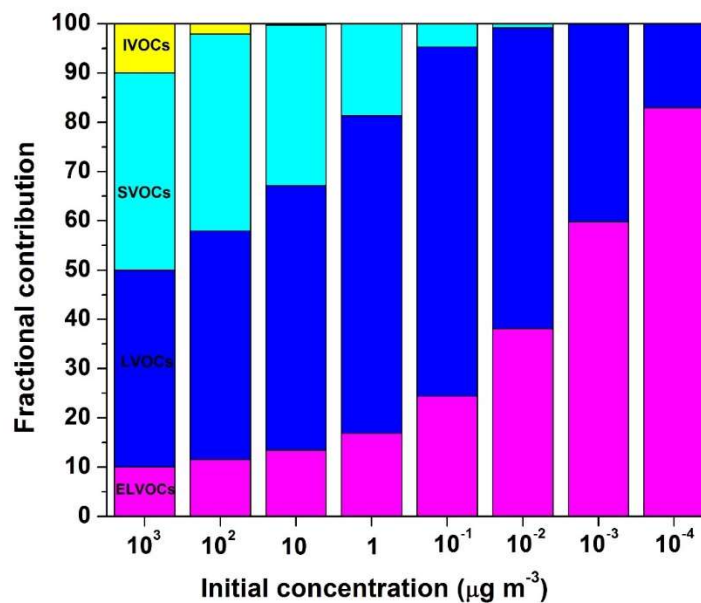


**Figure 3.4** OA composition versus the initial concentration of the OA. ELVOCs are shown with magenta, LVOCs with blue, SVOCs with cyan and IVOCs with yellow. The y axis represents the percentages of ELVOCs, LVOCs, SVOCs and IVOCs for each bin that represents the initial concentration of the OA.

For a concentration equal to  $1000 \mu\text{g m}^{-3}$  the OA consists of 10% ELVOCs, 40% LVOCs, 40% SVOCs and 10% IVOCs. When this initial concentration is diluted 1000 times and  $C_{OA} = 1 \mu\text{g m}^{-3}$  there are no more IVOCs in the OA and there are now around 15% ELVOCs, 65% LVOCs and

20% SVOCs. For further dilution, the OA consists mostly of ELVOCs and LVOCs. In the analysis later, in order to compare the volatility distributions and fractional contributions for each PMF factor of the two campaigns we will develop an approach to scale the results to the same concentration and then compare our findings.

### 3.6 Results and Discussion

#### 3.6.1 Organic aerosol volatility during Paris campaigns

The average loss-corrected OA thermograms for the two seasons are shown in Figure 3.5. The two thermograms seem very similar while differences are mostly noticeable at the high temperatures. In the winter, approximately 30% of the OA remained at 180°C, while in the summer thermogram less than 10% was present at the same temperature.

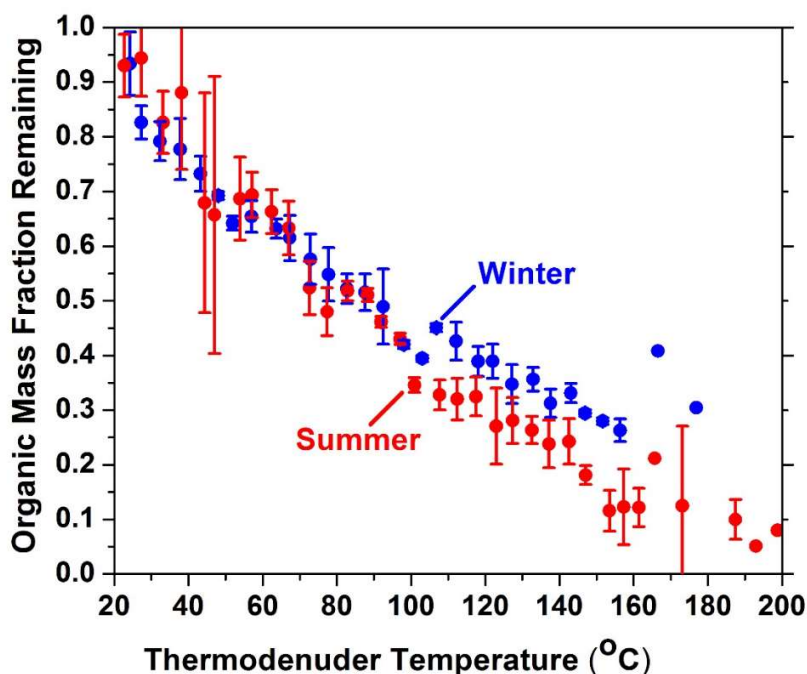


**Figure 3.5** Loss-corrected average OA thermograms for summer (red circles) and winter (blue squares) Paris campaigns. The error bars correspond to plus/minus 2 standard deviations of the mean. Points with no error bars correspond to a single measurement.

This might suggest more ELVOCs being present at winter. However, the summer thermogram shows that nearly 50% of the mass evaporated at a thermodenuder temperature of 83 °C ( $T_{50}$ ). The

winter measurements suggested a similar  $T_{50}$  value of 88 °C. This crude comparison of volatility through the corresponding thermograms suggests that the OA in the two seasons could have similar average volatility distributions. It is surprising that the seasonal differences in emissions are not reflected in the corresponding thermograms. We will examine the reasons for this similarity in the subsequent section by analyzing the volatility of the corresponding factors.

Using the mass transfer model of Riipinen et al. (2010) and the uncertainty estimation method of Karnezi et al. (2014) we calculated the volatility distributions for the total OA for the two seasons. The estimated volatility distributions for the total OA for the two seasons are depicted now in Figure 3.6 along with the best fit thermograms predicted from the model.

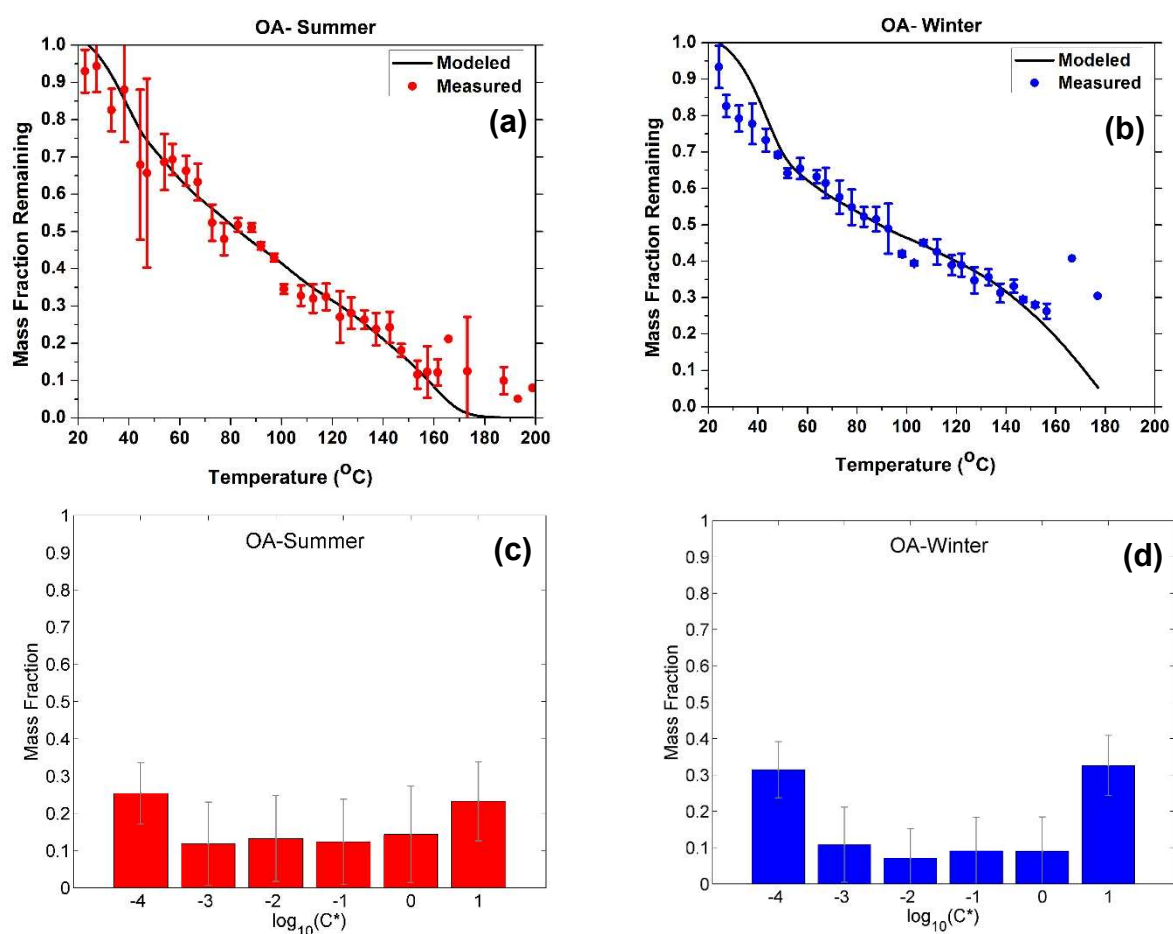


**Figure 3.6** (a) Average loss-corrected OA thermograms for summer (up left panel) and (b) winter (up right panel) OA Paris campaigns. The error bars correspond to plus/minus 2 standard deviations of the mean. The black line represents the best fit estimated thermogram. (c) Estimated volatility distributions for summer (down left panel) and (d) winter total Paris OA (down right panel). The error bars correspond to the fitting uncertainties according to the algorithm of Karnezi et al. (2014).

Typical values of  $100 \text{ kJ mol}^{-1}$  and 1.0 are assumed for the enthalpy of vaporization and accommodation coefficient. The estimated volatility distributions are quite similar to each other especially considering the corresponding uncertainties and they are characterized by higher concentrations of components with  $C^*=10^{-4}$  and  $10 \text{ } \mu\text{g m}^{-3}$ .

### 3.6.2 Organic aerosol volatility during the Athens campaign

Figure 3.7 shows the average loss-corrected thermogram of the total OA for the entire campaign and the estimated OA volatility distribution using the same method as in section 3.6.1. Half of the OA during the measurement period evaporated at  $80^\circ\text{C}$  ( $T_{50}=80^\circ\text{C}$ ). Roughly 30% remained at  $200^\circ\text{C}$  and this fraction did not decrease significantly as the temperature increased to  $400^\circ\text{C}$ . The estimated volatility distribution suggests that 30% of the organic compounds had a volatility less than  $10^{-4} \text{ } \mu\text{g m}^{-3}$  indicating that extremely low volatile organic compounds (ELVOCs) were present. Around 40% of the material was SVOCs and approximately 30% LVOCs.

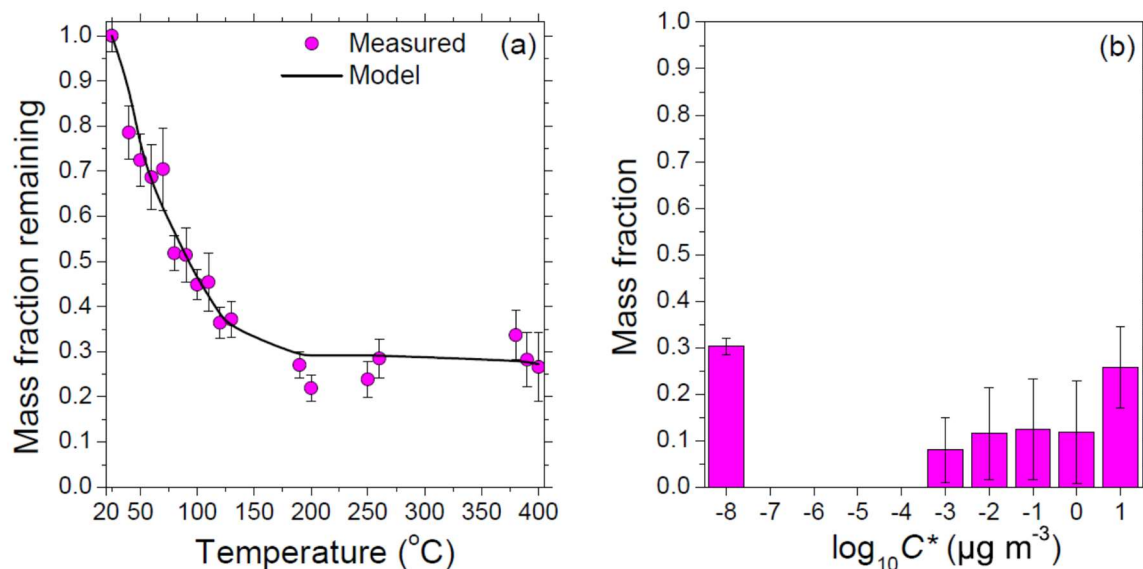


**Figure 3.7** (a) Average loss-corrected total OA thermogram for Athens campaign. Magenta circles represent the measurements with error bars representing the corresponding variability ( $\pm 1$  standard deviation of the mean). The black line represents the best fit estimated thermogram using the approach of Karnezi et al. (2014). (b) Estimated OA volatility distribution. Error bars represent the corresponding uncertainties according to the algorithm of Karnezi et al. (2014).

### 3.6.3 Volatility of organic aerosol components during Paris campaigns

Five PMF factors were determined for the summer dataset by Crippa et al. (2013a). Hydrocarbon-like OA (HOA) most closely resembles fresh vehicle emissions in that the mass spectrum resembles that of transportation sources. Cooking OA (COA) was also observed in the summer campaign, peaking during noon and evening meal times. Marine OA (MOA) was identified based on relatively high levels of organic sulfur and a strong correlation with methanesulfonic acid (MSA), which is a product of continued oxidation of phytoplankton decomposition products. Two SOA factors were also found: Semi-volatile oxygenated OA (SV-OOA) and low volatility oxygenated OA (LV-OOA). These two factors were differentiated based on their O:C ratio. The two secondary OA factors made up 57% of the total OA mass. The remaining factors contributed fairly similar average fractions of 18% for COA, 12% for HOA, and 13% for MOA. Detailed discussion of the PMF factors along with verification analysis were provided by Crippa et al. (2013a).

The PMF analysis for the winter campaign yielded four factors. The HOA and COA factors were again present. There was also a single secondary OA factor which was termed oxygenated OA (OOA). This factor could not be further separated into SV-OOA and LV-OOA. The final factor reported was biomass burning OA (BBOA), correlating with known molecular markers for residential wood burning (e.g., levoglucosan). The OOA factor was found to dominate the organic aerosol mass, contributing nearly 65% on average. The complete analysis and description of these factors can be found in Crippa et al. (2013b).

Using the mass transfer model from Riipinen et al. (2010) and the approach of Karnezi et al. (2014) we fitted the corresponding thermograms (Figure A.2), using a  $C^*$  bin solution with a variable mass fraction value for each bin. Specifically, for each factor we used an individual consecutive 6-bin solution (chosen as the 6-bin solution with the best fits) resulting in the volatility distributions, shown in Figure 3.8.

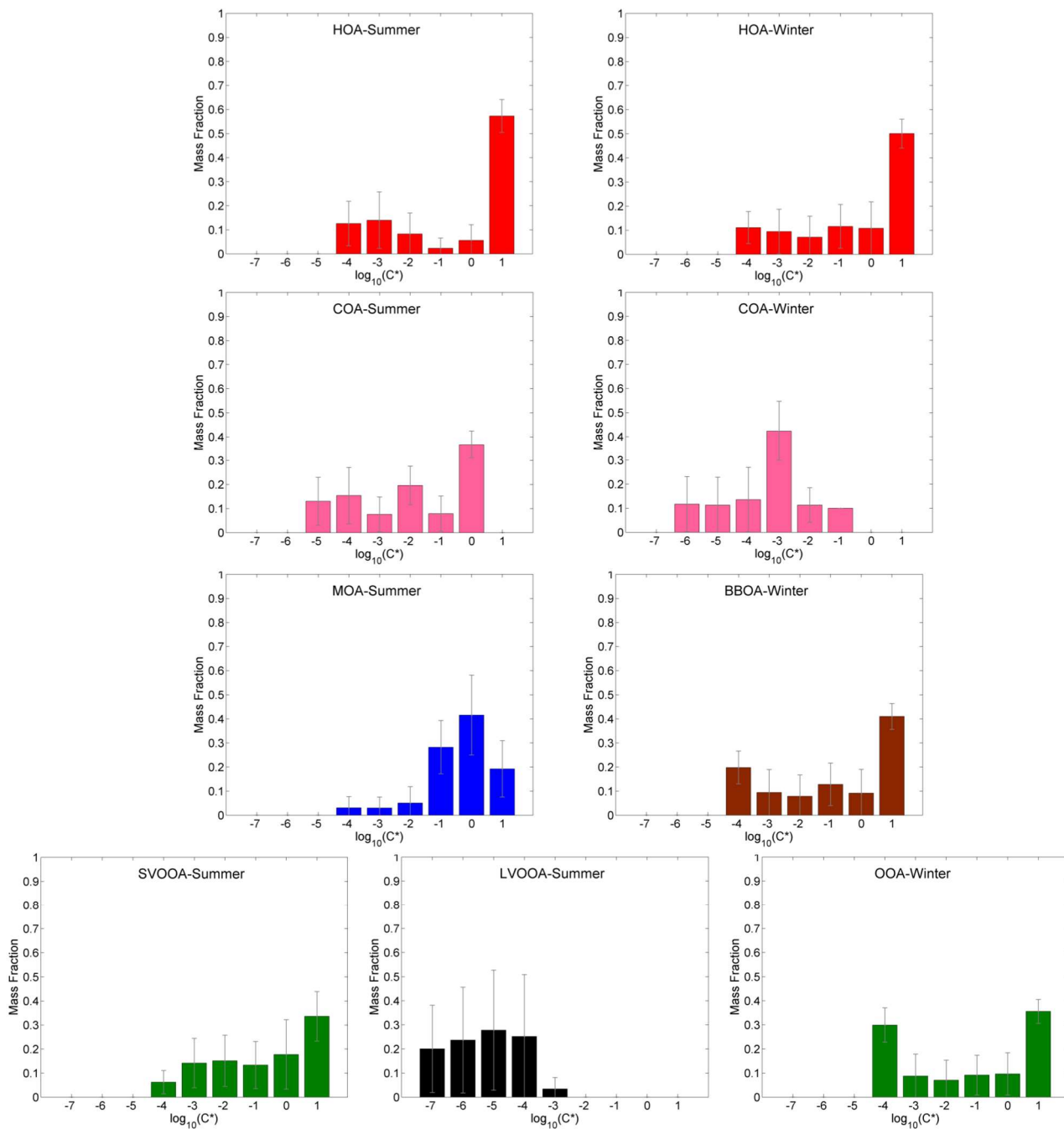


**Figure 3.8** Estimated volatility distributions for summer PMF factors (left panel) and winter PMF factors (right panel) during Paris campaigns. The error bars correspond to the fitting uncertainties according to the algorithm of Karnezis et al. (2014).

The modeled thermograms for all factors from both summer and winter campaigns are shown in Figure 3.9. Finally, the volatility distributions for each factor are summarized in Table A.1 in the supplementary information. The fitting of individual factor thermograms implicitly assumes that each factor had the same size distribution as the total OA and that the factors were present as an external mixture. To test the uncertainty introduced by this assumption we compared the volatility distribution of the total OA with the composition weighted sum of the volatility distributions of the individual OA factors for both summer and winter. The two distributions (total and sum of factors) agreed within a few percent for both seasons suggesting that the uncertainty is modest and within the uncertainty limits shown in the corresponding figures.

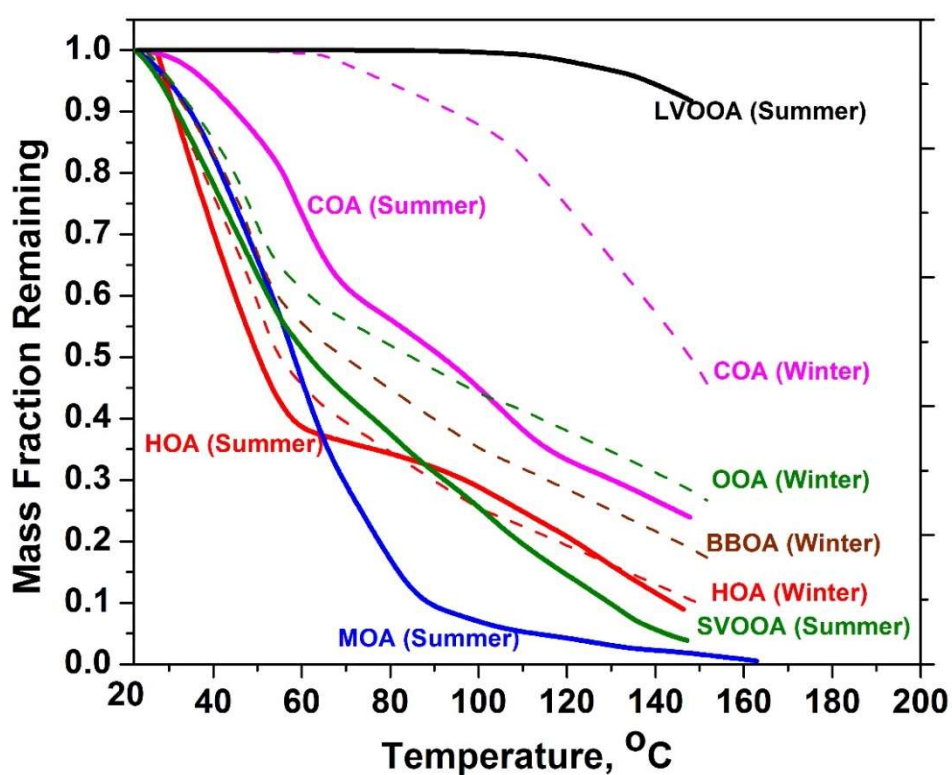


**Figure 3.9** Estimated best-fit thermograms for all PMF factors during Paris campaigns. The solid lines represent the thermograms for the summer campaign and the dashed lines the thermograms for the winter campaign.

The HOA factors for the summer and winter campaigns had very similar thermograms and volatility distributions with half of the material in the  $10 \mu\text{g m}^{-3}$  bin (Figure 3.8). Roughly 40% of the HOA in both seasons consisted of LVOCs and ELVOCs. This volatility similarity is consistent with the similarity in mass spectra derived by the PMF analysis (Figure 3.10a). The angle  $\theta$  between the corresponding vectors (treating the AMS spectra as vectors according to Kostenidou

et al. (2009)) was 14° suggesting similar chemical fingerprints. This is not surprising for a Megacity where the transportation and any industrial sources are expected to have chemically similar emissions in both summer and winter.

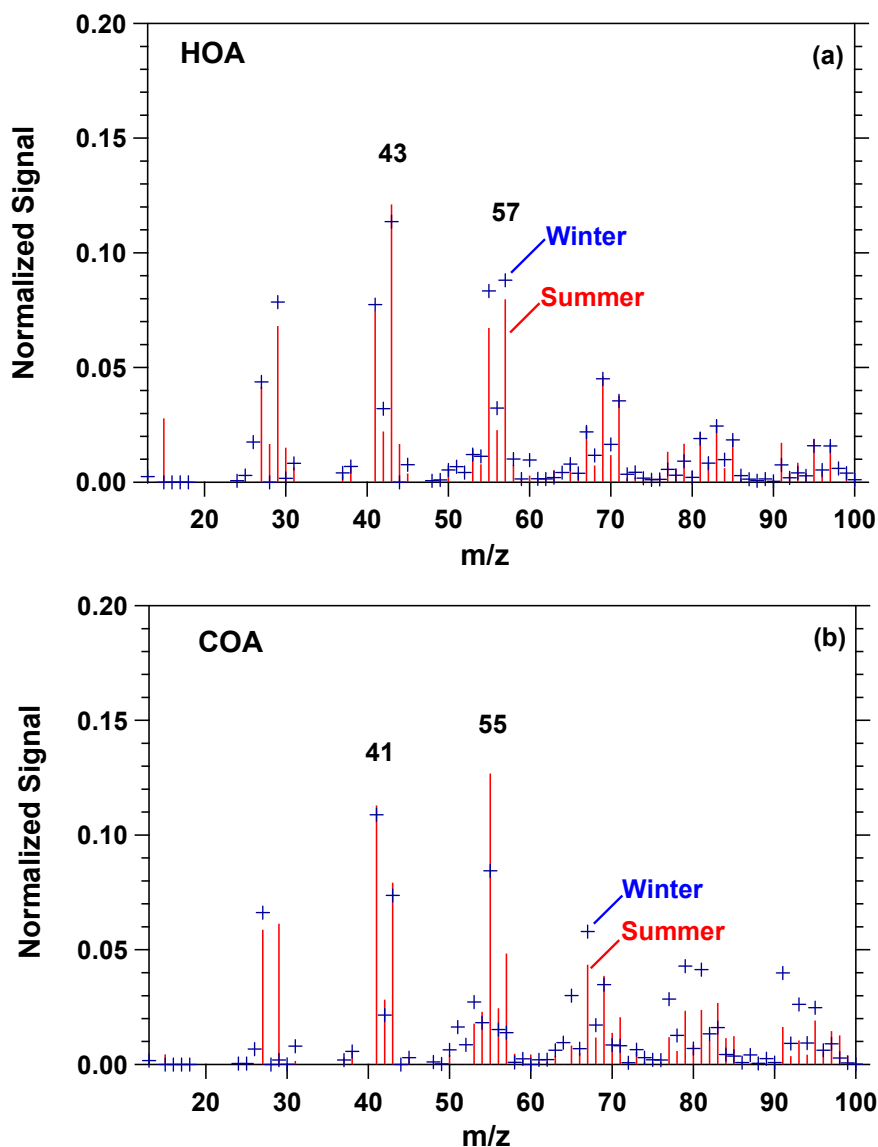


**Figure 3.10** Seasonal mass spectra comparison for (a) HOA and (b) COA in Paris winter and summer campaigns. Red lines correspond to the summer measurements while blue symbols correspond to the winter data.

Similar were also the  $T_{50}$  for the HOA factors with values of 49 °C and 54 °C for the summer and winter campaign, respectively. Cappa and Jimenez (2010) also estimated that the HOA in Mexico City had a wide volatility distribution with approximately 35% of its mass consisting of LVOCs

and ELVOCs while the remaining 65% was SVOCs. Almost 40% of the HOA had  $C^* \geq 10 \mu\text{g m}^{-3}$  which compares very well with the 50% estimated here.

The situation was quite different for the cooking OA factor. Here the seasonal differences were more pronounced for the thermograms (Figure 3.9), the estimated volatility distributions (Figure 3.8) and the corresponding mass spectra (Figure 3.10b). The winter COA was substantially less volatile than the summer COA, more than an order of magnitude based on average  $\log C^*$  values, weighted by the mass fraction of each bin (average  $C^* = 10^{-2} \mu\text{g m}^{-3}$  for the summer campaign and average  $C^* = 4 \times 10^{-4} \mu\text{g m}^{-3}$  for the winter campaign). The COA factor during the winter campaign did not contain semi-volatile components while 37% of the summer COA was semi-volatile. The COA winter factor consisted of ELVOCs (37%) and LVOCs (63%). The COA mass spectra in Figure 3.10b show that the winter COA was characterized by a higher fraction of molecular fragments at higher mass-to-charge ( $m/z$ ) ratio. This is consistent with organic components of longer carbon chain which, for the same level of oxidation, are expected to have lower volatility. The angle  $\theta$  between the COA spectra was  $26^\circ$ , suggesting a significant chemical difference. One explanation is that the cooking habits are different in the two seasons with outdoor cooking (e.g., barbecue) dominating in the summer and indoor cooking relying more on oil and butter, being more significant in the winter. The  $T_{50}$  for the COA factors were different as well, with values of  $91^\circ\text{C}$  and  $148^\circ\text{C}$  for the summer and winter campaign, respectively.

The LV-OOA factor detected in the summer had the lowest volatility (Figure 3.8) of all the derived factors. There was no sign of evaporation until the TD temperature reached nearly  $150^\circ\text{C}$  (Figure 3.9). We estimate that this factor consisted almost exclusively of OA with effective saturation concentrations equal to or lower than  $10^{-3} \mu\text{g m}^{-3}$ , which are almost exclusively ELVOCs. The average ambient concentration of this factor during the summer was  $0.12 \mu\text{g m}^{-3}$  and its average  $C^*$  was equal to  $5 \times 10^{-6} \mu\text{g m}^{-3}$ . Very low volatilities (practically all the OA had  $C^* \leq 10^{-3} \mu\text{g m}^{-3}$ ) were also estimated for LV-OOA by Cappa and Jimenez (2010) in Mexico City during the MILAGRO campaign.

The estimated volatility for the SV-OOA factor is consistent with its naming by Crippa et al. (2013a) as it was significantly higher than that of the LV-OOA (Figure 3.8). We estimated that roughly half of the SV-OOA was SVOCs while it contained also LVOCs (42%) and a small amount of ELVOCs (6%). Its  $T_{50}$  was  $61^\circ\text{C}$  and its average  $C^*$  was roughly  $0.2 \mu\text{g m}^{-3}$ . These values are once more generally consistent with the estimates of Cappa and Jimenez (2010) showing

that SVOCs dominated the SV-OOA during MILAGRO (approximately 40%) with LVOCs contributing another 35%.

The OOA factor determined in the winter had a volatility distribution (Figure 3.8), containing SVOCs (45%), LVOCs (25%) and ELVOCs (30%). The winter OOA and the summer SV-OOA spectra had a  $\theta$  angle of  $34^\circ$ , while there was an even larger discrepancy between the winter OOA and the summer LV-OOA with an angle of  $37^\circ$ . The  $T_{50}$  was equal to  $85^\circ\text{C}$ . These differences in mass spectra and  $T_{50}$  are consistent with the differences in volatility. The average volatility of OOA was much higher than LVOOA in summer but lower than SVOOA.

The marine OA (MOA) factor was only detected during the summer campaign at an average concentration of  $0.17 \mu\text{g m}^{-3}$ . Its volatility was relatively high (Figure 3.9), and almost all the MOA had evaporated at  $100^\circ\text{C}$ . The MOA factor consisted mainly of SVOCs (61%) and some LVOCs (36%). Its  $T_{50}$  was equal to  $58^\circ\text{C}$  and its average  $C^*$  was approximately  $0.4 \mu\text{g m}^{-3}$ .

The BBOA factor was present in the winter dataset with an average ambient concentration of  $0.6 \mu\text{g m}^{-3}$ . The corresponding estimated volatility distribution (Figure 3.8) shows that half of the BBOA factor consisted of SVOCs (with most material in the  $10 \mu\text{g m}^{-3}$  bin) and the other half of LVOCs and ELVOCs. A similar bimodal distribution was also found by May et al. (2013) with a peak at 0.01 and one at  $100 \mu\text{g m}^{-3}$  for controlled biomass burning in the laboratory. The difference in the location of the high volatility peak can potentially be explained by the wider range of concentrations in the experiments analyzed by May et al. (2013) compared to the limited range in the ambient Paris measurements. The more volatile BBOA components were never in the particulate phase in our dataset so their abundance cannot be determined. The BBOA  $T_{50}$  was  $70^\circ\text{C}$ , higher than that of HOA and less than those of COA and OOA. Finally, its average  $C^*$  was approximately  $0.1 \mu\text{g m}^{-3}$ . The BBOA in Mexico City was approximately half LVOCs and half SVOCs (Cappa and Jimenez, 2010) and had a much lower ELVOC fraction than the wintertime Paris BBOA in the present study.

### **3.6.4 Volatility of OA components during Athens campaign**

The PMF analysis resulted in a four-factor solution: an OOA factor together with three primary OA factors. A HOA factor mainly attributed to fresh vehicle emissions was observed especially during the morning rush hour. The mass spectrum of this factor resemble that of transportation

sources. A BBOA factor was also identified correlating well with known molecular markers for residential wood burning. BBOA increased during the evening. Finally, a factor attributed to cooking emissions (COA) was observed especially during early afternoon and night-time meal hours. 43% of the ambient OA originated from residential wood burning, another 24% was attributed to processed OA transported to the site from other areas, 17% was HOA, and 16% COA. A detailed discussion of these results can be found in Florou et al. (2016).

The average OA composition after the TD as a function of TD temperature is presented in Figure 3.11. As the temperature increases evaporation of the components of each factor took place, until approximately 200°C. At higher temperatures, little or no additional evaporation was observed. At temperatures near 400°C the contribution of OOA is considerably higher than that of the other factors but the contribution of the other factors is non-zero.

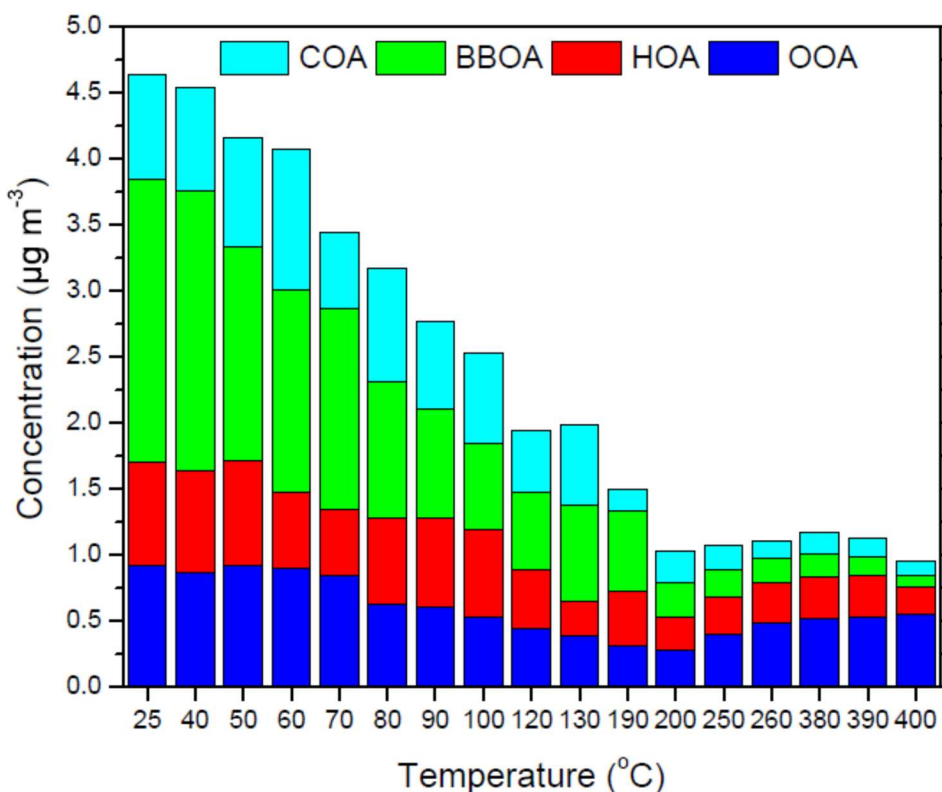


**Figure 3.11** Average concentrations of OA components after the TD as a function of the TD temperature for Athens winter campaign.

Gkatzelis et al. (2016) suggested that the conversion of POA to OOA in these measurements is low, and that a considerable fraction of the remaining OA is due to ELVOCs present. However, the possibility of reactions affecting the results at these temperatures cannot be discounted. The

stability of the spectra and the existence of HOA, BBOA, and COA signatures support the hypothesis that ELVOCs did exist in the OA.

Applying the approach of Karnezi et al. (2014) the volatility distribution of each factor was determined and the results are shown in Figure 3.12.

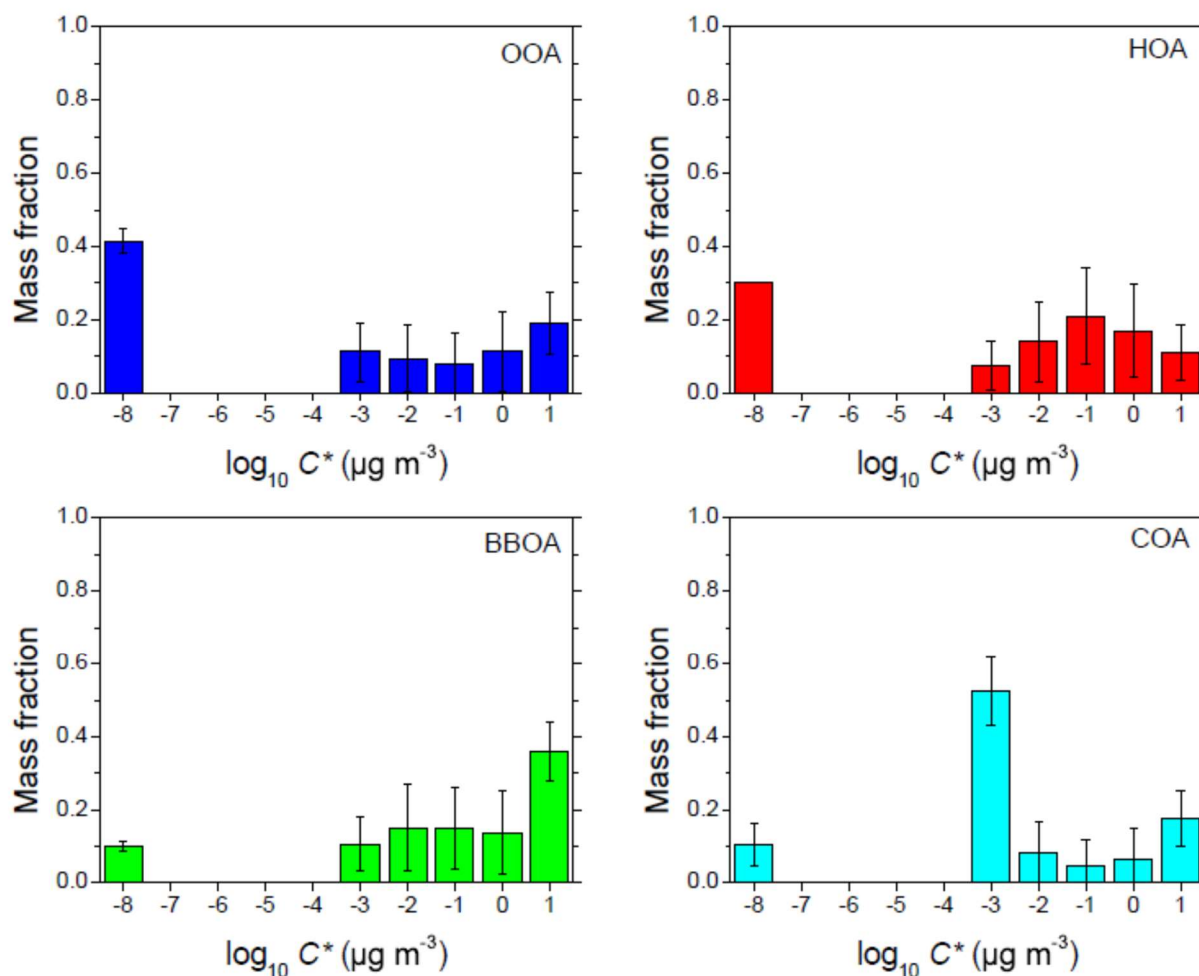


**Figure 3.12** Estimated volatility distributions of OA components during Athens winter campaign. Error bars represent the corresponding uncertainties according to the algorithm of Karnezi et al. (2014). Typical values of  $100 \text{ kJ mol}^{-1}$  and 1.0 were assumed for the enthalpy of vaporization and accommodation coefficient.

The corresponding thermograms showing the goodness of fit together with the measurements are depicted in Figure 3.13. The fitting of individual factor thermograms implicitly assumes that each factor had the same size distribution as the total OA and also that the factors were externally mixed. The uncertainty introduced by these two assumptions was implicitly evaluated comparing the estimated total OA volatility distribution of Figure 3.7b with the

composition-weighted average of the volatility distributions of the individual OA factors. The two distributions agreed within a few percent as depicted in Figure A.3.

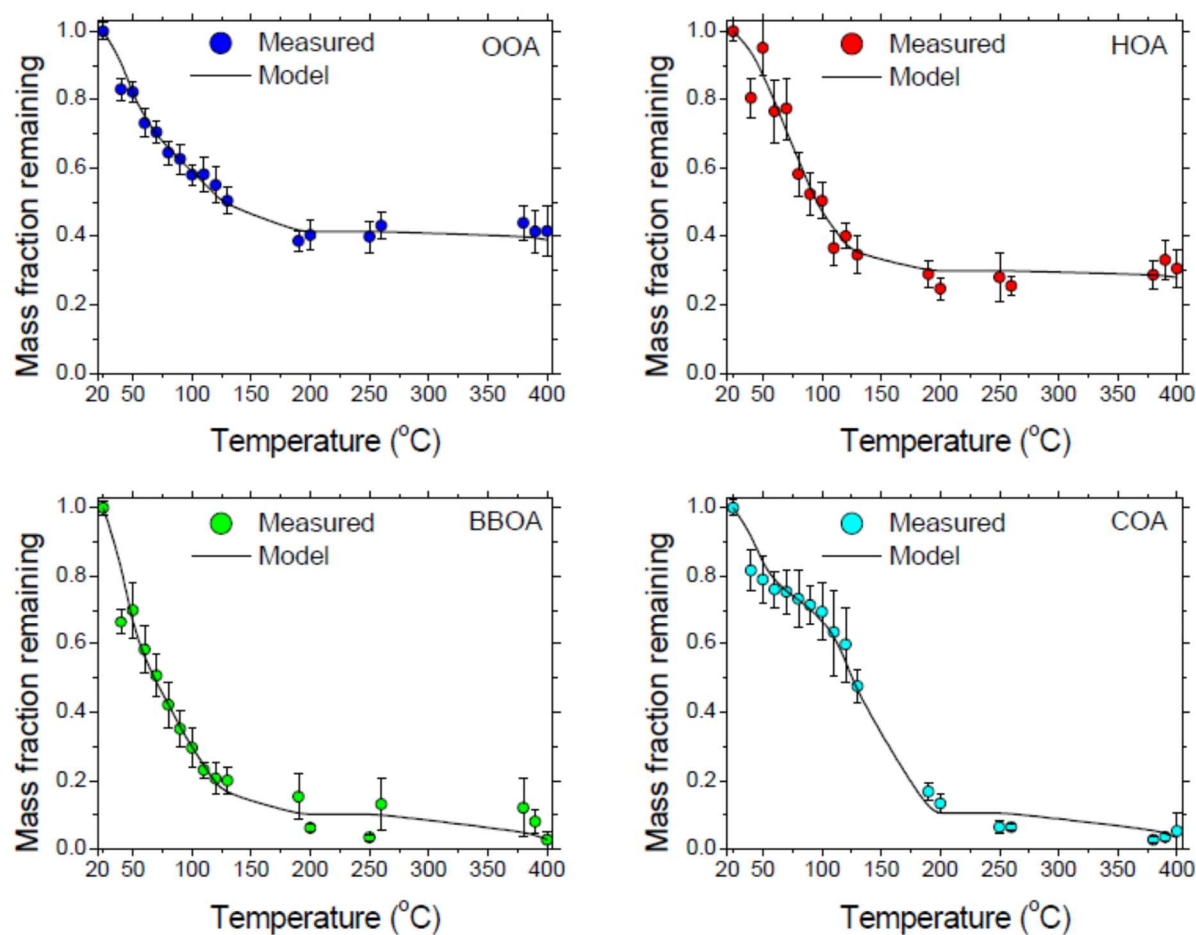


**Figure 3.13** Thermograms of the four PMF factors during Athens campaign. Circles correspond to the average loss corrected measurements along with their uncertainties ( $\pm 1$  standard deviation of the mean). Lines represent the best fit estimated thermograms by the model of Karnezi et al. (2014).

The average OOA ambient concentration was  $1.3 \mu\text{g m}^{-3}$  (Table 3.2). Its volatility distribution suggests that 40% of the OOA consisted of compounds with volatility less than  $10^{-4} \mu\text{g m}^{-3}$  that are categorized as extremely low volatile organic material (Murphy et al., 2014). The rest was LVOCs (30%) and SVOCs (30%) (Table A.2 and Figure 3.12). The average volatility, calculated as the  $\log C^*$  values weighted by the mass fraction of each bin, was of the order of  $10^{-4} \mu\text{g m}^{-3}$  (Table A.2). Its thermogram suggests that the  $T_{50}$  for OOA was almost  $125^\circ\text{C}$  (Figure 3.13).

The average HOA concentration was  $1.9 \mu\text{g m}^{-3}$  (Table 3.2). Approximately 30% of the HOA had volatility less than  $10^{-4} \mu\text{g m}^{-3}$  consisting of ELVOCs. The remaining 40% consisted of LVOCs and the last 30% of SVOCs (Table A.2 and Figure 3.12). The average volatility was of the order of  $10^{-3} \mu\text{g m}^{-3}$  (Table A.2), an order of magnitude higher than the OOA. The HOA  $T_{50}$  was approximately  $100^{\circ}\text{C}$  (Figure 3.13).

The average BBOA concentration was  $4.3 \mu\text{g m}^{-3}$  (Table 3.2). There was a small fraction of ELVOCs (approximately 10%), 40% was LVOCs, and 50% SVOCs (Table A.2 and Fig. 3.12). Its average volatility was of the order of  $10^{-1} \mu\text{g m}^{-3}$  (Table A.3). The corresponding BBOA thermogram suggests that its  $T_{50}$  was  $70^{\circ}\text{C}$  (Figure 3.13).

Finally, COA with an average concentration of  $1.2 \mu\text{g m}^{-3}$  (Table 3.2) had a bimodal volatility distribution exhibiting two peaks at  $10^{-3}$  and  $10 \mu\text{g m}^{-3}$  effective saturation concentrations (Table A.2 and Figure 3.12). This indicates that COA during winter-time in Athens is mainly a mixture of low and semi-volatile organic material. Some extremely low volatility material was also present with effective saturation concentration lower than  $10^{-4} \mu\text{g m}^{-3}$  (almost 10%). The COA  $T_{50}$  was almost  $120^{\circ}\text{C}$  (Figure 3.13), and its average  $C^*$  was of the order of  $10^{-2} \mu\text{g m}^{-3}$  (Table A.3).

### 3.7 Synthesis of Results in the 2D-VBS

The two-dimensional volatility basis set (2D-VBS) approach proposed by Donahue et al. (2012) aims to describe the absorptive partitioning of a large number of unknown organic compounds by lumping them into surrogates along axes of volatility and the O:C ratio (or carbon oxidation state,  $\text{OS}_c$ ). Donahue et al. (2012) provided rough estimates of factor locations on the 2D-VBS by extrapolating the available at that time ambient measurements. The 2D-VBS framework was employed in order to synthesize the above results, combining the bulk average O:C ratio and volatility distributions of the various factors. Each of the different factors had a distribution of O:C values, but this distribution cannot be determined from the AMS measurements.

For Paris campaigns, the HOA, BBOA, and COA factors all had relatively low O:C values and covered a wide range of volatilities (Figure 3.14). The MOA and secondary OA factors for both seasons had much higher O:C but also included components with a wide range of volatilities, with LV-OOA having the lowest one on average. The HOA during summer had higher O:C than HOA during winter, suggesting incomplete separation from aged HOA or potential differences in

their sources, while their volatility distribution was similar, as discussed earlier. The COA factor during the summer campaign, had slightly higher O:C and higher volatility than the COA from the winter campaign. The OOA during the winter had the highest O:C ratio but it had lower average volatility compared to the less oxidized SVOOA and higher volatility than the LVOOA.

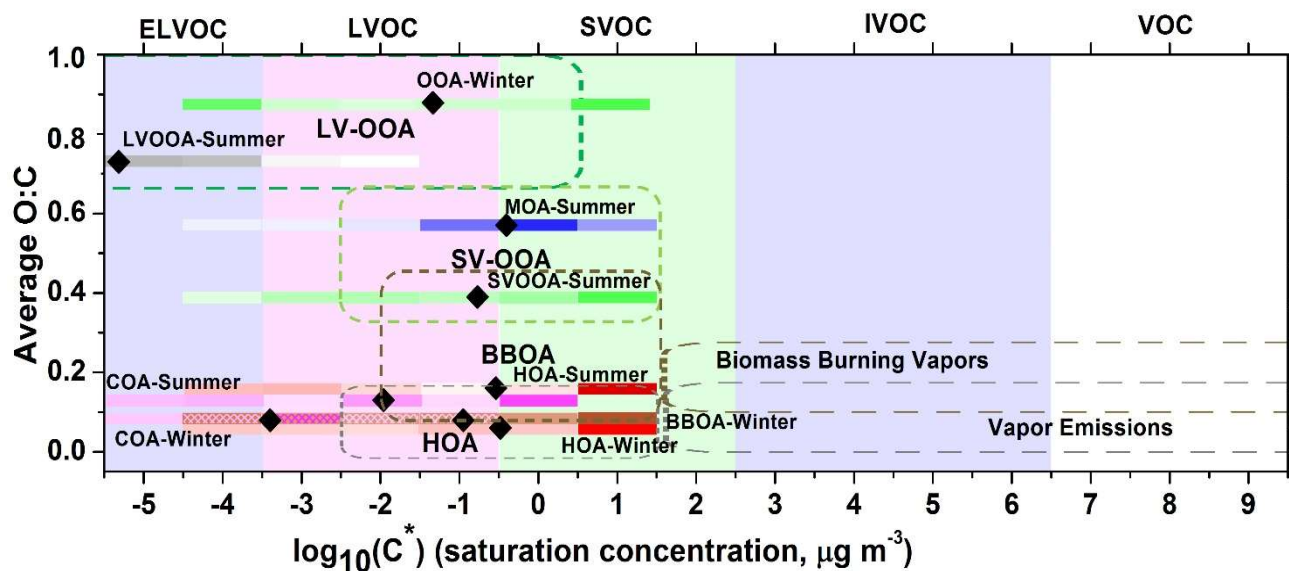


**Figure 3.14** Effective saturation concentration  $C^*$  and O:C (oxidation state on the left y-axis) for classes of organic species as shown in Donahue et al. (2012) along with estimated factors from the summer and winter Paris campaigns. The red bars represent the HOA factors, the pink are the COA factors, the green the SVOOA and OOA, the blue represents the MOA factor, the brown the BBOA factor and the black the LVOOA factor. The darker shading of the colored bars denotes a larger mass fraction for a given  $C^*$  bin. The diamonds represent the average  $\log_{10}(C^*)$  value of each PMF factor.

For Athens campaign, OOA, HOA, BBOA, and COA all covered a wide range of volatilities as depicted in Figure 3.15. The estimated HOA and BBOA factors in this study are in the expected region but also include an ELVOC component. COA is in the same range with HOA having a very similar O:C ratio and a slightly higher average volatility. OOA in these wintertime conditions had a moderate O:C ratio of 0.45 (closer to SV-OOA) and included both semi-volatile and extremely low volatility components.

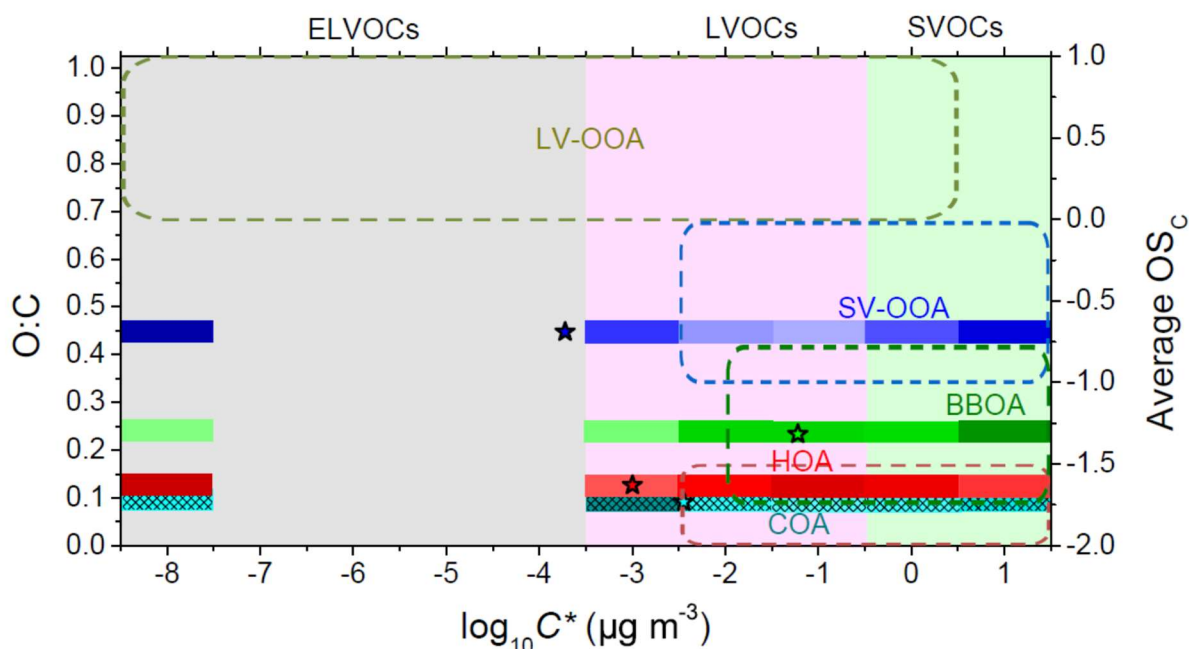


**Figure 3.15** Saturation concentration, mean O:C ratio (left y-axis) and mean carbon oxidation state ( $OS_c$ ) (right y-axis) for OA factors following Donahue et al. (2012) along with estimated factors from Athens winter campaign. The shaded areas indicate the locations of the various factors proposed by Donahue et al. (2012) while the colored horizontal bars the estimated locations of the factors. Blue bars represent OOA, red bars HOA, green bars BBOA, and cyan bars COA. Darker shading of the horizontal colored bars denotes larger mass fractional contribution for a given  $C^*$  bin. The stars represent the average  $\log_{10}(C^*)$  value for a given PMF factor.

These results indicate that there was not a direct link between the average volatility and the bulk average O:C for these OA components. This is actually the reason for the introduction of the 2D-VBS: the second dimension is needed to capture at least some of the chemical complexity of the multitude of organic compounds in atmospheric particulate matter.

The broad range of volatilities extending to the ELVOC range is one of the most important results of this study. Superimposition of the factors and those estimated by Donahue et al. (2012) indicates that the factor locations agree well with the exception of the ELVOCs. This is quite encouraging both for our results and our current understanding of the evolution of atmospheric OA. These results strongly suggest that the PMF separates their factors mainly based on their O:C and not so much based on their volatility. The use of the low-volatility and semi-volatile OOA terminology that has been used in the field is therefore problematic. Replacing it with more and less oxidized OOA is probably more in the right direction.

### 3.8 Estimation of vaporization enthalpy and accommodation coefficient

In the next step of the analysis, we applied the model again without specifying the vaporization enthalpy and the mass accommodation coefficient. The estimated effective vaporization enthalpies are shown in Figure 3.16 for the various campaigns and factors. Please note that a value of  $\Delta H_{\text{vap}} = 100 \text{ kJ mol}^{-1}$  has been assumed in the preceding analysis.

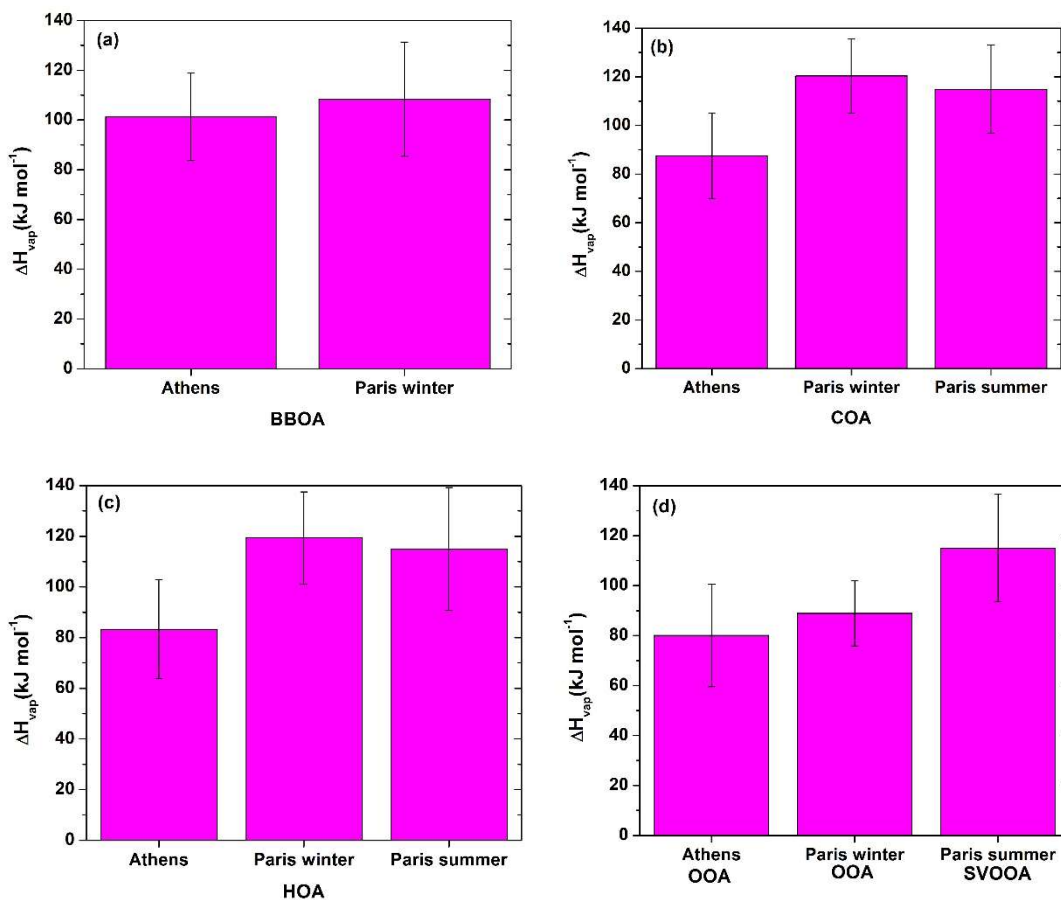


**Figure 3.16** Comparison of estimated vaporization enthalpies in the Athens and Paris campaigns for (a) BBOA, (b) COA, (c) HOA and (d) OOA for winter campaigns and SVOOA for the Paris summer campaign.

The estimated vaporization enthalpy for BBOA is around  $100 \text{ kJ mol}^{-1}$  for Athens and  $110 \text{ kJ mol}^{-1}$  for Paris. The uncertainty ranges include the assumed  $100 \text{ kJ mol}^{-1}$  in the initial simulations. The mass spectra of the two BBOA factors had an angle  $\theta$  of around  $20^\circ$  (Florou et al. 2016) suggesting more similarity but also some significant differences. For COA the  $\Delta H_{\text{vap}}$

values in Paris are around  $30 \text{ kJ mol}^{-1}$  higher than those in Athens. Once more the COA spectra in Athens and Paris had some notable differences ( $\theta$  values  $15\text{-}20^\circ$ ) that are consistent with different  $\Delta H_{\text{vap}}$  values. The same differences (higher  $\Delta H_{\text{vap}}$  for Paris) were found for HOA. In the last comparison, we use OOA from Athens and Paris winter campaign and SVOOA from Paris summer campaign. The wintertime OOA vaporization enthalpies were practically the same for the two campaigns, and around  $80\text{-}90 \text{ kJ mol}^{-1}$ . These values were lower than those of the summertime similar while the SV-OOA factor in Paris. In all cases though, the assumption of  $100 \text{ kJ mol}^{-1}$  that we used in our initial simulation is within the estimated uncertainty range and at most  $20 \text{ kJ mol}^{-1}$  from the estimated values.

For all factors from both campaigns we estimated high values for the accommodation coefficient, close to unity (Figure 3.17) which was the originally assumed value. These suggest that any resistances to mass transfer during the evaporation in the TD were indeed minor.

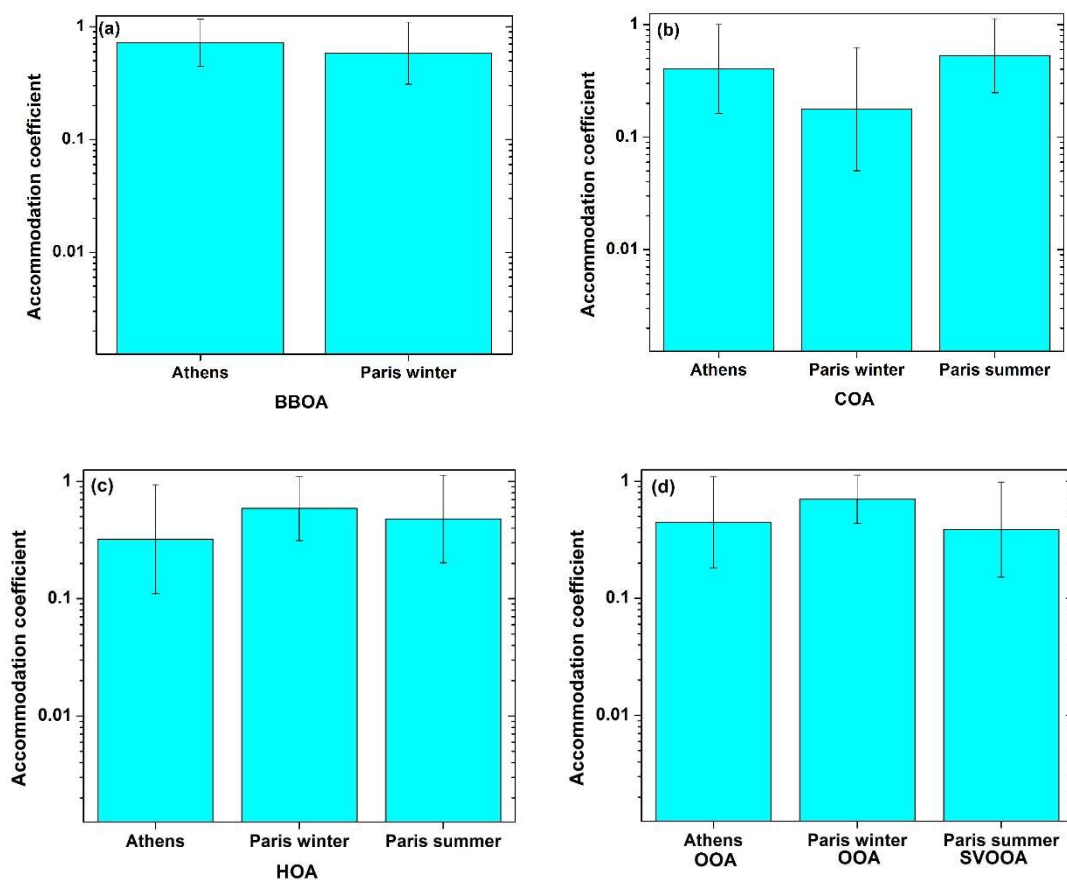


**Figure 3.17** Estimated accommodation coefficients for the Athens and Paris campaigns for: (a) BBOA, (b) COA, (c) HOA and (d) OOA for the winter campaigns and SV-OOA for Paris summer campaign.

Finally, the new estimated volatility distributions, after applying the mass transfer model again, varying the vaporization enthalpy and accommodation coefficient, were compared to the ones with the previous approach, using fixed values for the properties ( $\Delta H_{\text{vap}}= 100 \text{ kJ mol}^{-1}$  and  $a_m=1$ ). The new estimations and their uncertainties are similar to the previous estimations, with largest differences found on the cases of winter COA. In these components, the estimated vaporization enthalpy, ranged around  $20 \text{ kJ mol}^{-1}$  from the estimated values and there was predicted a lower accommodation coefficient of the order of 0.1. A comparison between the volatility distributions for the two approaches is shown in Figure A.4 in the Appendix.

### 3.9 Effects of OA concentration on estimated volatility distribution

The ambient concentration of the OA or of the PMF factors affects the estimated volatility distribution due to the partitioning of the organic component between the aerosol and the gas phases (Donahue et al., 2006). For a fairer comparison between the volatility distributions and furthermore the fractional contribution of the OA composition, we scaled all distributions to the same mass concentration of the OA. Figure 3.18 shows an example for the BBOA factor from Athens campaign and how the volatility distribution changes for an initial concentration of  $4.3 \mu\text{g m}^{-3}$  (average ambient mass concentration of BBOA in the Athens campaign) to an initial concentration of  $0.6 \mu\text{g m}^{-3}$  (average ambient mass concentration of BBOA in the Paris winter campaign).

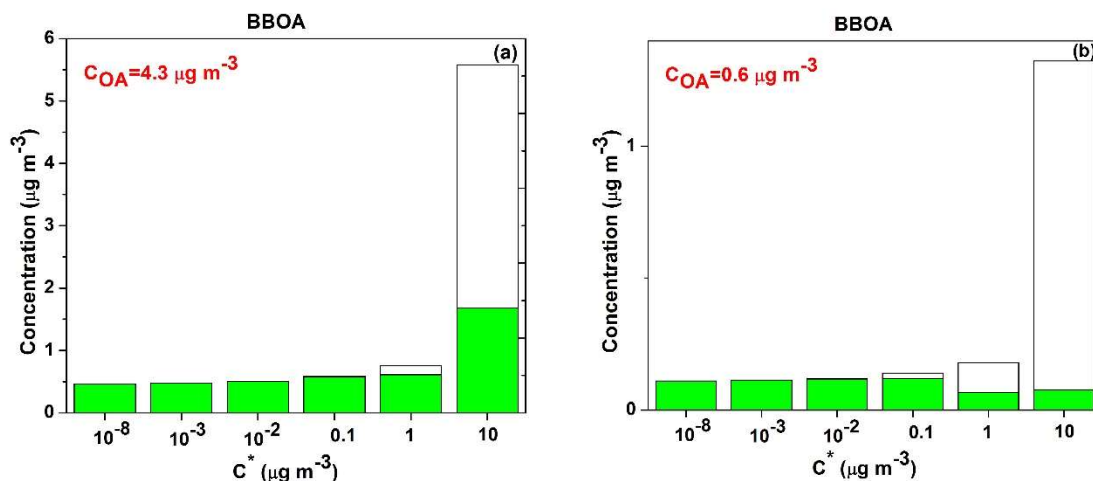


**Figure 3.18** Estimated concentrations of the BBOA components in the particulate phase (green) and gas phase in Athens for (a) for BBOA equal to  $4.3 \mu\text{g m}^{-3}$  and (b) for BBOA= $0.6 \mu\text{g m}^{-3}$ .

At the higher concentrations in Athens there is significant BBOA with  $C^*=10 \mu\text{g m}^{-3}$  (at 298 K). If the concentrations were much lower and similar to those in Paris ( $0.6 \mu\text{g m}^{-3}$ ) the  $C^*=10 \mu\text{g m}^{-3}$  components of the same BBOA would have much lower concentrations. As a result, the BBOA would appear to be less volatile even if we have assumed in this example that it has exactly the same volatility distribution.

The initial and final fractional contribution of OA composition for BBOA in Athens before and after scaling to the same average ambient concentration as in the Paris winter campaign is shown in Figure 3.19. After scaling to the lower Paris concentration levels the major contributor to BBOA is LVOCs and not SVOCs.

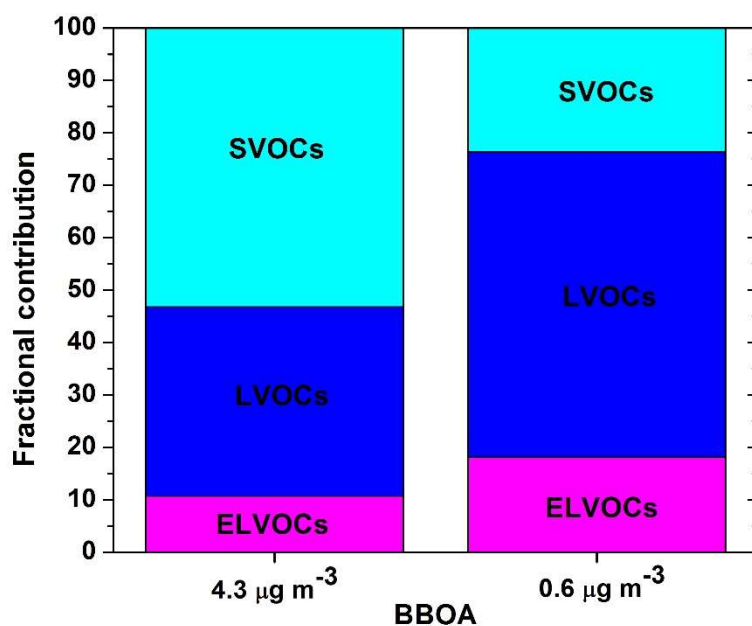


**Figure 3.19** Fractional composition of the BBOA factor. For initial concentration  $4.3 \mu\text{g m}^{-3}$  (Athens winter campaign average concentration of BBOA) and for  $0.6 \mu\text{g m}^{-3}$  (corresponding to the average BBOA in Paris).

We repeated this calculation for all factors in Athens, calculating the aerosol concentration for the Paris concentration levels. The results are summarized in Figure 3.20. The BBOA in both areas, Paris and Athens, contained roughly 20% ELVOCs. However, there were more SVOCs in Paris (50%) compared to Athens (25%).

The composition of the COA factors is quite different with the Paris COA having a significant ELVOC content, while the Athens COA has a SVOC fraction equal to almost 20% that is not present in Paris COA. These differences are consistent with the different cooking habits in

the two countries during the winter. Both winter studies agreed that 30% of the HOA consisted of LVOCs. The ELVOC fraction (30%) in Athens is higher than in Paris (15%) and both had a significant SVOC fraction (60% in Paris and 40% in Athens). The relatively small differences may be due to different transportation sources in these areas or could be partially due to the uncertainties of the corresponding analyses. The two OOA factors also had some similarity. The OOA factor included a lot more SVOCs (30%) compared to the OOA in Athens (15%). At the same time the Athens OOA had more ELVOCs and SVOCs.

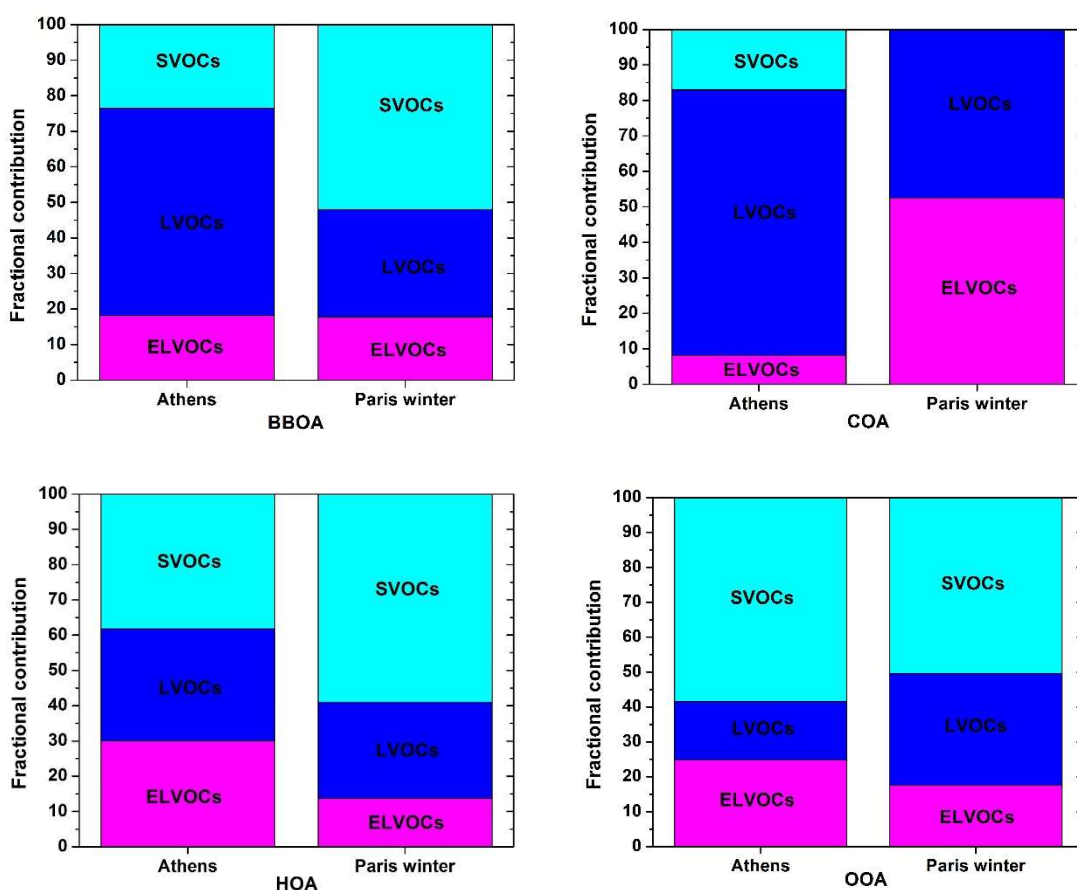


**Figure 3.20** Comparison of composition of the factors from the Athens and Paris winter campaigns at the Paris concentration levels. With magenta we represent the ELVOCs, with blue the LVOCs and with cyan the SVOCs.

The above results suggest both some similarities and also differences of the volatility distributions of the factors at the same concentration levels. The differences could be due to the different characteristics of the sources in the two regions and the differences in chemical processing (for the OOA). These differences, are, in a rough sense, consistent with the differences

in the AMS spectra of the corresponding factors ( $\theta$  equal to  $23^\circ$  for BBOA,  $17^\circ$  for COA,  $15^\circ$  for HOA and  $25^\circ$  for OOA).

### 3.10 Conclusions

Ambient experimental data from a thermodenuder (TD) coupled to a High-Resolution Time-of-Flight Aerosol Mass Spectrometer (HR-ToF-AMS) were obtained during two month-long (summer and winter) field campaigns in Paris, France and one wintertime campaign in Athens, Greece. Using a mass transfer model, together with the uncertainty estimation method of Karnezis et al. (2014), the volatility distribution of OA and its components was estimated.

For the winter and summer campaign in Paris the thermograms surprisingly did not show significant differences, while the estimated volatility distributions, were also similar, with a bimodal shape with two major peaks: one at  $C^*$  of the order of  $10^{-4} \mu\text{g m}^{-3}$  and the second at  $C^*$  of the order of  $10 \mu\text{g m}^{-3}$ . The volatility distributions of PMF factors were also derived during both campaigns. Five factors were determined for the summer dataset. Hydrocarbon-like OA (HOA), cooking OA (COA), marine OA (MOA) and two Secondary OA (SOA) factors were also identified: Semi-volatile oxygenated OA (SV-OOA) and low volatility oxygenated OA (LV-OOA). The PMF analysis for the winter campaign determined four factors. The HOA and COA factors were again identified. There was also a single secondary OA factor that was termed oxygenated OA (OOA). The final factor observed was biomass burning OA (BBOA).

The HOA factors for both campaigns in Paris had similar volatility distributions with half material being SVOCs. This similarity was consistent with the corresponding mass spectra derived by the PMF analysis and was not surprising for a city, with similar transportation and industrial emissions in both seasons. The summer COA was significantly more volatile than the winter COA. The winter COA did not contain any semi-volatile organic components (SVOCs) whereas 37% of the summer COA was semi-volatile. These differences in volatility were consistent with the differences in AMS spectra and could be due to different seasonal cooking habits. The LV-OOA factor detected in the summer had the lowest volatility of all the derived factors. The LV-OOA factor consisted nearly exclusively of ELVOCs (97%). Roughly half of the SV-OOA mass consisted of SVOCs while the rest was mainly LVOCs (42%). The OOA factor determined in the winter had a volatility distribution containing SVOCs (45%), ELVOCs (30%) and LVOCs (25%).

The marine OA (MOA) factor, only detected during the summer campaign, was relatively volatile. Half of the BBOA consisted of SVOCs and the other half of extremely low volatile and low volatile organic components. The BBOA was less volatile than the HOA factors but more volatile than COA and OOA.

Looking at the wintertime campaign in Athens the total OA was also estimated with a bimodal shape, with the difference that a very low bin was estimated for the volatility distribution (to the order of  $10^{-8} \mu\text{g m}^{-3}$ ) and it similarly consisted of 40% SVOCs, 30% LVOCs and 30% ELVOCs. PMF analysis, during this campaign resulted in three primary OA factors (HOA, BBOA and COA) and one secondary OA factor (OOA). 30% of the HOA was semi-volatile material (SVOCs) and 40% LVOCs. The rest of the material was ELVOCs. BBOA was the most volatile factor. 40% of the BBOA consisted of LVOCs and another 50% of SVOCs. However, a small amount of ELVOC material, around 10% of the BBOA, was present. LVOCs contributed 65% to the COA mass, with another 25% being SVOCs and the rest was ELVOCs. OOA was the least volatile factor. It consisted of 40% ELVOC material, almost 25% LVOCs and 35% SVOCs.

Combining the O:C ratio and volatility distributions of the various factors, we integrated our results from both campaigns into the 2D-VBS synthesizing the corresponding OA findings. The factor locations agreed well with the location of factors proposed by Donahue et al. (2012), with the exception of volatility distributions to even the ELVOC range. Terminology as more or less oxidized OOA is more correct for use in the field. The results suggest that the average O:C factor was not directly linked to its average volatility, underlining the importance of measuring both properties, and that all factors include compounds with a wide range of volatilities.

An intercomparison among the OA components of both campaigns and their physical properties was further investigated, with applying the mass transfer model once again and estimating the vaporization enthalpy and accommodation coefficient of the OA factors. For the vaporization enthalpy estimation, small differences were identified between the same OA factors of the campaigns. The uncertainties were similar and they were also within the initial  $100 \text{ kJ mol}^{-1}$  assumption, that we used in our initial simulations. For the accommodation coefficient, the predictions suggested low mass resistance for most of the factors, but with uncertainties covering even assumptions of values around 0.1, coming into agreement with Saleh et al. (2013).

Donahue et al. (2006) has shown that there is an interplay between the initial concentration of the OA and the partitioning in the gas/aerosol phase. After a scaling of the volatility distributions

of the various OA factors of both Athens and Paris campaigns, and the use of the same initial concentration, we could make a fair comparison of the fractional contribution of the OA composition. The results showed that there are differences, even more than 20% between the various components (ELVOCs, LVOCs and SVOCs) revealing the different characteristics of the sources and the chemical processing (for the OOA) of the two major cities.

### 3.11 References

An, W. J., Pathak, R. K., Lee, B.-H. and Pandis, S. N.: Aerosol volatility measurement using an improved thermodenuder: Application to secondary organic aerosol, *Journal of Aerosol Science*, 38, 305–314, 2007.

Baklanov, A., Lawrence, M. G. and Pandis, S. N.: Description of work document for the European Collaborative Project “Megacities: Emissions, urban, regional and Global Atmospheric POLLution and climate effects, and Integrated tools for assessment and mitigation” (MEGAPOLI) for the Seventh Framework Programme of the European Commission, <http://megapoli.info>, 2008.

Beekmann, M., Prévôt, A. S. H., Drewnick, F., Sciare, J., Pandis, S. N., Denier van der Gon, H. A. C., Crippa, M., Freutel, F., Poulain, L., Gherzi, V., Rodriguez, E., Beirle, S., Zotter, P., von der Weiden-Reinmuller, S. L., Bressi, M., Fountoukis, C., Petetin, H., Szidat, S., Schneider, J., Rosso, A., El Haddad, I., Megaritis, A., Zhang, Q. J., Michoud, V., Slowik, J. G., Moukhtar, S., Kolmonen, P., Stohl, A., Eckardt, S., Borbon, A., Gros, V., Marchand, N., Jaffrezo, J. L., Schwarzenboeck, A., Colomb, A., Wiedensohler, A., Borrmann, S., Lawrence, M., Baklanov, A., and Baltensperger, U. (2015). In-situ, satellite measurement and model evidence for a dominant regional contribution to fine particulate matter levels in the Paris megacity, *Atmospheric Chemistry and Physics*, 15, 9577-9591, 2015.

Burtscher, H., Baltensperger, U., Bukowiecki, N., Cohn, P., Hüglin, C., Mohr, M., Matter, U., Nyeki, S., Schmatloch, V. and Streit, N.: Separation of volatile and non-volatile aerosol fractions by thermodesorption: instrumental development and applications, *Journal of Aerosol Science*, 32, 427–442, 2001.

Caiazzo, F., Ashok, A., Waitz, I. A., Yim, S. H. L. and Barrett, S. R. H.: Air pollution and early deaths in the United States. Part I: Quantifying the impact of major sectors in 2005,

- Atmospheric Environment, 79, 198–208, 2013.
- Canagaratna, M. R., Jayne, J. T., Jimenez, J. L., Allan, J. D., Alfarra, M. R., Zhang, Q., Onasch, T. B., Drewnick, F., Coe, H., Middlebrook, A. M., Delia, A. E., Williams, L. R., Trimborn, A. M., Northway, M. J., DeCarlo, P. F., Kolb, C. E., Davidovits, D.R.: Chemical and microphysical characterization of ambient aerosols with the Aerodyne Aerosol mass Spectrometer, *Mass Spectrom. Rev.* 26, 185–222, 2007.
- Cappa, C. D. and Jimenez, J. L.: Quantitative estimates of the volatility of ambient organic aerosol, *Atmos. Chem. Phys.*, 10, 5409–5424, 2010.
- Crippa, M., Haddad, El, I., Slowik, J. G., DeCarlo, P. F., Mohr, C., Heringa, M. F., Chirico, R., Marchand, N., Sciare, J., Baltensperger, U. and Prévôt, A. S. H.: Identification of marine and continental aerosol sources in Paris using high resolution aerosol mass spectrometry, *J. Geophys. Res. Atmos.*, 118, 1950–1963, doi:10.1002/jgrd.50151, 2013a.
- Crippa, M., DeCarlo, P. F., Slowik, J. G., Mohr, C., Heringa, M. F., Chirico, R., Poulain, L., Freutel, F., Sciare, J., Cozic, J., Di Marco, C. F., Elsasser, M., Nicolas, J. B., Marchand, N., Abidi, E., Wiedensohler, A., Drewnick, F., Schneider, J., Borrmann, S., Nemitz, E., Zimmermann, R., Jaffrezo, J. L., Prévôt, A. S. H. and Baltensperger, U.: Wintertime aerosol chemical composition and source apportionment of the organic fraction in the metropolitan area of Paris, *Atmos. Chem. Phys.*, 2013b.
- DeCarlo, P. F., Kimmel, J. R., Trimborn, A., Northway, M. J., Jayne, J. T., Aiken, A. C., Gonin, M., Fuhrer, K., Horvath, T., Docherty, K. S., Worsnop, D. R. and Jimenez, J. L.: Field-deployable, high-resolution, time-of-flight aerosol mass spectrometer, *Anal. Chem.*, 78, 8281–8289, 2006.
- Donahue, N. M., Robinson, A. L., Stanier, C. O. and Pandis, S. N.: Coupled partitioning, dilution, and chemical aging of semivolatile organics, *Environ. Sci. Technol.*, 40, 2635–2643, 2006.
- Donahue, N. M., Kroll, J. H., Pandis, S. N. and Robinson, A. L.: A two-dimensional volatility basis set – Part 2: Diagnostics of organic-aerosol evolution, *Atmos. Chem. Phys.*, 12, 615–634, 2012.
- Florou, K., Papanastasiou, D. K., Pikridas, M., Kaltsonoudis C., Louvaris, E., Gkatzelis G. I.,

- Patoulias D., Mihalopoulos N., and Pandis, S.N.: The contribution of wood burning and other pollution sources to wintertime organic aerosol levels in two Greek cities, *Atmos. Chem. Phys. Discuss.*, 2016.
- Gkatzelis, G.I., Papanastasiou, D.K., Florou, K., Kaltsonoudis, C., Louvaris, E., Pandis, S.N.: Measurement of nonvolatile particle number size distribution, *Atmos. Meas. Tech.* 9, 103–114, 2016.
- Haefelin, M., Barthès, L., Bock, O., Boitel, C., Bony, S., Bouniol, D., Chepfer, H., Chiriaco, M., Cuesta, J., Delanoë, J., Drobinski, P., Dufresne, J. L., Flamant, C., Grall, M., Hodzic, A., Hourdin, F., Lapouge, F., Lemaître, Y., Mathieu, A., Morille, Y., Naud, C., Noël, V., O'Hirok, W., Pelon, J., Pietras, C., Protat, A., Romand, B., Scialom, G. and Vautard, R.: SIRTA, a ground-based atmospheric observatory for cloud and aerosol research, *Ann. Geophys.*, 23, 253–275, 2005.
- Huffman, J. A., Docherty, K. S., Aiken, A. C., Cubison, M. J., Ulbrich, I. M., DeCarlo, P. F., Sueper, D., Jayne, J. T., Worsnop, D. R., Ziemann, P. J. and Jimenez, J. L.: Chemically-resolved aerosol volatility measurements from two megacity field studies, *Atmos. Chem. Phys.*, 9, 7161–7182, 2009.
- IPCC (Intergovernmental Panel on Climate Change): *Climate Change 2014: Mitigation of Climate Change. Contribution of Working Group III to the Fifth Assessment Report of the Intergovernmental Panel on Climate Change*, Cambridge University Press, Cambridge, UK and New York, 2014.
- Kalberer, M., Paulsen, D., Sax, M., Steinbacher, M., Dommen, J., Prevot, A. S. H., Fisseha, R., Weingartner, E., Frankevich, V., Zenobi, R., and Baltensperger, U.: Identification of polymers as major components of atmospheric organic aerosols, *Science*, 303, 1659–1662, 2004.
- Karnezi, E., Riipinen, I. and Pandis, S.N. : Measuring the atmospheric organic aerosol volatility distribution: a theoretical analysis, *Atmos. Meas. Tech.*, 7, 2953–2965, 2014.
- Kostenidou, E., Pathak, R.K., Pandis, S.N. : An algorithm for the calculation of secondary organic aerosol density combining AMS and SMPS data, *Aerosol Sci. Technol.* 41, 1002–1010, 2007.

- Kostenidou, E., Lee, B. H., Engelhart, G. J., Pierce, J. R., and Pandis, S. N.: Mass spectra deconvolution of low, medium and high volatility biogenic secondary organic aerosol, *Environ. Sci. Technol.*, 43, 4884–4889, 2009.
- Lanz, V. A., Alfarra, M. R., Baltensperger, U., Buchmann, B., Hueglin, C. and Prévôt, A. S. H.: Source apportionment of submicron organic aerosols at an urban site by factor analytical modelling of aerosol mass spectra, *Atmos. Chem. Phys.*, 7, 1503–1522, 2007.
- Lee, B. H., Kostenidou, E., Hildebrandt, L., Riipinen, I., Engelhart, G. J., Mohr, C., DeCarlo, P. F., Mihalopoulos, N., Prevot, A. S. H., Baltensperger, U., Pandis, S. N.: Measurement of the ambient organic aerosol volatility distribution: application during the Finokalia Aerosol Measurement Experiment (FAME-2008), *Atmos. Chem. Phys.*, 10, 12149–12160, 2010.
- May, A. A., Levin, E. J. T., Hennigan, C. J., Riipinen, I., Lee, T., Collett, J. L., Jr., Jimenez, J. L., Kreidenweis, S. M. and Robinson, A. L.: Gas-particle partitioning of primary organic aerosol emissions: 3. Biomass burning, *J. Geophys. Res. Atmos.*, 118, 11,327–11,338, doi:10.1002/jgrd.50828, 2013.
- Murphy, B. N., Donahue, N. M., Robinson, A. L., and Pandis, S. N.: A naming convention for atmospheric organic aerosol, *Atmos. Chem. Phys.*, 14, 5825–5839, 2014.
- Paciga, A., Karnezi, E., Kostenidou, E., Hildebrandt, L., Psychoudaki, M., Engelhart, G.J., Lee, B.H., Crippa, M., Prévôt, A.S.H., Baltensperger, U., Pandis, S.N.: Volatility of organic aerosol and its components in the megacity of Paris, *Atmos. Chem. Phys.* 16, 2013–2023, 2016.
- Pope, C. A., III, Ezzati, M. and Dockery, D. W.: Fine-particulate air pollution and life expectancy in the United States, *New England Journal of Medicine*, 360, 376–386, 2009.
- Riipinen, I., Pierce, J. R., Donahue, N. M. and Pandis, S. N.: Equilibration time scales of organic aerosol inside thermodenuders: Evaporation kinetics versus thermodynamics, *Atmospheric Environment*, 44, 597–607, 2010.
- Saleh, R., Donahue, N. M. and Robinson, A. L.: Time scales for gas-particle partitioning equilibration of secondary organic aerosol formed from alpha-pinene ozonolysis, *Environ. Sci. Technol.*, 47, 5588–5594, 2013.

- Ulbrich, I. M., Canagaratna, M. R., Zhang, Q., Worsnop, D. R. and Jimenez, J. L.: Interpretation of organic components from Positive Matrix Factorization of aerosol mass spectrometric data, *Atmos. Chem. Phys.*, 9, 2891–2918, 2009.
- Wehner, B., Philippin, S., and Wiedensohler, A.: Design and calibration of a thermodenuder with an improved heating unit to measure the size-dependent volatile fraction of aerosol particles, *J. Aerosol Sci.*, 33, 1087–1093, 2002.
- Wehner, B., Philippin, S., Wiedensohler, A., Scheer, V., and Vogt, R.: Variability of non-volatile fractions of atmospheric aerosol particles with traffic influence, *Atmos. Environ.*, 38, 6081–6090, 2004.
- Zhang, Q., Jimenez, J. L., Canagaratna, M. R., Allan, J. D., Coe, H., Ulbrich, I., Alfarra, M. R., Takami, A., Middlebrook, A. M., Sun, Y. L., Dzepina, K., Dunlea, E., Docherty, K., DeCarlo, P. F., Salcedo, D., Onasch, T., Jayne, J. T., Miyoshi, T., Shimo, A., Hatakeyama, S., Takegawa, N., Kondo, Y., Schneider, J., Drewnick, F., Borrmann, S., Weimer, S., Demerjian, K., Williams, P., Bower, K., Bahreini, R., Cottrell, L., Griffin, R. J., Rautiainen, J., Sun, J. Y., Zhang, Y. M. and Worsnop, D. R.: Ubiquity and dominance of oxygenated species in organic aerosols in anthropogenically-influenced Northern Hemisphere midlatitudes, *Geophys. Res. Lett.*, 34, L13801, 2007.
- Zhang, Q., Jimenez, J. L., Canagaratna, M. R., Ulbrich, I. M., Ng, S. N., Worsnop, D. R., and Sun, Y.: Understanding atmospheric organic aerosols via factor analysis of aerosol mass spectrometry: a review, *Anal. Bioanal. Chem.*, 401, 3045–3067, 2011.

# **Chapter 4**

**Estimation of the volatility distribution of cooking organic aerosol combining  
thermodenuder and isothermal dilution measurements**

## 4.1 Introduction

Atmospheric aerosols have a significant impact both on human health (Pope et al., 2009; Caiazzo et al., 2013) and on Earth's climate due to their ability to scatter and absorb solar radiation and their effects on cloud properties and lifetimes (IPCC, 2014). These aerosols are comprised of a wide variety of chemical compounds, with organic components representing 20-90% of their submicron mass (Zhang et al., 2007). Organic aerosol (OA) can be emitted directly as primary particles (POA) from various anthropogenic and natural sources, or can be formed when gas-phase oxidation products of volatile (VOCs), intermediate volatility (IVOCs) and semi-volatile (SVOCs) organic compounds condense onto pre-existing particles (secondary organic aerosol, SOA). There is limited knowledge of the sources, chemical evolution, and physical properties of OA due to the complexity of the mostly unknown thousands of organic compounds that OA particles contain. These uncertainties often lead to erroneous predictions of OA concentrations by chemical transport models.

Volatility is one of the most important physical properties of OA as it determines the partitioning of its components between the gas and particulate phases, and eventually their atmospheric fate. Measurement of OA volatility is essential for the quantification of the rates of formation of SOA (Donahue et al., 2012). One of the most common techniques to constrain indirectly aerosol volatility requires the use of a thermodenuder (TD). The aerosol enters a heated tube where the most volatile components evaporate leaving behind the less volatile species in the particulate phase (Burtscher et al., 2001; Kalberer et al., 2004; Wehner et al., 2002, 2004; An et al., 2007). TDs usually consist of two sections: the heating section where the aerosol evaporation takes place and the denuder/cooling section. This second section often contains activated carbon in order to prevent re-condensation of the evaporated components. The typical result of a TD is the mass fraction remaining (MFR) of the aerosol as function of the TD temperature. The MFR depends on aerosol concentration, size, vaporization enthalpy, and potential mass transfer resistances (Riipinen et al., 2010).

TD measurements of OA volatility have received considerable attention recently, and have been performed both in the field (Huffman et al., 2009; Cappa and Jimenez, 2010; Lee et al., 2010; Louvaris et al., 2016) and in the laboratory (Saleh et al., 2008; Faulhaber et al., 2009; Lee et al., 2011). One of the major issues interpreting TD measurements is whether equilibrium has been reached in the heating section of the instrument. Riipinen et al. (2010) argued that OA practically

never reaches equilibrium in a TD at ambient concentration levels. For laboratory experiments equilibrium can be reached with the use of high organic aerosol loadings ( $>200 \mu\text{g m}^{-3}$ ) and heating section residence times of 30 s or longer (Saleh et al., 2008; Riipinen et al., 2010). TD measurements were performed by Lee et al. (2010, 2011) using multiple residence times. These authors argued that use of multiple residence times in the heating section of the TD can help to decouple mass transfer effects from thermodynamics. Similar conclusions were reached also by Riipinen et al. (2010) and Cappa (2010). Saleh et al. (2012) used a particle concentrator upstream of a TD in order to achieve higher ambient aerosol loadings so that the system could reach equilibrium. Their results suggested many accommodation coefficient values around 0.3 for the ambient aerosol that they examined. Volatility measurements based on longer equilibration timescales were performed for POA from a diesel engine and wood combustion using isothermal dilution (Grieshop et al., 2009). Cappa and Wilson (2011) studied the evolution of heating-induced evaporated OA mass spectra from lubricating oil and  $\alpha$ -pinene oxidation. They concluded that there were high mass transfer resistances (i.e. accommodation coefficient values of the order of  $10^{-4}$ ) for the SOA produced from  $\alpha$ -pinene ozonolysis. Saleh et al. (2013) measured the equilibration timescales for the gas to particle partitioning of SOA formed from  $\alpha$ -pinene ozonolysis using an accommodation coefficient of the order of 0.1.

Karnezi et al. (2014) proposed that the volatility distribution of complex OA can be better constrained combining TD and isothermal dilution measurements. Kolesar et al. (2015) combining rapid isothermal dilution with TD measurements argued that the volatility of SOA formed from  $\alpha$ -pinene ozonolysis is mostly independent of the SOA loading during temperature induced evaporation.

All the previous studies discussed above assumed a-priori values for the parameters that affect together with the volatility distribution the aerosol evaporation such as vaporization enthalpy and accommodation coefficient. Since the TD thermograms are sensitive to these parameters large uncertainties were reported for the volatility distributions. The performance of experiments at different time scales could allow the estimation of the volatility distribution together with the vaporization enthalpy and accommodation coefficient with lower uncertainty ranges.

In this section, we describe a new experimental technique to constrain the volatility distribution of organic aerosol using TD combined with isothermal dilution measurements following the suggestions of Karnezi et al. (2014). The experiments were performed by Dr.

Evangelos Louvaris in the FORTH chamber in Patras, Greece. The OA mass fraction remaining was measured as a function of temperature in the thermodenuder and in parallel as a function of time in a dilution chamber. TD measurements are corrected for size- and temperature- dependent losses and the dilution system measurements for size-dependent losses. Using these two sets of measurements together with the approach of Karnezi et al. (2014) suggested in Chapter 2 the volatility distribution of the OA and its effective enthalpy of vaporization ( $\Delta H_{\text{vap}}$ ) and effective accommodation coefficient ( $a_m$ ) are estimated in this work. Meat from charbroiling is used as an example for the application of the method.

## 4.2 Experimental description

Two smog chamber experiments were conducted in the FORTH smog chamber to constrain the volatility distribution of fresh OA emissions from meat charbroiling. A number of additional experiments focused on the characterization of the COA and its chemical aging (Kaltsonoudis et al. 2016 b). The experimental setup is shown in Figure 4.1. A metal bellows pump (model MB 602, Senior Aerospace) was used to transfer cooking emissions to an 8 m<sup>3</sup> Teflon chamber. Details for the meat charbroiling and the transferring process can be found in Kaltsonoudis et al. (2016 b). A TD (Louvaris et al., 2016) was placed upstream of a High-Resolution Time-of-Flight Aerosol Mass Spectrometer (HR-ToF-AMS Aerodyne Research Inc.) (Decarlo et al., 2006; Canagaratna et al., 2007) measuring the size-composition of the submicron non refractory material, and a Scanning Mobility Particle Sizer (SMPS 3936 TSI) measuring the particle size distribution. A dilution Teflon chamber (1 m<sup>3</sup>) was used for the isothermal dilution. The VOCs and the dilution ratio (DR) were measured by a PTR-MS (Ionicon Analytic). The OH radical concentrations were estimated using isotopically labeled butanol (1-butanol-d9, Sigma). The change of the concentration of the PTR-MS m/z 66 was used to calculate the OH concentrations based on the second-order reaction of d9-butanol with the OH radicals. The corresponding reaction constant used is  $3.4 \times 10^{12} \text{ cm}^3 \text{ molecule}^{-1} \text{ s}^{-1}$  (Barnet et al., 2012).

The SMPS was operated at a sampling flow rate of 1 L min<sup>-1</sup> and sheath flow rate of 5 L min<sup>-1</sup> sampling every 3 minutes. The HR-ToF-AMS was sampling every three minutes with 0.1 L min<sup>-1</sup> and was operated in the higher sensitivity mode (V-mode) (DeCarlo et al., 2006). The PTR-

MS was sampling with  $0.5 \text{ L min}^{-1}$ . Details about the PTR-MS measurements can be found in Kaltsonoudis et al. (2016 a).

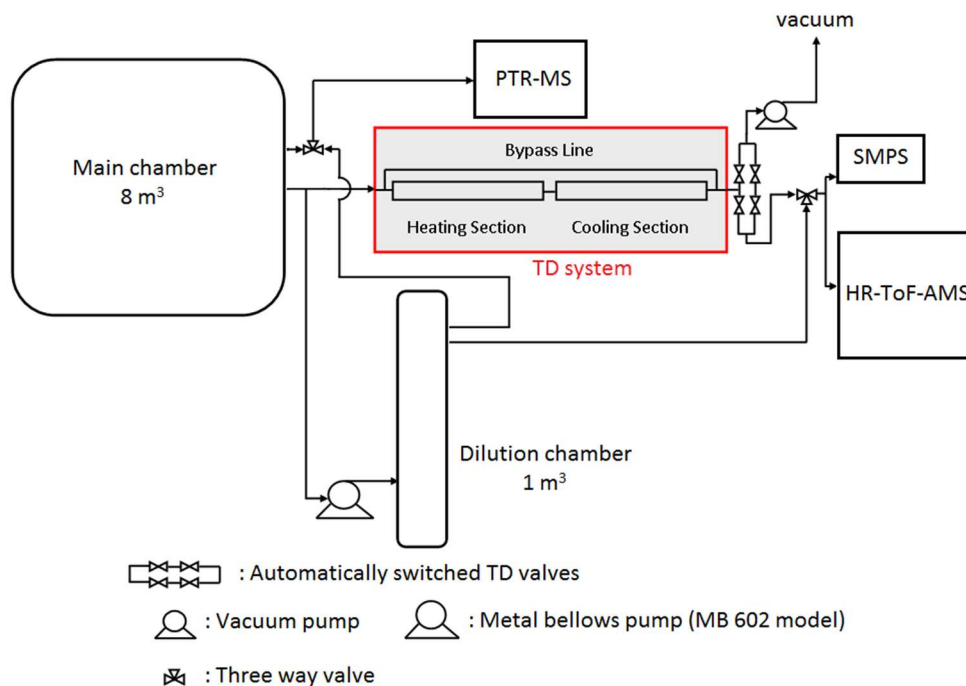


**Figure 4.1** Experimental setup used: The COA in the main chamber was characterized using a TD a HR-ToF-AMS, and an SMPS. A metal bellows MB 602 pump was used to transfer OA from the main to the dilution chamber. The COA in the dilution chamber was measured by the HR-ToF-AMS and the SMPS. A PTR-MS was used to measure the dilution ratio.

The TD was operated at temperatures ranging from 25 to 250°C. Sampling from the main chamber was alternated between bypass and TD every 3 min with computer-controlled valves. The changes in the particle mass concentration, and the size distribution were measured by both the HR-ToF-AMS and the SMPS resulting in thermograms of the MFR as a function of the TD temperature. The OA MFR was calculated as the ratio of organic mass concentration of a sample passing through the TD at time  $t_i$  over the average mass concentration of the ambient samples that passed through the bypass line at times  $t_{i-1}$  and  $t_{i+1}$ . The sample residence time in the centerline of the TD was 14 s at 298 K corresponding to an average residence time in the TD of 28 s.

The dilution chamber was initially partially filled with clean air. Then, the metal bellows pump was used to transfer cooking emissions from the main chamber to it diluting them in the process to close to ambient concentrations. Dilution measurements were performed every 9 min

by both the SMPS and the HR-ToF-AMS. The dilution ratio was calculated as the ratio of the PTR-MS m/z 66 concentration of the main chamber at time  $t_{0-1}$  over the PTR-MS m/z 66 concentration of the dilution chamber at time  $t_i$  for each dilution measurement. The dilution ratios during the isothermal dilution experiments are shown in Table 4.1 and were around  $11 \pm 0.5$  and  $14 \pm 0.5$  for Experiments 1 and 2 respectively. Table 4.1 summarizes the characteristics of each experiment. The residence time in the dilution chamber was a few hours. The mass fraction as a function of time during isothermal dilution was measured as the ratio of mass concentration at time  $t_i$  over the initial mass concentration in the dilution chamber at time  $t_0$ .

**Table 4.1** Summary of the Experiments characteristics

	Initial mass concentration ( $\mu\text{g m}^{-3}$ )		Initial particle size volume mode $D_p$ (nm)		Average dilution ratio
	Main chamber	Dilution chamber <sup>1</sup>	Main chamber	Dilution chamber	Dilution chamber
Experiment 1	541	26.5	248	210	$11 \pm 0.5$
Experiment 2	632	7.4	284	218	$14 \pm 0.5$

<sup>1</sup> The dilution chamber was filled after the OA characterization in the chamber was completed.

#### 4.2.1 Loss corrections

The thermodenuded OA was corrected for particle losses in the TD. To account for these losses, a sample flow rate, TD temperature- and size-dependent loss function was applied following Lee et al. (2010). The corrected MFR values were then averaged using temperature bins of 10°C.

The OA concentrations during the isothermal dilution experiments were also corrected for size dependent wall losses during the experiments. These losses were calculated for each experiment using the number concentration distributions measured by the SMPS. Linear fittings of the natural logarithm of the SMPS particle number distributions values for each size as a function of time allow the estimation of the size-dependent wall loss rate constant  $k_w(D_p)$ . Figure B.1 shows these loss rate constants as function of particle size for Experiment 1. These loss corrections were applied to the measured number distribution at each time step allowing the estimation of the corrected number and volume distributions. The accuracy of the corrections can be evaluated using the temporal evolution of the corrected total number concentration in the

chamber. Given the low number concentrations around 5000 particles  $\text{cm}^{-3}$  coagulation is negligible and the total number concentration should be constant. Figure B.2a shows that the corrected number concentration varies within almost 10% of its average value during 3 hours of the experiment. The corresponding corrected mass fraction values as a function of time during the isothermal dilution is shown in Figure B.2b. Even if the mass concentration was reduced by approximately 50%, the evaporation resulted in only 20% mass reduction.

A similar correction approach was followed for Experiment 2. The corrected number concentration as a function of time measured by the SMPS is shown in Figure B.3a. Their variation was less than 5% of their average suggesting that the correction was quite accurate. The evaporation resulted in only 20% mass reduction as is depicted in Figure B.3b.

As another quality assurance test the mass fraction values measured by the SMPS were compared to those measured by the HR-ToF-AMS assuming that the collection efficiency of the latter remained constant as the OA evaporated (Figure B.4). No discernible differences were observed between the two measurements.

#### **4.2.2 Determination of the volatility distributions**

The dynamic mass transfer model of Riipinen et al. (2010) together with the error minimization approach proposed by Karnezi et al. (2014) were used for the determination of the volatility distributions. Inputs for the model include the initial OA mass concentrations for the TD and the isothermal dilution chamber obtained by the HR-ToF-AMS, the initial particle sizes obtained by the SMPS, the residence times of both systems, and the dilution ratio of the isothermal dilution system. The initial mass concentration for the TD experiments was of the order of  $10^2 \mu\text{g m}^{-3}$  whereas for the dilution experiment was of the orders of  $10 \mu\text{g m}^{-3}$ . Table 4.1 summarizes the major inputs of the model. The corrected mass fraction values determined by the HR-ToF-AMS were used as inputs for the isothermal dilution experiment. The TD HR-ToF-AMS corrected MFR values were also used as inputs for the TD experiment.

The volatility distribution was expressed with a range of logarithmically spaced  $C^*$  bins along a volatility axis (Donahue et al., 2006). Several combinations of  $C^*$  bins can be used in order to represent the volatility of the OA compounds. For our analysis, a set of six volatility bins ranging from  $10^{-3}$  to  $10^3 \mu\text{g m}^{-3}$  were used. The sensitivity of our results to the assumed range of volatilities is discussed in a subsequent section.

## 4.3 Results and discussion

### 4.3.1 Volatility distribution of cooking organic aerosol (COA)

The estimated COA volatility distribution for Experiment 1 is depicted in Figure 4.2. The average volatility calculated as the average  $\log_{10}C^*$  weighted by the mass fraction of each bin was around  $0.1 \mu\text{g m}^{-3}$ . According to these results, the COA at around  $550 \mu\text{g m}^{-3}$  consisted of 60% low volatility organic compounds (LVOCs), 30% semi-volatile (SVOCs), and 10% intermediate volatility (IVOCs) organic compounds (Figure 4.3c). The estimated effective vaporization enthalpy was  $100 \pm 14 \text{ kJ mol}^{-1}$  (Figure 4.3a) and the effective accommodation coefficient was equal to 0.06 but with corresponding uncertainty range covering more than an order of magnitude (Figure 4.3b).

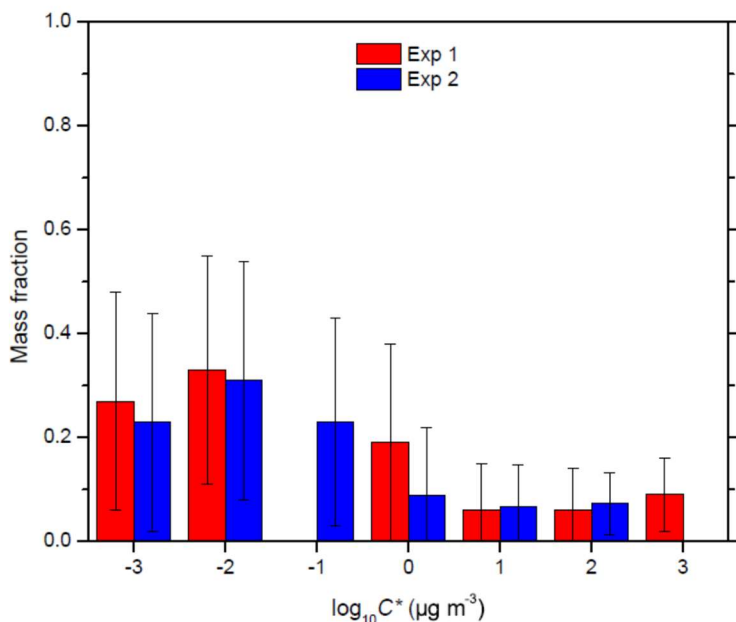


**Figure 4.2** Estimated volatility distributions for Experiment 1 (red bars) and for Experiment 2 (blue bars) using the approach of Karnezi et al. (2014). The error bars represent the uncertainty range.

The corresponding TD thermogram and the dilution curve for Experiment 1 are depicted in Figure 4.4. Almost all the COA evaporated at  $200^\circ\text{C}$  while approximately 20% of the COA evaporated at ambient temperature after isothermal dilution. On the one hand the model predicted pretty well the measured TD MFR but tended to overpredict the observed evaporation in the dilution curve. Some of this discrepancy is due to the wall-loss correction uncertainty. According to the model, the small

amount of IVOCs that existed initially in the particle phase evaporated at 50°C in the TD (Figure 4.4a). The SVOCs evaporated at 125°C and the COA remaining at higher temperatures consisted entirely of LVOCs. The IVOCs, according once more to the model, evaporated after 10 min of dilution and the SVOCs after approximately 30 min. Table B.1 summarizes the estimated volatility distribution along with the estimated effective parameters that affect volatility, and the calculated average volatilities for the two experiments.

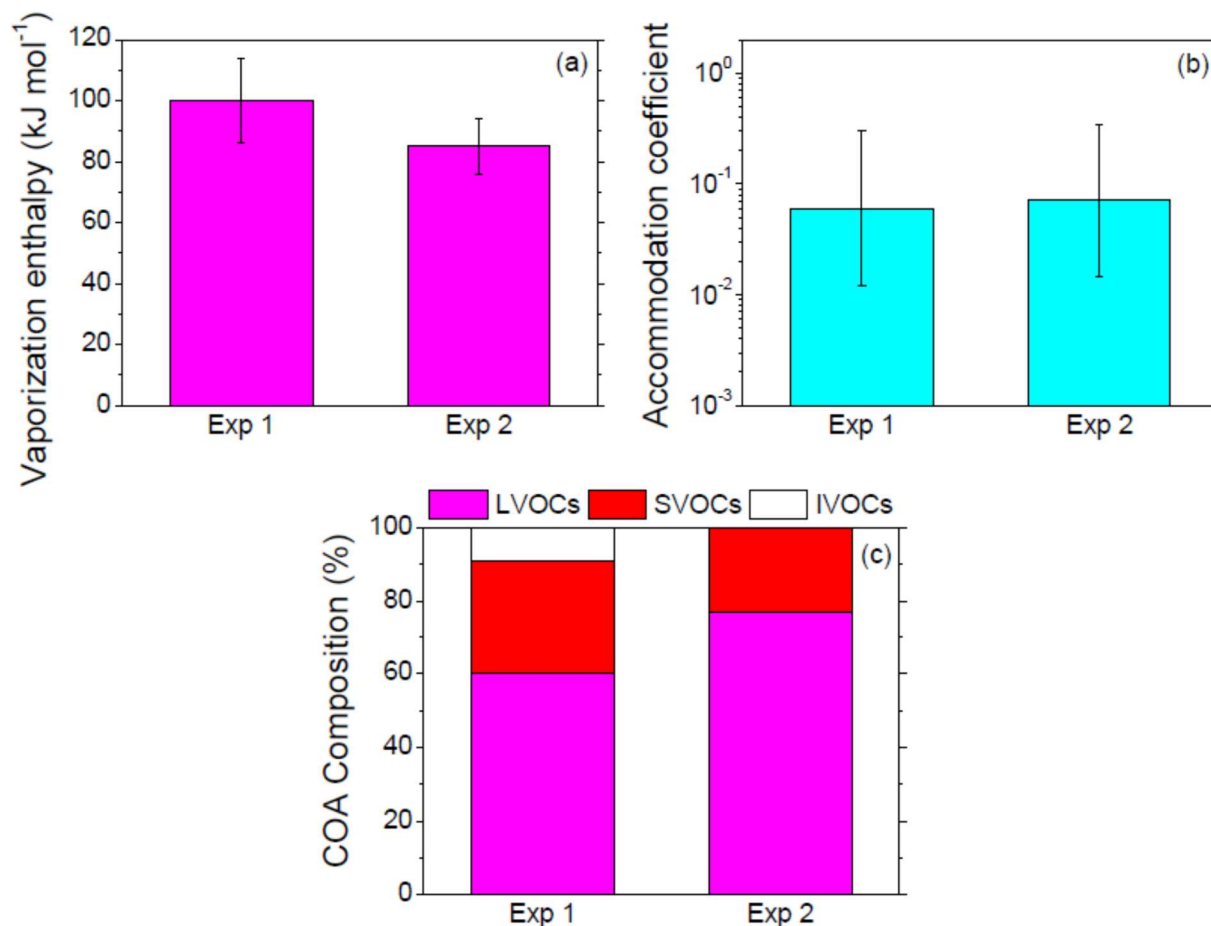


**Figure 4.3** (a) Estimated effective vaporizations enthalpies along with their uncertainties for both experiments using the approach of Karnezi et al. (2014). (b) Estimated effective accommodation coefficients along with their uncertainties for both experiments. (c) COA mass composition of both experiments. LVOCs are represented in magenta, SVOCs in red, and IVOCs in white.

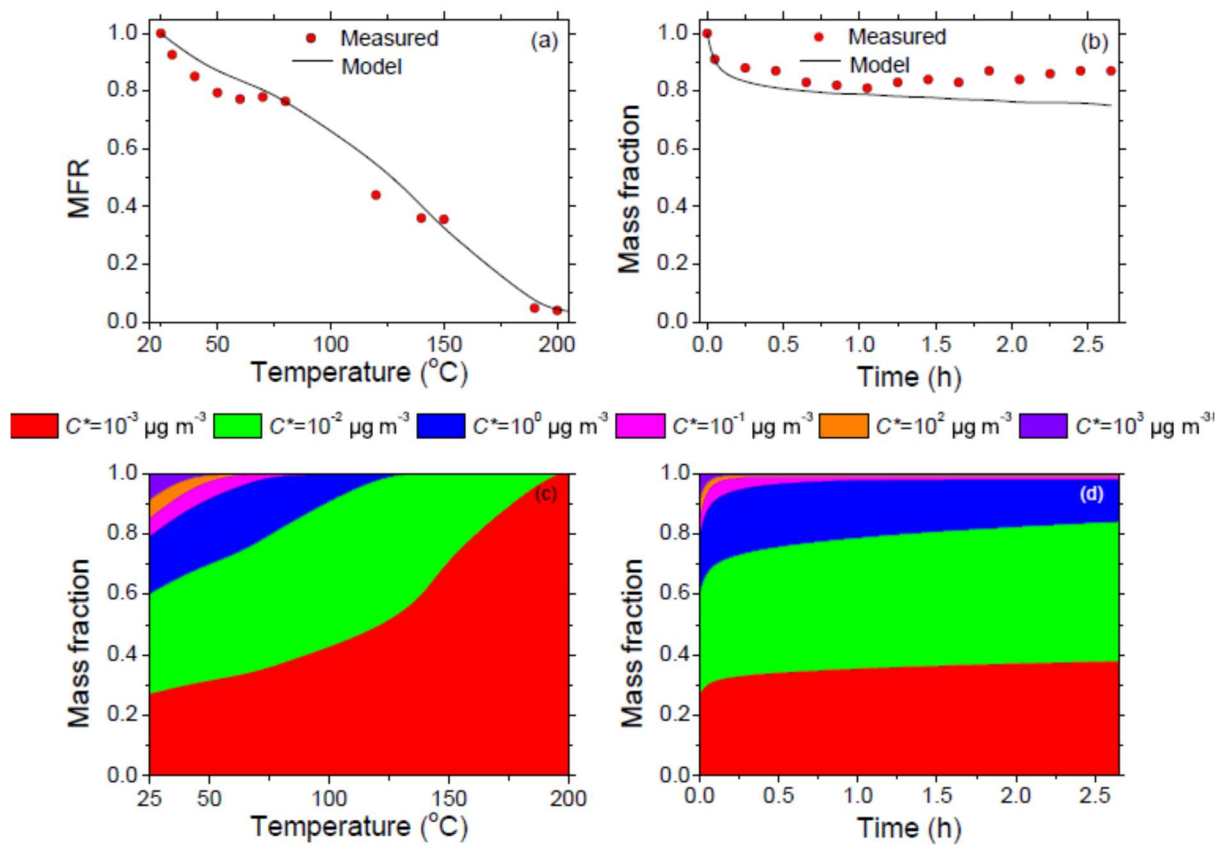


**Figure 4.4** (a) Thermogram of the OA TD measurements of Experiment 1. The red circles represent the loss-corrected measurements and the black line represents the best fit estimated by the model of Karnezi et al. (2014). (b) Mass fraction during isothermal dilution as a function of time for Exp. 1. Red circles represent the loss-corrected measurements and the black line the estimated best model fit. (c) Predicted COA composition for different effective saturation concentrations as a function of TD temperature. Red color represents the contribution of the components with  $C^* = 10^{-3} \mu\text{g m}^{-3}$ , green the  $C^* = 10^{-2} \mu\text{g m}^{-3}$ , blue the  $C^* = 1 \mu\text{g m}^{-3}$ , magenta the  $C^* = 10 \mu\text{g m}^{-3}$ , orange the  $C^* = 10^2 \mu\text{g m}^{-3}$ , and finally violet for the  $C^* = 10^3 \mu\text{g m}^{-3}$ . (d) COA composition for different effective saturation concentrations as a function of time during isothermal dilution.

Kostenidou et al. (2009) proposed the theta angle ( $\theta$ ) as an indicator of mass spectra similarity by treating AMS spectra as vectors and calculating the corresponding angle  $\theta$ . Lower  $\theta$  angles imply more similar spectra. Figure 4.5a presents the comparison between the average initial AMS normalized mass spectra of the COA at ambient temperature ( $25^\circ\text{C}$ ) and the average mass spectra in the TD at  $200^\circ\text{C}$ . The two mass spectra were quite similar with each other having angle  $\theta$  of 11 degrees ( $R^2=0.958$ ). Figure 4.5b depicts the comparison of AMS mass spectra at the onset of dilution with that at one hour after dilution, and the one at the end of the experiment. The

resulting  $\theta$  angles between the compared mass spectra were 3 to 4 degrees ( $R^2$  ranging from 0.994 to 0.997) showing the similarity of the spectra during the dilution experiment.

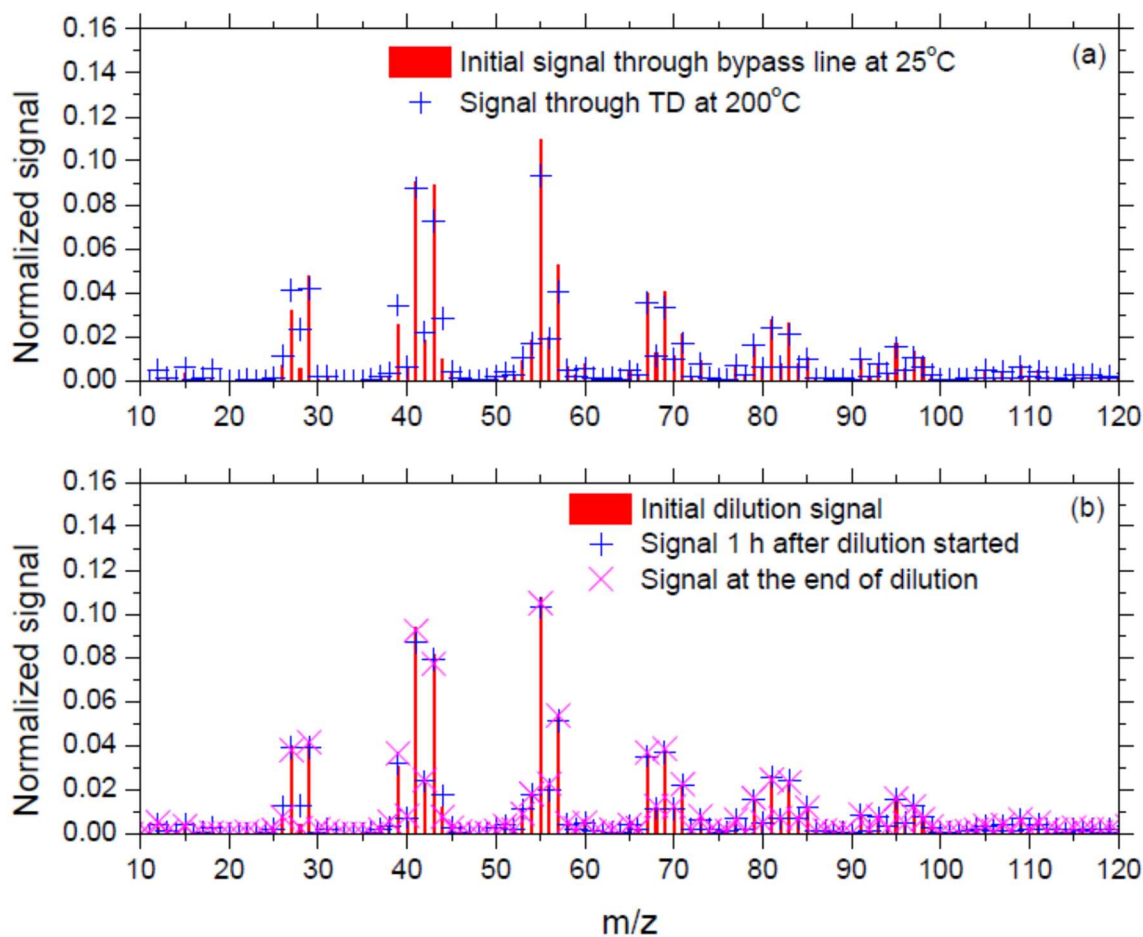


**Figure 4.5** (a) Normalized HR-ToF-AMS mass spectra of the COA at ambient temperature (red bars) compared to that in the TD at 200°C (blue crosses). (b) Normalized HR-ToF-AMS mass spectra at the onset of dilution experiment (red bars) compared to those measured after one hour (blue crosses), and those at the end of the experiment (magenta crosses).

The estimated volatility distribution of Experiment 2 is shown in Figure 4.2. The average  $\log_{10}C^*$  was approximately  $0.05 \mu\text{g m}^{-3}$ . The COA consisted of 75% LVOCs and 25% of SVOCs as depicted in Figure 4.3c. The vaporization enthalpy was  $85 \pm 9 \text{ kJ mol}^{-1}$ , and the accommodation coefficient was equal to 0.07 showing an uncertainty range larger than an order of magnitude.

The TD thermogram and the corresponding dilution curve of Experiment 2 are depicted in Figure 4.6. The COA evaporated completely at 225°C in the TD. 20% of the COA evaporated at ambient temperature during dilution. The model tended to overpredict the evaporation in the TD

in the 50-150°C range while it reproduced well the dilution measurements. According to the model once again the SVOCs evaporated at 130°C and the COA remaining at higher temperatures consisted entirely of LVOCs (Figure 4.6c). During isothermal dilution, the model predicted that after 10 minutes the SVOCs evaporated (Figure 4.6d).

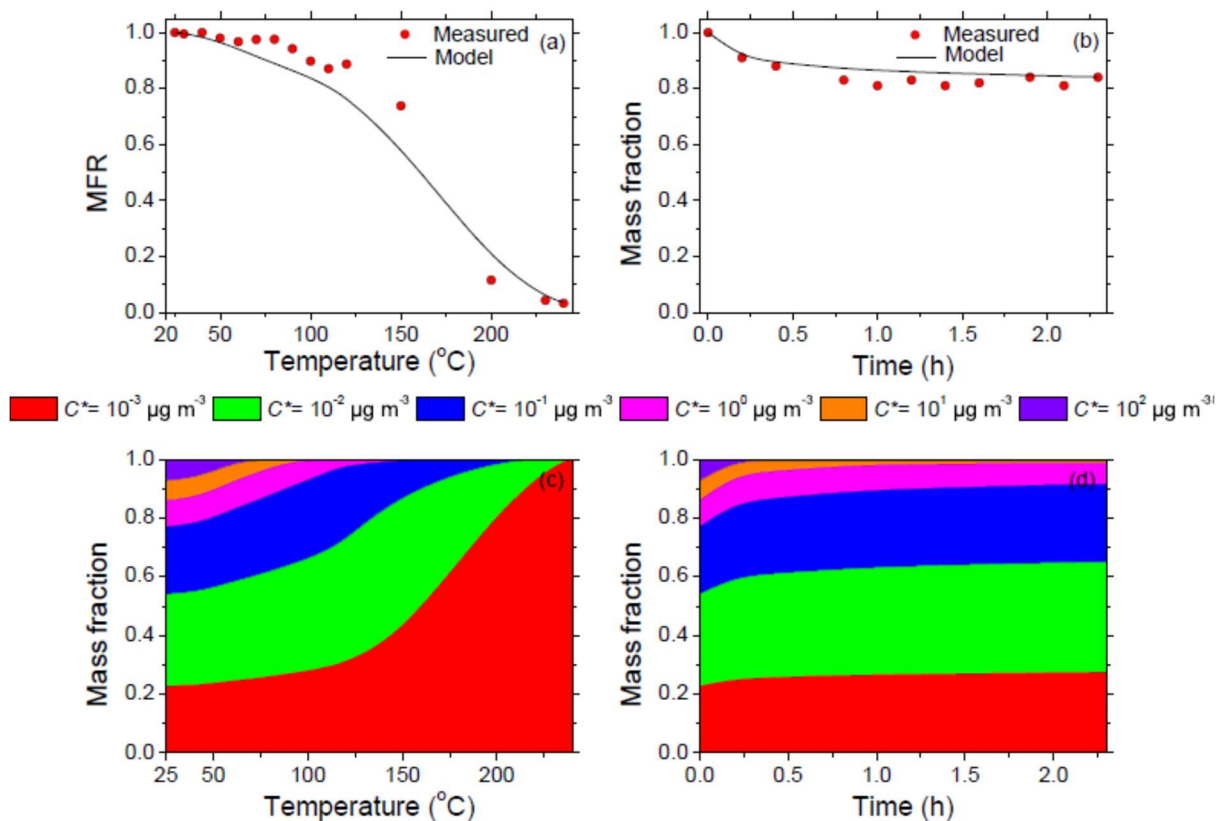


**Figure 4.6** (a) Thermogram of the OA TD measurements of Experiment 2. The red circles represent the loss-corrected measurements and the black line represents the best fit estimated by the model of Karnezi et al. (2014). (b) Mass fraction during isothermal dilution as a function of time for Exp. 2. Red circles represent the loss-corrected measurements and the black line the estimated best model fit. (c) Predicted COA composition for different effective saturation concentrations as a function of TD temperature. Red color represents the contribution of the components with  $C^* = 10^{-3} \mu\text{g m}^{-3}$ , green the  $C^* = 10^{-2} \mu\text{g m}^{-3}$ , blue the  $C^* = 1 \mu\text{g m}^{-3}$ , magenta the  $C^* = 10 \mu\text{g m}^{-3}$ , orange the  $C^* = 10^2 \mu\text{g m}^{-3}$ , and finally violet for the  $C^* = 10^3 \mu\text{g m}^{-3}$ . (d) COA composition for different effective saturation concentrations as a function of time during isothermal dilution.

The estimated effective vaporization enthalpy for Experiment 1 was  $100 \pm 14$ , while for Experiment 2 was  $85 \pm 9 \text{ kJ mol}^{-1}$ . The estimated effective accommodation coefficients of both

experiments were almost equal (0.06 and 0.07 respectively) showing the same uncertainty range of more than an order of magnitude. These results suggest that the COA in both experiments had similar volatility distributions considering both the measurement and experimental uncertainty. The main difference between the results was that during Experiment 1 a 10% of IVOCs appeared to be present in the particulate phase (Figure 4.3c). The average  $\log_{10}C^*$  (Table B.1) that were calculated suggested that the COA of Experiment 2 ( $\log_{10}C^*$  almost 0.05) was slightly less volatile by almost half an order of magnitude than that of Experiment 1 ( $\log_{10}C^*$  almost 0.1). This could be due to the different experimental conditions (each experiment is different) or could just reflect the uncertainty of our approach.

### **4.3.2 Sensitivity analysis**

#### **4.3.2.1 Sensitivity to accommodation coefficient**

During these tests the volatility distributions and effective vaporization enthalpies were estimated for both experiments by assuming fixed accommodation coefficient values. Table B.2 and Figure B.5 summarize the estimated volatility distributions during these tests. Assuming an accommodation coefficient half an order of magnitude lower than the estimated one for the base case (0.01 instead of 0.06 for Experiment 1 and 0.07 for Experiment 2), the IVOC fraction of the COA remained the same but the SVOCs increased by 15% (from 30% to 45%) and the LVOCs decreased by the same amount (from 60% to 45%) compared to the base case.

Assuming an  $a_m$  equal to 0.1 the LVOCs increased by almost 10% (from 60% to 70%) and the SVOCs decreased by the same percentage (from 30% to 20%), while the IVOCs remained once again the same (Figure B.5). For a further increase of  $a_m$  to unity the LVOCs increased by 15% (from 60% to 75%) and the SVOCs decreased by the same percentage (from 30% to 15%), while the IVOCs fraction remained the same (Figure B.5). The estimated effective vaporization enthalpies were almost equal to those estimated in the base case (around 100 and 85  $\text{kJ mol}^{-1}$  for Experiment 1 and 2 respectively) for all the investigated accommodation coefficients during this analysis (Table B.2).

Summarizing, varying the accommodation coefficient from 0.01 to 1 compared to the estimated 0.06-0.07 resulted in small changes (less than 5%) in the estimated enthalpy of

vaporization and the IVOC content of COA. The SVOCs and IVOCs changed by less than 15% in these tests.

#### **4.3.2.2 Sensitivity to vaporization enthalpy**

During these tests the volatility distributions and effective accommodation coefficients were estimated for both experiments assuming fixed values of the effective vaporization enthalpy. Values of 150 and 80 kJ mol<sup>-1</sup> were used in these tests for both experiments. These should be compared to the estimated values of 100 kJ mol<sup>-1</sup> for the first experiment and 85 kJ mol<sup>-1</sup> for the second.

For the high value of the vaporization enthalpy (150 kJ mol<sup>-1</sup>) the estimated average volatility was lower by approximately half an order of magnitude compared to that of the base case (Table B.2). The LVOCs increased by 5-10% and the SVOCs decreased by the same amount, while the IVOC fraction remained approximately the same. Figure B.6 shows the estimated volatility distributions and COA compositions of both experiments for all the cases of this analysis. The estimated accommodation coefficients were almost half an order of magnitude lower compared to the base case values (Table B.2).

Assuming a vaporization enthalpy of 80 kJ mol<sup>-1</sup> the corresponding volatilities for both experiments increased by approximately a factor of two. The LVOC fraction for this case decreased by 5-10% and a corresponding increase was estimated for the SVOCs. Once again, the IVOC fraction remained the same. The estimated accommodation coefficients were similar to the base case.

The above results suggest that changes in vaporization by 20-50 kJ mol<sup>-1</sup> result in changes in the volatility distribution by less than half an order of magnitude. Higher values of the enthalpy are balanced with lower volatilities and vice versa. The accommodation coefficient is more sensitive in this case to increasing vaporization enthalpy values than to lower ones.

#### **4.4 Benefits of combining TD and Isothermal dilution**

In order to evaluate the benefits of the combination of thermodenuder and isothermal dilution measurements the above results were compared to the results obtained by using only the thermodenuder data. The algorithm of Karnezi et al. (2014) was used also to estimate the volatility

distributions and vaporization enthalpy and accommodation using only the thermodenuder measurements. The corresponding results are shown in Figure 4.7 and Table B.1.

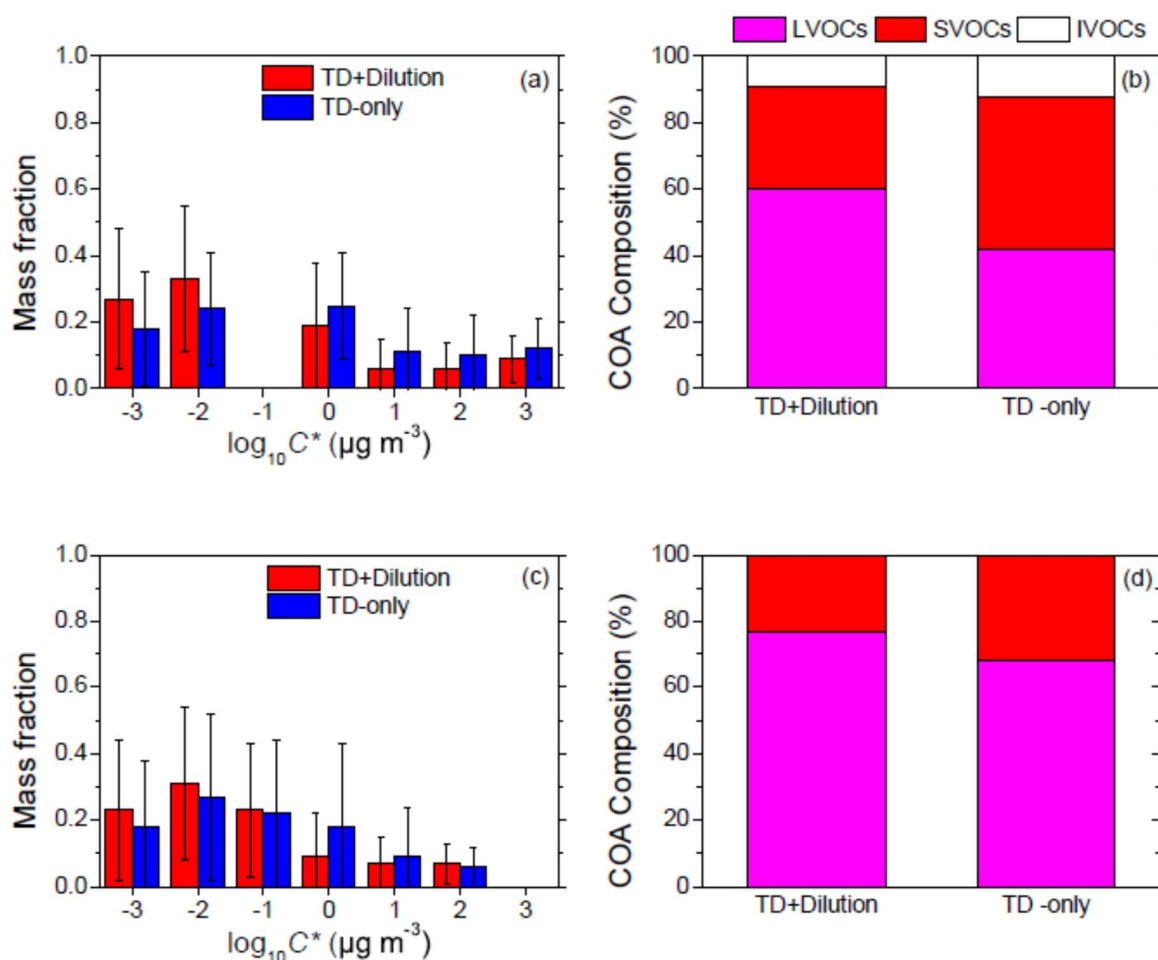


**Figure 4.7** (a) Estimated volatility distributions of the COA along with their uncertainties for Experiment 1 using the approach of Karnezi et al. (2014). Red bars represent the volatility distribution using the combination of thermodenuder and isothermal dilution measurements whereas blue bars represent the volatility distribution using only thermodenuder measurements (b) COA compositions for the two cases of (a). LVOCs are in magenta, SVOCs in red, and IVOCs in white. (c) Estimated volatility distributions of the COA for Experiment 2 using the approach of Karnezi et al. (2014). Red bars represent the volatility distribution using the combination of thermodenuder and isothermal dilution measurements whereas blue bars represent the volatility distribution using only thermodenuder measurements. (d) COA compositions for the two cases of (c). LVOCs are in magenta, SVOCs in red.

The combination of thermodenuder and dilution measurements resulted in a less volatile COA in both cases. In Experiment 1 the average volatility was reduced by almost half an order of

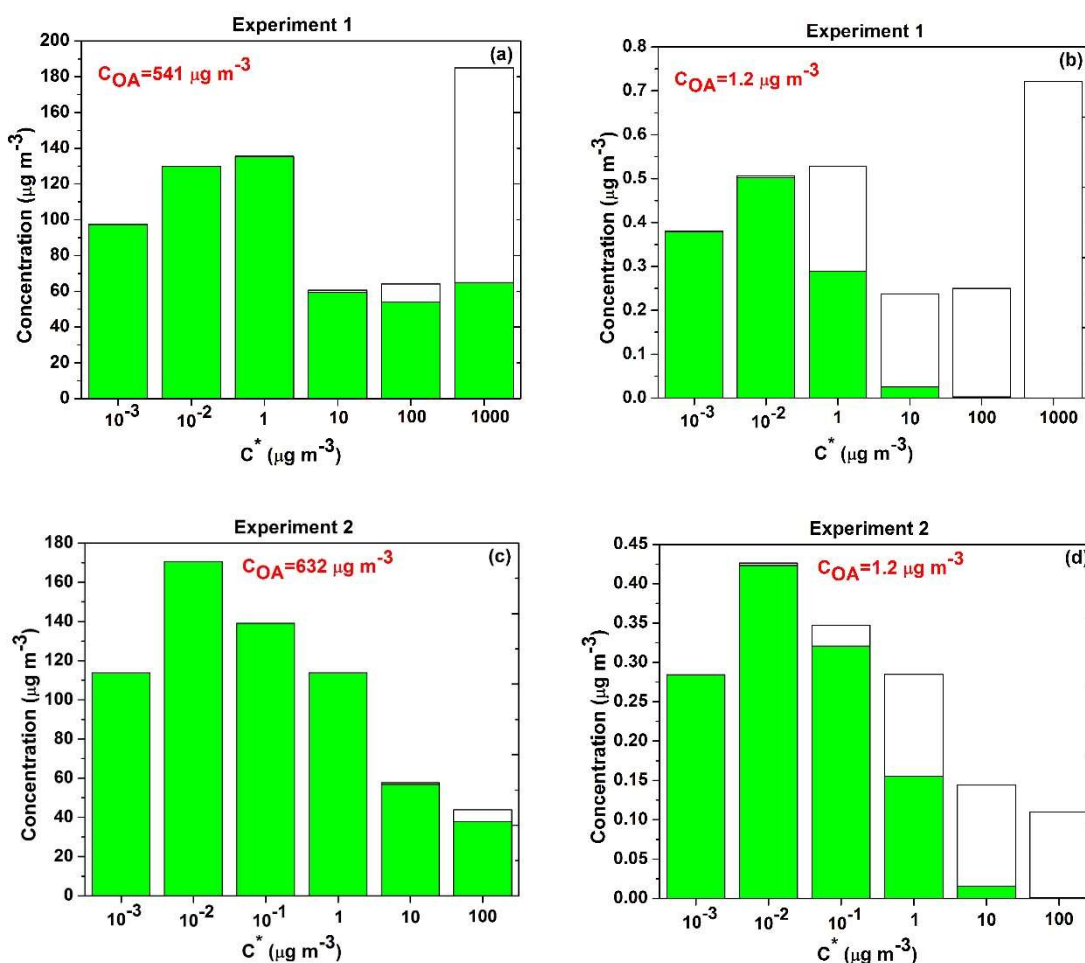
magnitude (0.44 to 0.1  $\mu\text{g m}^{-3}$ ). The same behavior was also found for Experiment 2 in which the average volatility was reduced from 0.08 to 0.047  $\mu\text{g m}^{-3}$ . The combined approach suggested that COA consisted of 60% LVOCs, 30% SVOCs, and 10% IVOCs while the TD-only approach suggested almost 40% LVOCs, 50% SVOCs, and 10% IVOCs for Experiment 1. The combined approach suggested for Experiment 2 that the COA consisted of 77% LVOCs and 23% SVOCs, while the TD-only approach suggested mass fraction contributions to the COA composition of 68% for LVOCs and 32% for SVOCs.

The combination of thermodenuder and isothermal dilution measurements led to a reduction of the uncertainty range for the more volatile OA components with effective saturation concentrations from 10 to 1000  $\mu\text{g m}^{-3}$ . Moreover, the uncertainty ranges of the estimated effective vaporization enthalpies were 10-15  $\text{kJ mol}^{-1}$  when the combined approach was used compared to the 15-20  $\text{kJ mol}^{-1}$  for the TD only approach. The corresponding uncertainties of the effective accommodation coefficients were ranging by an order of magnitude in both approaches showing a little less variability when using TD and dilution approach.

#### **4.5 Comparison of laboratory COA with the ambient COA factor**

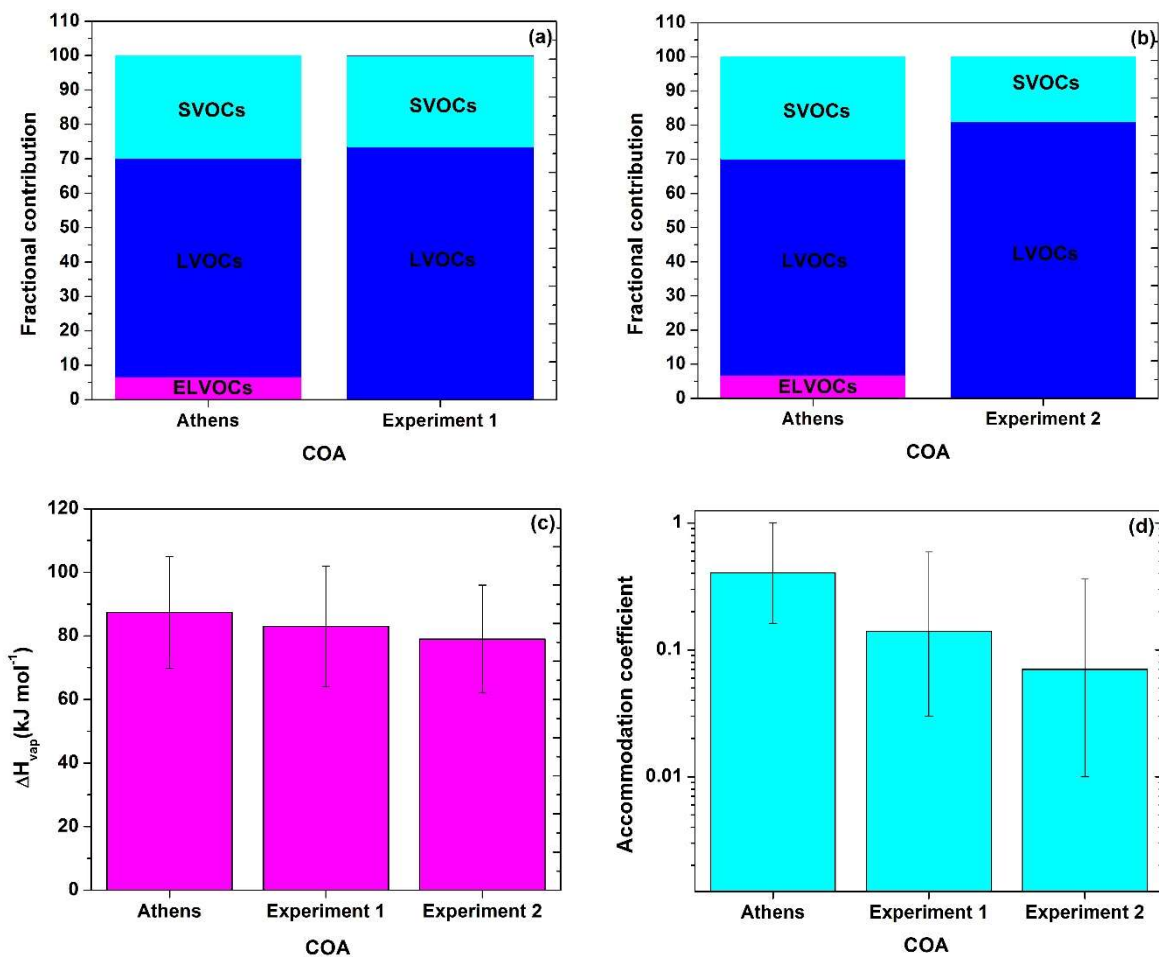
The laboratory COA from meat charbroiling and its properties can be compared to the ambient COA factor determined in the Athens campaign and discussed in Chapter 3 (Louvaris et al., 2017). As described in Section 3.5 of Chapter 3, there is an interplay between the initial concentration of the OA and the partitioning in the gas/aerosol phase (Donahue et al., 2006). For a fair comparison between the volatility distributions and furthermore the fractional contribution of the OA composition, we determined the volatility distributions of the 2 experiments to the average ambient COA concentration in Athens, a value equal to 1.2  $\mu\text{g m}^{-3}$ .

Figure 4.8 shows the changes of the volatility distributions for both experiments of meat charbroiling moving from the concentrations of 541  $\mu\text{g m}^{-3}$  and 632  $\mu\text{g m}^{-3}$  in the chamber experiments to an initial concentration of 1.2  $\mu\text{g m}^{-3}$  corresponding to the ambient concentration levels. At the lower concentration levels, the higher volatility components evaporate completely or partially and this results in a different volatility distribution, with no more IVOCs and fewer SVOCs in the particulate phase.



**Figure 4.8** Partitioning of COA components, with total loadings (in  $\mu\text{g m}^{-3}$ ) shown with full bars and the condensed-phase portion with filled (green) bars. For experiment 1: (a) for initial concentration of OA,  $C_{\text{OA}}=541 \mu\text{g m}^{-3}$  (laboratory level), (b) for  $C_{\text{OA}}=1.2 \mu\text{g m}^{-3}$  (after repartitioning) and for experiment 2: (c) for initial concentration of OA,  $C_{\text{OA}}=642 \mu\text{g m}^{-3}$  (laboratory level), (d) for  $C_{\text{OA}}=1.2 \mu\text{g m}^{-3}$  (after repartitioning).

The COA composition in the laboratory experiments and in the Athens campaign are compared in Figure 4.9 at the same concentration level. The compositions are quite similar, with the main difference being the absence of ELVOCs in the laboratory cooking OA, while these components represented 7% of the ambient COA during the winter in Athens. LVOCs dominated during both the Athens winter campaign and the laboratory experiments. The effective  $\Delta H_{\text{vap}}$  were similar and within the uncertainty levels. For the accommodation coefficient, the uncertainty is high in all cases, with some suggestion of lower resistances in the ambient than in the laboratory COA.



**Figure 4.9** Comparison of the COA composition (a) between the Athens winter COA factor (Louvaris et al., 2017) and Experiment 1. and (b) between the Athens winter COA factor and Experiment 2. The comparison of estimated (c) vaporization enthalpy and (d) accommodation coefficient is also shown.

These results are consistent with the relatively small differences in AMS mass spectra of the ambient COA factor and the laboratory COA (Figure B.7). The corresponding  $\theta$  angles were 13-15°. Some difference is expected due to the different concentration levels discussed above.

## 4.6 Conclusions

A new experimental method was developed for the determination of the organic aerosol (OA) volatility distribution combining thermodenuder and isothermal dilution measurements along with the approach proposed by Karnezi et al. (2014). The combination of TD and isothermal dilution

for the estimation of the volatility distribution was tested using cooking OA from meat grilling. Size dependent losses were taken into account for the correction of both thermodenuder and dilution measurements.

All the COA evaporated in the TD at 225°C while 80% remained after dilution by a factor of 10 at ambient temperature. The COA average volatility was between 0.05 and 0.1  $\mu\text{g m}^{-3}$  and it consisted of 60-75% LVOCs, 25-30% SVOCs, and a small fraction (10%) of IVOCs at concentrations close to 500  $\mu\text{g m}^{-3}$ . The estimated effective vaporization enthalpy was  $100 \pm 15 \text{ kJ mol}^{-1}$ , and the effective accommodation coefficient was around 0.05.

Changes by half or more than an order of magnitude in accommodation coefficient values resulted in half an order of magnitude change of the average volatility while the estimated vaporization enthalpy was almost the same. Similar results were found for a change of the effective vaporization enthalpy by 20-50  $\text{kJ mol}^{-1}$ . The LVOC and SVOC fractions changed by 5-15% while the IVOCs remained practically the same.

The use of only TD measurements resulted in an overestimation of the SVOC fraction of COA leading to a shifting of volatility towards higher values. Use of the isothermal dilution resulted in decrease of the uncertainty of the higher volatility components and of the estimated effective enthalpy of vaporization.

The apparent differences in volatility distributions of the ambient COA factor determined in Athens and the laboratory COA were due to the different concentrations during the two measurements. After calculation of the expected volatility distribution of the COA at ambient levels the distributions were consistent with each other.

#### 4.7 References

- An, W. J., Pathak, R. K., Lee, B. H. and Pandis, S. N.: Aerosol volatility measurement using an improved thermodenuder: Application to secondary organic aerosol, *J. Aerosol Sci.*, 38, 305–314, 2007.
- Barnet, P., Dommen, J., DeCarlo, P. F., Tritscher, T., Praplan, A. P., Platt, S. M., Prévôt, A. S. H., Donahue, N. M. and Baltensperger, U.: OH clock determination by proton transfer reaction mass spectrometry at an environmental chamber, *Atmos. Meas. Tech.*, 5, 647–656, 2012.

- Burtscher, H., Baltensperger, U., Bukowiecki, N., Cohn, P., Hüglin, C., Mohr, M., Matter, U., Nyeki, S., Schmatloch, V., Streit, N. and Weingartner, E.: Separation of volatile and non-volatile aerosol fractions by thermodesorption: Instrumental development and applications, *J. Aerosol Sci.*, 32, 427–442, 2001.
- Caiazzo, F., Ashok, A., Waitz, I. A., Yim, S. H. L. and Barrett, S. R. H.: Air pollution and early deaths in the United States. Part I: Quantifying the impact of major sectors in 2005, *Atmos. Environ.*, 79, 198–208, 2013.
- Canagaratna, M. R., Jayne, J. T., Jimenez, J. L., Allan, J. D., Alfarra, M. R., Zhang, Q., Onasch, T. B., Drewnick, F., Coe, H., Middlebrook, A. M., Delia, A. E., Williams, L. R., Trimborn, A. M., Northway, M. J., DeCarlo, P. F., Kolb, C. E., Davidovits, D. R.: Chemical and microphysical characterization of ambient aerosols with the Aerodyne Aerosol mass Spectrometer, *Mass Spectrom. Rev.*, 26, 185–222, 2007.
- Cappa, C. D.: A model of aerosol evaporation kinetics in a thermodenuder, *Atmos. Meas. Tech.*, 3, 579–592, 2010.
- Cappa, C. D. and Jimenez, J. L.: Quantitative estimates of the volatility of ambient organic aerosol, *Atmos. Chem. Phys.*, 10, 5409–5424, 2010.
- Cappa, C. D. and Wilson, K. R.: Evolution of organic aerosol mass spectra upon heating: Implications for OA phase and partitioning behavior, *Atmos. Chem. Phys.*, 11, 1895–1911, 2011.
- Decarlo, P. F., Kimmel, J. R., Trimborn, A., Northway, M. J., Jayne, J. T., Aiken, A. C., Gonin, M., Fuhrer, K., Horvath, T., Docherty, K. S., Worsnop, D. R. and Jimenez, J. L.: Aerosol Mass Spectrometer, *Anal. Chem.*, 78, 8281–8289, 2006.
- Donahue, N. M., Robinson, A. L., Stanier, C. O. and Pandis, S. N.: Coupled partitioning, dilution, and chemical aging of semivolatile organics, *Environ. Sci. Technol.*, 40, 2635–2643, 2006.
- Donahue, N. M., Kroll, J. H., Pandis, S. N. and Robinson, A. L.: A two-dimensional volatility basis set-Part 2: Diagnostics of organic-aerosol evolution, *Atmos. Chem. Phys.*, 12, 615–634, 2012.
- IPCC (Intergovernmental Panel on Climate Change): Climate Change 2014: Mitigation of Climate Change. Contribution of Working Group III to the Fifth Assessment Report of the Intergovernmental Panel on Climate Change, Cambridge University Press, Cambridge, UK and New York, 2014.

- Faulhaber, A. E., Thomas, B. M., Jimenez, J. L., Jayne, J. T., Worsnop, D. R. and Ziemann, P. J.: Characterization of a thermodenuder-particle beam mass spectrometer system for the study of organic aerosol volatility and composition, *Atmos. Meas. Tech.*, 2, 15–31, 2009.
- Grieshop, A. P., Miracolo, M. A., Donahue, N. M. and Robinson, A. L.: Constraining the volatility distribution and gas-particle partitioning of combustion aerosols using isothermal dilution and thermodenuder measurements, *Environ. Sci. Technol.*, 43, 4750–4756, 2009.
- Huffman, J. A., Docherty, K. S., Mohr, C., Cubison, M. J., Ulbrich, I. M., Ziemann, P. J., Onasch, T. B., and Jimenez, J. L.: Chemically-resolved volatility measurements of organic aerosol from different source, *Environ. Sci. Technol.*, 43, 5351–5357, 2009.
- Kalberer, M., Paulsen, D., Sax, M., Steinbacher, M., Dommen, J., Prévôt, A. S. H., Fisseha, R., Weingartner, E., Frankevich, V., Zenobi, R. and Baltensperger, U.: Identification of Polymers as Major Components of atmospheric organic aerosols, *Science*, 303, 1659–1662, 2004.
- Kaltsonoudis, C., Kostenidou, E., Florou, K., Psychoudaki, M., and Pandis, S. N.: Temporal variability and sources of VOCs in urban areas of the eastern Mediterranean, *Atmos. Chem. Phys.*, 16, 14825–14842, 2016a.
- Kaltsonoudis, C., Kostenidou, E., Louvaris, E., Psychoudaki, M., Tsiligiannis, E., Florou, K., Liangou, A., and Pandis, S. N.: Characterization of fresh and aged organic aerosol emissions from meat charbroiling, *Atmos. Chem. Phys. Discuss.*, in review, 2016b.
- Karnezi, E., Riipinen, I. and Pandis, S. N.: Measuring the atmospheric organic aerosol volatility distribution: A theoretical analysis, *Atmos. Meas. Tech.*, 7, 2953–2965, 2014.
- Kolesar, K. R., Chen, C., Johnson, D. and Cappa, C. D.: The influences of mass loading and rapid dilution of secondary organic aerosol on particle volatility, *Atmos. Chem. Phys.*, 15, 9327–9343, 2015.
- Kostenidou, E., Lee, B. H., Engelhart, G. J., Pierce, J. R. and Pandis, S. N.: Mass spectra deconvolution of low, medium, and high volatility biogenic secondary organic aerosol, *Environ. Sci. Technol.*, 43, 4884–4889, 2009.
- Lee, B. H., Kostenidou, E., Hildebrandt, L., Riipinen, I., Engelhart, G. J., Mohr, C., Decarlo, P. F., Mihalopoulos, N., Prevot, A. S. H., Baltensperger, U. and Pandis, S. N.: Measurement of the ambient organic aerosol volatility distribution: Application during the Finokalia Aerosol Measurement Experiment (FAME-2008), *Atmos. Chem. Phys.*, 10, 12149–12160, 2010.

- Lee, B. H., Pierce, J. R., Engelhart, G. J. and Pandis, S. N.: Volatility of secondary organic aerosol from the ozonolysis of monoterpenes, *Atmos. Environ.*, 45, 2443–2452, 2011.
- Louvaris, E. E., Florou, K., Karnezi, E., Papanastasiou, D. K., Gkatzelis, G. I. and Pandis, S. N.: Volatility of source apportioned wintertime organic aerosol in the city of Athens, *Atmos. Env.* (under review), 2017.
- Pathak, R. K., Presto, A. A., Lane, T. E., Stanier, C. O., Donahue, N. M. and Pandis, S. N.: Ozonolysis of  $\alpha$ -pinene: parameterization of secondary organic aerosol mass fraction, *Atmos. Chem. Phys.*, 7, 3811–3821, 2007.
- Pope, C. A., Ezzati, M., Dockery, D. W., Pope III, C. A., Ezzati, M. and Dockery, D. W.: Fine-particulate air pollution and life expectancy in the United States, *N. Engl. J. Med.*, 360, 376–386, 2009.
- Riipinen, I., Pierce, J. R., Donahue, N. M. and Pandis, S. N.: Equilibration time scales of organic aerosol inside thermodenuders: Evaporation kinetics versus thermodynamics, *Atmos. Environ.*, 44, 597–607, 2010.
- Saleh, R., Walker, J. and Khlystov, A.: Determination of saturation pressure and enthalpy of vaporization of semi-volatile aerosols: The integrated volume method, *J. Aerosol Sci.*, 39, 876–887, 2008.
- Saleh, R., Khlystov, A. and Shihadeh, A.: Determination of evaporation coefficients of ambient and laboratory-generated semivolatile organic aerosols from phase equilibration kinetics in a thermodenuder, *Aerosol Sci. Technol.*, 46, 22–30, 2012.
- Saleh, R., Donahue, N. M. and Robinson, A. L.: Time scales for gas-particle partitioning equilibration of secondary organic aerosol formed from alpha-pinene ozonolysis, *Environ. Sci. Technol.*, 47, 5588–5594, 2013.
- Wehner, B., Philippin, S. and Wiedensohler, A.: Design and calibration of a thermodenuder with an improved heating unit to measure the size-dependent volatile fraction of aerosol particles, *J. Aerosol Sci.*, 33, 1087–1093, 2002.
- Wehner, B., Philippin, S., Wiedensohler, A., Scheer, V. and Vogt, R.: Variability of non-volatile fractions of atmospheric aerosol particles with traffic influence, *Atmos. Environ.*, 38, 6081–6090, 2004.
- Zhang, Q., Jimenez, J. L., Canagaratna, M. R., Allan, J. D., Coe, H., Ulbrich, I., Alfarra, M. R., Takami, A., Middlebrook, A. M., Sun, Y. L., Dzepina, K., Dunlea, E., Docherty, K.,

DeCarlo, P. F., Salcedo, D., Onasch, T., Jayne, J. T., Miyoshi, T., Shimono, A., Hatakeyama, S., Takegawa, N., Kondo, Y., Schneider, J., Drewnick, F., Borrmann, S., Weimer, S., Demerjian, K., Williams, P., Bower, K., Bahreini, R., Cottrell, L., Griffin, R. J., Rautiainen, J., Sun, J. Y., Zhang, Y. M. and Worsnop, D. R.: Ubiquity and dominance of oxygenated species in organic aerosols in anthropogenically-influenced Northern Hemisphere midlatitudes, *Geophys. Res. Lett.*, 34, 2007.

# **Chapter 5**

**Simulation of atmospheric organic aerosol using its volatility-oxygen content distribution during the PEGASOS 2012 campaign in Po Valley, Italy**

## 5.1 Introduction

Atmospheric aerosol plays an important role in the Earth's energy balance by absorbing and scattering solar radiation (direct effect) and influencing the properties and lifetime of clouds (indirect effects) (IPCC, 2014). At the same time, these particles have significant negative effects on human health, including premature death, increases in respiratory illnesses and cardiopulmonary mortality (Pope et al., 2009; Caiazzo et al., 2013).

Aerosols contain a wide variety of inorganic and organic compounds, with organics representing about 50% of the fine ( $< 1 \mu\text{m}$ ) aerosol mass (Zhang et al., 2007). OA originates from many different natural and anthropogenic sources and processes. It can be emitted directly from fossil fuel and biomass combustion (so called primary organic aerosol, POA) or can be formed by the atmospheric oxidation of organic vapors (secondary organic aerosol, SOA). The oxidation pathways of organic compounds are complex and the corresponding reactions lead to hundreds or even thousands of mostly unknown oxygenated products. As a result, our understanding of OA formation mechanisms and its chemical and physical properties remains incomplete.

The use of lumped species is a computationally efficient approach for the representation of OA in atmospheric chemical transport models (Pandis et al., 1992). The volatility basis set (VBS) framework (Donahue et al., 2006) lumps compounds into surrogates along an axis of volatility. This approach typically employs species with effective saturation concentrations at 298 K separated by one order of magnitude, with values ranging from, say, 0.01 to  $10^6 \mu\text{g m}^{-3}$ . By quantifying the volatility distributions of primary and secondary OA, a physically reasonable, yet suitable for large-scale chemical transport models (CTMs), description of semi-volatile organics can be obtained (Lane et al., 2008).

The VBS framework was extended by Donahue et al. (2011; 2012) adding another dimension, the oxygen content (expressed as the O:C ratio), for the description of the OA chemical aging reactions. In the first application of this framework in a CTM, Murphy et al. (2011) used 12 logarithmically spaced volatility bins (effective saturation concentration  $C^*$  varying from  $10^{-5}$  to  $10^6 \mu\text{g m}^{-3}$  at 298 K) and 13 bins of O:C (from 0 to 1.2 with a step of 0.1). In this way 156 surrogate species were included in the model for each OA type. Five organic aerosol types were simulated separately: anthropogenic secondary organic aerosol (aSOA-v) produced during the oxidation of anthropogenic VOCs, biogenic secondary organic aerosol (bSOA), fresh primary organic aerosol

(POA), secondary organic aerosol from the oxidation of semivolatile OA (SOA-sv) and SOA from the oxidation of intermediate volatility compounds (SOA-iv).

Murphy et al. (2011; 2012) used a one-dimensional Lagrangian CTM (PMCAMx-Trj), as the host model for the simulations. PMCAMx-Trj simulates the chemical evolution of a column of air as it travels towards a user-selected receptor site. Three alternative parameterizations of the OA formation and chemical aging were evaluated using measurements of O:C and OA in three European sites (Murphy et al., 2011; 2012). The simplest approach parameterizing the chemical aging of anthropogenic compounds assuming a net reduction of volatility by one bin during every aging reaction step accompanied by an increase of one or two oxygen atoms with an equal probability was the most successful. A more complex formulation of the chemical aging assuming that functionalization is the only process taking place overpredicted the OA concentration and underpredicted the O:C ratio in most cases. Adding fragmentation reactions together with the functionalization gave promising results, but it was clear that the various parameters of the scheme were not well constrained leading to large uncertainties in the simulation results especially during summertime. Murphy et al. (2012) concluded that the 2D-VBS scheme that was used needs additional testing before it is ready for application in three-dimensional CTMs.

In Murphy and Pandis (2009; 2010) and Murphy et al. (2012) formation of significant bSOA during second and later generation aging reactions led to overestimation of OA concentration at both urban and rural sites. However, the first generation products of the oxidation of biogenic VOCs do continue to react in the atmosphere (Ng et al., 2006; Tritscher et al., 2011; Zhao et al., 2015; Szidat et al., 2006; Gilardoni et al., 2011; Yttri et al., 2011). The net effect on ambient bSOA levels of these chemical aging reactions remains uncertain.

Fragmentation of organic compounds during chemical aging is an important reaction pathway (Chacon-Madrid and Donahue, 2011; Murphy et al., 2011; Hermansson et al., 2014). During fragmentation reactions carbon bonds break, resulting in smaller compounds which are more volatile than their precursors. A fragmentation probability depending on the O:C ratio has been used in the 2D-VBS framework (Donahue et al. 2011; 2012). A fragmentation probability ranging from 0-0.4 has been used in the statistical oxidation model (SOM) that uses the carbon (C) and oxygen (O) atoms per compound as the independent variables (Cappa and Wilson, 2012). While the fragmentation pathways are clearly important for the OA levels their parameterizations in existing models remain quite uncertain (Murphy et al., 2012).

The effect of temperature on the partitioning of OA components between the gas and particulate phases represents another source of uncertainty. Sheehan and Bowman (2001), concluded that a decrease in temperature can result in an increase of SOA by as much as 150% depending on the assumed vaporization enthalpy. This effect can theoretically lead to significant OA vertical gradients. Murphy et al. (2011) during the 2D-VBS application in Finokalia, Greece in FAME-08 reported low sensitivity of the OA concentration and O:C ratio measurements to the assumed vaporization enthalpy, with higher values leading to lower O:C ratios.

In this study, we evaluate different chemical aging mechanisms in the 2D-VBS approach focusing on the Po Valley in Italy. Extensive measurements were performed both at the ground and aloft from June 6 until July 8, 2012. Po Valley has major air quality problems due to both industrial and agricultural sources. A number of alternative chemical aging mechanisms are evaluated comparing the 2D-VBS predictions against the PEGASOS measurements. The role of bSOA chemical aging is explored. Finally, the sensitivity of the model to the assumed effective vaporization enthalpy is quantified in an effort to constrain this uncertain variable using the measurements aloft.

## **5.2 Lagrangian CTM Description**

A one-dimensional Lagrangian chemical transport model (PMCAMx-Trj) (Murphy et al., 2011; 2012) simulating the air parcels that arrive at the desired receptor location is used as the host for the 2D-VBS module. The model solves the general dynamic equation taking into account all relevant atmospheric processes: atmospheric transport, gas and aqueous phase chemistry, dry and wet deposition of gases and aerosols and vertical turbulent dispersion together with area and point emissions. Ten computational cells are used with heights varying from 60 m near the ground to almost 3 km. The SAPRC-99 (Carter, 2000) chemical mechanism is used for the simulation of gas-phase chemistry. The meteorological parameters (horizontal winds, temperature, pressure, vertical dispersion coefficients, water vapor, clouds, rainfall and land use) used as inputs in the model are provided by the Weather Research and Forecasting (WRF) model. The WRF simulation was periodically re-initialized (every 3 days) to ensure the accuracy of the inputs to the CTM. Area and point emissions were also provided by the inputs of the regular PMCAMx simulation for the European domain. Anthropogenic and biogenic emissions are provided as hourly gridded fields. The GEMS dataset (Visschedijk et al., 2007) is used for the emissions of anthropogenic gases.

Anthropogenic emissions of organic and elemental carbon are based on the Pan-European Carbonaceous Aerosol Inventory developed during EUCAARI (Kulmala et al., 2009). Biogenic gridded emissions are produced from the combination of three different models. The Model of Emissions of Gases and Aerosols from Nature (MEGAN) provides the emissions from ecosystems (Guenther et al., 2006) and the O’Dowd et al. (2008) model provides the marine aerosol emissions. Finally, wildfire emissions are also included (Sofiev et al., 2008a, b). Details of the emission inventory used for Europe can be found in Fountoukis et al. (2011). In order to implement these emissions in our 2D-VBS model we used the same volatility distribution of the emissions as in the original work (Fountoukis et al., 2011) and used the Murphy et al. (2012) methodology for mapping these to the 2D-VBS. Vertically resolved initial conditions and the top boundary conditions for PMCAMx-Trj were obtained from the corresponding output of the PMCAMx simulation for the same period.

### **5.3 Simulated periods**

Six air parcels arriving at 3:00, 7:00, 11:00, 15:00, 19:00 and 23:00 local time (UTC+1) in the ground site of San Pietro Capofiume were simulated for a total of 7 days (15, 26, 27, and 28 of June and 4, 5 and 8 of July 2012). The air masses in the simulated trajectories originated all from the Atlantic Ocean. We avoided days during which air masses originated from Africa since emission inventories for Africa are quite uncertain. We chose days for which the trajectories at the different altitudes originated all from the same region. The Hybrid Single Particle Lagrangian Integrated Trajectory HYSPLIT model (Draxler et al., 2009) was used to calculate 72 h back trajectories arriving at the receptor site. For consistency, we used the same WRF meteorological data as input to HYSPLIT to calculate the back trajectories. Following Murphy et al. (2011) we used the ensemble average of 20 trajectories with varied heights from 60 m up to 3 km.

The twenty 72 h HYSPLIT back trajectories arriving at San Pietro Capofiume at 3:00 LT on July 8, 2012 are shown in Figure 5.1 as an example. They all originated from the eastern Atlantic Ocean, passed a day over the ocean and then travelled over Portugal and Spain for another day. The air masses continued over the Mediterranean Sea, Western Italy, and a few hours later arrived in the receptor site of San Pietro Capofiume. The HYSPLIT clustering analysis utility was used to estimate the average trajectory that was used in the simulations (Figure 5.1).

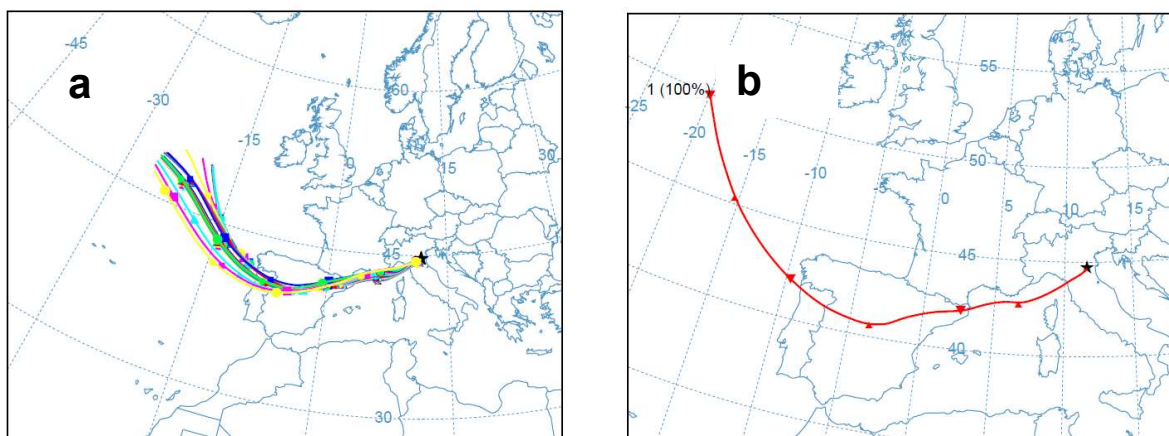


**Figure 5.1** (a) The ensemble of 20 trajectories calculated by HYSPLIT for air parcels arriving at the San Pietro Capofiume site on 8 July 2012 at 3:00 LT and (b) the ensemble average trajectory calculated by the HYSPLIT clustering utility.

Zeppelin flights over Po Valley took place on 20, 21, 22 and 24 of June of 2012 and 1, 3 and 4 of July 2012. The HYSPLIT model was once again used to calculate trajectories arriving at the receptor site around Po Valley. All the flights took place between 4:00 LT until 13:00 LT. The flight path of the Zeppelin for June 4, 2012 is shown in Figure C.1 in the Appendix as an example. The flight took place between 5:00 LT and 10:00 LT and the measurements took place in the nighttime boundary layer, the residual layer but also in the mixed layer later in the day.

## 5.4 Chemical Aging Schemes

In our simulations, we considered three different functionalization schemes, two bSOA chemical aging parameterizations and explored the use of fragmentation mechanisms. These are summarized below.

### 5.4.1 Functionalization schemes

#### (a) Simple scheme (1-bin)

The first functionalization scheme used in our simulations was the simple scheme of Murphy et al. (2012) that had the best performance in the cases simulated in that study. In this scheme, there is one volatility bin reduction for every reaction with a simultaneous increase in oxygen atoms, with a probability of 50% for an increase of 1 oxygen atom and 50% probability for an increase of

2 oxygen atoms. The calculation of the O:C change from the number of added oxygen atoms is based on Donahue et al. (2011). The chemical aging reaction constants that are used for the reactions with OH are the same as in the base case of Murphy et al. (2011) with values equal to  $1 \times 10^{-11} \text{ cm}^3 \text{ molec}^{-1} \text{ s}^{-1}$  for anthropogenic SOA from VOCs (aSOA-v) and biogenic SOA (bSOA) and  $4 \times 10^{-11} \text{ cm}^3 \text{ molec}^{-1} \text{ s}^{-1}$  for SOA from semivolatile OA (SOA-sv) and intermediate volatility compounds (SOA-iv).

### **(b) Two-bin shift simple scheme (2-bin)**

In the second functionalization scheme a two-volatility bin reduction is assumed for every reaction with a simultaneous increase in oxygen atoms. A 50% probability for the increase of 1 oxygen atom and 50% probability for the increase of 2 oxygen atoms are used. The calculation of the O:C shift in bins from the number of added oxygen atoms is based again on Donahue et al. (2011). This functionalization scheme assumes a more rapid reduction in volatility for every reaction and uses the same reaction constants for the reactions with OH as in the base case of Murphy et al. (2011).

### **(c) Detailed scheme (DET)**

The third aging scheme is the detailed functionalization scheme introduced by Donahue et al. (2011). This is a more rigorous scheme compared to the previous two conservative aging parameterizations. Following Murphy et al. (2012), there is a 30% probability of adding one O atom, 50% probability of adding two O atoms, and 20% probability of adding three O atoms. Each addition of O atoms results in a different distribution of volatility reductions, with an average reduction of -1.75 in  $\log_{10}C^*$  per oxygen group added. These additions of O atoms are translated to changes of O:C ratios following Murphy et al. (2012). The functionalization kernel is applied to all species in the 2D-VBS upon OH reaction. Again the chemical aging reaction constants that are used for the reaction with OH are the same as the two functionalization schemes described above.

### 5.4.2 bSOA aging parameterizations

Two different parameterizations of bSOA aging are explored. In the first scheme the chemical aging of biogenic SOA is assumed to result in a negligible net change in volatility but an increase in O:C (Murphy et al., 2011). This scheme is consistent with the lack of bSOA aging that has been used in PMCAMx (Murphy and Pandis, 2009; 2010) and is called in the rest of the paper no-bSOA aging even if the O:C of bSOA does change.

In the second scheme, bSOA components are assumed to age similarly to aSOA, with their processing leading not only to changes in O:C ratio, but also to a net reduction of their volatility. We explore all three functionalization schemes, the simple scheme (1-bin), the faster functionalization (2-bin) and the detailed functionalization scheme (DET) together with the two bSOA aging parameterizations.

### 5.4.3 Fragmentation parameterizations

As in Murphy et al. (2012) the bond cleavage is assumed to happen randomly and to be uniformly distributed throughout the carbon backbone. For these fragmented compounds the functionalization kernel is applied and this will lead to increases in volatility. The fragmentation probability in our simulations is allowed to range from zero (for no fragmentation) to unity.

## 5.5 Combination of parameterizations

In our simulations, we used all combinations of the three functionalization schemes (1-bin, 2-bin or DET), the two bSOA aging schemes and simulated fragmentation assuming fragmentation probability  $b$  ranging from zero to 1. In Table 5.1 we summarize the parameterizations that were finally chosen for the simulations. For each of the six combinations of functionalization and bSOA aging we assumed zero fragmentation probability (6 cases) plus we determined the fragmentation probability  $b$  that resulted in the minimum error for the average OA concentration. The determination of the “optimum” fragmentation probability for each case is shown in Figure C.4. For the 1-bin functionalization scheme and considering no bSOA production during aging the OA was underpredicted for fragmentation probabilities even low as 5% so in this case the optimum  $b$  was equal to zero and this became the same as the 1-bin simple scheme of Murphy et al. (2012).

**Table 5.1** Characteristics of the different parameterizations used in our simulations.

Parameterization Name	Functionalization scheme	bSOA increase during aging	Fragmentation probability	Comments
1-bin	1-bin	No	b=0	
1-bin/bSOA	1-bin	Yes	b=0	
1-bin	1-bin	No	b=0-1	Optimum for b=0, same as 1-bin case
1-bin/bSOA/b=0.15	1-bin	Yes	b=0-1	Optimum for b=0.15
2-bin	2-bin	No	b=0	
2-bin/bSOA	2-bin	Yes	b=0	
2-bin/b=0.1	2-bin	No	b=0-1	Optimum for b=0.1
2-bin/bSOA/b=0.4	2-bin	Yes	b=0-1	Optimum for b=0.4
DET	DET	No	b=0	
DET/bSOA	DET	Yes	b=0	
DET/b=0.3	DET	No	b=0-1	Optimum for b=0.3
DET/bSOA/b=0.7	DET	Yes	b=0-1	Optimum for b=0.7

## 5.6 Evaluation of parameterizations

The prediction skill of our simulations is quantified in terms of the fractional error, the fractional bias, the absolute error, the absolute bias and the root mean square error. These are calculated using:

$$\text{Fractional Error} = \frac{2}{n} \sum_{i=1}^n \frac{|P_i - M_i|}{(P_i + M_i)}$$

$$\text{Fractional Bias} = \frac{2}{n} \sum_{i=1}^n \frac{(P_i - M_i)}{(P_i + M_i)}$$

$$\text{Absolute Error} = \frac{1}{n} \sum_{i=1}^n |P_i - M_i|$$

$$\text{Absolute Bias} = \frac{1}{n} \sum_{i=1}^n (P_i - M_i)$$

$$\text{Root Mean Square Error} = \sqrt{\frac{1}{n} \sum_{i=1}^n (P_i - M_i)^2}$$

where  $P_i$  represents the model prediction value,  $M_i$  is the corresponding measured value and  $n$  is the total number of data points.

## 5.7 Results

### 5.7.1 Simple functionalization (1-bin case)

The first set of simulations used the simple functionalization scheme (1-bin), assuming negligible addition/production bSOA during aging (no bSOA aging) and neglected fragmentation assuming that the employed functionalization scheme represents the net effect of these pathways. This case is the same as the base case of Murphy et al. (2012). In this scheme, there is a modest volatility reduction as the organic vapors react with OH. The prediction skill metrics of the model 4-hour average O:C and OA concentration against the averaged ground measurements for the seven selected days during PEGASOS 2012 campaign are summarized in Tables 5.2 and 5.3 respectively.

**Table 5.2** Performance metrics of different parameterizations during the PEGASOS campaign for ground O:C measurements. The measured average O:C was 0.58.

<b>2D-VBS Parameterization</b>	<b>Predicted Average</b>	<b>Fractional Error</b>	<b>Fractional Bias</b>	<b>Absolute Error</b>	<b>Absolute Bias</b>	<b>Root Mean Square Error</b>
1-bin	0.64	0.1	0.09	0.06	0.06	0.08
1-bin/bSOA	0.55	0.07	-0.06	0.04	-0.03	0.05
1-bin/bSOA/b=0.15	0.56	0.07	-0.04	0.04	-0.02	0.05
2-bin	0.63	0.09	0.08	0.05	0.05	0.06
2-bin/bSOA	0.53	0.10	-0.10	0.05	-0.05	0.06
2-bin/b=0.1	0.65	0.12	0.11	0.07	0.07	0.08
2-bin/bSOA/b=0.4	0.58	0.05	0.0	0.03	0.00	0.04
DET	0.41	0.34	-0.34	0.17	-0.17	0.17
DET/bSOA	0.35	0.49	-0.49	0.23	-0.23	0.23
DET/b=0.3	0.57	0.05	-0.03	0.03	-0.01	0.04
DET/bSOA/b=0.7	0.62	0.08	0.06	0.05	0.04	0.05

**Table 5.3** Performance metrics of different parameterizations during the PEGASOS campaign for ground OA mass measurements. The measured average organic aerosol concentration was  $2.8 \mu\text{g m}^{-3}$ .

<b>2D-VBS Parameterization</b>	<b>Predicted Average (<math>\mu\text{g m}^{-3}</math>)</b>	<b>Fractional Error</b>	<b>Fractional Bias</b>	<b>Absolute Error (<math>\mu\text{g m}^{-3}</math>)</b>	<b>Absolute Bias (<math>\mu\text{g m}^{-3}</math>)</b>	<b>Root Mean Square Error (<math>\mu\text{g m}^{-3}</math>)</b>
1-bin	2.6	0.29	-0.12	0.78	-0.25	0.89
1-bin/bSOA	3.8	0.3	0.26	1.09	0.97	1.50
1-bin/bSOA/b=0.15	2.9	0.27	-0.02	0.79	0.05	0.96
2-bin	3.4	0.23	0.16	0.76	0.56	1.06
2-bin/bSOA	5	0.54	0.54	2.21	2.21	2.53
2-bin/b=0.1	2.9	0.21	0.01	0.62	0.07	0.85
2-bin/bSOA/b=0.4	3.1	0.22	0.07	0.71	0.3	0.96
DET	3.2	0.21	0.11	0.67	0.4	0.93
DET/bSOA	5.4	0.6	0.6	2.53	2.53	2.80
DET/b=0.3	2.9	0.22	0.00	0.66	0.1	0.84
DET/bSOA/b=0.7	2.9	0.24	0.02	0.71	0.12	0.87

The average predicted diurnal variation of O:C at the ground level, is presented in Figure 5.2. Predicted O:C increased during the afternoon due to the production of secondary OA and photochemical processing (evaporation, oxidation in the gas phase and recondensation) of the

primary OA. The model predictions, agree within experimental error with the measurements, with some discrepancies in the afternoon where the model tends to overpredict O:C. They both suggest relatively oxidized OA with modest average diurnal O:C variation. The average predicted O:C is 0.64 and the average measured is 0.58 (Table 5.2). The fractional error and bias for the 4-hour average O:C were less than 10%.

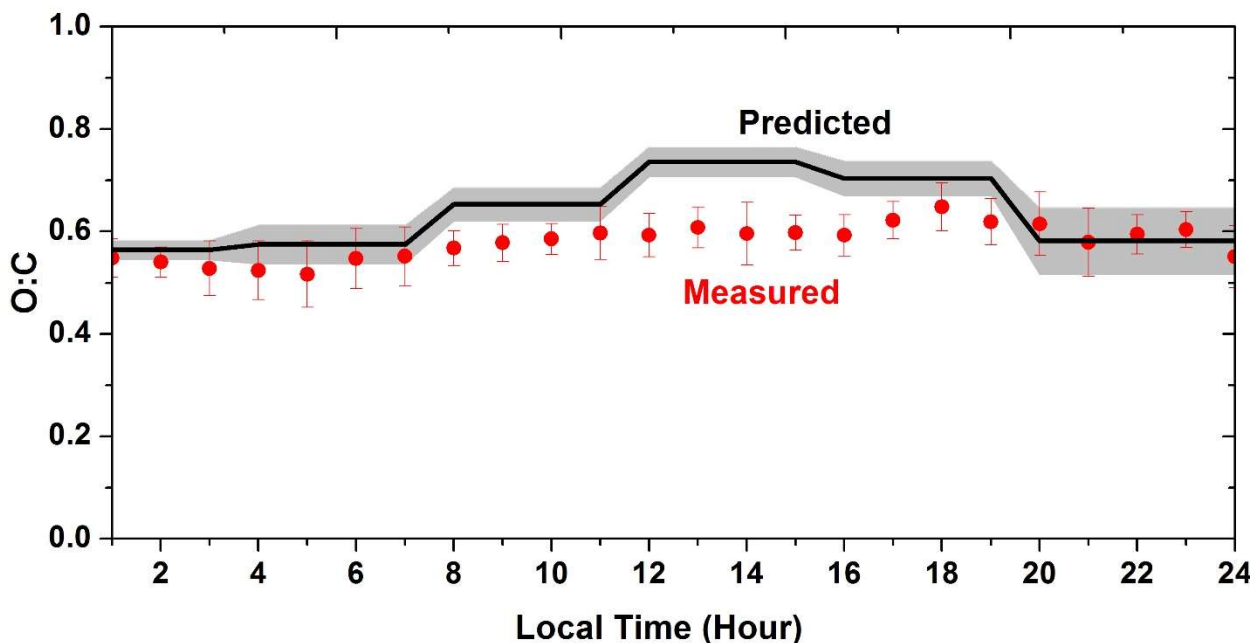


**Figure 5.2** Average O:C diurnal evolution at the ground level in San Pietro Capofiume for the 1-bin simulation. The black line shows the model predictions and the shaded area corresponds to one standard deviation. The red symbols represent the AMS measurements and the error bars correspond to one standard deviation.

The predicted average O:C vertical model profile is compared to the airborne measurements, in Figure 5.3. Model predictions, agree with the measurements within experimental error and both suggest an oxidized aerosol. The average predicted O:C was equal to 0.59, while the average measured O:C was 0.58. The vertical profile for both the predictions and Zeppelin measurements was relatively flat inside the lowest 1 km.

The predicted average diurnal profile of the OA mass concentration for the 1-bin case is shown in Figure 5.4. The average predicted OA is equal to  $2.6 \mu\text{g m}^{-3}$  and is predicted to be higher during the night time for this specific period. The average measured concentration during the same period was  $2.8 \mu\text{g m}^{-3}$ . The absolute error was equal to  $0.78 \mu\text{g m}^{-3}$  and the fractional bias was

12%. The anthropogenic SOA and SOA from IVOCs oxidation dominate the predicted OA composition, with biogenic SOA increasing during night time. SOA-iv is predicted to contribute 36% to the total OA. Anthropogenic and biogenic SOA are predicted to account for 22 and 17% respectively and SOA-sv and POA represent around 10% each (Figure C.3).

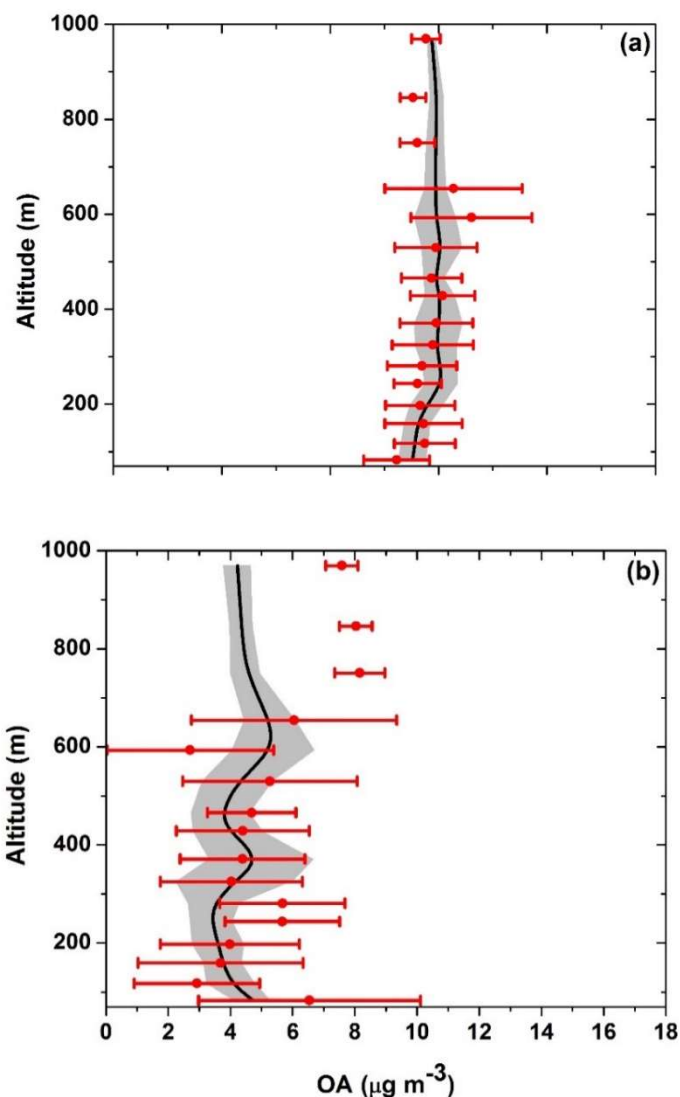


**Figure 5.3** Average vertical predicted and measured (1-bin case) (a) O:C ratio and (b) organic aerosol mass concentration for the Zeppelin measurements over Po Valley. The black line shows the model predictions and the shaded areas the standard deviation. The red symbols represent the AMS Zeppelin measurements and the error bars correspond to one standard deviation.

The average vertical predicted profile for all Zeppelin flights is compared with the corresponding measurements in Figure 5.3b. The average measured OA for these periods was

equal to  $4.7 \mu\text{g m}^{-3}$  while the average predicted  $4.2 \mu\text{g m}^{-3}$ . Model predictions are within experimental error, for altitudes lower than 700 m. The three data points at higher altitudes are all from a single flight on June 20, 2012 during which the model underpredicted the OA aloft.

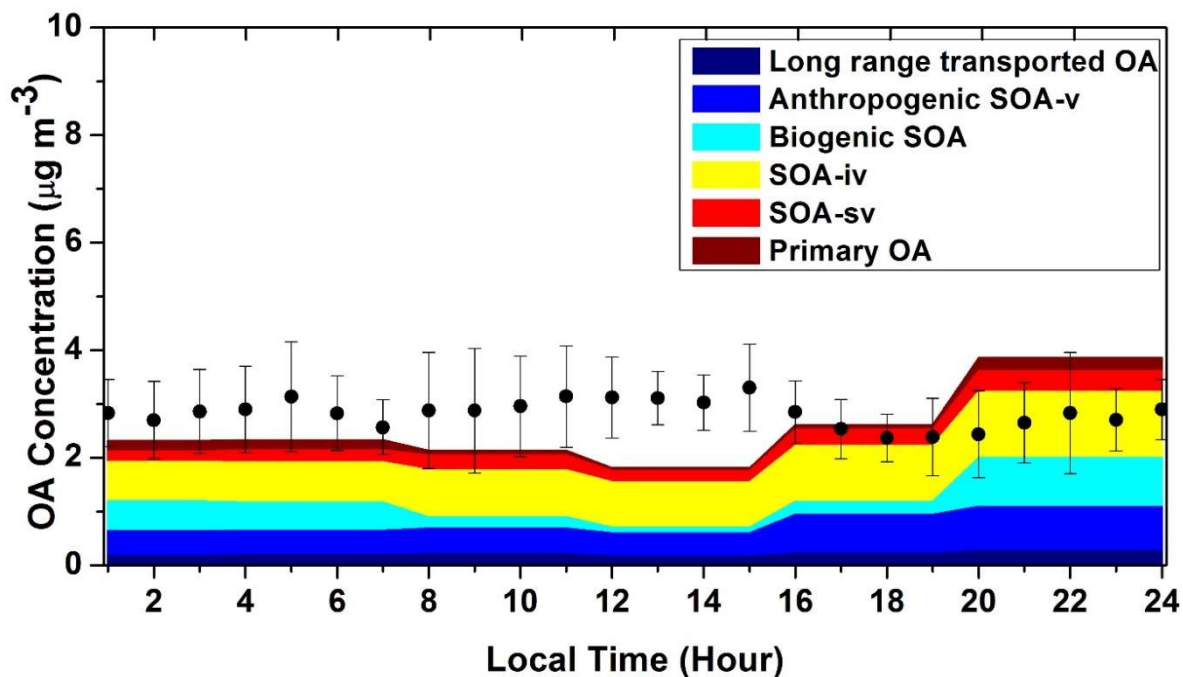


**Figure 5.4** Average diurnal profile at the ground level OA in San Pietro Capofiume. With dark blue we represent the OA from long range transport, with blue the anthropogenic SOA produced during the oxidation of anthropogenic VOCs (aSOA-v), with cyan the biogenic SOA (bSOA), with yellow the SOA from oxidation of intermediate volatility compounds (SOA-iv), with red the SOA from the oxidation of semivolatile OA (SOA-sv) and finally with dark red the fresh primary organic aerosol (FPOA). The AMS measurements are shown with black symbols and the error bars correspond to one standard deviation.

### 5.7.2 Effect of functionalization scheme

Using the 2-bin simple functionalization scheme the fractional error and bias for O:C ratio are around 10%, similar to the 1-bin parameterization. The average predicted OA is equal to  $3.4 \mu\text{g m}^{-3}$  (Table 5.3) with similar fractional error and bias with the 1-bin case. The average volatility distribution and O:C ratio of OA at the ground level is shown in Figure C.2. The OA mass, using this functionalization scheme is distributed towards smaller volatilities, compared to the 1-bin

case, almost one bin to the left (Figure C.2b), while the OA mass is distributed around similar values for the O:C ratio with a diurnal ground average equal to 0.63 (Table 5.2), where 0.58 is the average for the measurements.

The detailed functionalization scheme, underpredicted the O:C, with fractional bias equal to 34% and an average O:C equal to 0.41 (Table 5.2), when the average measured was 0.58. This is consistent with the conclusions of Murphy et al. (2011; 2012), about the tendency of this aggressive functionalization scheme to seriously underpredict O:C. The performance of this scheme, was better for the OA mass concentration with an average predicted value equal to  $3.2 \mu\text{g m}^{-3}$  (Table 5.3) close to the average measured value ( $2.8 \mu\text{g m}^{-3}$ ). The OA mass concentration fractional bias was equal to 11% while the fractional error was 21%. In this functionalization scheme the predicted OA has a wider distribution in the 2D space than the 2 previous schemes and lower O:C ratios and volatilities. (Figure C.2c).

### 5.7.3 Effect of bSOA production during aging

The potential importance of net bSOA production during the chemical aging reactions can be investigated using the results of the 1-bin/bSOA simulations. The average predicted O:C for the ground level using this parameterization is 0.55 which is consistent with the measured 0.58 (Table 5.2). The fractional error and bias of O:C are less than 10%. However, the OA concentration is overpredicted with an average value of  $3.8 \mu\text{g m}^{-3}$ , compared to the measured  $2.8 \mu\text{g m}^{-3}$  (Table 5.2). The OA concentration fractional bias and error were 26% and 30% respectively. This is consistent with the conclusions of Hermansson et al. (2014), Lane et al. (2008) and Murphy and Pandis (2009) that treating only the functionalization of bSOA while neglecting fragmentation leads to overpredictions of OA concentrations.

The same behavior was observed in the 2-bin/bSOA simulation in which PMCAMx-Trj predicted an average ground O:C equal to 0.53 with fractional bias less than 10% but overpredicted OA with an average equal to  $5 \mu\text{g m}^{-3}$  and a high fractional bias of 54%. Finally, in the DET/bSOA case, the model seriously underpredicted O:C with an average value equal to 0.35 and fractional bias equal to 50% and overpredicted OA concentration with an average equal to  $5.4 \mu\text{g m}^{-3}$  and a high fractional bias of 60%. In all of these cases addition of significant later generation bSOA production leads to significant errors in the model predictions.

#### 5.7.4 The role of fragmentation

To explore the role of fragmentation the 1-bin simple functionalization scheme was first used, assuming additional production of bSOA during aging combined with the fragmentation parameterization varying the fragmentation probability from zero to one. An optimum fragmentation probability equal to 0.15 was estimated (Figure C.4b). The average predicted O:C for this model configuration (1-bin/bSOA/ $b=0.15$ ) was equal to 0.56 in good agreement with the measurements and a fractional bias of 4% (Table 5.2). The average predicted OA was equal to  $2.9 \mu\text{g m}^{-3}$  with a fractional bias of just 2%.

The second functionalization scheme (2-bin case) was also tested without and with bSOA aging, (2-bin and 2-bin/bSOA cases respectively). In the first case, the optimum  $b$  was estimated to be equal to 0.1 and in the second case, assuming bSOA aging, it was equal to 0.4 (Figures C.4c and C.4d) For both model configurations, the performance was satisfactory (fractional biases less than 10% and fractional errors less than 25%) for both O:C and OA mass (Table 5.2 and 5.3).

In the last test, the detailed functionalization scheme (DET case) was used. In the previous simulations the DET and DET/bSOA parameterizations resulted in high underpredictions of the O:C ratio and overprediction of the OA concentration for DET/bSOA case. In the DET parameterization, the optimum  $b$  was estimated to be equal to 0.3 and in the second case, assuming bSOA aging, it was equal to 0.7 (Figures C.4e and C.4f). These schemes performed well with fractional biases less than 10% and fractional errors less than 25% for OA and less than 10% for O:C.

For all three aging schemes, including suitable fragmentation schemes, resulted in satisfactory results compared to the measurements at the ground level. The situation was similar for the Zeppelin measurements as shown in Figure C.5 in the Appendix. All these parameterizations resulted in similar vertical profiles of O:C and OA with similar agreement with the measurements.

#### 5.7.5 Synthesis of results

The previous results suggest that there are seven aging parameterizations from those examined that reproduce well both the ground and Zeppelin measurements. These are:

- the simple functionalization scheme and assuming negligible bSOA aging (1-bin case) corresponding to the base case in Murphy et al. (2011),
- the 1-bin shift with bSOA aging and a fragmentation probability equal to 15% (1-bin/bSOA/b=0.15); the 2-bin shift without bSOA aging (2-bin),
- the 2-bin shift without bSOA aging and a fragmentation probability equal to 10% (2-bin/b=0.1),
- the 2-bin shift with bSOA aging and a fragmentation probability equal to 40% (2-bin/bSOA/b=0.4),
- the detailed functionalization scheme, without bSOA aging and a fragmentation probability equal to 30% (DET/b=0.3),
- the detailed functionalization scheme with bSOA aging and fragmentation probability equal to 70% (DET/bSOA/b=0.7).

Parameterizations that appear to be inconsistent with the measurements are the ones that use the detailed functionalization scheme, without any fragmentation schemes leading to underprediction of the O:C. Parameterizations including net bSOA production during the chemical aging reactions and neglecting fragmentation were also inconsistent with the measurements resulting in overpredictions of the OA levels.

These seven aging schemes predict different OA composition (Figure 5.5) while all perform well enough compared to the measurements. Anthropogenic SOA from VOCs is predicted to contribute between 14 and 27% of the total OA (Figure C.3a). It is a high contributor for the simulations assuming negligible additional production of bSOA during chemical aging. The parameterization using the faster functionalization scheme (2-bin) predicts the highest percentage of 27% while the scheme with the detailed functionalization, additional bSOA production and rapid fragmentation (DET/ bSOA/b=0.7) predicts the lowest (14%).

The predicted contribution of biogenic SOA was the most variable ranging from 16 to 45% of the total OA depending on the scheme (Figure C.3b). The highest contribution, as expected, was predicted by the schemes assuming production of bSOA during aging. The highest fraction (45%) was predicted using the 2-bin shift functionalization parameterization and fragmentation by 40% (2-bin/bSOA/b=0.4). The lower bSOA concentrations were predicted by the four schemes assuming negligible net bSOA production during aging.

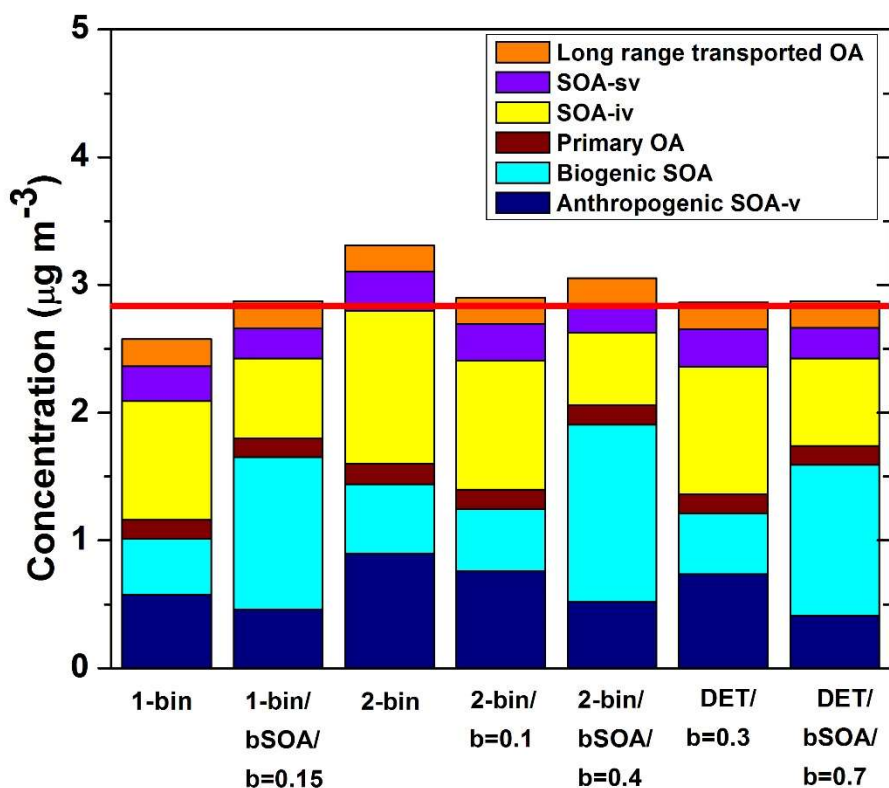


**Figure 5.5** Predicted OA composition for the schemes with good performance for San Pietro Capofiume. The red line indicates the average measured OA equal to  $2.8 \mu\text{g m}^{-3}$ .

SOA from the oxidation of intermediate volatility compounds varied between 19 and 36% depending on the model (Figure C.3c). The lowest contributions were predicted by the simulations in which the bSOA concentration was high. The primary OA varied from 5 to 6%, the OA from long range transport from 6 to 8%, and the SOA from evaporation of the primary and subsequent oxidation from 7 to 11%.

These results are encouraging because the various parameterizations even if they are quite different they give a rather consistent picture (with the picture of the bSOA maybe) about the various pathways contributing to the OA levels in this area.

### 5.7.6 The role of vaporization enthalpy

Three different effective vaporization enthalpies equal to 30, 75 and  $150 \text{ kJ mol}^{-1}$  were used together with the simple functionalization scheme (1-bin case). All three simulations, predicted

the same flat diurnal profile for both the O:C and OA concentration, with differences less than 20%, mostly in the first hours of the day (Figure 5.6). The predictions of the scheme with the higher vaporization enthalpy tend to be a little closer to the ground measurements of O:C. As vaporization enthalpy increased, the predicted O:C ratio decreased and OA concentration increased (Table C.1) However, the differences were small with the average O:C ranging from 0.59 for the 150 kJ mol<sup>-1</sup> case to 0.64 for the 30 kJ mol<sup>-1</sup> case while the measured average value was 0.58. The fractional biases for O:C were similar ranging from 2% for a vaporization enthalpy equal to 150 kJ mol<sup>-1</sup> to 10% for 30 kJ mol<sup>-1</sup>. The results for the OA concentration were similar.

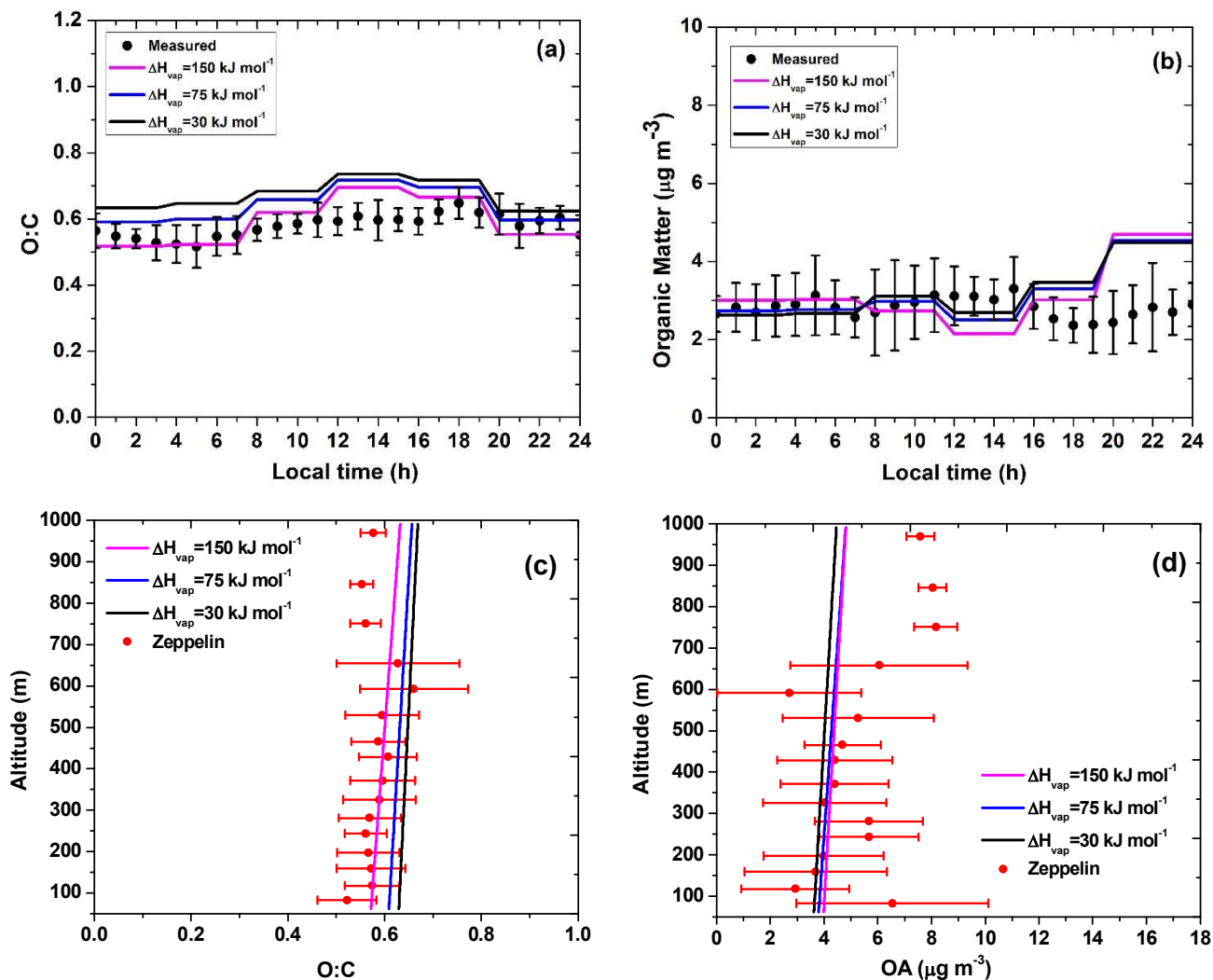


**Figure 5.6** Diurnally average (a) O:C ratios and (b) organic aerosol mass concentrations. Average vertical organic aerosol (c) O:C and (d) organic aerosol mass concentrations assuming in the model  $\Delta H_{vap} = 30 \text{ kJ mol}^{-1}$  (black line),  $\Delta H_{vap} = 75 \text{ kJ mol}^{-1}$  (blue line), and  $\Delta H_{vap} = 150 \text{ kJ mol}^{-1}$  (magenta line) for the Po Valley in Italy. The black symbols show the ground AMS measurements. The red symbols show the Zeppelin measurements. The error bars represent one standard deviation.

The comparison of the model predictions with the vertical profiles from the Zeppelin measurements showed similar results (Figure 5.6). The predicted vertical profiles of O:C and OA concentration were once more not that sensitive to the assumed effective vaporization enthalpy. This lack of sensitivity can be explained by the intricate interplay between the changes in partitioning of the semivolatile compounds and their gas-phase chemical aging reactions.

For values of  $\Delta H_{\text{vap}}$  that favor the partitioning of the OA components to the gas phase the resulting decrease in OA concentrations is partially offset by an acceleration of the gas-phase chemical aging reactions and the additional SOA production. Vice-versa for  $\Delta H_{\text{vap}}$  values that favor the partitioning to the particulate phase the resulting OA increase is balanced by a reduction in the aging rate.

## 5.8 Conclusions

The effects of the parameterization of the chemical aging processes of atmospheric organic compounds on organic aerosol (OA) concentration and chemical composition were investigated by using different formulations of the two-dimensional Volatility Basis Set (2D-VBS) together with ground and airborne measurements in the Po Valley in Italy.

We applied firstly the simple aging mechanism of the base case (Murphy et al., 2012), presented here as the 1-bin case. The predictions of the model, were satisfactory both at the ground and aloft, within experimental variability and with fractional biases for the 4-hour average O:C and OA concentration around 10%. The vertical profile for both predictions of the 1-bin case and Zeppelin measurements was relatively flat inside the lowest 1 km and the diurnal variation in O:C ratio was modest. They both suggested a relatively oxidized OA for Po Valley in Italy with an average O:C around 0.6. Anthropogenic SOA and SOA from intermediate volatility compounds oxidation dominated the predicted OA composition based on this parameterization.

Seven aging schemes (out of more than a hundred tested), with different assumed functionalizations, bSOA aging and fragmentation were found to reproduce well the ground and Zeppelin O:C and OA measurements. Anthropogenic SOA from VOCs was predicted to contribute between 15 and 25% of the total OA and SOA from the oxidation of intermediate volatility compounds oxidation between 20 and 35%. The contribution of biogenic SOA varied from 15 to 45%, depending on the parameterization scheme. POA was around 5%, the OA from long range

transport varied from 6 to 8% and the SOA from evaporation of the primary and subsequent oxidation from 7 to 11%. These results are encouraging because despite the uncertainty introduced by the different schemes, their predictions about source contributions are relatively robust.

Addition of bSOA produced during the corresponding chemical aging reactions in the functionalization-only schemes resulted in overpredictions of the OA. Addition of significant fragmentation (fragmentation probabilities ranging from 15 to 70%) was necessary to balance this additional source. This is clearly a topic that deserves additional research both in the laboratory and in the field.

There was also surprising low sensitivity of predicted OA concentration and O:C both at the ground and aloft to enthalpy of vaporization. Using three different vaporization enthalpies equal to 30, 75 and 150 kJ mol<sup>-1</sup>, the model predictions showed a very similar flat diurnal profile for O:C and OA concentration at the ground with differences less than 20% and being within experimental variability. Similar were the conclusions for the vertical profiles of the model in comparison to the Zeppelin measurements. The interplay between the partitioning of the compounds and the chemical aging reactions as well as the small temperature sensitivity, for altitudes until 600 m might explain this small sensitivity to vaporization enthalpy. There was some weak evidence though that the higher values (like 150 kJ mol<sup>-1</sup>) are in better agreement with the O:C observations at the ground and aloft.

## 5.9 References

- Caiazzo, F., Ashok, A., Waitz, I. A., Yim, S. H. L. and Barrett, S. R. H.: Air pollution and early deaths in the United States. Part I: Quantifying the impact of major sectors in 2005, *Atmospheric Environment*, 79, 198–208, 2013.
- Cappa, C. D. and Wilson, K. R.: Multi-generation gas-phase oxidation, equilibrium partitioning, and the formation and evolution of secondary organic aerosol, *Atmos. Chem. Phys.*, 12, 9505–9528, 2012.
- Cappa, C. D., Zhang, X., Loza, C. L., Craven, J. S., Yee, L. D., and Seinfeld, J. H.: Application of the Statistical Oxidation Model (SOM) to secondary organic aerosol formation from photooxidation of C12 alkanes, *Atmos. Chem. Phys.*, 13, 1591–1606, 2013.

- Carter, W. P. L.: Programs and files implementing the SAPRC-99 mechanism and its associated emissions processing procedures for Models-3 and other regional models, 31 January, 2000.
- Chacon-Madrid, H. J. and Donahue, N. M.: Fragmentation vs. functionalization: chemical aging and organic aerosol formation, *Atmos. Chem. Phys.*, 11, 10553–10563, 2011.
- Donahue, N. M., Robinson, A. L., Stanier, C. O., and Pandis, S. N.: Coupled partitioning, dilution, and chemical aging of semivolatile organics, *Environ. Sci. Technol.*, 40, 2635–2643, 2006.
- Donahue, N. M., Kroll, J. H., Pandis, S. N., and Robinson, A. L.: A two-dimensional volatility basis set: 1. organic-aerosol mixing thermodynamics, *Atmos. Chem. Phys.*, 11, 3303–3318, 2011.
- Donahue, N. M., Epstein, S. A., Pandis, S. N., and Robinson, A. L.: A two-dimensional volatility basis set – Part 2: Diagnostics of organic-aerosol evolution, *Atmos. Chem. Phys.*, 12, 615–634, 2012.
- Draxler, R., Stunder, B., Rolph, G., Stein, A., and Taylor, A.: HYSPLIT4 User's Guide, NOAA Silver Spring, MD, 231, 2009.
- Fountoukis C., Racherla P. N., Denier van der Gon H. A. C., Polymeneas P., Charalampidis P. E., Pilinis C., Wiedensohler A., Dall'Osto M., O'Dowd C., and S. N. Pandis: Evaluation of a three-dimensional chemical transport model (PMCAMx) in the European domain during the EUCAARI May 2008 campaign, *Atmos. Chem. Phys.*, 11, 10331–10347, 2011.
- Gilardoni, S., Vignati, E., Cavalli, F., Putaud, J. P., Larsen, B. R., Karl, M., Stenstrom, K., Genberg, J., Henne, S., and Dentener, F.: Better constraints on sources of carbonaceous aerosols using a combined  $^{14}\text{C}$  - macro tracer analysis in a European rural background site, *Atmos. Chem. Phys.*, 11, 5685–5700, 2011.
- Guenther, A., Karl, T., Harley, P., Wiedinmyer, C., Palmer, P. I., and Geron, C.: Estimates of global terrestrial isoprene emissions using MEGAN (Model of Emissions of Gases and Aerosols from Nature), *Atmos. Chem. Phys.*, 6, 3181–3210, 2006.
- Hermansson, E., Roldin, P., Rusanen, A., Mogensen, D., Kivekäs, N., Väänänen, R., Boy, M., and Swietlicki, E.: Biogenic SOA formation through gas-phase oxidation and gas-to-particle partitioning – a comparison between process models of varying complexity, *Atmos. Chem. Phys.*, 14, 11853–11869, 2014.

- IPCC (Intergovernmental Panel on Climate Change): Climate Change 2014: Mitigation of Climate Change. Contribution of Working Group III to the Fifth Assessment Report of the Intergovernmental Panel on Climate Change, Cambridge University Press, Cambridge, UK and New York, 2014.
- Jathar, S. H., Cappa, C. D., Wexler, A. S., Seinfeld, J. H. and Kleeman, M. J.: Multi-generational oxidation model to simulate secondary organic aerosol in a 3-D air quality model, *Geosci. Model Dev.*, 8, 2553-2567, 2015.
- Jimenez, J. L., Canagaratna, M. R., Donahue, N. M., Prévôt, A. S. H., Zhang, Q., Kroll, J. H., DeCarlo, P. F., Allan, J. D., Coe, H., Ng, N. L., Aiken, A. C., Docherty, K., Ulbrich, I., Grieshop, A.P., Robinson, A. L., Duplissy, J., Smith, J. D., Wilson, K. R., Lanz, V. A., Hueglin, C., Sun, Y. L., Tian, J., Laaksonen, A., Raatikainen, T., Rautiainen, J., Vaattovaara, P., Ehn, M., Kulmala, M., Tomlinson, J. M., Collins, D. R., Cubison, M. J., Dunlea, E., Huffman, J. A., Onasch, T. B., Alfarra, M. R., Williams, P., Bower, K., Kondo, Y., Schneider, J., Drewnick, F., Borrmann, S., Weimer, S., Demerjian, K., Salcedo, D., Cottrell, L., Griffin, R. J., Takami, A., Miyoshi, T., Hatakeyama, S., Shimono, A., Sun, J. Y., Zhang, Y. M., Dzepina, K., Kimmel, J. R., Sueper, D., Jayne, J. T., Herndon, S. C., Trimborn, A., Williams, L. R., Wood, E. C., Middlebrook, A. M., Kolb, C. E., Baltensperger, U., and Worsnop, D. R.: Evolution of organic aerosols in the atmosphere, *Science*, 326, 1525–1529, 2009.
- Kulmala, M., Asmil, A., Lappalainen, H. K., Carslaw, K. S., Poschl, U., Baltensperger, U., Hoy, O., Brenquier, J.-L., Pandis, S. N., Facchini, M. C., Hansson, H. C., Wiedensohler, A., and O’Dowd, C. D.: Introduction: European Integrated Project on Aerosol Cloud Climate and Air Quality interactions (EUCAARI) – integrating aerosol research from nano to global scales, *Atmos. Chem. Phys.*, 9, 2825–2841, 2009.
- Lane, T. E., Donahue, N. M., and Pandis, S. N.: Simulating secondary organic aerosol formation using the volatility basis-set approach in a chemical transport model, *Atmos. Environ.*, 42, 7439–7451, 2008.
- Murphy, B. N. and Pandis, S. N.: Simulating the formation of semivolatile primary and secondary organic aerosol in a regional chemical transport model, *Environ. Sci. Technol.*, 43, 4722–4728, 2009.

- Murphy, B. N. and Pandis, S. N.: Exploring summertime organic aerosol formation in the eastern United States using a regional-scale budget approach and ambient measurements, *J. Geophys. Res.*, 115, D24216, 10.1029/2010jd014418, 2010.
- Murphy, B. N., Donahue, N. M., Fountoukis, C., and Pandis, S. N.: Simulating the oxygen content of ambient organic aerosol with the 2D volatility basis set, *Atmos. Chem. Phys.*, 11, 7859-7873, 2011.
- Murphy, B. N., Donahue, N. M., Fountoukis, C., Dall'Osto, M., Dowd, C.O., Kiendler-Scharr, A., and Pandis, S. N.: Functionalization and fragmentation during ambient organic aerosol aging: application of the 2-D volatility basis set to field studies, *Atmos. Chem. Phys.*, 12, 10797-10816, 2012.
- Ng, N. L., Kroll, J. H., Keywood, M. D., Bahreini, R., Varutbangkul, V., Flagan, R. C., and Seinfeld, J. H.: Contribution of first- versus second-generation products to secondary organic aerosols formed in the oxidation of biogenic hydrocarbons, *Environ. Sci. Technol.*, 40, 2283–2297, 2006.
- O'Dowd, C. D., Langmann, B., Varghese, S., Scannell, C., Ceburnis, D., and Facchini, M. C.: A combined organic-inorganic sea spray source function, *Geophys. Res. Lett.*, 35, L01801, 10.1029/2007GL030331, 2008.
- Pandis S. N., Harley R. A., Cass G. R. and Seinfeld J. H.: Secondary Organic Aerosol Formation and Transport, *Atmos. Environ.*, 26, 2266-2282, 1992.
- Pathak, R. K., Presto, A. A., Lane, T. E., Stanier, C. O., Donahue, N. M., and Pandis, S. N.: Ozonolysis of  $\alpha$ -pinene: parameterization of secondary organic aerosol mass fraction, *Atmos. Chem. Phys.*, 7, 3811–3821, 2007.
- Pope, C. A., III, Ezzati, M. and Dockery, D. W.: Fine-particulate air pollution and life expectancy in the United States, *New England Journal of Medicine*, 360, 376–386, 2009.
- Sheehan, P. E. and Bowman, F. M.: Estimated effects of temperature on secondary organic aerosol concentrations, *Environ. Sci. Technol.*, 35, 2129–2135, 2001.
- Shrivastava, M., Fast, J., Easter, R., Gustafson Jr., W. I., Zaveri, R. A., Jimenez, J. L., Saide, P., and Hodzic, A.: Modeling organic aerosols in a megacity: comparison of simple and complex representations of the volatility basis set approach, *Atmos. Chem. Phys.*, 11, 6639–6662, 2011.

- Sofiev, M., Lanne, M., Vankevich, R., Prank, M., Karppinen, A., and Kukkonen, J.: Impact of wild-land fires on European air quality in 2006–2008, *Modeling, Monitoring and Management of Forest Fires*, WIT Trans. Ecol. Envir., 119, 353–361, 2008a.
- Sofiev, M., Vankevich, R., Lanne, M., Koskinen, J., and Kukkonen, J.: On integration of a Fire Assimilation System and a chemical transport model for near-real-time monitoring of the impact of wild-land fires on atmospheric composition and air quality, *Modeling, Monitoring and Management of Forest Fires*, WIT Trans. Ecol. Envir., 119, 343–351, 2008b.
- Stanier, C. O., Donahue, N., Pandis, S. N.: Parameterization of secondary organic aerosol mass fractions from smog chamber data, *Atmos. Environ.*, 42, 2276–2299, 2008.
- Szidat, S., Jenk, T. M., Synal, H.-A., Kalberer, M., Wacker, L., Hajdas, I., Kasper-Giebl, A., and Baltensperger, U.: Contributions of fossil fuel, biomass-burning, and biogenic emissions to carbonaceous aerosols in Zurich as traced by  $^{14}\text{C}$ , *J. Geophys. Res.*, 111, D07206, 10.1029/2005JD006590, 2006.
- Tritscher, T., Dommen, J., DeCarlo, P. F., Barmet, P. B., Pra-plan, A. P., Weingartner, E., Gysel, M., Prévôt, A. S. H., Riipinen, I., Donahue, N. M., and Baltensperger, U.: Volatility and hygroscopicity of aging secondary organic aerosol in a smog chamber, *Atmos. Chem. Phys.*, 11, 11477–11496, 2011.
- Visschedijk, A. J., Zandveld, P., and Denier van der Gon, H. A. C.: TNO Report 2007 A-R0233/B: A high resolution gridded European emission database for the EU integrated project GEMS, Organization for Applied Scientific Research, The Netherlands, 2007.
- Yttri, K. E., Simpson, D., Nøjgaard, J. K., Kristensen, K., Genberg, J., Stenström, K., Swietlicki, E., Hillamo, R., Aurela, M., Bauer, H., Offenberg, J. H., Jaoui, M., Dye, C., Eckhardt, S., Burkhardt, J. F., Stohl, A., and Glasius, M.: Source apportionment of the summer time carbonaceous aerosol at Nordic rural background sites, *Atmos. Chem. Phys.*, 11, 13339–13357, 2011.
- Zhang, Q., Jimenez, J. L., Canagaratna, M. R., Allan, J. D., Coe, H., Ulbrich, I., Alfarra, M. R., Takami, A., Middlebrook, A. M., Sun, Y. L., Dzepina, K., Dunlea, E., Docherty, K., DeCarlo, P. F., Salcedo, D., Onasch, T., Jayne, J. T., Miyoshi, T., Shimojo, A., Hatakeyama, S., Takegawa, N., Kondo, Y., Schneider, J., Drewnick, F., Borrmann, S., Weimer, S., Demerjian, K., Williams, P., Bower, K., Bahreini, R., Cottrell, L., Griffin, R. J., Rautiainen,

- J., Sun, J. Y., Zhang, Y. M., and Worsnop, D. R.: Ubiquity and dominance of oxygenated species in organic aerosols in anthropogenically-influenced Northern Hemisphere midlatitudes, *Geophys. Res. Lett.*, 34, L13801, 10.1029/2007GL029979, 2007.
- Zhang, Q. J., Beekmann, M., Drewnick, F., Freutel, F., Schneider, J., Crippa, M., Prévôt, A. S. H., Baltensperger, U., Poulain, L., Wiedensohler, A., Sciare, J., Gros, V., Borbon, A., Colomb, A., Michoud, V., Doussin, J. F., Denier van der Gon, H. A. C., Haeffelin, M., Dupont, J. C., Siour, G., Petetin, H., Bessagnet, B., Pandis, S. N., Hodzic, A., Sanchez, O., Honoré, C., and Perrussel, O.: Formation of organic aerosol in the Paris region during the MEGAPOLI summer campaign: evaluation of the volatility-basis-set approach within the CHIMERE model, *Atmos. Chem. Phys.*, 13, 5767–5790, 2013.
- Zhao, B., Wang, S., Donahue, N. M., Chuang, W., Hildebrandt-Ruiz, L., Ng, N. L., Wang, Y., and Hao, J.: Evaluation of one-dimensional and two-dimensional volatility basis sets in simulating the aging of secondary organic aerosol with smog-chamber experiments, *Environ. Sci. Technol.*, 49, 2245–2254, 2015.

# **Chapter 6**

**Simulation of atmospheric organic aerosol using its volatility-oxygen content distribution during the PEGASOS 2013 campaign in Finland**

## 6.1 Introduction

Aerosol particles or else particulate matter, are liquid or solid airborne particles that are ubiquitous in the atmosphere. They affect our lives by reducing visibility and influencing the climate due to their absorption/reflection of incoming solar radiation and role in cloud formation (IPCC 2014). Finally, they have serious adverse health effects (Nel et al. 2005; Pope et al., 2009; Caiazzo et al., 2013).

Organic aerosol is a major component especially of the submicrometer atmospheric particulate matter (Zhang et al. 2007; Jimenez et al. 2009). OA is either emitted directly into the atmosphere as particulate matter (primary organic aerosol, POA) or is formed by gas-to-particle conversion of volatile, intermediate volatility and semivolatile organic compounds (secondary OA, SOA). The oxidation reactions though of organic compounds lead to thousands of mostly unknown oxygenated products. Our understanding of OA formation mechanisms and physical properties is incomplete.

Terrestrial vegetation emits a variety of biogenic volatile organic compounds into the atmosphere (Guenther et al. 1995), some of which are subsequently oxidized forming among other products secondary organic aerosol. Boreal forests produce a large amount of SOA mainly due to emitted monoterpenes and sesquiterpenes (Seinfeld and Pandis, 2006). The biogenic SOA fraction has been found to represent 10 to 65% of the measured OA in or near forested regions (Szidat et al., 2009; Fu et al., 2010; Schwartz et al., 2010; Finessi et al., 2012).

The use of lumped species allows the computational efficient representation of OA in atmospheric chemical transport models (Pandis et al., 1992). The volatility basis set (VBS) framework (Donahue et al., 2006) lumps organic compounds into surrogates along an axis of volatility. This approach typically employs species with effective saturation concentrations at 298 K separated by one order of magnitude, with values ranging from, say, 0.01 to  $10^6 \mu\text{g m}^{-3}$ . By quantifying the volatility distributions of primary and secondary OA, a physically reasonable, yet suitable for large-scale chemical transport models (CTMs), description of semi-volatile organics can be obtained (Lane et al., 2008).

The VBS framework was extended by Donahue et al. (2011; 2012) adding another dimension, the oxygen content (expressed as the O:C ratio), for the description of the OA chemical aging reactions. Murphy et al. (2011; 2012) used a one-dimensional Lagrangian chemical transport

model (PMCAMx-Trj), as the host model for the simulations. PMCAMx-Trj simulates the chemical evolution of a column of air as it travels towards a user-selected receptor site. In Chapter 5, we used this Lagrangian CTM using the 2D-VBS framework and evaluated different parameterizations of OA formation and chemical aging, including functionalization or fragmentation mechanisms and using two different parameterization of bSOA aging.

In this Chapter, we will evaluate the same chemical aging mechanisms in the 2D-VBS approach for the rural forested area of Hyytiälä in southern Finland during PEGASOS campaign in 2013. Hyytiälä represents a continental background boreal forest and the PMCAMx-Trj application on this area will allow the testing of the 2D-VBS in an environment that is dominated by biogenic emissions.

## **6.2 Application of 2D-VBS in Finland**

### **6.2.1 Site description and measurement period**

Measurements were performed at the Hyytiälä SMEAR II (Station for Measuring Forest Ecosystem – Atmosphere Relations) site during the PEGASOS 2013 campaign. The site (Hari and Kulmala, 2005) is a rural forested station in southern Finland ( $61^{\circ} 51^{\circ}\text{N}$ ,  $24^{\circ} 17^{\circ}\text{E}$ , 181 m above sea level), in the middle of a more than 40-yr old Scots pine stand. The nearest urban locations are Tampere about 50 km to the south-west (200000 inhabitants) and Jyväskylä 100 km to the north-east (130000 inhabitants).

ACSM (Aerosol Chemical Speciation Monitor) measurements were performed, analyzed and provided by Mikko Äijälä from the University of Helsinki. A description of the ACSM and basic data processing can be found in Ng et al. (2011). The period of the measurements is from 19 of April 23, 2013 until June 19, 2013.

### **6.2.2 PMCAMx-Trj model**

We used the one-dimensional Lagrangian chemical transport model PMCAMx-Trj with the 2D-VBS module (Murphy et al., 2011; 2012) simulating the air parcels that arrive at Hyytiälä. The

model solves the general dynamic equation taking into account the relevant atmospheric processes: atmospheric transport, gas and aqueous-phase chemistry, dry and wet deposition of gases and aerosols and vertical turbulent dispersion, aerosol dynamics, inorganic and organic aerosol formation together with area and point emissions. Ten computational cells are used with heights varying from 60 m near the ground to almost 3 km. The SAPRC-99 (Carter, 2000) chemical mechanism is used for the simulation of gas-phase chemistry. The meteorological parameters (horizontal winds, temperature, pressure, vertical dispersion coefficients, water vapor, clouds, rainfall and land use) used as inputs in the model are provided by the Weather Research and Forecasting (WRF) model. The WRF simulation was periodically re-initialized (every 3 days) to ensure the accuracy of the inputs to the CTM. Area and point emissions were also provided by the inputs of the regular PMCAMx simulation for the European domain. The procedure is described in Section 5.2. Vertically resolved initial conditions and the top boundary conditions for PMCAMx-Trj were obtained from the corresponding output of the PMCAMx simulation for the same period of spring-early summer 2013.

### **6.2.3 Simulated periods**

The Hybrid Single Particle Lagrangian Integrated Trajectory HYSPLIT model (Draxler et al., 2009) was used to calculate 72 h back trajectories arriving at the receptor site of Hyytiälä. Six air parcels arriving at 3:00, 7:00, 11:00, 15:00, 19:00 and 23:00 local time (UTC+2) in the ground forested site were simulated for a total of 8 days (April 28, May 7, 11, 15 and 26 and June 9, 10 and 11). The air masses from the beginning of the campaign until middle of May originated mostly from the Atlantic, and arrived at Hyytiälä either directly from the west over Scandinavia or from the south, passing over the Baltic Sea. After mid-May, air masses started often from the east or north east, either from the Arctic Ocean or from west Russia. During the last weeks the situation changed again with air masses arriving from the Atlantic passing over Scandinavia. Our meteorological analysis is consistent with the conclusions of Nieminen et al. (2015). We selected days for which the trajectories at the different altitudes originated all from the same region. For consistency, we used the same WRF meteorological data as input to HYSPLIT to calculate the back trajectories. Following Murphy et al. (2011) we used the ensemble average of 20 trajectories

with varied heights from 60 m up to 3 km, similarly to the application to Po Valley in Italy in Chapter 5.

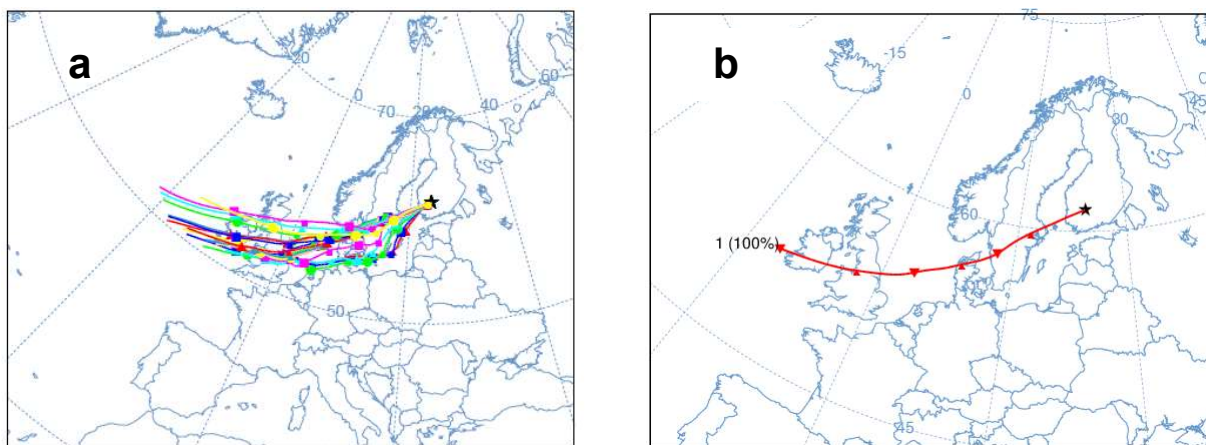


**Figure 6.1** (a) The ensemble of 20 trajectories calculated by HYSPLIT for air parcels arriving at the site of Hyytiälä on 7 May 2013 at 17:00 LT and (b) the ensemble average trajectory calculated by the HYSPLIT clustering utility.

The twenty 72 h HYSPLIT back trajectories arriving at Hyytiälä at 17:00 LT on May 7, 2013 are shown in Figure 6.1a as an example. They all originated from the eastern Atlantic Ocean, passed a day over the ocean and then over Ireland and the United Kingdom. During the next day they passed over the North Sea and Denmark. The air masses continued over Sweden and the Baltic Sea, and a few hours later arrived in the receptor site of Hyytiälä. The HYSPLIT clustering analysis utility was used to estimate the average trajectory that was used in the simulations (Figure 6.1b).

#### 6.2.4 Chemical Aging Schemes

In our simulations, we considered a series of aging parameterizations, taking into account three different functionalization schemes, two biogenic SOA aging schemes and also different fragmentation probabilities. These parameterizations have been described in detail in Chapter 5. In the simulations here, we will use the same parameterizations to test their robustness when applied in a very different environment. Table 1 summarizes the 11 parameterizations that were used in the simulations of Chapter 5.

**Table 6.1** Characteristics of different parameterizations used in our simulations.

<b>Parameterization Name</b>	<b>Functionalization scheme</b>	<b>bSOA increase during aging</b>	<b>Fragmentation probability</b>
1-bin	1-bin	No	b=0
1-bin/bSOA	1-bin	Yes	b=0
1-bin/bSOA/b=0.15	1-bin	Yes	b=0.15
2-bin	2-bin	No	b=0
2-bin/bSOA	2-bin	Yes	b=0
2-bin/b=0.1	2-bin	No	b=0.1
2-bin/bSOA/b=0.4	2-bin	Yes	b=0.4
DET	DET	No	b=0
DET/bSOA	DET	Yes	b=0
DET/b=0.3	DET	No	b=0.3
DET/bSOA/b=0.7	DET	Yes	b=0.7

### 6.2.5 Evaluation of parameterizations

The prediction skill of PMCAMx-Trj for the different parameterizations is quantified in terms of the fractional error, the fractional bias, the absolute error, the absolute bias and the root mean square error, similarly to Chapter 5. The equations that are used to calculate these metrics are shown below:

$$\text{Fractional Error} = \frac{2}{n} \sum_{i=1}^n \frac{|P_i - M_i|}{(P_i + M_i)}$$

$$\text{Fractional Bias} = \frac{2}{n} \sum_{i=1}^n \frac{(P_i - M_i)}{(P_i + M_i)}$$

$$\text{Absolute Error} = \frac{1}{n} \sum_{i=1}^n |P_i - M_i|$$

$$\text{Absolute Bias} = \frac{1}{n} \sum_{i=1}^n (P_i - M_i)$$

$$\text{Root Mean Square Error} = \sqrt{\frac{1}{n} \sum_{i=1}^n (P_i - M_i)^2}$$

where  $P_i$  represents the model predicted value for data point,  $M_i$  is the corresponding measured value and  $n$  is the total number of data points.

## 6.3 Results

### 6.3.1 Simple functionalization scheme (1-bin case)

The first set of simulations used the simple functionalization scheme (1-bin), which assumes a one volatility bin reduction for every reaction with a simultaneous increase in oxygen atoms, with a probability of 50% for an increase of 1 oxygen atom and 50% probability for an increase of 2 oxygen atoms. It also assumes negligible additional production of bSOA during aging (no bSOA aging) and no fragmentation of the organic compounds. Implicitly this scheme assumes that the functionalization represents the net effect of these pathways. The prediction skill metrics of the model 4-hour average OA concentration against the averaged ground measurements for the seven selected days during PEGASOS 2013 campaign are summarized in Table 6.2.

The predicted average diurnal profile of OA mass concentration, for the 1-bin scheme is shown in Figure 6.2. The average predicted OA is equal to  $2.3 \mu\text{g m}^{-3}$  and the average measured concentration during the same period was  $2.1 \mu\text{g m}^{-3}$  (Table 6.2). This scheme was the most successful in predicting the OA concentration of all parameterizations used (Table 6.2). It had the lowest root mean square error, as well as the lowest fractional bias (-5%) and one of the lowest fractional errors (38%). Most of the error is present during the first hours of the day when the model overpredicts the OA mass concentration (Figure 6.2).

**Table 6.2** Performance metrics of different parameterizations during the PEGASOS 2013 campaign for ground OA concentration. The measured average organic aerosol mass concentration was  $2.1 \mu\text{g m}^{-3}$ .

<b>2D-VBS Parameterization</b>	<b>Predicted Average (<math>\mu\text{g m}^{-3}</math>)</b>	<b>Fractional Error</b>	<b>Fractional Bias</b>	<b>Absolute Error (<math>\mu\text{g m}^{-3}</math>)</b>	<b>Absolute Bias (<math>\mu\text{g m}^{-3}</math>)</b>	<b>Root Mean Square Error (<math>\mu\text{g m}^{-3}</math>)</b>
1-bin	2.32	0.38	-0.05	0.92	0.23	1.16
1-bin/bSOA	4.21	0.51	0.45	2.22	2.12	3.39
1-bin/bSOA/b=0.15	2.91	0.34	0.17	1.1	0.82	1.69
2-bin	2.59	0.31	0.07	0.92	0.5	1.35
2-bin/bSOA	4.2	0.56	0.56	2.11	2.11	2.85
2-bin/b=0.1	2.46	0.34	0.02	0.91	0.38	1.25
2-bin/bSOA/b=0.4	2.98	0.31	0.22	1.06	0.90	1.67
DET	3.5	0.42	0.25	1.70	1.42	2.77
DET/bSOA	4.58	0.59	0.59	2.49	2.49	3.52
DET/b=0.3	2.45	0.33	0.02	0.89	0.36	1.21
DET/bSOA/b=0.7	2.73	0.26	0.15	0.84	0.64	1.33

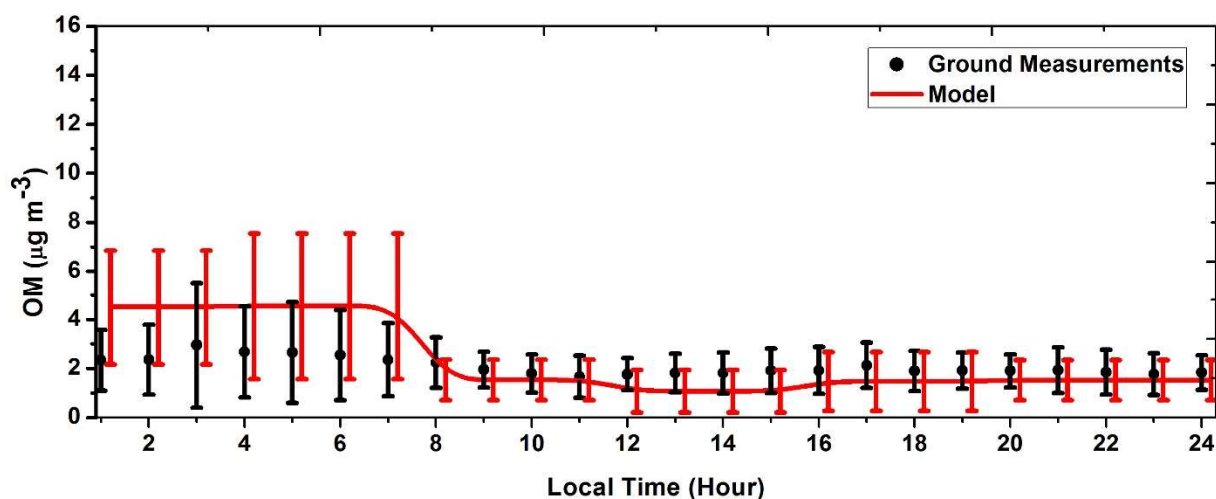


**Figure 6.2** Average diurnal OA mass concentration at the ground level in Hyytiälä for the 1-bin simulation. The red line shows the model predictions and the black symbols represent the ACSM measurements. The error bars correspond to one standard deviation.

The biogenic SOA dominates the predicted OA composition, as expected for a forested environment, contributing 41% of the total OA on average (Figure 6.3). SOA from the oxidation of intermediate volatility compounds contributed 27% and anthropogenic SOA from VOCs was another 16%. The remaining was due to primary OA (4%), SOA from evaporation of the primary and subsequent oxidation and OA from long range transport by 6% each.

### 6.3.2 Effect of functionalization scheme

The second simple functionalization scheme (2-bin), assuming no addition or production of bSOA and neglecting fragmentation predicted average OA equal to  $2.6 \mu\text{g m}^{-3}$  (Table 6.2). Its root mean square error was higher than that of the 1-bin case, its fractional bias similar and its fractional error a little less. Overall its performance was quite similar to that of the 1-bin scheme.

The performance of the detailed functionalization scheme for OA concentration was significantly worse than the two previous functionalization schemes with the scheme tending to overpredict OA (fractional bias 25%) and a root mean square error more than double that of the simple 1-bin scheme. The performance of the two simple functionalization schemes (1-bin and 2-bin), was better than the detailed functionalization scheme, a result similar to that in San Pietro Capofiume in Chapter 5.

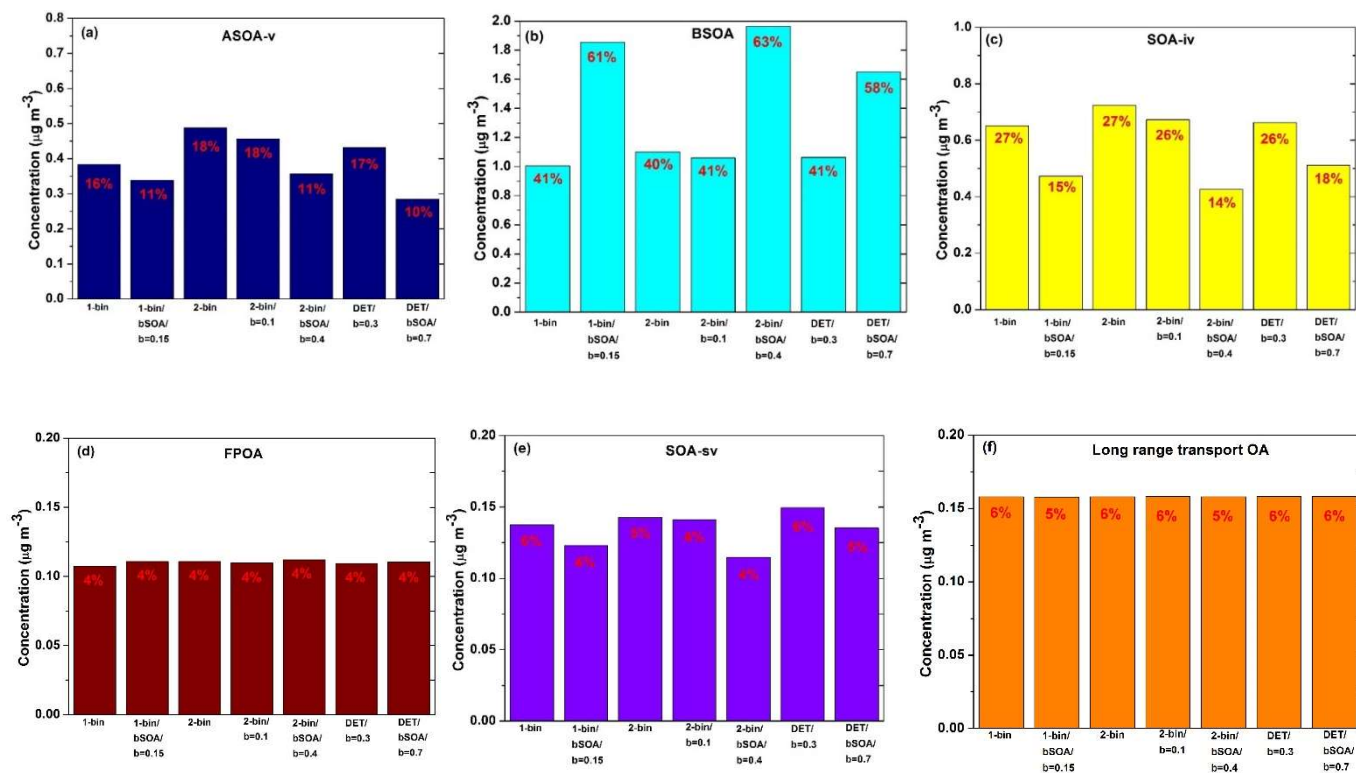


**Figure 6.3** Predicted contribution of (a) ASOA-v, (b) BSOA, (c) SOA from oxidation of intermediate volatility organic compounds, (d) FPOA, (e) SOA from oxidation of evaporated POA, and (f) OA from long range transport using various aging parameterizations.

### 6.3.3 Effect of additional bSOA production during aging

The potential importance of net bSOA production during the chemical aging reactions was investigated using the results of the 1-bin/bSOA simulations. The OA concentration in this case is seriously overpredicted with an average value of  $4.2 \mu\text{g m}^{-3}$  compared to the measured average of  $2.1 \mu\text{g m}^{-3}$  (Table 6.2). The OA concentration fractional bias and error were 51% and 45% respectively and the root mean square error was equal to  $3.39 \mu\text{g m}^{-3}$ . This is consistent with previous conclusions that treating only the functionalization of bSOA while neglecting fragmentation leads to serious overpredictions of OA levels. The 2-bin/bSOA scheme was characterized by similar overpredictions with a root mean square error equal to  $2.85 \mu\text{g m}^{-3}$  and a high fractional bias of 56%. Finally, the DET/bSOA scheme overpredicted OA mass with a fractional bias of almost 60%.

These simulations, treating only the functionalization of bSOA while neglecting fragmentation, all overpredicted the OA mass concentration similarly to Chapter 5. These results are consistent with the conclusions of Lane et al. (2008) for the Eastern US, Murphy and Pandis (2009) and Hermansson et al. (2014) for Europe.

#### 6.3.4 The role of fragmentation

To explore the role of fragmentation the 1-bin simple functionalization scheme was first used, assuming addition/production of bSOA during aging and combined with the fragmentation parameterization with the fragmentation probability equal to 15% as estimated in Chapter 5. The average predicted OA mass was equal to  $2.9 \mu\text{g m}^{-3}$  with a fractional bias of 17% and a root mean square error equal to  $1.69 \mu\text{g m}^{-3}$ . This scheme does overpredict OA in contrast to the simple scheme, but the deterioration in performance is small to moderate.

The 2-bin functionalization scheme, neglecting bSOA aging and assuming a fragmentation probability  $b=0.1$  performed a little better (lower bias and root mean square error) than the 2-bin scheme. However, the improvements were small (reduction of bias by 5% and of root mean square error by  $0.1 \mu\text{g m}^{-3}$ ) while the absolute error was almost the same. The 2-bin functionalization, with bSOA and more rapid fragmentation ( $b=0.4$ ) performed a little worse than the previous schemes with a tendency to overpredict OA (fractional bias 22%).

In the next set of simulations, the detailed functionalization scheme (DET case) was used assuming a fragmentation probability equal to 30%. This scheme performed quite well with a fractional bias of only 2% and a fractional error of 33%. Its root mean square error was just  $0.05 \mu\text{g m}^{-3}$  higher than that of the simple 1-bin scheme. Combining the detailed functionalization, bSOA aging and very rapid fragmentation ( $b=0.7$ ) reduced the fractional error to 26%, but increased the bias to 15%.

Overall, the results are rather encouraging because the optimized schemes determined in the Po Valley simulations appear to perform well in the very different environment of Southern Finland.

For all three aging schemes, fragmentation of the particles led to closer prediction of the OA mass concentration, while in some cases more fragmentation, than the probabilities calculated in Chapter 5, were even needed.

### 6.3.5 Synthesis of results

The previous results suggest that parameterizations that appear to be inconsistent with the measurements are the ones that use the detailed functionalization scheme, without any fragmentation of the OA namely the DET and DET/ bSOA schemes. Moreover, parameterizations including net bSOA production during the chemical aging reactions and neglecting fragmentation also led to significant overpredictions of the OA levels for all three functionalization schemes used (1-bin/bSOA, 2-bin/bSOA and DET/bSOA). Adding fragmentation was essential for the better reproduction of the ground measurements. These are summarized in Figure 6.4.

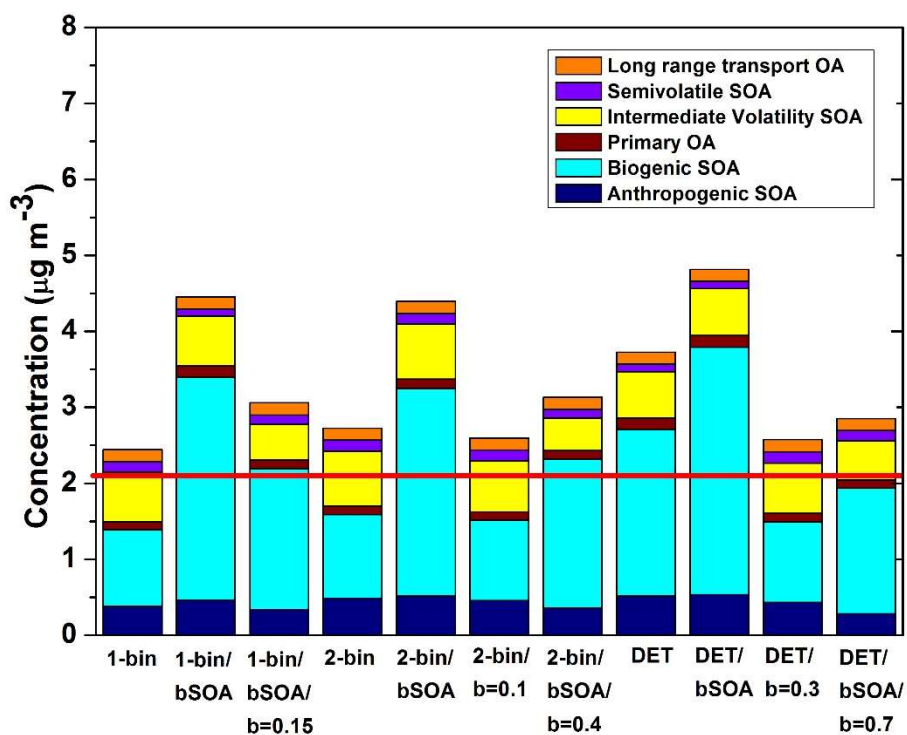


**Figure 6.4** Predicted OA composition for the schemes with good performance for Hyttiälä. The red line indicates the average measured OA equal to  $2.1 \mu\text{g m}^{-3}$ .

### 6.3.6 Predicted OA composition

From the eleven cases that were tested and evaluated, there are seven aging parameterizations that reproduce better the ground level OA measurements. The contribution of biogenic SOA varied

from 40 to 63% of the total OA (Figure 6.3) depending on the parameterization. The highest bSOA concentration was predicted by the aging schemes that assume production of bSOA during the aging reactions. The highest contributor (63%) was for the scheme assuming a 2-bin shift functionalization and fragmentation with 40% probability (2-bin/bSOA/b=0.4). The rest of the cases predicted lower bSOA levels, around 40%.

Anthropogenic SOA from VOCs oxidation was predicted to contribute between 11 and 18% of the total OA (Figure 6.3). Its low levels are consistent with the rural forested area of the boreal station of Hyytiälä.

SOA from the oxidation of intermediate volatility compounds varied between 14 and 27%. The lowest contributions were predicted by the simulations that had high bSOA levels. The highest contributions (27%) was predicted by the simulations using the simple (1-bin) and faster (2-bin) functionalization scheme.

The fresh POA was 4% of the total OA, the SOA from the oxidation of evaporated POA 4-6%, and the OA from long range transport 5-6%.

## 6.4 Conclusions

The effects of different parameterization of chemical aging processes of atmospheric organic compounds on organic aerosol (OA) concentration and chemical composition were investigated by using the two-dimensional Volatility Basis Set (2D-VBS) together with ground measurements in the boreal environment of Hyytiälä. The parameterizations used were the same as in Chapter 5, including those optimized for the Po Valley polluted environment.

Despite the very different environment, the performance of all parameterizations was surprisingly similar to that in the Po Valley. The simple functionalization only parameterization of Murphy et al. (2012) had for one more time the best performance. This simple scheme appears for some reason that is not well understood to capture the behavior of OA in a lot of different environments both rural and polluted. Its variation with a 2-bin change performed almost as well. Schemes adding significant bSOA during aging reactions, or assuming aggressive functionalization were once more the worst performers. Addition of fragmentation was needed for these schemes.

The fragmentation schemes with the probability values optimized for Po Valley performed quite well in this case too. Increasing fragmentation rates are needed to “balance” the assumed net bSOA production during aging as the functionalization scheme becomes more aggressive.

Despite their differences, the seven schemes that performed well for OA predicted similar OA composition for the simulated period: 40-63% biogenic SOA, 11-18% SOA from anthropogenic VOCs, 14-27% SOA from IVOCs, 4% POA, 4-6% SOA from evaporated POA, and 5-6% from long range transport. This agreement is encouraging about our ability to constrain the SOA sources.

## 6.5 References

- Caiazzo, F., Ashok, A., Waitz, I. A., Yim, S. H. L. and Barrett, S. R. H.: Air pollution and early deaths in the United States. Part I: Quantifying the impact of major sectors in 2005, *Atmospheric Environment*, 79, 198–208, 2013.
- Carter, W. P. L.: Programs and files implementing the SAPRC-99 mechanism and its associated emissions processing procedures for Models-3 and other regional models, 31 January, 2000.
- Donahue, N. M., Robinson, A. L., Stanier, C. O., and Pandis, S. N.: Coupled partitioning, dilution, and chemical aging of semivolatile organics, *Environ. Sci. Technol.*, 40, 2635-2643, 2006.
- Donahue, N. M., Kroll, J. H., Pandis, S. N., and Robinson, A. L.: A two-dimensional volatility basis set: 1. organic-aerosol mixing thermodynamics, *Atmos. Chem. Phys.*, 11, 3303–3318, 2011.
- Donahue, N. M., Epstein, S. A., Pandis, S. N., and Robinson, A. L.: A two-dimensional volatility basis set – Part 2: Diagnostics of organic-aerosol evolution, *Atmos. Chem. Phys.*, 12, 615–634, 2012.
- Draxler, R., Stunder, B., Rolph, G., Stein, A., and Taylor, A.: HYSPLIT4 User’s Guide, NOAA Silver Spring, MD, 231, 2009.
- Finessi, E., Decesari, S., Paglione, M., Giulianelli, L., Carbone, C., Gilardoni, S., Fuzzi, S., Saarikoski, S., Raatikainen, T., Hillamo, R., Allan, J., Mentel, T. F., Tiitta, P., Laaksonen, A., Petaja, T., Kulmala, M., Worsnop, D. R., and Facchini, M. C.: Determination of the

- biogenic secondary organic aerosol fraction in the boreal forest by nmr spectroscopy, *Atmos. Chem. Phys.*, 12, 941–959, 2012.
- Fu, P. Q., Kawamura, K., Kanaya, Y., and Wang, Z. F.: Contributions of biogenic volatile organic compounds to the formation of secondary organic aerosols over mt tai, central east china, *Atmos. Environ.*, 44, 4817–4826, 2010.
- Guenther, A., Hewitt, C. N., Erickson, D., Fall, R., Geron, C., Gredel, T., Harley, P., Klinger, L., Lerdau, M., Mckay, W. A., Pierce, T., Scholes, B., Steinbrecher, R., Tallamraju, R., Taylor, J., and Zimmerman, P.: A global model of natural volatile organic compound emissions, *J. Geophys. Res.*, 100, 8873–8892, doi:10.1029/94JD02950, 1995.
- Hari, P. and Kulmala, M.: Station for Measuring Ecosystem-Atmosphere Relations (SMEAR II), *Boreal Env. Res.*, 10, 315–322, 2005.
- Hermansson, E., Roldin, P., Rusanen, A., Mogensen, D., Kivekäs, N., Väänänen, R., Boy, M., and Swietlicki, E.: Biogenic SOA formation through gas-phase oxidation and gas-to-particle partitioning – a comparison between process models of varying complexity, *Atmos. Chem. Phys.*, 14, 11853–11869, 2014.
- IPCC (Intergovernmental Panel on Climate Change): *Climate Change 2014: Mitigation of Climate Change. Contribution of Working Group III to the Fifth Assessment Report of the Intergovernmental Panel on Climate Change*, Cambridge University Press, Cambridge, UK and New York, 2014.
- Jimenez, J. L., Canagaratna, M. R., Donahue, N. M., Prévôt, A. S. H., Zhang, Q., Kroll, J. H., DeCarlo, P. F., Allan, J. D., Coe, H., Ng, N. L., Aiken, A. C., Docherty, K., Ulbrich, I., Grieshop, A.P., Robinson, A. L., Duplissy, J., Smith, J. D., Wilson, K. R., Lanz, V. A., Hueglin, C., Sun, Y. L., Tian, J., Laaksonen, A., Raatikainen, T., Rautiainen, J., Vaattovaara, P., Ehn, M., Kulmala, M., Tomlinson, J. M., Collins, D. R., Cubison, M. J., Dunlea, E., Huffman, J. A., Onasch, T. B., Alfarra, M. R., Williams, P., Bower, K., Kondo, Y., Schneider, J., Drewnick, F., Borrmann, S., Weimer, S., Demerjian, K., Salcedo, D., Cottrell, L., Griffin, R. J., Takami, A., Miyoshi, T., Hatakeyama, S., Shimono, A., Sun, J. Y., Zhang, Y. M., Dzepina, K., Kimmel, J. R., Sueper, D., Jayne, J. T., Herndon, S. C., Trimborn, A., Williams, L. R., Wood, E. C., Middlebrook, A. M., Kolb, C. E., Baltensperger, U., and Worsnop, D. R.: Evolution of organic aerosols in the atmosphere, *Science*, 326, 1525–1529, 2009.

- Lane, T. E., Donahue, N. M., and Pandis, S. N.: Simulating secondary organic aerosol formation using the volatility basis-set approach in a chemical transport model, *Atmos. Environ.*, 42, 7439–7451, 2008.
- Murphy, B. N. and Pandis, S. N.: Simulating the formation of semivolatile primary and secondary organic aerosol in a regional chemical transport model, *Environ. Sci. Technol.*, 43, 4722–4728, 2009.
- Murphy, B. N., Donahue, N. M., Fountoukis, C., and Pandis, S. N.: Simulating the oxygen content of ambient organic aerosol with the 2D volatility basis set, *Atmos. Chem. Phys.*, 11, 7859–7873, 2011.
- Murphy, B. N., Donahue, N. M., Fountoukis, C., Dall’Osto, M., Dowd, C.O., Kiendler-Scharr, A., and Pandis, S. N.: Functionalization and fragmentation during ambient organic aerosol aging: application of the 2-D volatility basis set to field studies, *Atmos. Chem. Phys.*, 12, 10797–10816, 2012.
- Nel, A.: Air Pollution-Related Illness: Effects of Particles, *Science*, 308, 804–806, 2005.
- Ng, N. L., Herndon, S. C., Trimborn, A., Canagaratna, M. R., Croteau, P., Onasch, T. M., Sueper, D., and Worsnop, D. R.: An Aerosol Chemical Speciation Monitor (ACSM) for routine monitoring of atmospheric aerosol composition, *Aerosol Sci. Technol.*, 45, 770–784, 2011.
- Nieminen, T., Yli-Juuti, T., Manninen, H. E., Petäjä, T., Kerminen, V.-M., and Kulmala, M.: Technical note: New particle formation event forecasts during PEGASOS-Zeppelin Northern mission 2013 in Hyytiälä, Finland, *Atmos. Chem. Phys.*, 15, 12385–12396, 2015.
- Pandis S. N., Harley R. A., Cass G. R. and Seinfeld J. H.: Secondary Organic Aerosol Formation and Transport, *Atmos. Environ.*, 26, 2266–2282, 1992.
- Pathak, R. K., Presto, A. A., Lane, T. E., Stanier, C. O., Donahue, N. M., and Pandis, S. N.: Ozonolysis of  $\alpha$ -pinene: parameterization of secondary organic aerosol mass fraction, *Atmos. Chem. Phys.*, 7, 3811–3821, 2007.
- Pope, C. A., III, Ezzati, M. and Dockery, D. W.: Fine-particulate air pollution and life expectancy in the United States, *New England Journal of Medicine*, 360, 376–386, 2009.
- Schwartz, R. E., Russell, L. M., Sjostedt, S. J., Vlasenko, A., Slowik, J. G., Abbatt, J. P. D., Macdonald, A. M., Li, S. M., Liggio, J., Toom-Sauntry, D., and Leitch, W. R.: Biogenic oxidized organic functional groups in aerosol particles from a mountain forest site and their similarities to laboratory chamber products, *Atmos. Chem. Phys.*, 10, 5075–5088, 2010.

- Seinfeld, J.H. and Pandis, S.N.: Atmospheric Chemistry and Physics, second ed., John Wiley and Sons, Hoboken, New Jersey, USA, 2006.
- Sheehan, P. E. and Bowman, F. M.: Estimated effects of temperature on secondary organic aerosol concentrations, *Environ. Sci. Technol.*, 35, 2129–2135, 2001.
- Shrivastava, M., Fast, J., Easter, R., Gustafson Jr., W. I., Zaveri, R. A., Jimenez, J. L., Saide, P., and Hodzic, A.: Modeling organic aerosols in a megacity: comparison of simple and complex representations of the volatility basis set approach, *Atmos. Chem. Phys.*, 11, 6639–6662, 2011.
- Sofiev, M., Lanne, M., Vankevich, R., Prank, M., Karppinen, A., and Kukkonen, J.: Impact of wild-land fires on European air quality in 2006–2008, *Modeling, Monitoring and Management of Forest Fires*, *WIT Trans. Ecol. Envir.*, 119, 353–361, 2008a.
- Sofiev, M., Vankevich, R., Lanne, M., Koskinen, J., and Kukkonen, J.: On integration of a Fire Assimilation System and a chemical transport model for near-real-time monitoring of the impact of wild-land fires on atmospheric composition and air quality, *Modeling, Monitoring and Management of Forest Fires*, *WIT Trans. Ecol. Envir.*, 119, 343–351, 2008b.
- Stanier, C. O., Donahue, N., Pandis, S. N.: Parameterization of secondary organic aerosol mass fractions from smog chamber data, *Atmos. Environ.*, 42, 2276–2299, 2008.
- Szidat, S., Ruff, M., Perron, N., Wacker, L., Synal, H. A., Hallquist, M., Shannigrahi, A. S., Yttri, K. E., Dye, C., and Simpson, D.: Fossil and non-fossil sources of organic carbon (oc) and elemental carbon (ec) in goteborg, sweden, *Atmos. Chem. Phys.*, 9, 1521-1535, 2009.
- Zhang, Q., Jimenez, J. L., Canagaratna, M. R., Allan, J. D., Coe, H., Ulbrich, I., Alfarra, M. R., Takami, A., Middlebrook, A. M., Sun, Y. L., Dzepina, K., Dunlea, E., Docherty, K., DeCarlo, P. F., Salcedo, D., Onasch, T., Jayne, J. T., Miyoshi, T., Shimono, A., Hatakeyama, S., Takegawa, N., Kondo, Y., Schneider, J., Drewnick, F., Borrmann, S., Weimer, S., Demerjian, K., Williams, P., Bower, K., Bahreini, R., Cottrell, L., Griffin, R. J., Rautiainen, J., Sun, J. Y., Zhang, Y. M., and Worsnop, D. R.: Ubiquity and dominance of oxygenated species in organic aerosols in anthropogenically-influenced Northern Hemisphere midlatitudes, *Geophys. Res. Lett.*, 34, L13801, 10.1029/2007GL029979, 2007.

# **Chapter 7**

## **Conclusions and future work**

## 7.1 Conclusions

Organic compounds represent a significant fraction of submicrometer atmospheric aerosol mass. Even if most of these compounds are semi-volatile in atmospheric concentrations, the ambient organic aerosol volatility is quite uncertain. The focus of this work was to gain insights into estimating the volatility of the organic aerosol in both ambient and experimental data and being able to estimate also properties that affect volatility such as the vaporization enthalpy and accommodation coefficient. Simulations using the volatility-oxygen content distribution (2D-VBS) of the organic aerosol (Donahue et al. 2011; 2012), as a proposed framework of representing the numerous unknown compounds of the organic aerosol, is further constrain the different parameterizations and mechanisms of OA chemical aging in the ambient air.

A theoretical analysis of methods for estimating the OA volatility distribution using the measurements of a thermodenuder (TD) was performed. The thermograms, or else the aerosol mass fraction remaining (MFR) at a given temperature, after passing through the TD, have been used in previous studies as the “fingerprint” of the volatility of the organic aerosol. Multiple combinations of parameters ( $C^*$ ,  $\Delta H_{\text{vap}}$ ,  $a_m$ ) can lead to practical indistinguishable thermograms during TD measurements. The estimated volatility distribution, based on the minimum error, can be wrong by several orders of magnitude due to the multiple solutions that exist leading to multiple local minima of the objective function. We introduced a new method combining forward modeling, introduction of experimental error and inverse modeling with error minimization for the interpretation of existing TD measurements. With this method, using an ensemble of ‘best solutions’ we were able to calculate a best estimate and an uncertainty range for the estimated volatility distribution, the vaporization enthalpy and the accommodation coefficient. We showed that this uncertainty range is often large and sometimes does not even include the true value of the properties, with the exception in the estimation of the vaporization enthalpy where the errors are around 5-20% in most cases tested.

Experimental approaches that would improve the method were also explored. The performance of TD measurements under multiple residence times resulted in a small to modest improvement of the results since equilibrium was still not reached. The idea of using experiments in a totally longer timescale in order to achieve equilibrium was then examined with the use of dilution measurements. Use of isothermal dilution on its own instead of TD measurements led to worse

estimates of the volatility distribution compared to the TD. However, combining both TD and isothermal dilution measurements led to promising results in the majority of the cases. Cases for which problems remained included those in which the OA does not come close to equilibrium after dilution or when the corresponding evaporated fraction is less than 20%. Increased dilution and longer residence times could help in these cases. The approach combining TD and isothermal dilution measurements was recommended for future studies of OA volatility in both the lab and the field.

Ambient experimental data from a thermodenuder (TD) coupled to a High-Resolution Time-of-Flight Aerosol Mass Spectrometer (HR-ToF-AMS) collected in Paris and Athens were analyzed using the approach developed in the first part of this work. For the winter and summer campaign in Paris the thermograms surprisingly did not show significant differences, while the estimated volatility distributions, were also similar, with a bimodal shape with two major peaks: one at  $C^*$  of the order of  $10^{-4} \mu\text{g m}^{-3}$  and the second at  $C^*$  of the order of  $10 \mu\text{g m}^{-3}$ . The volatility distributions of PMF factors were also derived during both campaigns. Five factors were determined for the summer dataset. Hydrocarbon-like OA (HOA), cooking OA (COA), marine OA (MOA) and two Secondary OA (SOA) factors were also identified: Semi-volatile oxygenated OA (SV-OOA) and low volatility oxygenated OA (LV-OOA). The PMF analysis for the winter campaign determined four factors. The HOA and COA factors were again identified. There was also a single secondary OA factor that was termed oxygenated OA (OOA). The final factor observed was biomass burning OA (BBOA). The HOA factors for both campaigns in Paris had similar volatility distributions with half material being SVOCs. This similarity was consistent with the corresponding mass spectra derived by the PMF analysis and was not surprising for a city, with similar transportation and industrial emissions in both seasons. The summer COA was significantly more volatile than the winter COA. The winter COA did not contain any semi-volatile organic components (SVOCs) whereas 37% of the summer COA was semi-volatile. These differences in volatility were consistent with the differences in AMS spectra and could be due to different seasonal cooking habits. The LV-OOA factor detected in the summer had the lowest volatility of all the derived factors. The LV-OOA factor consisted nearly exclusively of ELVOCs (97%). Roughly half of the SV-OOA mass consisted of SVOCs while the rest was mainly LVOCs (42%). The OOA factor determined in the winter had a volatility distribution containing SVOCs (45%), ELVOCs (30%) and LVOCs (25%). The marine OA (MOA) factor, only detected during the summer campaign,

was relatively volatile. Half of the BBOA consisted of SVOCs and the other half of extremely low volatile and low volatile organic components. The BBOA was less volatile than the HOA factors but more volatile than COA and OOA.

The OA in Athens consisted of 40% SVOCs, 30% LVOCs and 30% ELVOCs. PMF analysis, during this campaign resulted in three primary OA factors (HOA, BBOA and COA) and one secondary OA factor (OOA). 30% of the HOA was semi-volatile material (SVOCs) and 40% LVOCs. The rest of the material was ELVOCs. BBOA was the most volatile factor. 40% of the BBOA consisted of LVOCs and another 50% of SVOCs. However, a small amount of ELVOC material, around 10% of the BBOA, was present. LVOCs contributed 65% to the COA mass, with another 25% being SVOCs and the rest was ELVOCs. OOA was the least volatile factor. It consisted of 40% ELVOC material, almost 25% LVOCs and 35% SVOCs. Combining the O:C ratio and volatility distributions of the various factors, we integrated our results from both campaigns into the 2D-VBS synthesizing the corresponding OA findings. The factor locations agreed well with the location of factors proposed by Donahue et al. (2012), with the exception of the ELVOC components of most factors. The average O:C was not directly linked to the factor's volatility distribution, underlining the importance of measuring both properties.

The combination of TD and isothermal dilution for the estimation of the volatility distribution was tested experimentally using cooking OA from meat grilling. Size dependent losses were taken into account for the correction of both thermogravimetric and dilution measurements. All the COA evaporated in the TD at 225°C while 80% remained after dilution by a factor of 10 at ambient temperature. The COA average volatility was between 0.05 and 0.1  $\mu\text{g m}^{-3}$  and it consisted of 60-75% LVOCs, 25-30% SVOCs, and a small fraction (10%) of IVOCs at concentrations close to 500  $\mu\text{g m}^{-3}$ . The estimated effective vaporization enthalpy was  $100 \pm 15 \text{ kJ mol}^{-1}$ , and the effective accommodation coefficient was around 0.05. The apparent differences in volatility distributions of the ambient COA factor determined in Athens and the laboratory COA were due to the different concentrations during the two measurements. After calculation of the expected volatility distribution of the COA at ambient levels the distributions were consistent with each other. The use of only TD measurements resulted in an overestimation of the SVOC fraction of COA leading to a shifting of volatility toward higher values. Use of isothermal dilution resulted in decrease of

the uncertainty of the higher volatility components and of the estimated effective enthalpy of vaporization.

The effects of the parameterization of the chemical aging processes of atmospheric organic compounds on organic aerosol (OA) concentration and chemical composition were investigated by using different formulations of the two-dimensional Volatility Basis Set (2D-VBS) together with ground and airborne measurements in the Po Valley in Italy. The predictions of the simple functionalization model of Murphy et al. (2012), were satisfactory both at the ground and aloft, within experimental variability and with fractional biases for the 4-hour average O:C and OA concentration around 10%. The vertical profile for both predictions of the 1-bin case and Zeppelin measurements was relatively flat inside the lowest 1 km and the diurnal variation in O:C ratio was modest. They both suggested a relatively oxidized OA for Po Valley in Italy with an average O:C around 0.6. Anthropogenic SOA and SOA from intermediate volatility compounds oxidation dominated the predicted OA composition based on this parameterization. Seven aging schemes (out of more than a hundred tested), with different assumed functionalizations, bSOA aging and fragmentation were found to reproduce well the ground and Zeppelin O:C and OA measurements. Anthropogenic SOA from VOCs was predicted to contribute between 15 and 25% of the total OA and SOA from the oxidation of intermediate volatility compounds oxidation between 20 and 35%. The contribution of biogenic SOA varied from 15 to 45%, depending on the parameterization scheme. POA was around 5%, the OA from long range transport varied from 6 to 8% and the SOA from evaporation of the primary and subsequent oxidation from 7 to 11%. These results are encouraging because despite the uncertainty introduced by the different schemes, their predictions about source contributions are relatively robust. Addition of bSOA produced during the corresponding chemical aging reactions in the functionalization-only schemes resulted in overpredictions of the OA. Addition of significant fragmentation (fragmentation probabilities ranging from 15 to 70%) was necessary to balance this additional source. This is clearly a topic that deserves additional research both in the laboratory and in the field. There was also surprising low sensitivity of predicted OA concentration and O:C both at the ground and aloft to enthalpy of vaporization.

Finally, the above “optimized” chemical aging schemes were applied in a very different environment, the boreal forest and their results were compared to ground measurements in

Hyttiälä, Finland. Despite the very different environment, the performance of all parameterizations was surprisingly similar to that in the Po Valley. The simple functionalization only parameterization of Murphy et al. (2012) had for one more time the best performance. This simple scheme appears for some reason that is not well understood to capture the behavior of OA in a lot of different environments both rural and polluted. Its variation with a 2-bin change performed almost as well. Schemes adding significant bSOA during aging reactions, or assuming aggressive functionalization were once more the worst performers. Addition of fragmentation was needed for these schemes. The fragmentation schemes with the probability values optimized for Po Valley performed quite well in this case too. Increasing fragmentation rates are needed to “balance” the assumed net bSOA production during aging as the functionalization scheme becomes more aggressive. Despite their differences, the seven schemes that performed well for OA predicted similar OA composition for the simulated period: 40-63% biogenic SOA, 11-18% SOA from anthropogenic VOCs, 14-27% SOA from IVOCs, 4% POA, 4-6% SOA from evaporated POA, and 5-6% from long range transport. This agreement is encouraging about our ability to constrain the SOA sources.

## **7.2 Future work**

### **7.2.1 Use of thermodenuder and Isothermal Dilution Measurements for the estimation of volatility of ambient OA.**

A new experimental approach, using not only thermodenuder but also isothermal dilution measurements was evaluated, in Chapter 4, with meat charbroiling or cooking OA in the lab used for the application of this method. Until now, campaigns have been estimating volatility using only TD measurements. Use of isothermal dilution too can reduce significantly the uncertainty of these measurements. Experimental challenges related to the lower, compared to the lab, concentrations of the ambient OA must be also addressed. Saleh et al. (2012) used a particle concentrator upstream of a TD in order to achieve higher ambient aerosol loadings. An idea would be to use initially a similar particle concentrator before the isothermal dilution reactor.

### 7.2.2 Simulation of volatility - oxygen content distribution of the OA during SOAS campaign

The Southern Oxidant and Aerosol Study (SOAS) campaign took place in the Southeast US. This area is an ideal location to study biogenic-anthropogenic pollutant interactions due to the proximity of vegetative emissions with a variety of man-made emissions sources. The comprehensive data sets collected in this area (including TD measurements) can help further constrain the various 2D-VBS schemes especially regarding the bSOA aging process.

### 7.3 References

- Donahue, N. M., Kroll, J. H., Pandis, S. N., and Robinson, A. L.: A two-dimensional volatility basis set: 1. organic-aerosol mixing thermodynamics, *Atmos. Chem. Phys.*, 11, 3303–3318, 10.5194/acp-11-3303-2011, 2011.
- Donahue, N. M., Kroll, J. H., Pandis, S. N., and Robinson, A. L.: A two-dimensional volatility basis set – Part 2: Diagnostics of organic-aerosol evolution, *Atmos. Chem. Phys.*, 12, 615–634, 10.5194/acp-12-615-2012, 2012.
- Murphy, B. N., Donahue, N. M., Fountoukis, C., Dall’Osto, M., Dowd, C.O., Kiendler-Scharr, A., and Pandis, S. N.: Functionalization and fragmentation during ambient organic aerosol aging: application of the 2-D volatility basis set to field studies, *Atmos. Chem. Phys.*, 12, 10797-10816, 10.5194/acp-12-10797-10816-2012, 2012.
- Saleh, R., Khlystov, A. and Shihadeh, A.: Determination of evaporation coefficients of ambient and laboratory-generated semivolatile organic aerosols from phase equilibration kinetics in a thermodenuder, *Aerosol Sci. Technol.*, 46, 22–30, 2012.

# Appendices

## Appendix A

### Estimation of the volatility distribution of ambient organic aerosol and its components using thermodenuder measurements

**Table A.1** Estimated volatility distributions for the OA and the PMF factors from Paris summer and winter campaign.<sup>a</sup>

$C^*$									
OA Type	$10^{-7}$	$10^{-6}$	$10^{-5}$	$10^{-4}$	$10^{-3}$	$10^{-2}$	$10^{-1}$	1	10
<b>Summer 2009</b>									
HOA	-	-	-	0.13	0.14	0.08	0.02	0.06	0.57
COA	-	-	0.13	0.15	0.07	0.2	0.08	0.37	-
MOA	-	-	-	0.03	0.03	0.05	0.28	0.42	0.19
SV-OOA	-	-	-	0.06	0.14	0.15	0.13	0.18	0.34
LV-OOA	0.2	0.24	0.28	0.25	0.03	-	-	-	-
<b>Winter 2010</b>									
HOA	-	-	-	0.11	0.09	0.07	0.12	0.11	0.5
COA	-	0.12	0.11	0.14	0.42	0.11	0.1	-	-
BBOA	-	-	-	0.2	0.09	0.08	0.13	0.09	0.41
OOA	-	-	-	0.3	0.09	0.07	0.09	0.1	0.35

<sup>a</sup> Expressed as fractions of the OA with  $C^* \leq 10 \mu\text{g m}^{-3}$ .

**Table A.2** Estimated volatility distributions for the OA and the PMF factors for Athens campaign.

Saturation concentration $C^*$ ( $\mu\text{g m}^{-3}$ )						
OA Type	$10^{-8}$	$10^{-3}$	$10^{-2}$	$10^{-1}$	1	10
OOA	0.41	0.11	0.09	0.08	0.11	0.20
HOA	0.30	0.07	0.14	0.21	0.17	0.11
BBOA	0.10	0.10	0.15	0.15	0.14	0.36
COA	0.10	0.52	0.08	0.05	0.07	0.18
Total OA	0.30	0.08	0.12	0.12	0.12	0.26

**Table A.3** Calculated average volatilities as  $\log_{10}C^*$  values weighted by the mass fractions of each bin for Athens winter campaign.

OA Type	OOA	HOA	BBOA	COA	Total OA
<b>Average volatility <math>\log_{10}C^*</math> (<math>\mu\text{g m}^{-3}</math>)</b>	-3.72	-3.00	-1.22	-2.45	-2.76

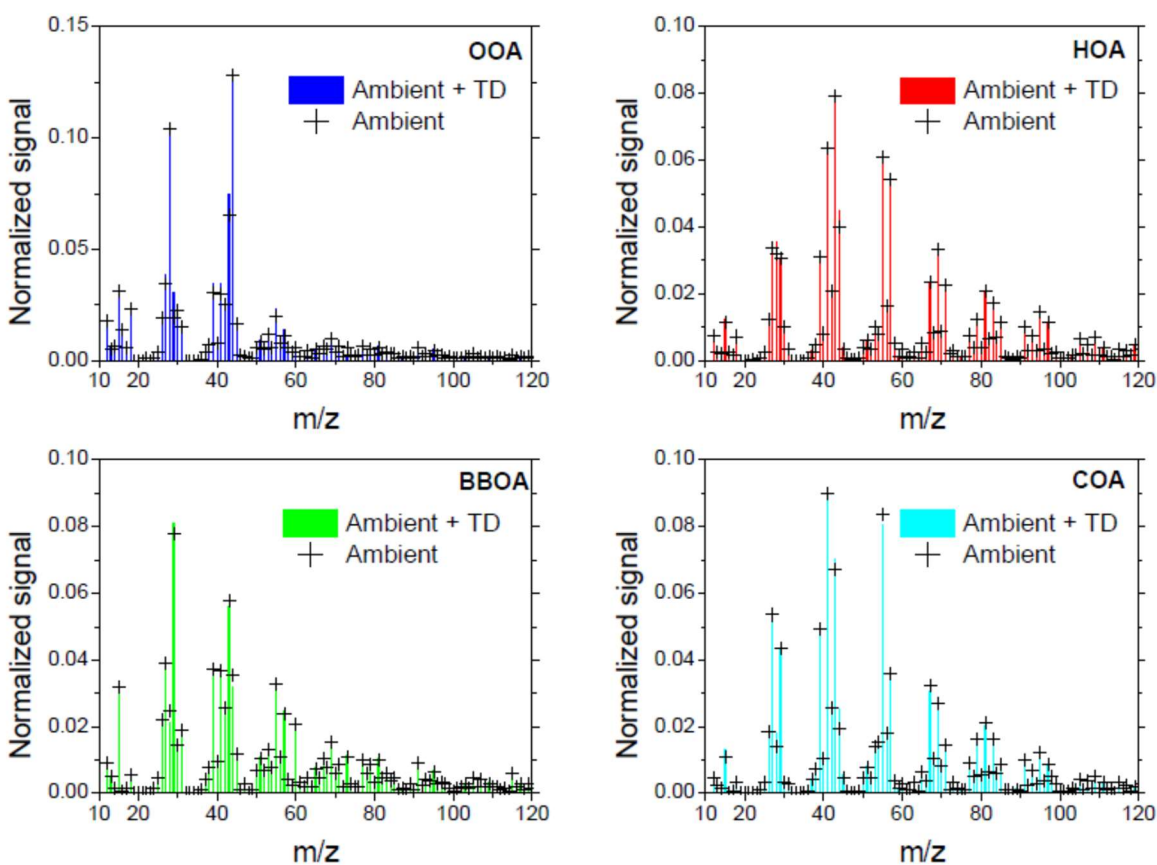


**Figure A.1** Comparison of mass spectra of ambient OA PMF factors analysis (bars) and ambient plus thermodenuder PMF analysis (crosses) during Athens winter 2013 campaign.

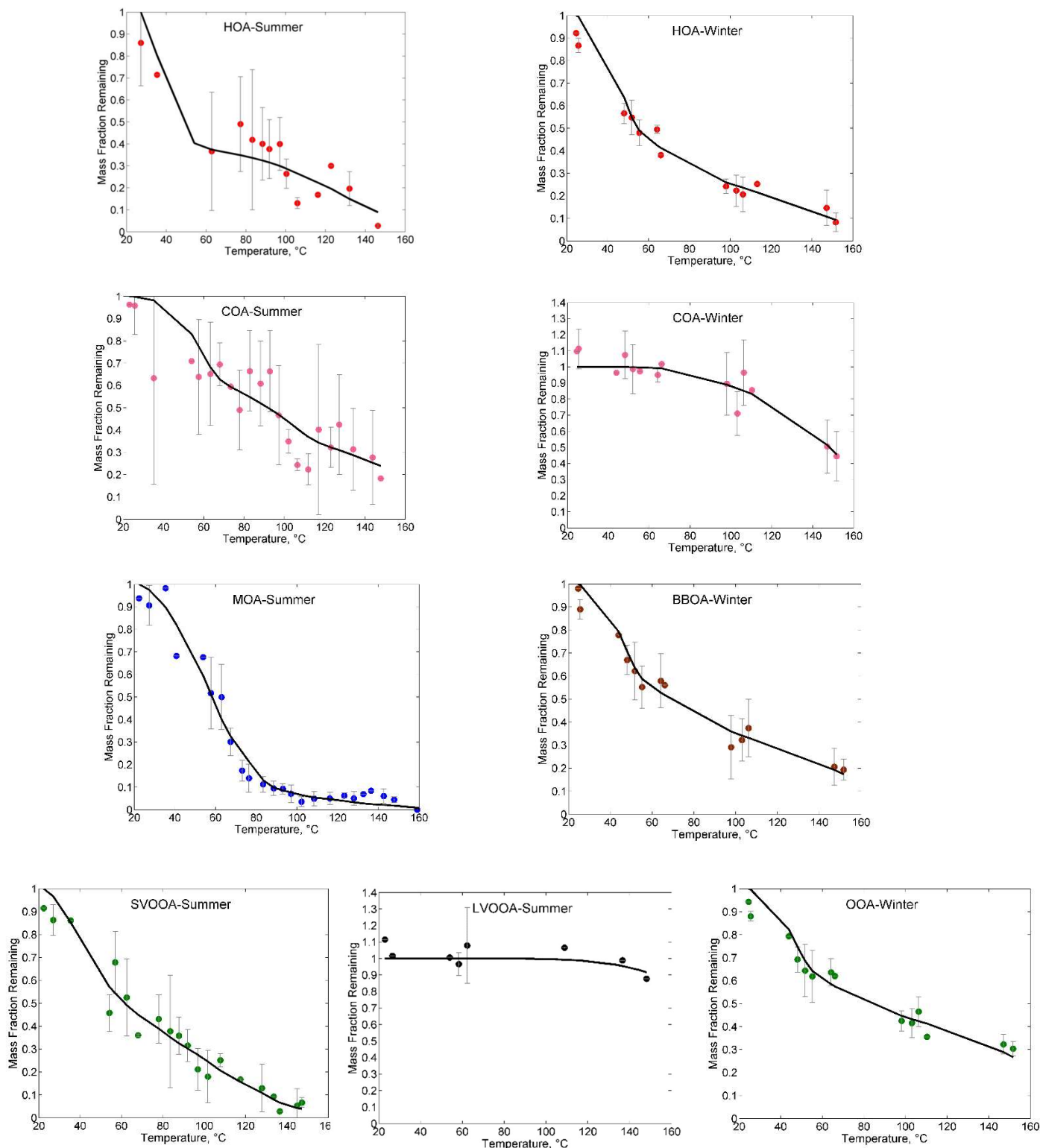


**Figure A.2** Corrected thermograms along with the error bars representing the standard deviation of the data, with best-fit volatility distributions (solid line) for PMF factors during Paris summer and winter campaign. A few points in the LV-OOA summer graph with very high uncertainties are not shown.

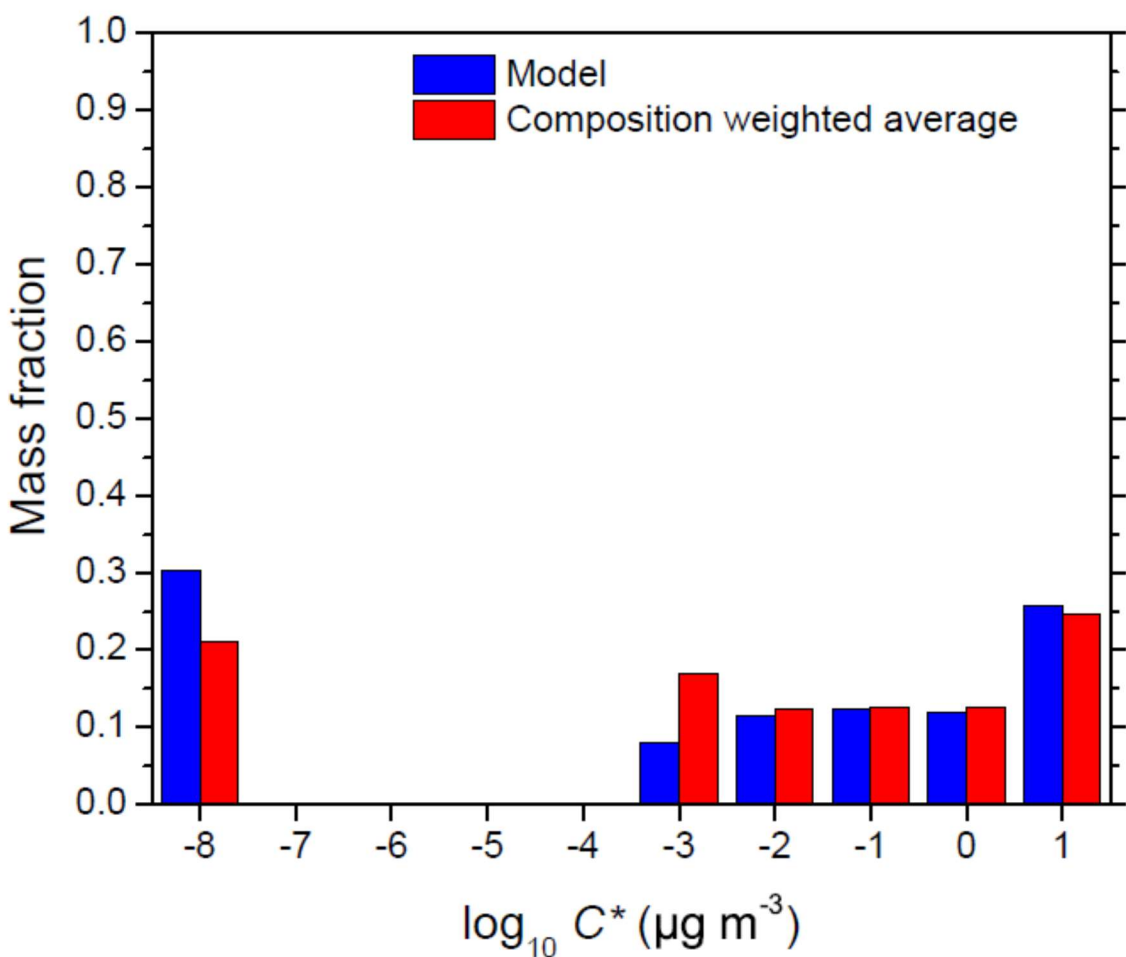


**Figure A.3** Comparison of total OA volatility distributions during Athens winter 2013 campaign estimated by the model of Karnezi et al. (2014) (blue bars) with those calculated by the composition weighted average method (red bars).

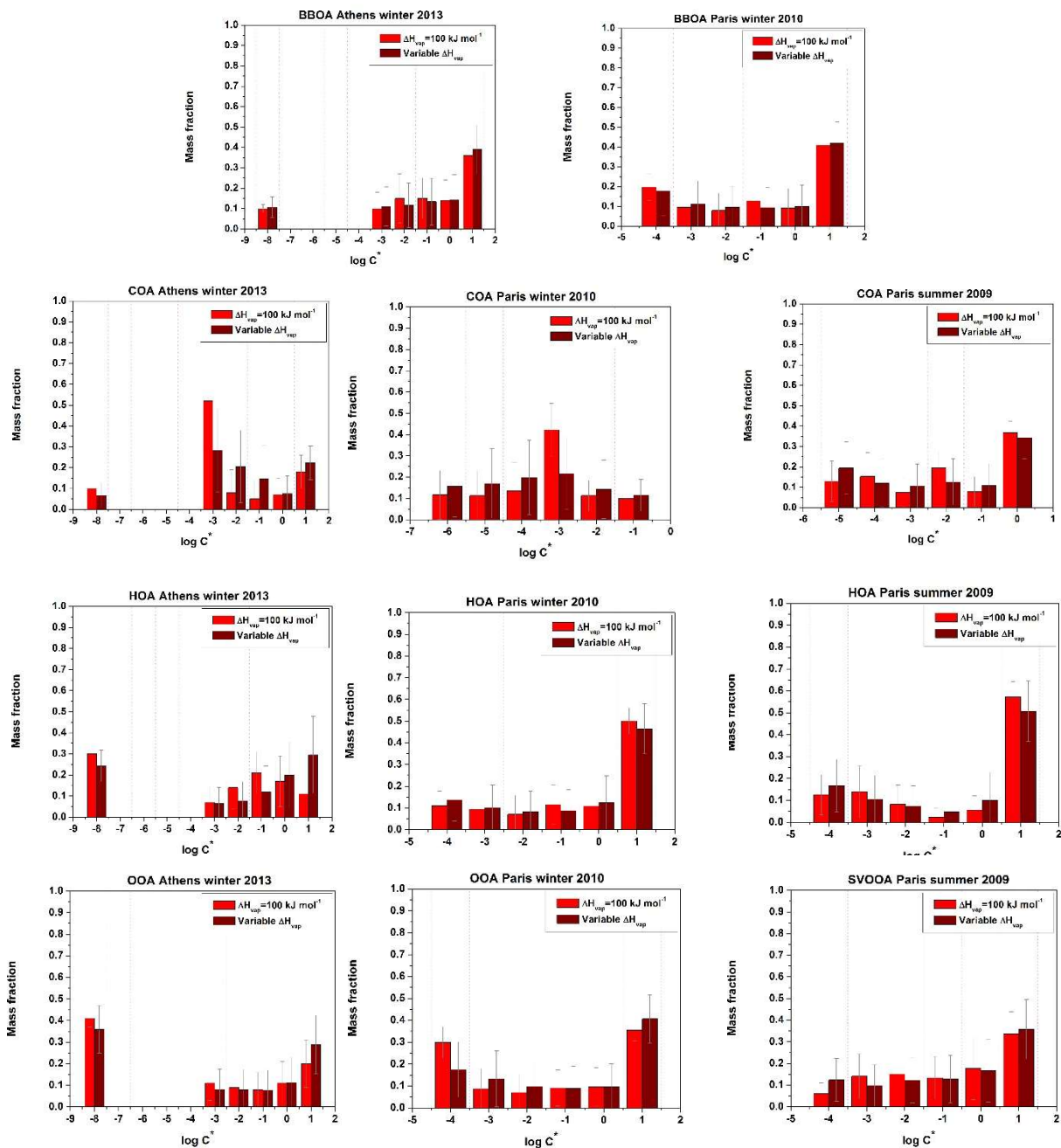


**Figure A.4** Estimated volatility distributions of various OA components during wintertime Athens and Paris summer and winter campaigns for 2 different approaches, using assumed (red bars) or variable (dark red bars)  $\Delta H_{\text{vap}}$ .

Reference:

Karnezi, E., Riipinen, I. and Pandis, S. N.: Measuring the atmospheric organic aerosol volatility distribution: A theoretical analysis, *Atmos. Meas. Tech.*, 7, 2953–2965, 2014.

## Appendix B

### Estimation of the volatility distribution of cooking organic aerosol combining thermodenuder and isothermal dilution measurements

**Table B.1** Estimated volatility distributions for the COA along with estimated properties of the two experiments using both TD and isothermal dilution measurements and only TD measurements using the approach of Karnezi et al. (2014).

Saturation concentration $C^*$ ( $\mu\text{g m}^{-3}$ )	Exp 1		Exp 2	
	TD + Dilution	TD - only	TD + Dilution	TD - only
$10^{-3}$	0.27	0.18	0.23	0.18
$10^{-2}$	0.33	0.24	0.31	0.27
$10^{-1}$	-	-	0.23	0.22
$10^0$	0.19	0.25	0.09	0.18
$10^1$	0.06	0.11	0.07	0.09
$10^2$	0.06	0.10	0.07	0.06
$10^3$	0.09	0.12	-	-
$\Delta H_{\text{vap}}$ ( $\text{kJ mol}^{-1}$ )	$100 \pm 14$	$83 \pm 19$	$85 \pm 9$	$79 \pm 17$
Accommodation coefficient	0.06 (0.01-0.30) <sup>a</sup>	0.14 (0.03-0.59) <sup>a</sup>	0.07 (0.01-0.34) <sup>a</sup>	0.07 (0.01-0.36) <sup>a</sup>
Average volatility $\log_{10} C^*$ ( $\mu\text{g m}^{-3}$ )	0.1	0.44	0.047	0.08

<sup>a</sup> The values in parenthesis represent the corresponding uncertainties for the estimated accommodation coefficients

**Table B.2** Estimated volatility distributions for the sensitivity to the parameter estimation using the approach of Karnezi et al. (2014).

	Saturation concentration ( $\mu\text{g m}^{-3}$ )							$\log_{10}$ ( $\mu\text{g m}^{-3}$ )	$\Delta H_{\text{vap}}$ ( $\text{kJ mol}^{-1}$ )	Accommodation coefficient
	$10^{-3}$	$10^{-2}$	$10^{-1}$	$10^0$	$10^1$	$10^2$	$10^3$			
<b>Exp 1</b>										
Base case	0.27	0.33	-	0.19	0.06	0.06	0.09	0.1	$100 \pm 14$	0.06 (0.01-0.30) <sup>a</sup>
Sensitivity to $a_m$										
$a_m=0.01$	0.20	0.25	-	0.30	0.09	0.07	0.09	0.25	$104 \pm 20$	0.01
$a_m=0.1$	0.29	0.40	-	0.13	0.04	0.06	0.08	0.053	$98 \pm 6$	0.1
$a_m=1.0$	0.35	0.40	-	0.06	0.03	0.06	0.10	0.04	$95 \pm 8$	1.0
Sensitivity to $\Delta H_{\text{vap}}$										
$\Delta H_{\text{vap}} = 80 \text{ kJ mol}^{-1}$	0.10	0.39	-	0.32	0.05	0.05	0.09	0.25	80	0.07 (0.02-0.44) <sup>a</sup>
$\Delta H_{\text{vap}} = 150 \text{ kJ mol}^{-1}$	0.50	0.20	-	0.10	0.04	0.06	0.10	0.036	150	0.01(0.009-0.13) <sup>a</sup>
<b>Exp 2</b>										
Base case	0.23	0.31	0.23	0.09	0.07	0.07	-	0.047	$85 \pm 9$	0.07 (0.01-0.34) <sup>a</sup>
Sensitivity to $a_m$										
$a_m=0.01$	0.14	0.24	0.30	0.14	0.09	0.09	-	0.12	$89 \pm 10$	0.01
$a_m=0.1$	0.24	0.36	0.20	0.07	0.06	0.07	-	0.036	$84 \pm 8$	0.1
$a_m=1.0$	0.33	0.35	0.16	0.04	0.05	0.07	-	0.022	$82 \pm 5$	1.0
Sensitivity to $\Delta H_{\text{vap}}$										
$\Delta H_{\text{vap}} = 80 \text{ kJ mol}^{-1}$	0.16	0.32	0.27	0.11	0.07	0.07	-	0.066	80	0.09 (0.02-0.44) <sup>a</sup>
$\Delta H_{\text{vap}} = 150 \text{ kJ mol}^{-1}$	0.35	0.33	0.12	0.05	0.06	0.09	-	0.026	150	0.025(0.01-0.085) <sup>a</sup>

<sup>a</sup> The values in parenthesis represent the corresponding uncertainties for the estimated accommodation coefficients

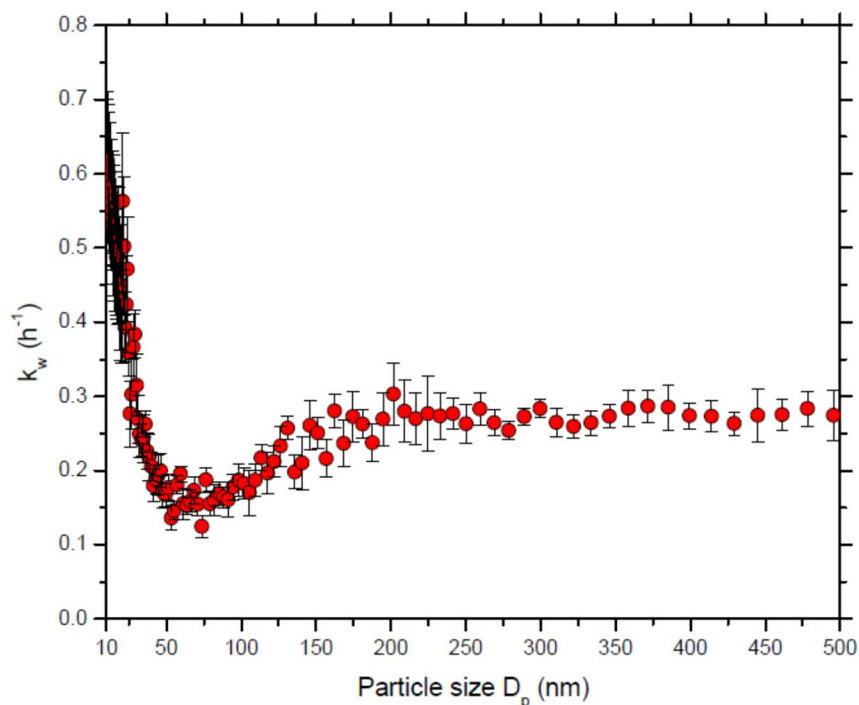


**Figure B.1** Wall loss rate constants as a function of particle size (red circles) for the isothermal dilution chamber during Exp. 1. The error bars represent the  $\pm 1$  standard deviation.

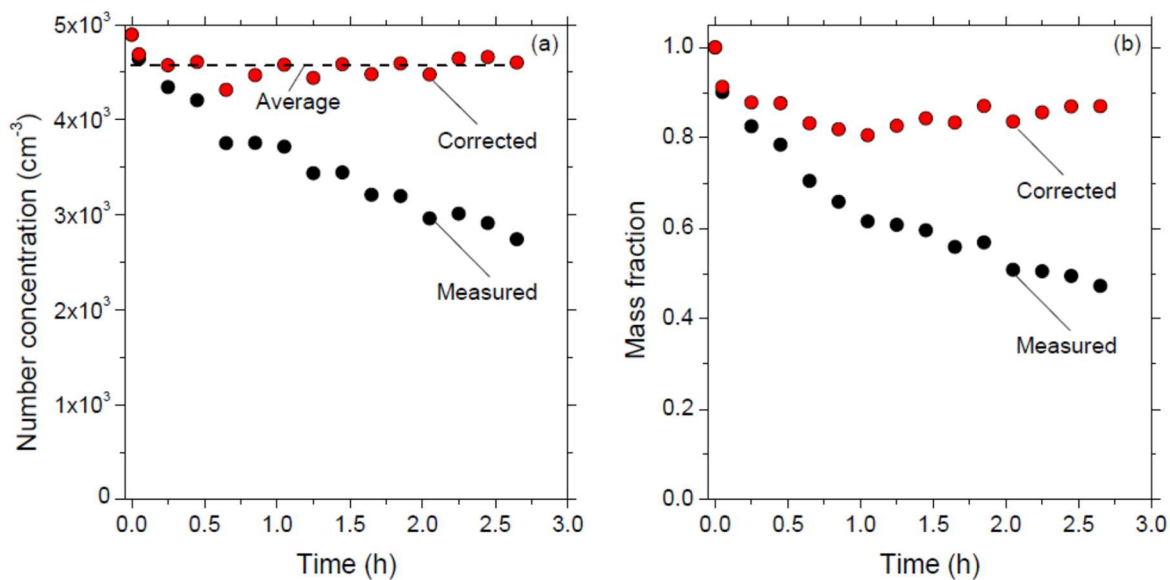


**Figure B.2** (a) Number concentration during isothermal dilution of Exp. 1 as a function of time measured by the SMPS. (b) Mass fraction as function of time during isothermal dilution of Exp. 1 measured by the SMPS.

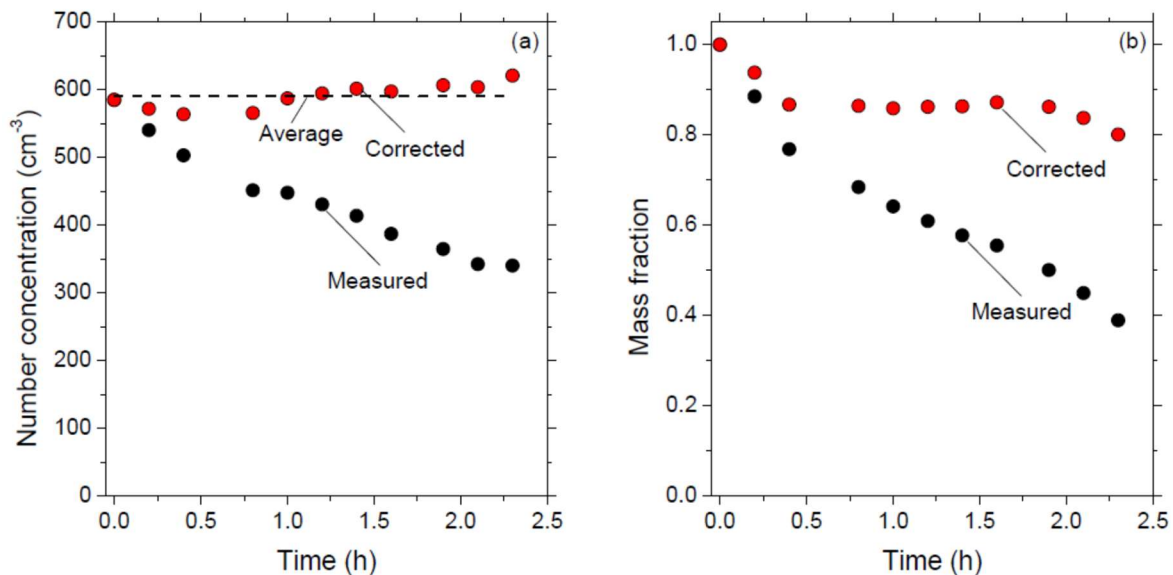


**Figure B.3** (a) Number concentration during isothermal dilution of Exp. 2 as a function of time measured by the SMPS. (b) Mass fraction as function of time during isothermal dilution of Exp. 2 measured by the SMPS.

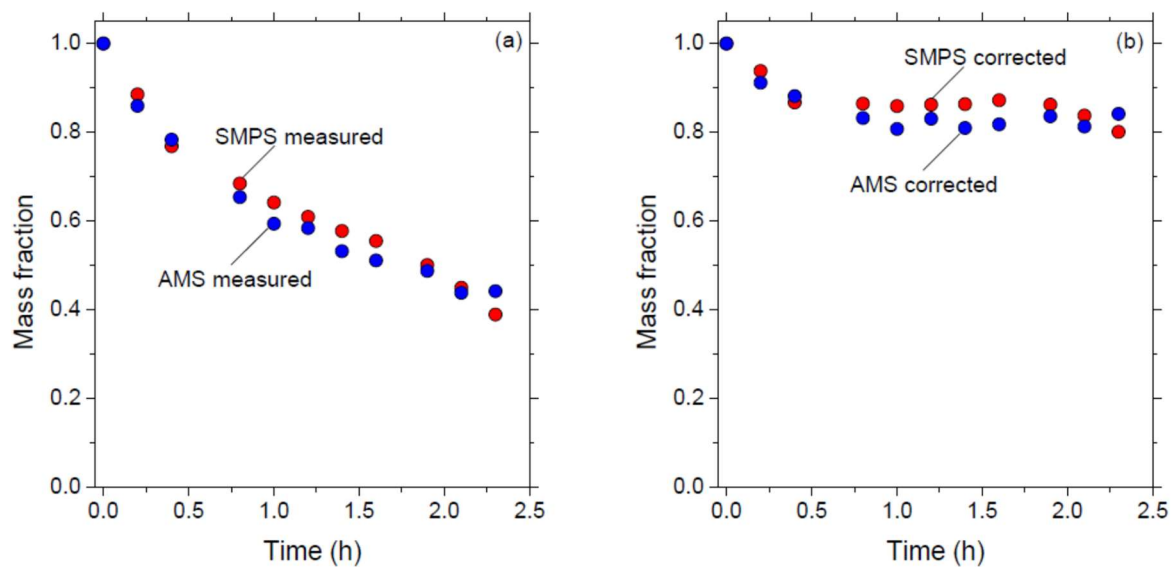


**Figure B.4** (a) Measured mass fractions as function of time during isothermal dilution of Exp. 2. (b) Corrected mass fractions as a function of time during isothermal dilution of Exp. 2.

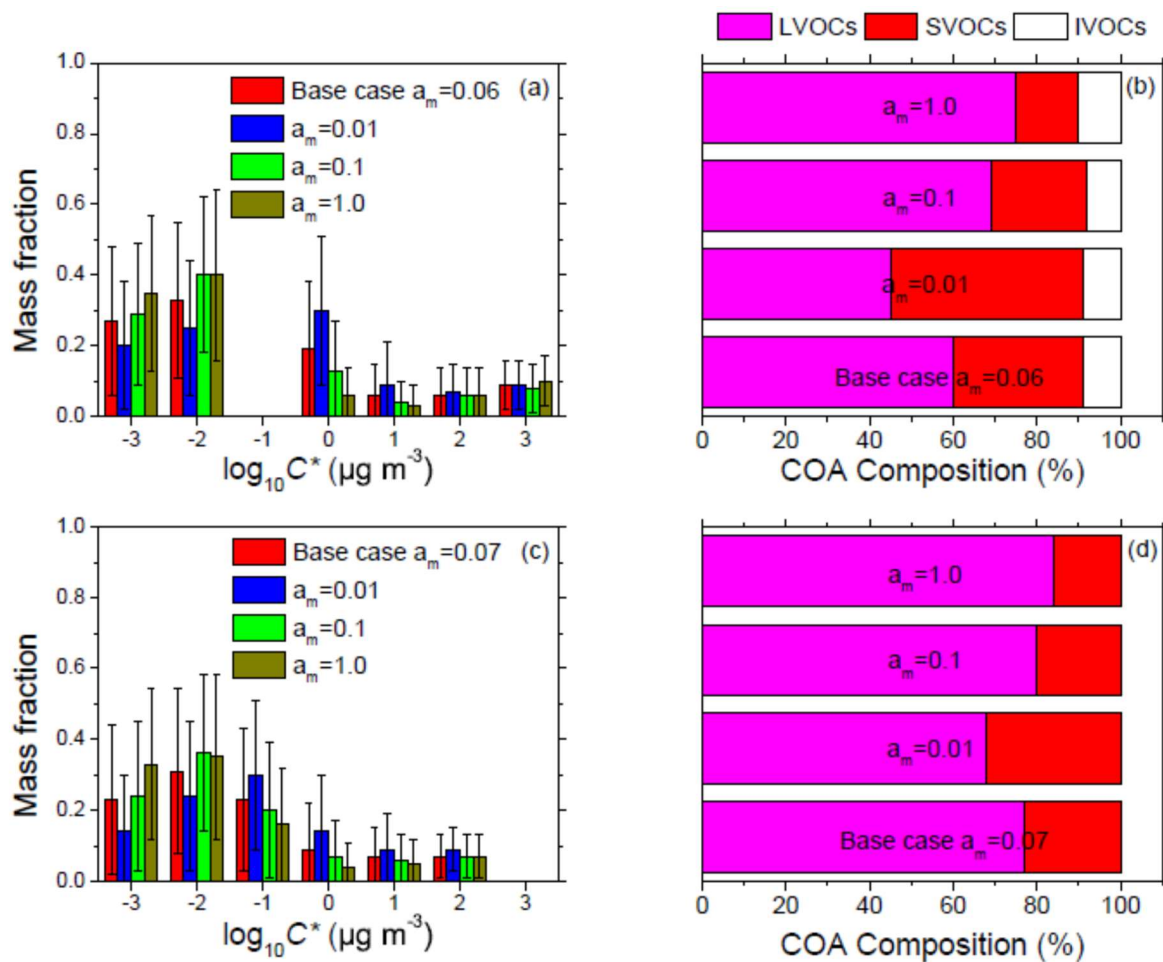


**Figure B.5** (a) Estimated volatility distributions assuming different accommodation coefficients for Exp. 1 using the approach of Karnezi et al. (2014). The error bars represent the corresponding uncertainty ranges. Red, blue, green, and dark yellow bars represent the estimated volatility distributions for the base case,  $a_m=0.01$ ,  $a_m = 0.1$ , and  $a_m = 1.0$  respectively. (b) Corresponding COA composition of Exp. 1. LVOCs are represented in magenta, SVOCs in red, and IVOCs in white. (c) Estimated volatility distributions for different accommodation coefficients for Exp. 2 using the approach of Karnezi et al. (2014). The error bars represent the corresponding uncertainty ranges. Red, blue, green, and dark yellow bars represent the estimated volatility distributions for the base case,  $a_m=0.01$ ,  $a_m = 0.1$ , and  $a_m = 1.0$  respectively. (d) Corresponding COA composition of Exp. 2. LVOCs are represented in magenta, SVOCs in red.

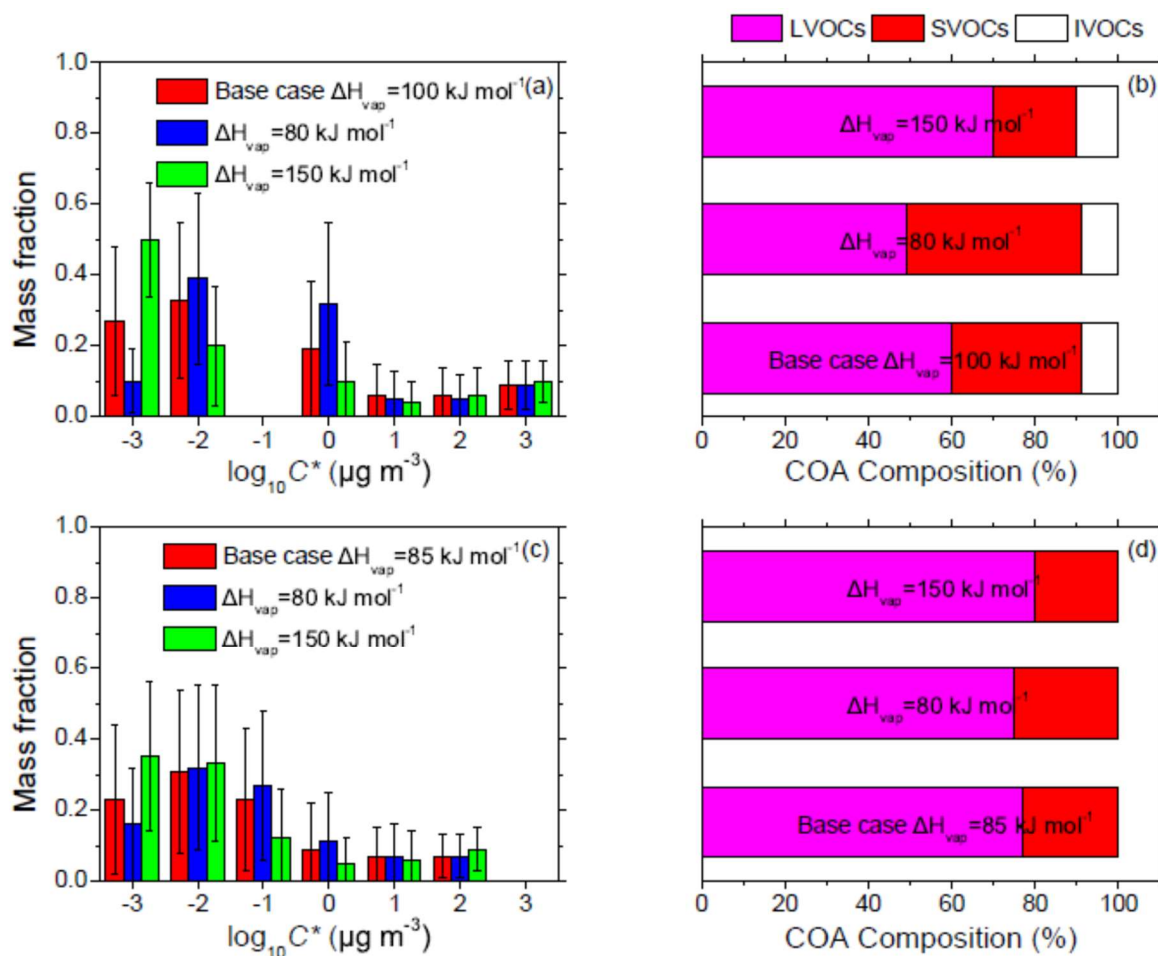


**Figure B.6** (a) Estimated volatility distributions assuming different vaporization enthalpies for Exp. 1 using the approach of Karnezi et al. (2014). The error bars represent the corresponding uncertainty ranges. Red, blue, and green bars represent the estimated volatility distributions for the base case,  $\Delta H_{\text{vap}}=80 \text{ kJ mol}^{-1}$ , and  $\Delta H_{\text{vap}}=150 \text{ kJ mol}^{-1}$  respectively. (b) Corresponding COA composition of Exp. 1. LVOCs are represented in magenta, SVOCs in red, and IVOCs in white. (c) Estimated volatility distributions assuming different vaporization enthalpies for Exp. 2 using the approach of Karnezi et al. (2014). The error bars represent the corresponding uncertainty ranges. Red, blue, and green bars represent the estimated volatility distributions for the base case,  $\Delta H_{\text{vap}}=80 \text{ kJ mol}^{-1}$ , and  $\Delta H_{\text{vap}}=150 \text{ kJ mol}^{-1}$  respectively. (d) Corresponding COA composition of Exp. 2. LVOCs are represented in magenta, SVOCs in red.

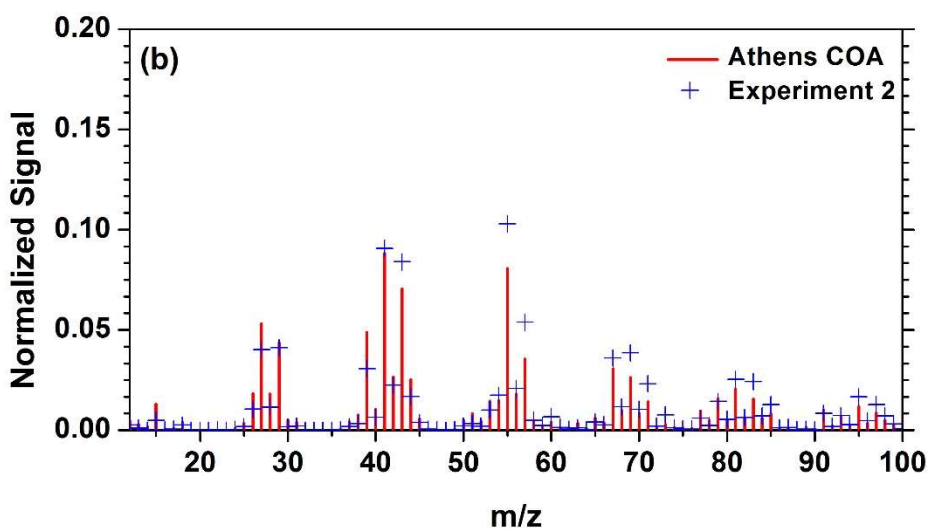
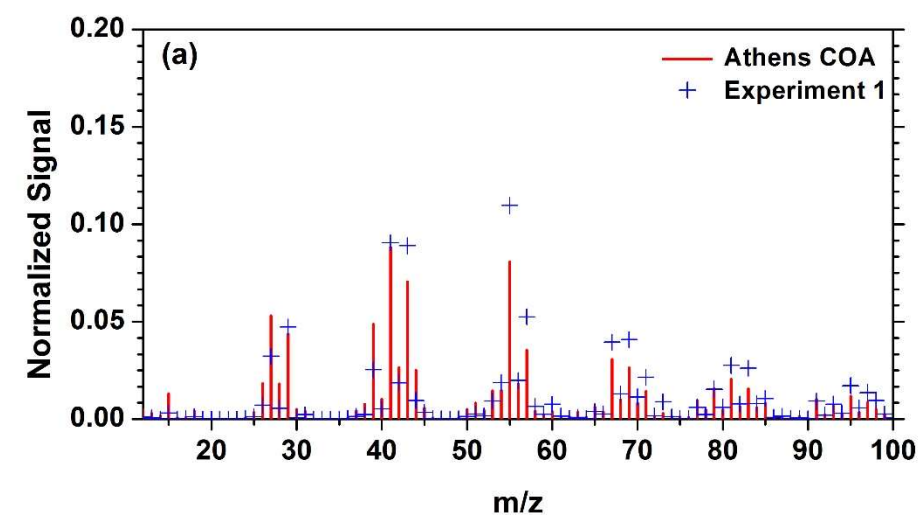


**Figure B.7** Bypass AMS spectra for Athens winter campaign and COA factor (Louvaris et al., 2017) for (a) Experiment 1 COA and (b) Experiment 2 COA from meat charbroiling.

## References

- Karnezi, E., Riipinen, I. and Pandis, S. N.: Measuring the atmospheric organic aerosol volatility distribution: A theoretical analysis, *Atmos. Meas. Tech.*, 7, 2953–2965, 2014.
- Louvaris, E. E., Florou, K., Karnezi, E., Papanastasiou, D. K., Gkatzelis, G. I. and Pandis, S. N.: Volatility of source apportioned wintertime organic aerosol in the city of Athens, *Atmos. Env.* (under review), 2017.

## Appendix C

### Simulation of atmospheric organic aerosol using its volatility-oxygen content distribution during the PEGASOS 2012 campaign in Po Valley, Italy

**Table C.1** Performance of simulations with various vaporization enthalpies for the 1-bin parameterization during PEGASOS campaign for O:C measurements at the ground.

Simulation	Measured Average	Predicted Average	Fractional Error	Fractional Bias	Absolute Error	Absolute Bias
1-bin with $\Delta H_{\text{vap}} = 30$ $\text{kJ mol}^{-1}$	0.58	0.64	0.14	0.10	0.09	0.06
1-bin with $\Delta H_{\text{vap}} = 75$ $\text{kJ mol}^{-1}$		0.62	0.12	0.07	0.07	0.04
1-bin with $\Delta H_{\text{vap}} = 150$ $\text{kJ mol}^{-1}$		0.59	0.11	0.02	0.06	0.007



**Figure C.1** The path that the Zeppelin followed during one representative day (July 4, 2012), over the Po Valley in Italy.

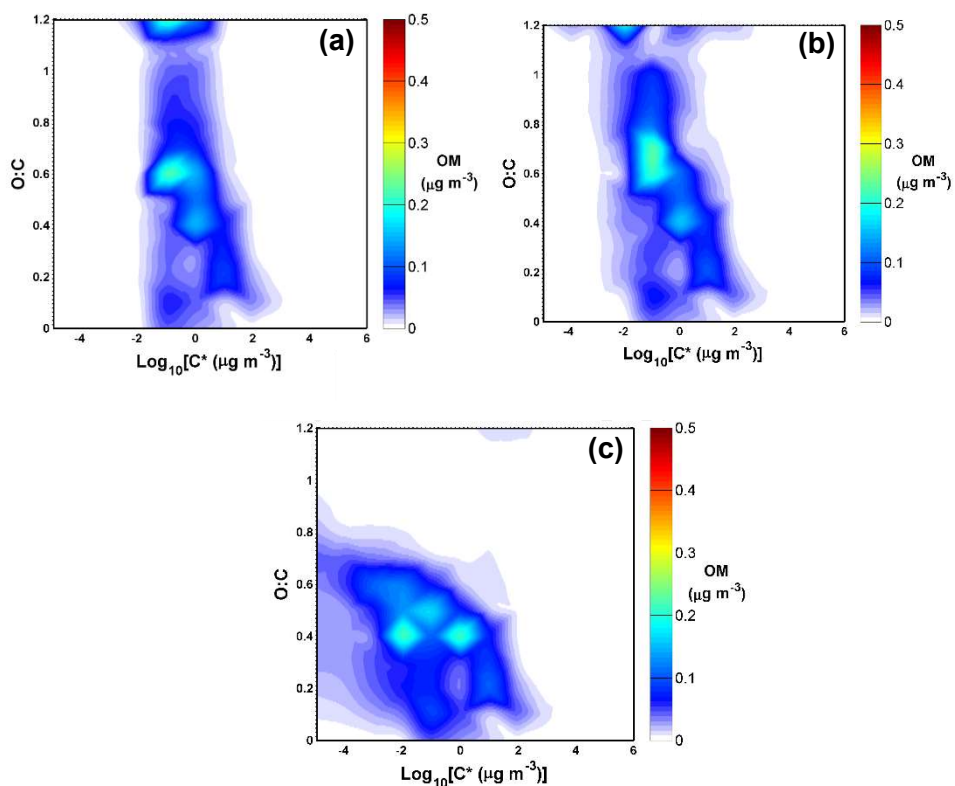


**Figure C.2** Average O:C-volatility distribution of OA mass concentration on San Pietro Capofiume using (a) the simple scheme (1-bin), (b) the two-bin shift simple scheme (2-bin) and (c) the detailed functionalization scheme (DET).

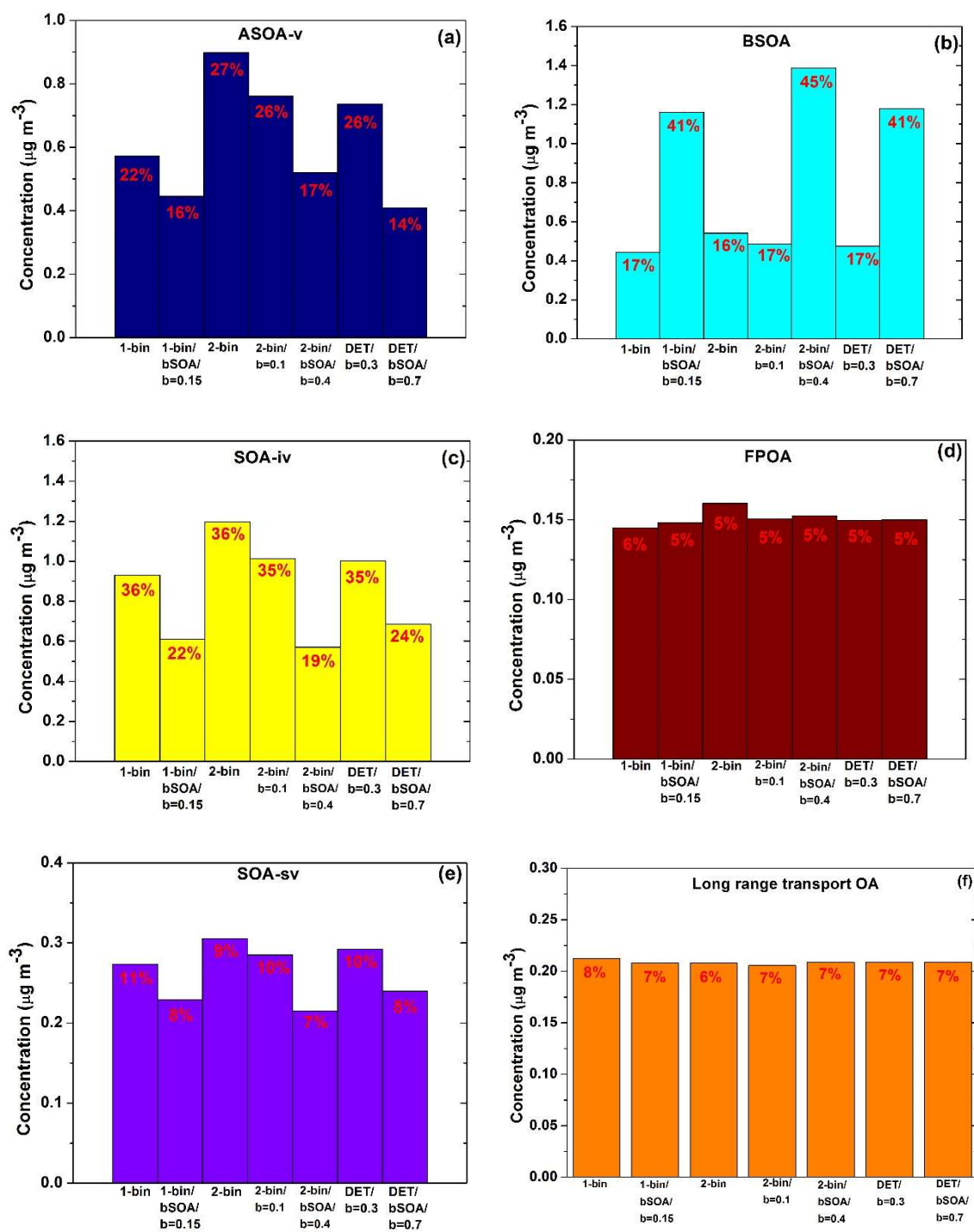


**Figure C.3** Predicted contribution of (a) ASOA-v, (b) bSOA, (c) SOA from oxidation of intermediate volatility organic compounds (SOA-iv), (d) FPOA, (e) SOA from oxidation of evaporated POA, and (f) OA from long range transport for the various aging parameterizations.

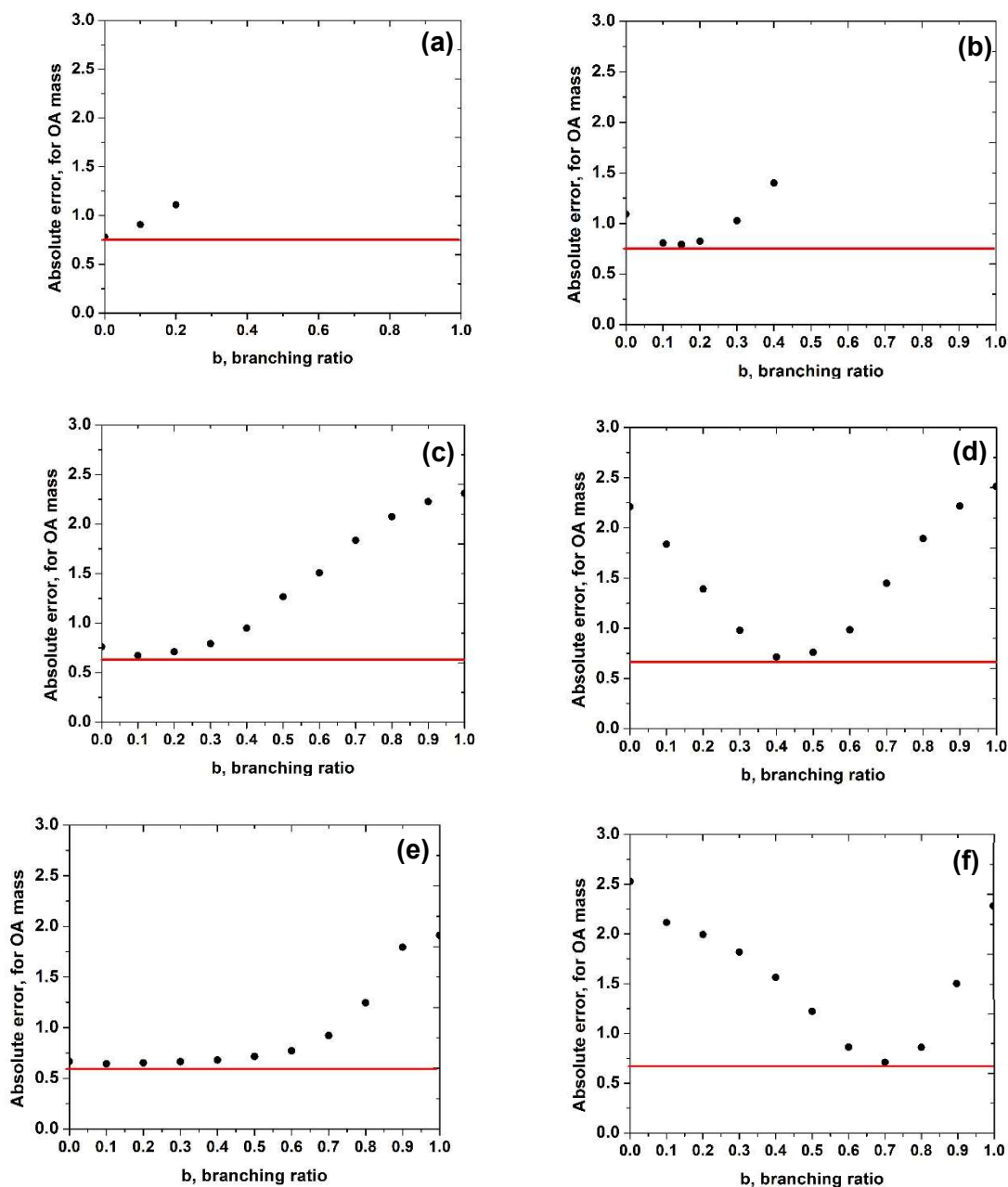


**Figure C.4** Estimation of optimum branching ratio (fragmentation probability) for fragmentation for the: (a) simple functionalization (1-bin), (b) simple functionalization with bSOA aging (1-bin/bSOA), (c) 2-bin functionalization (2-bin), (d) 2-bin functionalization with bSOA aging (2-bin/bSOA), (e) detailed functionalization scheme (DET) and (f) detailed functionalization with bSOA aging (DET/bSOA). The red line shows the minimum absolute error. Note that for the first case of 1-bin parameterization the optimum is at  $b=0$ .

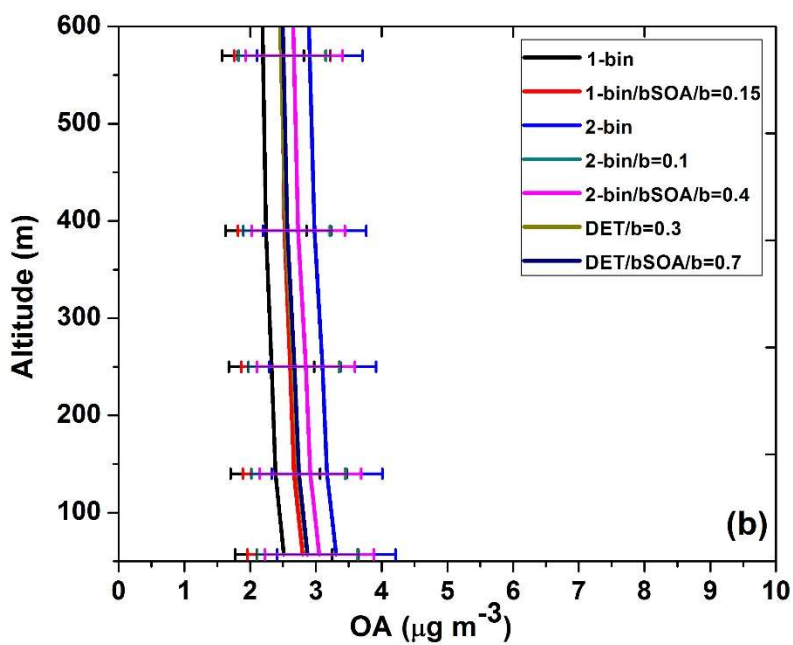
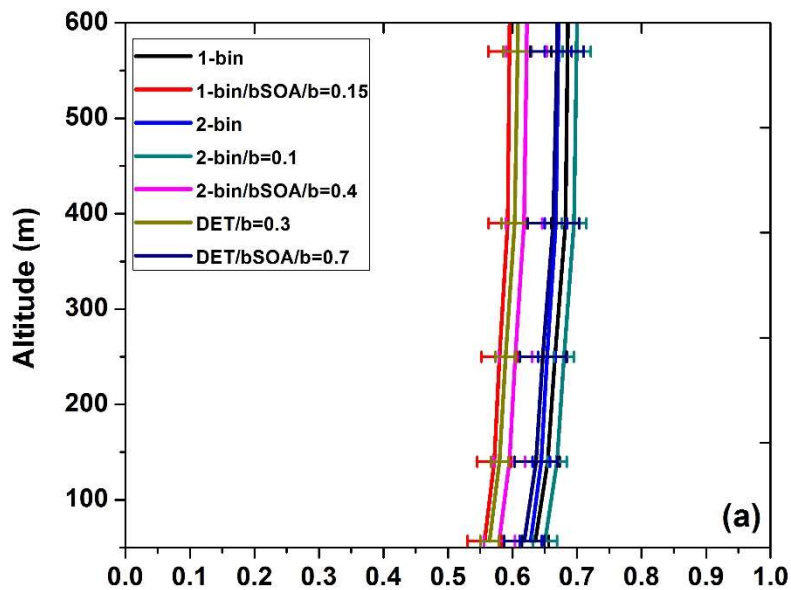


**Figure C.5** Averaged vertical profiles for (a) O:C ratio and (b) OA mass concentration using various parameterizations.